

https://dspace.org/

Design and evaluation of metal-liganded bioactive delivery system for enhanced oral bioavailability

M'bitsi-Ibouily, Gretta

2019
https://hdl.handle.net/10539/29801

Downloaded from a DSpace repository. https://dspace.org/

DESIGN AND EVALUATION OF METAL-LIGANDED BIOACTIVE DELIVERY SYSTEM FOR ENHANCED ORAL BIOAVAILABILITY

GRETTA CORNELIA M'BITSI-IBOUILY

A thesis submitted to the Faculty of Health Sciences, University of the Witwatersrand, Johannesburg, in fulfilment of the requirements for the degree of Doctor of Philosophy

Supervisor:

Professor Viness Pillay

Department of Pharmacy and Pharmacology, University of the Witwatersrand, Johannesburg, South Africa

Co-Supervisors:

Professor Yahya E. Choonara

Department of Pharmacy and Pharmacology, University of the Witwatersrand, Johannesburg, South Africa

Professor Girish Modi

Department of Neurology, University of the Witwatersrand, Johannesburg, South Africa

Dr Thashree Marimuthu

Department of Pharmacy and Pharmacology, University of the Witwatersrand, Johannesburg, South Africa

Johannesburg, 2019

DECLARATION

I, Gretta Cornelia M'bitsi-Ibouily, declare that this thesis is my own work. It has been submitted for the degree of Doctor of Philosophy in the Faculty of Health Sciences at the University of Witwatersrand, Johannesburg, South Africa. It has not been submitted before for any degree or examination at this or any other University.

……

Signed at …… this day of …….. 2019

RESEARCH OUTPUTS

Publications

1. Gretta C. M'bitsi-Ibouily, Thashree Marimuthu, Pradeep Kumar, Lisa C. du Toit, Yahya E. Choonara, Pierre P. D. Kondiah and Viness Pillay. Outlook on the Application of Metal-Liganded Bioactives for Stimuli-Responsive Release, *Molecules* 2017, 22 (12), 2065-2076. (Appendix A1).

2. Gretta C. M'bitsi-Ibouily, Thashree Marimuthu, Pradeep Kumar, Yahya E. Choonara, Lisa C. du Toit, Priyamvada Pradeep, Girish Modi, Viness Pillay. Synthesis, Characterisation and *In Vitro* Permeation, Dissolution and Cytotoxic Evaluation of Ruthenium (II)-Liganded Sulpiride and Amino Alcohol, *Scientific Reports* 2019, 9 (1), 4146-4163. (Appendix A2).

Conference proceedings

1. Gretta C. M'bitsi-Ibouily, Thashree Marimuthu, Yahya E. Choonara, Lisa C. du Toit, Pradeep Kumar, Pierre P.D. Kondiah, G. Modi and Viness Pillay. Overcoming the challenges of sulpiride pharmacokinetics through metal coordination and nanotechnology. **Podium presentation**, Wits School of Therapeutics Research Day, 12 September 2017. (Appendix B1).

2. Gretta C. M'bitsi-Ibouily, Thashree Marimuthu, Yahya E. Choonara, Lisa C. du Toit, Pradeep Kumar, G. Modi, Pierre P.D. Kondiah and Viness Pillay. Novel metal complex polymer nanocomposite with enhanced intestinal permeability and controlled release of sulpiride drug. **Poster presentation**, Wits Faculty of Health Sciences Research Day, 6 September 2018. (Appendix B2).

ACKNOWLEDGEMENTS

The pursuit of a PhD is one of my most challenging undertaking yet. I would like to express my deepest gratitude to all who have contributed to the completion of this journey.

To God Almighty, without Whom none of this would be possible.

To my parents Béatrice Kantsou, Paul-Marie Ibouily Nzamba and Marcel Doupamby Matoka, thank you for your love, patience, support and sacrifices. To my siblings, Nelly Koumba Ibouily and Alain Gildas Robaky, thank you for the continued emotional support. A special thank you to my eldest sister Nanice Tsigui for her interest in my project, advice, prayers and for lifting my spirit when times were tough. To my uncle Jean-François Ndongou, thank you for your support. I am truly blessed to have an amazing family and I hope to continue to make you all proud.

My sincere gratitude goes to my ever-loving husband, Stéphane Jacques Soami Mabiala, for his love, motivation, support, patience and his never-failing faith in me. Thank you for being my exceptional life partner. To my adorable daughter Théa Yessie Soami Mabiala, thank you for changing my life for the better. To my in-laws, your encouragements were greatly appreciated. I am infinitely grateful to God for bringing all of you into my life.

I would like to express my gratitude to Prof. Viness Pillay, Prof. Yahya E. Choonara, Prof Girish Modi, Dr Thashree Marimuthu, Dr Pradeep Kumar, Prof Lisa du Toit, Dr Mershen Govender, Dr Sunaina Indermun and Dr Pierre P.D. Kondiah for their guidance, encouragement and useful critique to this research work.

My profound gratitude goes to all my close friends, who have become my family, for their constant encouragements. Thank you for your friendship, prayers, humorous motivation and good memories in all aspects of my life. Special thanks to Parfait Nzamba for his assistance in all computer-related crises, to Danisa Mikala for her involvement in solving my bursary-related incidents, to Orphée Njoh for her company during all-night experiments, to Laetye Koumba for her availability to kindly babysit my daughter whenever needed, to Larissa Kunakey and Sandrine Kougou for their encouraging words.

To all my fellow researchers, your assistance, great or small, has helped me in completing this work. I am grateful to all of you. Special thanks to Dr Olufemi Akilo, Dr Samson Adeyemi, Dr Margaret Siyawamwaya, Mr. Mduduzi Sithole, Mr. Patrick Komane, Ms. Lara Freidus and Ms. Lusanda Mapela for your academic, moral support and the much-needed chats and laughs throughout the duration of my project.

To the technical staff of the Department of Pharmacy and Pharmacology, Ms. Busi Nompumelelo Damane, Mr. Sello Ramarumo, Ms. Pride Mothobi, Mr. Kleinbooi Mohlabi, Mr. Bafana Themba and Mrs. Phumzile Madondo, I sincerely thank you for your assistance. A special thank you to the staff of the Central Animal Services of the University of the Witwatersrand for the all the help and assistance provided to me in the conducting of my animal studies.

I would like to acknowledge the National Research Fund (NRF) and the Agence Nationale des Bourses du Gabon (ANBG) for the financial assistance provided towards this project. Opinions expressed and conclusions arrived at, are those of the author and are not necessarily to be attributed to the NRF nor the ANBG.

"Whatever you do, work heartily, as for the Lord and not for men"
Collossians 3.23.

ABSTRACT

The oral delivery of drugs, especially solid formulations, is one of the most common and widely used routes of drug administration, accounting for approximately 50% of all dosage forms currently on the market. Nevertheless, oral drug delivery of poorly soluble and permeable drugs can be particularly challenging, resulting in low bioavailability and high dosages of these drugs. Consequently, patient compliance is reduced, thereby negatively affecting the intended therapeutic intervention. The preference of patients for the oral route is particularly true in chronic drug therapy, as is the case in the treatment of schizophrenia, due to its convenience and non-invasiveness. Schizophrenia is a severe and incapacitating mental disorder with serious consequences if not properly treated. Sulpiride (SPR) is an antipsychotic agent with proven efficacy in reducing both the positive and negative symptoms of schizophrenia. However, this drug displays various pharmacokinetic limitations including poor aqueous solubility, limited permeability, burst drug release, short half-life and low bioavailability. Sulpiride therapy therefore requires large doses to reach therapeutic efficacy and hence multiple drug administrations. As a result of such therapy regimen, undesirable side effects are experienced and patient compliance is compromised, which ultimately results in lower clinical outcomes. This study reports the design, formulation, characterization and evaluation of a Metal Complex Polymer Nanocomposite (MCPN) delivery system for the sustained oral delivery of sulpiride.

A transition metal organometallic complex of ruthenium (Ru) was designed using Ru as an inert drug carrier complexed to sulpiride to obtain a metal-liganded bioactive, [Ru(*p* -cymene)((R)-(+)-2-amino-3-phenyl-1-propanol)(SPR)]PF_6. A series of analogues were thus designed, synthesized and characterized employing elemental analysis, Fourier Transform Infrared Spectroscopy (FTIR), Nuclear Magnetic Resonance (NMR), thermal analyses and Ultraviolet-Visible (UV-Vis). The metal-liganded bioactive was then evaluated for solubility of SPR in different solvents, *ex vivo* permeation of SPR through porcine intestine, and *in vitro* release of SPR in different pH environments. SPR liganded to the metal exhibited enhanced aqueous solubility (1668 mg/L ± 1.38) and intestinal relative permeability (27.20%) but burst drug release was still observed *in vitro*.

The obtained metal-liganded bioactive was then encapsulated into polymeric nanoparticles using Eudragit® RS 100 and polyvinyl alcohol (PVA) to obtain the MCPN delivery system. The biodegradable copolymer Eudragit® RS 100 was used to protect the metal-liganded bioactive from bond cleavage in gastric pH and provide sustained drug release, while the water-soluble synthetic polymer PVA was used as the aqueous phase for nanoparticle production and to maintain sustained drug release. The designed MCPN was synthesized and evaluated for particle size, zeta potential, entrapment efficiency and drug loading. Further characterization included Differential Scanning Calorimetry (DSC), FTIR and Scanning Electron Microscopy (SEM). The MCPN was then evaluated for *ex vivo* permeation of SPR through porcine intestine, *in vitro* release of SPR in simulated gastric, intestinal and systemic circulation environments. The Taguchi design method with L9 orthogonal array was used to optimize the MCPN formulation. The optimized MCPN formulation was evaluated for *in vitro* toxicity in Caco-2 cell line. SPR in optimized MCPN (particle size: 92.77±3.96, zeta potential: -32.23±3.07, entrapment efficiency: 87.82% and drug loading: 27.45%) resulted in improved intestinal relative permeability (75.65%) and a sustained *in vitro* drug release profile orally, with no noticeable toxic effects on the intestinal epithelium tissue.

The *in vivo* study involved the oral administration of conventional capsule and MCPN capsule to pigs for a comparative study of the two formulations and the collection of blood samples at specified time points for the quantification of SPR and Ru in the animals' plasma using Ultra Performance Liquid Chromatography (UPLC) and Inductively Coupled Plasma-Mass Spectrometry (ICP-MS), respectively. Pharmacokinetic modelling determined sulpiride release, that was best described by a non-compartmental model. The MCPN capsule exhibited a higher SPR peak plasma concentration (C_{max} = 0.9895 µg/mL), reached at an increased time (t_{max} = 12 hours) compared to the conventional capsule (C_{max} = 0.8719 µg/mL and t_{max} = 6 hours). The MCPN delivery system improved the bioavailability of SPR by 25.04% (from 30.26% for the conventional capsule to 55.30% for the MCPN capsule). A Level-A *in vitro-in vivo* correlation was developed that detailed a 79% predictability of sulpiride release. The quantification of Ru in the plasma, liver and kidneys of each pig after MCPN capsule administration using ICP-MS revealed no hematologic, hepatic or renal toxicity associated to the presence of Ru in the MCPN delivery system.

The MCPN delivery system provided enhanced bioavailability of SPR through SPR gastric pH protection, improved SPR aqueous solubility, enhanced intestinal permeability (lipid solubility) and reduced particle size of the formulation. Finally, the MCPN exhibited sustained release of SPR, which allows for maintained therapeutic concentrations of the drug in the systemic circulation throughout the dosing interval, resulting in a lower dosage, reduced side-effects and ultimately improved patient compliance. The combination of metal complexation and nanotechnology was successful in improving the oral bioavailability of sulpiride.

DEDICATION

To my beloved mother, Béatrice Kantsou.

Thank you for teaching me the importance of education and hard work. Thank you for showing me the value of patience and perseverance. Thank you for making me the woman I am today. For your endless love, sacrifice, support, advice, strength and prayers throughout my studies, I dedicate this thesis to you.

To my precious daughter, Théa Yessie Soami Mabiala.

You have made me stronger, better and more fulfilled than I could have ever imagined. Thank you for your contagious joy of life that brightens my world and gives me the courage to become the best version of myself. I hope to make you proud and inspire you. I love you more than words can ever express.

ANIMAL ETHICS DECLARATION

I, Gretta Cornelia M'bitsi-Ibouily, hereby confirm the study entitled "In Vivo Assessment of Innovative Polymeric Oral Drug Delivery Systems in Large White Pigs" was approved by the Animal Ethics Screening Committee (AESC) of the University of the Witwatersrand with Ethics Clearance Number 2017/08/52/C (Appendix C1). The approval for the use of animal tissue samples letter from the University of the Witwatersrand is attached in Appendix C2.

TABLE OF CONTENTS

DECLARATION ii

RESEARCH OUTPUTS iii

ACKNOWLEDGEMENTS iv

ABSTRACT vi

DEDICATION vii

ANIMAL ETHICS DECLARATION viii

LIST OF EQUATIONS xix

LIST OF FIGURES xx

LIST OF TABLES xxiii

LIST OF COMMONLY USED ABBREVIATIONS xxiv

CHAPTER 1
INTRODUCTION AND BACKGROUNG

1.1. BACKGROUND OF THIS STUDY 1

1.2. RATIONALE AND MOTIVATION FOR THIS STUDY 4

1.3. AIM AND OBJECTIVES OF THIS STUDY 6

1.4. NOVELTY OF THIS STUDY 7

1.5. OVERVIEW OF THIS THESIS 8

CHAPTER 2
OUTLOOK ON THE APPLICATION OF METAL-LIGANDED BIOACTIVES FOR STIMULI-RESPONSIVE RELEASE

2.1. INTRODUCTION 9

2.2. pH-TRIGGERED BIOACTIVE RELEASE 11

2.2.1. Bioinspired Materials 11

2.2.2. Self-Assembled Metal-Liganded Bioactives 14

2.3. LIGHT-TRIGGERED BIOACTIVE RELEASE 15

2.3.1. Ruthenium Cage Complexes 15

2.4. REDOX-TRIGGERED BIOACTIVE RELEASE 18

2.5. ION ACTIVATION-TRIGGERED RELEASE OF BIOACTIVE 20

2.6. CONCLUDING REMARKS 20

CHAPTER 3
SYNTHESIS, CHARACTERIZATION AND IN VITRO PERMEATION, DISSOLUTION AND CYTOTOXIC EVALUATION OF RUTHENIUM(II)-LIGANDED SULPIRIDE AND AMINO ALCOHOL

3.1. INTRODUCTION 23

3.2. MATERIALS AND METHODS 25

3.2.1. Materials 25

3.2.2. Instruments 26

3.2.3. Formation/Dissociation constant of the complex [Ru(p-cymene)Cl(SPR)] 26

3.2.3.1. Preparation of $1x10^{-1}$ M [Ru(p-cymene)Cl_2] and $1x10^{-1}$ M SPR 26

3.2.3.2. Procedure for continuous variation method (Job's method) 26

3.2.4. Synthesis of Metal Complexes 27

3.2.4.1. Representative synthesis of the precursor complexes **1-5** 27

3.3.4.2. Representative synthesis of the final complexes **1a**-**5a** 29

3.2.5. Solubility Studies of free SPR and SPR in complexes 1a, 3a and 5a 32

3.2.6. Dissolution studies of free SPR and SPR in complexes 1a, 3a and 5a 33

3.2.7. Permeation studies of free SPR and SPR in complexes 1a, 3a and 5a 34

3.2.8. In vitro toxicity testing of free SPR and SPR in complexes 1a, 3a and 5a using Caco-2 cell line 35

3.2.8.1. Caco-2 cell line culturing 36

3.2.8.2. Cell counting using trypan blue solution assay and a haemocytometer 36

3.2.8.3. In vitro cytotoxicity evaluation using methyl thiazolyl tetrazolium (MTT) assay 36

3.3. RESULTS AND DISCUSSION 37

3.3.1. Formation/Dissociation constant of the complex [Ru(p-cymene)Cl(SPR)] 37

3.3.2. Infrared (IR) spectra with assignments of L1-5, complexes 1-5 and complexes 1a-5a 38

3.3.3. NMR spectra with assignments of L1-5, complexes 1-5 and complexes 1a-5a 41

3.3.4. Thermal analyses (TG, DTG and DSC) studies of L1-5, complexes 1-5 and complexes 1a-5a 45

3.3.5. Ultraviolet-Visible (UV-Vis) spectra of SPR, complexes 1-5 and complexes 1a-5a 45

3.3.6. Fluorescence study 48

3.3.7. Solubility studies of free SPR and SPR in complexes 1a, 3a and 5a 49

3.3.8. Dissolution studies of free SPR and SPR in complexes 1a, 3a and 5a 51
3.3.9. Permeation studies of free SPR and SPR in complexes 1a, 3a and 5a 53
3.3.10. Effects of free SPR and SPR in complexes 1a, 3a and 5a on Caco-2 cell viability 52
3.4. CONCLUDING REMARKS 55

CHAPTER 4
DEVELOPMENT AND IN VITRO EVALUATION OF NOVEL METAL COMPLEX POLYMER NANOCOMPOSITE (MCPN) OF SULPIRIDE DRUG

4.1. INTRODUCTION 56

4.2. MATERIALS AND METHODS 57

4.2.1. Materials 57

4.2.2. Preparation of the MCPN (emulsion solvent evaporation) 57

4.2.2.1. Experimental Design 58

4.1.1.1. Optimization of MCPN parameters 58

4.2.3. Evaluation of prepared MCPN formulations 59

4.2.3.1 Measurement of particle size and zeta potential 59

4.2.3.2. Measurement of drug entrapment efficiency and drug loading 60

4.2.3.3. Differential Scanning Calorimetry (DSC) of complex 1a, Eudragit® RS 100 and MCPN formulations 60

4.2.3.4. Fourier Transform Infrared (FTIR) Spectroscopy of complex 1a, Eudragit® RS 100 and MCPN formulations 60

4.2.3.5. Surface morphology analysis of MCPN 60

4.2.3.6. *Ex vivo* permeation studies of free SPR, SPR in complex **1a** and SPR in MCPN formulations 61

4.2.3.7. *In vitro* drug release study of free SPR, SPR in complex **1a** and SPR in MCPN formulations 62

4.2.4. *In vitro* toxicity testing of SPR in complex 1a and optimized MCPN using Caco-2 cell line 60

4.2.4.1. Caco-2 cell line culturing 63

4.2.4.2. Cell counting using trypan blue solution assay and a haemocytometer 63

4.2.4.3. *In vitro* cytotoxicity evaluation using 3-4,5-Dimethylthiazol-2-yl)-2,5- 63

4.3. RESULTS AND DISCUSSION 64

4.3.4. Particle size and zeta potential 64

4.3.4.1. Taguchi analysis response for MCPN particle size 65

4.3.5. Drug entrapment efficiency and drug loading 66

4.3.5.1. Taguchi analysis response for MCPN drug entrapment efficiency and drug loading 66

4.3.6. Differential scanning calorimetry (DSC) analysis of complex 1a, Eudragit® RS 100 and F2 67

4.3.7. Infrared (IR) spectral analysis of complex 1a, Eudragit® RS 100 and MCPN formulations 69
4.3.8. MCPN surface morphology 70
4.3.9. Permeation studies of complex 1a and MCPN formulations F1-F9 70
4.3.9.1. Taguchi analysis response for MCPN mean dissolution time 71
4.3.10. *In vitro* drug release study 72
4.3.10.1. Taguchi analysis response for SPR mean dissolution time 73
4.3.11. Optimized MCPN formulation 74
4.3.12. Effects of SPR in complex 1a and SPR in optimized MCPN on Caco-2 cell viability 75
4.4. CONCLUDING REMARKS 76

CHAPTER 5
IN VIVO ANALYSIS OF THE METAL COMPLEX POLYMER NANOCOMPOSITE IN RELATION TO MARKETED FORUMULATION IN THE LARGE WHITE PIG

5.1. INTRODUCTION 77

5.1. MATERIALS AND METHODS 78

5.1.1. Materials 78

5.1.2. Methods 78

5.1.2.1. Habituation of pigs prior to the start of the study 78

5.1.2.2. Surgical attachment of a catheter into the jugular vein for blood sampling .. 79

5.2.3.3. *In vivo* analysis using the Large White pig model 81

5.2.3.4. Eglonyl® and MCPN capsule administration to the large white pigs 83

5.2.3.5. Intravenous (IV) sulpiride administration to the large white pig 84

5.2.3.6. Collection and handling of animals' blood samples 85

5.2.3.7. Quantification of *in vivo* Release of the formulations administered using Ultra-Performance Liquid Chromatography Analysis 86

5.2.3.8. Pharmacokinetic modelling using non-compartmental analysis 87

5.2.3.9. Establishment of *in vitro-in vivo* correlation 88

5.2.3.10. Inductively coupled plasma-mass spectrometry (ICP-MS) for Ru element quantification in plasma and organs 88

5.2. RESULTS AND DISCUSSION 89

5.2.1. Behavioural evaluation of pigs post-surgery 89

5.2.2. Validation of the liquid-liquid extraction procedure 89

5.2.3. *In vivo* release of sulpiride from the MCPN 89

5.2.4. Interpretation of the extravascular non-compartmental pharmacokinetic model analysis 92

5.2.5. *In vitro-in vivo* correlation establishment 95

5.2.6. Ru element quantification in plasma, liver and kidneys of each pig 97

5.3. CONCLUDING REMARKS 99

CHAPTER 6
CONCLUSIONS AND RECOMMENDATIONS

6.1. CONCLUSIONS 100

6.2. RECOMMENDATIONS 101

REFERENCES AND APPENDICES

REFERENCES 103

APPENDIX A1 117

APPENDIX A2 118

APPENDIX B1 119

APPENDIX B2 120

APPENDIX C1 121

APPENDIX C2 122

APPENDIX D 123

LIST OF EQUATIONS

Equation 3.1. Stability Constant (K)..... 26

Equation 3.2. Dissociation Constant (K_d) 27

Equation 3.3. Cumulative amount of drug permeated..... 35

Equation 3.4. Flux (J) equation 35

Equation 3.5. Percentage cell viability..... 37

Equation 4.1. Percentage entrapment efficiency 60

Equation 4.2. Percentage drug loading 60

Equation 5.1. Bioavailability equation..... 85

LIST OF FIGURES

Figure 1.1. Schematic representation of the synthesis of ternary metal complexes of sulpiride. 5

Figure 1.2. Schematic representation of sulpiride ternary metal complex encapsulation into the polymer matrix to form the MCPN delivery system. 6

Figure 2.1. (**a**,**b**) Graphical representation based on X-ray single-crystal diffraction data of complexation between Zn ions (green), with O donor in Hppa, in bdc (red) with another Zn ion with N donor in Hppa (blue); (**c**) The structure of the MOF a 2D interpenetrated network with 6-membered rings; (**d**) Reported release profile of Hppa from MOF. Reproduced with permission from the Royal Society of Chemistry (Duan et al., 2015). 12

Figure 2.2. (**a**) Coordination between phenethylamine and available sites of Mg^{2+}. The illustrated model is proposed from X-ray powder diffraction data, where green, red, blue, and gray spheres represent Mg, O, N, and C atoms, respectively. The hydrogen atoms have been removed for clarity; (**b**) the observed release of both phenethylamine and olsalazine from the MOF in phosphate buffer medium of pH 7.4, at 37 °C. Reproduced from with permission from the American Chemical Society (Levine et al., 2016). 13

Figure 2.3. (**a**) Scheme depicting drug loading into PEG113-PBHEm-PSn micelles promoted by the metal coordination of copper to both doxorubicin and histidine followed by (**b**) pH-responsive release of the bioactive. Reproduced with permission from the Royal Chemical Society (Bai et al., 2015). 15

Figure 2.4. Ru(II) polypyridyl complexes that release neuroactives upon light irradiation. .. 16

Figure 2.5. Activation of Ru(II) complex by green light with release of econazole. 18

Figure 2.6. Graphical representation of the coordinating polymer based on (4-pyridylthio)methane (SCS) repeat units (black solid line), which is coordinated to the Zn-liganded Ibuprofen complex (Zn show in red and ibuprofen in green) followed by the anion exchange-triggered release of ibuprofen. Reproduced with permission from the Royal Chemical Society (Bustamante et al., 2013)..... 20

Figure 3.1. Synthesis procedure of ternary metal complexes of sulpiride. L1 is used as an example of ancillary ligand. 27

Figure 3.2. Schematic of the rotating paddle method..... 33

Figure 3.3. Schematic of a Franz diffusion cell. 34

Figure 3.4. Job's curve for the formation constant of equimolar solutions of SPR and Ru (II). 38

Figure 3.5. FTIR spectra of a) Sulpiride (SPR), b) (R)-(+)-2-amino-3-phenyl-1-propanol (L1), c) [Ru(p-cymene)((R)-(+)-2-amino-3-phenyl-1-propanol)] (Complex **1**) and d) [Ru(p-cymene)((R)-(+)-2-amino-3-phenyl-1-propanol)(sulpiride)]PF_6 (Complex **1a**). 40
Figure 3.6. ^{1}H NMR spectra with assignments of a) Sulpiride (SPR) in dmso-d6 and b) (R)-(+)-2-amino-3-phenyl-1-propanol (L1) in $CDCl_3$-d..... 42
Figure 3.7. ^{1}H NMR spectra with assignments of c) [Ru(p-cymene)((R)-(+)-2-amino-3-phenyl-1-propanol)] (Complex **1**) in dmso-d6, d) [Ru(p-cymene)((R)-(+)-2-amino-3-phenyl-1-propanol)(sulpiride)]PF_6 (Complex **1a**) in dmso-d6. 43
Figure 3.8. ^{31}P NMR spectrum with assignments for e) [Ru(p-cymene)((R)-(+)-2-amino-3-phenyl-1-propanol)(sulpiride)]PF_6 (Complex **1a**) in dmso-d6. 43
Figure 3.9.^{13}C NMR spectra with assignments of a) Sulpiride (SPR) in dmso-d6, b) (R)-(+)-2-amino-3-phenyl-1-propanol (L1) in $CDCl_3$-d, c) [Ru(p-cymene)((R)-(+)-2-amino-3-phenyl-1-propanol)] (Complex **1**) in dmso-d6 and d) [Ru(p-cymene)((R)-(+)-2-amino-3-phenyl-1-propanol)(sulpiride)]PF_6 (Complex **1a**) in dmso-d6. 44
Figure 3.10. TGA thermograms of a) Sulpiride (SPR), b) [Ru(*p*-cymene)((R)-(+)-2-amino-3-phenyl-1-propanol)] (Complex **1**) and c) [Ru(*p*-cymene)((R)-(+)-2-amino-3-phenyl-1-propanol)(sulpiride)]PF_6 (Complex **1a**)..... 45
Figure 3.11. DSC curves of a) Sulpiride (SPR), b) [Ru(*p*-cymene)((R)-(+)-2-amino-3-phenyl-1-propanol)] (Complex **1**) and c) [Ru(*p*-cymene)((R)-(+)-2-amino-3-phenyl-1-propanol)(sulpiride)]PF_6 (Complex **1a**)..... 46
Figure 3.12. UV-Vis spectra of sulpiride (SPR), dichloro(p-cymene)ruthenium(II) dimer (Ru(p-cymene)Cl_2), [Ru(p-cymene)((R)-(+)-2-amino-3-phenyl-1-propanol)] (Complex **1**) and [Ru(p-cymene)((R)-(+)-2-amino-3-phenyl-1-propanol)(sulpiride)]PF_6 (Complex **1a**). 48
Figure 3.13. Fluorescence spectrum of complex **1a** in methanol. 49
Figure 3.14. Dissolution profiles of sulpiride (SPR) and [Ru(p-cymene)((R)-(+)-2-amino-3-phenyl-1-propanol) (sulpiride)]PF_6 (Complex **1a**) in PBS buffer at different pH values. 51
Figure 3.15. Percentage Caco 2 cell viability following treatment with SPR, complexes **1a**, **3a** and **5a.**..... 55
Figure 4.1. Structure of [Ru(p-cymene)((R)-(+)-2-amino-3-phenyl-1-propanol) (sulpiride)]PF_6 (Complex **1a**). 57
Figure 4.2. Schematic of MCPN preparation 58
Figure 4.3. Graphs showing signal to noise ratio for MCPN particle size. 65
Figure 4.4. Graphs showing signal to nose ratio for a) MCPN drug entrapment efficiency and b) MCPN drug loading..... 66
Figure 4.5. Differential scanning calorimetry thermograms for complex **1a**, Eudragit® RS100 and F2. 68
Figure 4.6. Differential scanning calorimetry thermograms for MCPN formulations F1-F9 .. 68

Figure 4.7. Fourier transform infrared spectra for SPR, complex **1a**, Eudragit® RS100 and F1-F9. 69
Figure 4.8. Scanning electron micrographs for F2 MCPN formulation at 6,511 and 3,498 magnification powers. 70
Figure 4.9. Graphs showing signal to noise ratio for SPR cumulative relative permeability 71
Figure 4.10. Dissolution profiles of Eglonyl®, SPR in complex **1a** and SPR in MCPN formulations F1-F9 in gastric/intestinal pH simulated solutions (pH 1.2 for first 2 hours; pH 6.8 for following 4 hours; pH 7.4 up to 24 hours). 73
Figure 4.11. Graphs showing signal to noise ratio for SPR mean dissolution time. 73
Figure 4.12. Mean particle size distribution profile for optimized MCPN. 74
Figure 4.13. Average zeta potential distribution profile for optimized MCPN. 75
Figure 4.14. Percentage Caco 2 cell viability following treatment with complex **1a** and optimized MCPN. 76
Figure 5.1. Digital images of (a) farm unit, (b) group housing, (c) individual housing and (d) daily habituation. 79
Figure 5.2. Digital images of (a) anaesthetics administration and (b) anaesthesia maintenance. 80
Figure 5.3. Digital pictures of (a) exposed jugular vein, (b) intra-jugular catheter insertion, (c) post-surgical suture and (d) external injection ports of the intra-jugular catheter. 81
Figure 5.4. Flow diagram illustrating the allocation of pigs into the conventional and experimental groups for *in vivo* studies. 82
Figure 5.5. Digital pictures of (a) anaesthesia maintenance, (b) and (c) intragastric tube insertion for capsule administration 84
Figure 5.6. Blood sampling process though the external ports of the intra-jugular catheter. 85
Figure 5.7. Chromatogram of sulpiride in plasma with its internal standard 90
Figure 5.8. Calibration curve of sulpiride at 300 nm 90
Figure 5.9. Plasma concentration profiles of sulpiride from Eglonyl® (conventional) and MCPN capsules (MEC=Minimum Effective Concentration; MSC=Maximum Safe Concentration). . 91
Figure 5.10. *In vitro* and *in vivo* drug release profiles of sulpiride from the MCPN obtained by deconvolution analysis. 96
Figure 5.11. Levy plot depicting the relationship between the percentage of sulpiride released *in vitro* and the percentage of sulpiride released *in vivo*. 97

LIST OF TABLES

Table 2.1. Summary of recent stimuli responsive metal-liganded bioactive drug delivery systems..... 22
Table 3.1. Experimental data of ruthenium(II)-sulpiride complex by continuous variation method..... 37
Table 3.2. IR spectra (4000-650 cm^{-1}) of the SPR drug and its ternary metal complexes.... 41
Table 3.3.Selected ^{1}H NMR (500 MHz, DMSO-d6) and ^{13}C NMR (126 MHz, DMSO-d6) chemical shifts (ppm) of sulpiride and complexes **1a-5a.** 44
Table 3.4. Thermal analyses (TG and DSC) of SPR and its series of ruthenium (II) metal complexes..... 47
Table 3.5. Solubility values of free SPR and SPR in Ru(II) metal complexes in different solvents (mg/L). 50
Table 3.6. Cumulative permeability and cumulative relative permeability of free SPR, SPR released from metal complexes **1a**, **3a** and **5a**..... 53
Table 4.1. MCPN parameters with their respective levels 59
Table 4.2. Formulations to be prepared according to L9 orthogonal array for MCPN optimization..... 59
Table 4.3. Mean particle size, polydispersity index, zeta potential, percent entrapment efficiency and percent drug loading measurements for all MCPN formulations 65
Table 4.4. Response table for means for MCPN particle size 65
Table 4.5. Response table for means for MCPN drug entrapment efficiency and drug loading 66
Table 4.6. Cumulative permeability and cumulative relative permeability of free SPR, SPR released from complex **1a** and SPR released from MCPN formulation F1-F9 71
Table 4.7. Response table for means for SPR cumulative relative permeability. 72
Table 4.8. Response table for means for SPR mean dissolution time..... 74
Table 5.1. Mobile phases and prime solvents used for determination of sulpiride in pigs' plasma samples..... 86
Table 5.2. Extravascular pharmacokinetic analysis results of the non-compartmental analysis of sulpiride from Eglonyl® and the MCPN 94
Table 5.3. Total Ru concentrations in pigs plasma (µg/kg) at different time points post MCPN dosing 98
Table 5.4. Total Ru concentrations in pigs' livers and kidneys (µg/kg) 24 hours post MCPN dosing 98

LIST OF COMMONLY USED ABBREVIATIONS

BCS - Biopharmaceutics System

DSC - Differential Scanning Calorimetry

FTIR - Fourier Transform Infrared Spectroscopy

IS - Internal standard

MCPN - Metal Complex Polymer Nanocomposite

NMR - Nuclear Magnetic Resonance

PVA - Polyvinyl Alcohol

Ru - Ruthenium

SPR - Sulpiride

TGA - Thermogravimetric Analysis

UPLC - Ultra Performance Liquid Chromatography

UV-Vis - Ultraviolet Visible

CHAPTER 1
INTRODUCTION AND BACKGROUND

1.1. BACKGROUND OF THIS STUDY

Schizophrenia is a severe mental disorder that usually starts in young adulthood and affects about 1% of the adult population worldwide (Omori and Wang, 2009; Rössler et al., 2005). It is characterized by hallucinations and delusions (positive symptoms) as well as social withdrawal, loss of motivation (negative symptoms) and cognitive deficit (Smyth and Lawrie, 2013). Schizophrenia is known to have chronic features that result in one third of the people affected being likely to endure symptoms over a decade and only a minority of the people with schizophrenia fully recover (Wang and Sampson, 1996; Rössler *et al*., 2005). Additionally, schizophrenia often leads to mental and social disability, coupled with a reduction in life expectancy by approximately ten years. This is mainly as a consequence of increase suicide rates associated with patients suffering from schizophrenia (Rössler et al., 2005). Consequently, schizophrenia is a direct burden to those affected as well as to their relatives who care for them and is therefore among the most burdensome diseases in the world. Despite many decades of research, the pharmacotherapy of schizophrenia is still challenging (Kane and Correll, 2010).

Sulpiride (SPR) is a substituted benzamide derivative used for the treatment of schizophrenia (Ibrahim et al., 2014; Kecel-Gunduz et al., 2014). SPR is a selective antagonist of the dopamine D2 and D3 receptors in the brain (Horacek et al., 2006; Kecel-Gunduz et al., 2014). The antipsychotic activity of SPR is reported to occur via several mechanistic steps. Initially, SPR preferentially blocks the D3 receptors in the limbic cortex and this leads to regionally selective anti-dopaminergic activity which, in turn, results in a noticeable effect on the positive symptoms of schizophrenia. Thereafter, SPR blocks the presynaptic D2 receptors, which causes an increase in dopamine output into the striatum and this produces a decline of extrapyramidal symptoms (EPS), while maintaining a high rate of D3/D2 receptor antagonism in the thalamus and temporal cortex. Ultimately, the increased level of dopamine in the prefrontal cortex is accountable for the effects on both the negative and cognitive symptoms of schizophrenia (Horacek et al., 2006).

The oral delivery of drugs, especially solid formulations (tablets, capsules) is one of the most common and widely used routes of drug administration, accounting for approximately 50% of all dosage forms currently on the market (Debotton and Dahan, 2017). Oral administration is suitable for different drug candidates, safe, cost-effective and provides good physical and

chemical stability, high level of patient acceptability and ease of accurate dosing (Al-Hilal et al., 2013). The preference of patients for the oral route is particularly true in chronic drug therapy, as is the case in antipsychotic treatment, due to its convenience and non-invasiveness (Dening *et al*., 2016). However, oral delivery of poorly soluble and poorly permeable drugs, such as SPR, falling within the Biopharmaceutics Classification System (BCS) class IV, can be particularly challenging, resulting in low bioavailability and high dosages of these drugs (Ibrahim et al., 2014; Kawabata et al., 2011). In fact, although SPR is an effective antipsychotic drug, with regards to its pharmacokinetic features, it lacks the necessary functional groups to improve lipophilicity. Therefore, sulpiride poorly penetrates the intestinal membrane (Parikh et al., 2010). Moreover, the gastrointestinal absorption of SPR after oral administration is slow and poor resulting in a bioavailability of approximately 30%. Additionally, SPR has a relatively short half-life of 6 to 8 hours (Huang et al., 2001). These properties of SPR result in patients needing high doses of the drug to be treated, with a frequent dosing schedule such as a 400 mg tablet to be taken three times a day to reach a maximum daily dosage of 1200 mg. The challenge is that high doses of SPR negatively affect patient compliance and result in undesirable side effects such as dizziness, tremor, sleeping disturbances, over-stimulation, agitation, hyperprolactinemia, mild extrapyramidal and cardiovascular effects (Ibrahim et al., 2014; Wockhardt, 2010). Despite all these limitations, SPR remains an effective antipsychotic. It is therefore crucial to develop novel approaches to reduce the oral dosage of SPR via the enhancement of its aqueous solubility and lipid solubility, as well as the increase of its half-life (Lai et al., 2014, 2013; Wang and Sampson, 1996).

Metal coordinated drug research has expanded significantly in the last 50 years, however only a small percentage of reported complexes reach the market, highlighting the scope and need for further research in this field. An exemplary marketed drug is cisplatin (Spreckelmeyer et al., 2014), a popular anti-cancer complex which gained clinical acceptance in 1978 and thereafter fuelled the development of a library of metal based anti-cancer agents (van Rijt and Sadler, 2009). Metal coordinated drugs, also known as metal-liganded bioactives, have since become a viable research field with increasing commercial premise (Leung et al., 2015), and can be broadly classified into different developmental areas, e.g. anti-cancer metallodrugs focused on targeted delivery; anti-viral, anti-microbial and anti-diabetic metallodrugs; anti-parasitic, anti-inflammatory and anti-neurodegenerative metallodrugs; diagnostic and therapeutic radiopharmaceuticals (Barry and Sadler, 2013; Gaynor and Griffith, 2012; Hambley, 2007; Krstic et al., 2015; Leung et al., 2015; Renfrew, 2014a). However, the use of metal coordination to design metal complexes with selective metal-bioactive bond breakage to thereby release the bioactive is relatively less studied. Furthermore, studies on

mechanisms to control the bioactive release rates from metal-bioactive complexes are still rare.

Transition metals, which are used in metal coordination chemistry, possess partially filled d-orbitals in the neutral or cationic state. To this extent, transition metals can function as Lewis acids or electron lone pair acceptors (Frik et al., 2015; Ma and Moulton, 2011; Rafique et al., 2010). Additionally, the filled d-orbitals of the metal can participate in back donation of electrons to the anti-bonding orbitals of the bioactive. This results in a "push-pull" effect that enables the properties of the complex to be fine-tuned (Price et al., 2014). The bioactive must therefore have a donor available to form a coordinate bond, which is one of the limitations of metal coordination. Coordination complexes using the transient metal as a drug carrier have subsequently shown their usefulness as both diagnostic and therapeutic agents (Mjos and Orvig, 2014). Metal carriers are a simple drug delivery strategy with the ability to induce pharmacokinetic changes to improve solubility, bioavailability, permeation and controlled drug release, while avoiding the time-consuming and costly drug discovery process (Mjos and Orvig, 2014; Tiwari et al., 2012; Wang et al., 2013; Weiner et al., 2000).

Nanotechnology involves the engineering of functional systems at the molecular scale. Such systems are characterized by unique physical, optical and electronic features that are attractive for disciplines ranging from materials science to biomedicine (Bamrungsap et al., 2012). One of the most active research areas of nanotechnology is nanomedicine, which applies nanotechnology to highly specific medical interventions for the prevention, diagnosis and treatment of diseases. Currently, nanomedicine is dominated by drug delivery systems, with performances of intelligent drug delivery systems being continuously improved with the purpose to maximize therapeutic activity and to minimize undesirable side-effects (Safari and Zarnegar, 2014). Nanoparticles of biodegradable polymers are of particular interest due to the diverse possibilities with regards to their conjugation with numerous medications, markers and other biologically active compounds. Nanoparticles have the capacity to enter body tissues due to their small size, their surface charge and their lipophilicity, which is a great advantage for drugs to achieve their optimal therapeutic effect (De Jong and Borm, 2008; Dimitrijevic and Pantic, 2014; Fond et al., 2013).

This research focuses on using a metal carrier to improve the aqueous solubility and membrane permeability of orally administered bioactives and on the use of polymeric nanoencapsulation to achieve sustained drug release. This study aims to use a transition metal as a drug carrier by coordinating a neuro-active drug to it to obtain a metal-liganded bioactive. A modified version of the bioactive is thus designed, that exhibits improved pharmacokinetics. The obtained metal-liganded bioactive is then encapsulated into polymeric

nanoparticles to form a novel Metal Complex Polymer Nanocomposite (MCPN) delivery system. The designed drug delivery system results in a sustained drug release profile orally, which allows for maintained therapeutic concentrations of the drug in the systemic circulation throughout the dosing interval, resulting in enhanced bioavailability, lower dosage, reduced side-effects and improved patient compliance (Gil *et al*., 2006).

1.2. RATIONALE AND MOTIVATION FOR THIS STUDY

This research study proposed to develop a novel Metal Complex Polymer Nanocomposite (MCPN) delivery system loaded with a neuro-active drug for oral administration as a capsule.

The lipophilic properties of ruthenium are reported in literature, thus ruthenium is used as the transition metal carrier for the designed metal-liganded bioactive (Lv et al., 2015; Shweshein et al., 2014). The neuro-active drug sulpiride (SPR) was chosen as the bioactive for this work due to its poor aqueous solubility, low intestinal permeability, burst release and short half-life. Although many atypical antipsychotics were developed after SPR, they are more expensive and thus are an added financial burden on the health care system (Lai et al., 2013; Omori and Wang, 2009). SPR, on the other hand, is a relatively inexpensive drug (Wang and Sampson, 1996; Omori and Wang, 2009; Lai *et al*., 2013). Notably, previous studies have shown non-inferiority of typical antipsychotics to atypical antipsychotics in terms of quality of life, overall symptoms control and associated cost (Jones et al., 2006). Furthermore, a study investigating the persistence use of antipsychotic revealed that, when compared to haloperidol (widely prescribed typical antipsychotic) and risperidone (atypical antipsychotic), SPR had better clinical efficacy and relative lower side effects in controlling schizophrenic symptoms than the other two antipsychotics (Lai et al., 2013). Finally, the complexation and characterization of SPR analogues containing various first row transition metals (Fe (II), Mn(II), Co(II), Cu(II), Ni(II) and Zn(II)) have been reported. It was proposed that SPR preferentially binds to the metal centre in a monodentate fashion via the “O” of the carbonyl group of the benzamide (Mohamed and Soliman, 2010). To the best of our knowledge these complexes where not evaluated as antipsychotic drugs nor for pharmacokinetic improvement of SPR, but rather for their antimicrobial activity. Based on these findings, SPR was chosen as the model drug that has the potential to function as a ligand (it can coordinate to a transition metal to form a complex). Metal-liganded SPR was expected to provide the drug with improved aqueous solubility and lipophilicity, enhanced bioavailability, and longer half-life than the free SPR. An ancillary modulating ligand was used for the stability of the metal complex and a ternary metal complex of sulpiride was obtained. This ligand was varied to investigate its possible effect on the dissolution and permeation profiles of complexed SPR. Figure 1.1 is a schematic

representation of the synthesis of ternary metal complexes of SPR (metal-liganded bioactive). The ruthenium-SPR-ancillary ligand complex that resulted in the most promising slow dissolution and high permeability profiles of SPR was selected for further studies.

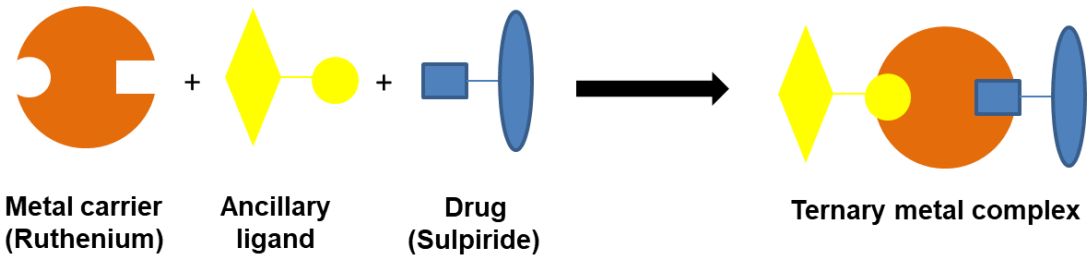


Figure 1.1. Schematic representation of the synthesis of ternary metal complexes of sulpiride.

SPR is fast dissolving in acidic pH environments and the ruthenium-SPR coordinative bond is sensitive to low pH; therefore, different polymer combinations were tested for protection of the metal complex in acidic pH in order to prevent premature release of SPR. Finally, the biodegradable copolymer Eudragit® RS 100 was used in the final formulation to protect the metal complex from bond cleavage in the stomach and provide sustained drug release, while the water soluble synthetic polymer polyvinyl alcohol was used as the aqueous phase for nanoparticle production and for the maintenance of sustained drug release (Adibkia et al., 2011; Gaur et al., 2014; Kurchania et al., 2014; Mabrouk et al., 2015). Therefore, the solubility and permeability of SPR is enhanced by the MCPN delivery system to achieve the maximum absorption through the small intestinal duodenal epithelium.

The MCPN delivery system comprised of the metal complex (ruthenium-sulpiride-ancillary ligand), encapsulated into Eudragit® RS 100 and PVA. The nano-sized final formulation was obtained by emulsion solvent evaporation method to produce a free-flowing powder of nanoparticles. This SPR-loaded MCPN delivery system may be an alternative formulation for the already existing SPR formulation on the market. The selected polymers and the chosen size were proposed in order to achieve a pH-responsive dissolution and increased intestinal permeability of the oral drug. The MCPN delivery system was proposed to give an enhanced bioavailability compared to the existing formulation in the market, due to the improved lipid solubility and reduced size as mentioned. The targeted area for the drug absorption is the small intestinal region. Figure 1.2. depicts the process of metal-liganded bioactive encapsulation into the polymer matrix to form the MCPN delivery system.

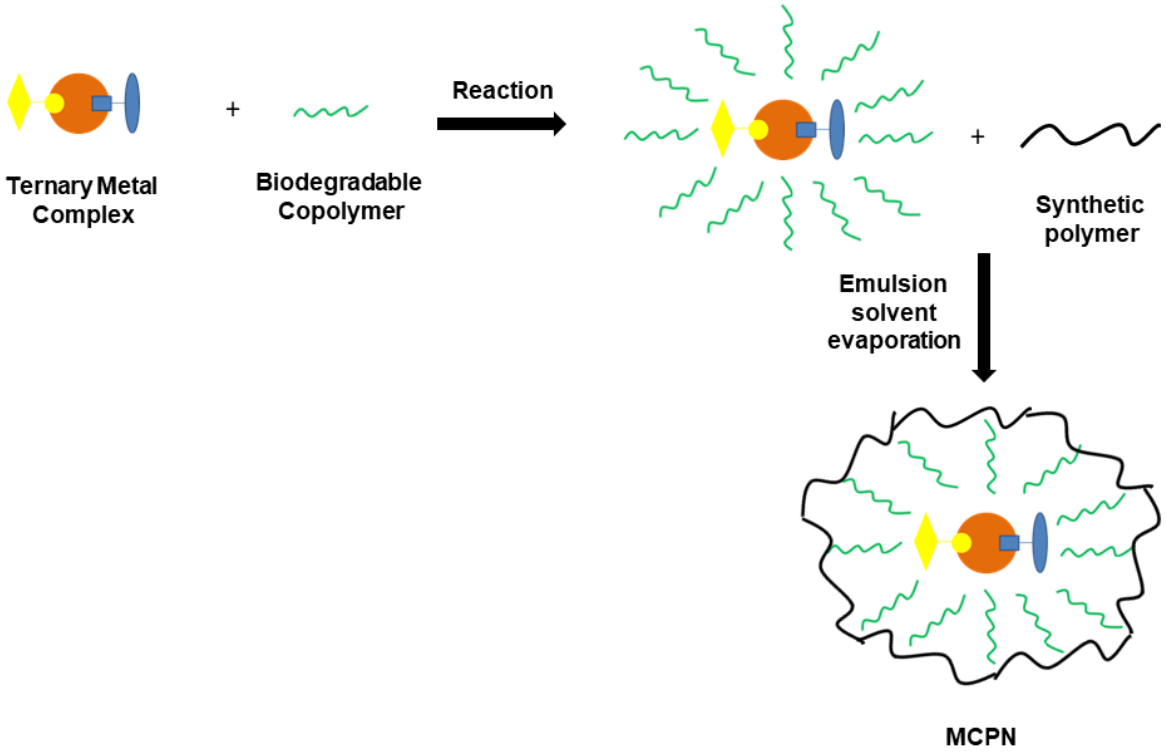


Figure 1.2. Schematic representation of sulpiride ternary metal complex encapsulation into the polymer matrix to form the MCPN delivery system.

Various drug delivery strategies have been developed to overcome the challenge of low drug solubility, limited permeation and short half-life following oral drug administration. These include metal drug carriers and polymeric nanoparticles but many of the drugs incorporated into these drug delivery systems still present multiple side-effects and high toxicity attributed to both their low solubility and the drug delivery method. The designed MCPN delivery system will be beneficial because it combines the benefits of an inert metal drug carrier and polymeric nanoparticles and therefore results in a metal-liganded drug entrapped in the core of the drug delivery system. This nanocomposite has the potential to enhance the solubility and permeation of the encapsulated drug and to exhibit pH-responsive sustained drug release following oral administration.

1.3. AIM AND OBJECTIVES OF THIS STUDY

The aim of this study was to combine metal coordination (improved intestinal permeability) and nanotechnology (pH-responsive sustained drug release) to design a pH-responsive novel Metal Complex Polymer Nanocomposite oral drug delivery system, with the ability to improve

the oral bioavailability of drugs with poor solubility and low permeability. This aim was achieved with the following objectives:

1. To design, synthesize and characterize a series of metal-liganded SPR by altering the ancillary ligand on the molecule.
2. To perform solubility studies of free SPR and metal-liganded SPR.
3. To perform *ex vivo* tissue permeation studies of metal-liganded SPR, using pig intestinal tissue.
4. To perform *in vitro* drug release studies to determine the release behaviour of metal-liganded SPR.
5. To formulate nanoparticles of metal-liganded SPR with polymers to obtain the MCPN delivery system.
6. To optimize the developed MCPN delivery system using a L9 orthogonal array construction.
7. To perform *ex vivo* tissue permeation studies of SPR in the MCPN delivery system, using pig intestinal tissue.
8. To perform *in vitro* drug release studies to determine the release behaviour of SPR from the MCPN delivery system.
9. To perform *in vitro* cytotoxicity studies of the optimized MCPN delivery system using Caco-2 cells.
10. To conduct *in vivo* drug release studies to assess the MCPN delivery system using the Large White Pig as an animal model.

1.4. NOVELTY OF THIS STUDY

1. Novel ternary metal complexes of sulpiride were synthesized and fully characterized.
2. An integrated novel drug delivery system known as MCPN has been developed to overcome the challenges associated with poor solubility, low permeability, short half-life and poor bioavailability of orally administered drugs. The MCPN comprises of a novel ternary metal complex of sulpiride nano-encapsulated into a polymer matrix. This drug delivery system is completely novel and has not been formulated in any previous studies published.
3. The novel MCPN delivery system's formulation was obtained by an innovative combination of two processes: metal complexation and emulsion solvent evaporation.

1.5. OVERVIEW OF THIS THESIS

Chapter 1 provides an introduction and background of the study, emphasizing the challenges experienced with oral drug delivery of poorly soluble and permeable drugs. The rationale and motivation for this research as well as the aim and objectives are outlined in detail in this chapter.

Chapter 2 provides a literature review, focusing on the application of metal-liganded bioactives for stimuli-responsive drug release. The techniques that incorporate the metal coordination strategy with additional cutting-edge formulation protocols in order to maintain the controlled stimuli-responsive metal-liganded bioactive delivery mode and prevent premature release of the bioactive were enumerated.

Chapter 3 provides a description of the synthesis and characterization of ternary metal complexes of sulpiride. The stability constant of the ruthenium-SPR complex was determined using Job's method. The ternary metal complexes were characterized by elemental analysis, Fourier Transform Infrared Spectroscopy (FTIR), Nuclear Magnetic Resonance (NMR), thermal analyses and Ultraviolet-Visible (UV-Vis). Solubility, dissolution and permeation studies of metal-liganded sulpiride were undertaken.

Chapter 4 provides a description of formulating a novel MCPN delivery system and optimizing the formulation. The formulation was optimized using five main parameters, namely: particle size, drug entrapment, solubility, permeation efficiency and sustained drug release. Following L9 orthogonal array construction, an optimized formulation was determined. Cytocompatibility analysis of the formulation using Caco-2 cell line was undertaken.

Chapter 5 provides *in vivo* studies using a Large White Pig model for clinical pharmacokinetic evaluation. At predetermined time intervals, blood samples were collected and analysed, after dosing the synthesized MCPN and comparative formulations. The amount of SPR present in plasma was detected and quantified using Ultra Performance Liquid Chromatography (UPLC), thereby determining the percentage bioavailability of drug. The amount of Ru present in plasma, liver and kidneys of the animals was detected and quantified using Inductively coupled plasma-mass spectrometry (ICP-MS), thereby investigating any metal toxicity to the animal model.

Chapter 6 provides a conclusion to the study and future recommendations in the application of MCPN for drug delivery.

CHAPTER 2
OUTLOOK ON THE APPLICATION OF METAL-LIGANDED BIOACTIVES FOR STIMULI-RESPONSIVE RELEASE

2.1. INTRODUCTION

Bio-inspired metal coordination has demonstrated a growth in applications in the field of drug delivery (Ejima et al., 2017; Grindy and Holten-Andersen, 2017; Rojas et al., 2017). Recent reports have highlighted the release of the drug cargoes through the dissociation of bespoke metal–ligand bonds (Liang et al., 2014, 2017, 2016) or metal–biomolecule bonds (Chen et al., 2017). An alternative approach to these methodologies is the direct coordination of the bioactive to the metal centre, which results in metal-liganded bioactive complexes. These complexes are advantageous as they are capable of delivering the bioactive through selective release mechanism(s) (Renfrew, 2014a). Metal–liganded bioactives in the context of this chapter refer to the coordination of a market-available pharmaceutical agent to a metal centre to produce a novel and more effective drug delivery system. Notably, the introduction of the metal centre can control the mechanism by which the drug is delivered without changing the drug action or therapeutic activity. Furthermore, this is a relatively more facile route to enhancing both the pharmacokinetic and pharmacodynamic properties of the parent bioactive.

Approximately 60–70% of drug molecules suffer from poor aqueous solubility and/or low permeability following oral delivery (Gupta et al., 2013). The coordination of drugs to metal centres is a promising approach that has the potential to improve both the aqueous and lipid solubility of poorly absorbed bioactives (Piccariello, 2013). The increase in lipid solubility has been primarily attributed to chelation effects, which result in a delocalization of electron density among the donors of the bioactive and/or ancillary ligand. This has been reported to increase the lipophilic character of the metal-liganded bioactive, and promotes permeation through the lipid layers of the target cell membranes (Siddappa et al., 2014; Singh et al., 2004). The corresponding improvement in aqueous solubility can be attributed to the inherent hydrophilic nature of metals; for example, bis(esomeprazole) magnesium complexes are relatively more soluble than the parent drug, esomeprazole (Johnson and Hedge, 2002). In addition, oral bioavailability can be improved if a drug is formulated with a delivery system that has the ability to release substrates that inhibit the back-efflux process (Baluom et al., 2001). An example of drug efflux in the gastrointestinal tract is the ability of P-glycoprotein to pump drugs back into the lumen, decreasing absorption and lowering bioavailability. The metal complex itself (or upon functionalization with ancillary ligands) could potentially inhibit this process, thereby increasing absorption. Drug solubilization by complexation through non-covalent interactions

can also be achieved through the preparation of protein-liganded bioactives (Loftsson, 2017). A recent report has shown the use of natural proteins such as serum albumin for complexation to rifapentine (Ostrovskii et al., 2016), which resulted in improved oral bioavailability of rifapentine coupled with relative improved stability of the resulting protein-liganded rifapentine solutions. However, other protein-liganded drug complexes are generally more susceptible to quick degradation (Ostrovskii et al., 2016) and in these instances metal complexation provides more stable complexes due to formation of bonds through e^- sharing compared to covalent interactions. Furthermore, proteins have specific available donors based within their network and these donor sites are arranged randomly within the protein network; therefore, specificity to the bioactive is low and early bioactive release is possible in the presence of other competing drugs. On the contrary, metal complexation offers more control as a metal centre can be chosen based on the donors available on the bioactive and ligands, and the coordination sphere around the metal centre results in a spatial arrangement of bioactive and other ligands emanating in a defined geometry. The effects of metal complexation are therefore uniformly distributed over the coordination sphere and this offers a further opportunity to tailor the properties of the metal-liganded complex.

Alternatively, and perhaps a more ingenious opportunity, lies in the fact that metal-liganded bioactive coordinative bonds are responsive to environmental stimuli, e.g., pH, redox potential, or localized application of light. Therefore, a research niche exists for the development of controlled-through-stimuli-triggered bioactive release systems enabled by metal complexation. This smart drug delivery biomaterial approach (Lu et al., 2017) can result in lower systemic toxicity. A more specific example is the complex $[Cu(fen)_2(im)_2]$, where Cu = copper(II) ion; fen = fenoprofenate anion from fenoprofen (bioactive); and im = imidazole (ancillary ligand), with the overall complex reported to have enhanced analgesic activity and reduced ulcerogenic action compared to the free drug, fenoprofen (Agotegaray et al., 2014). To date, stimuli-responsive metal-liganded bioactive systems have found application in the release of small molecules such as CO_2, and NO (Haas and Franz, 2009; Smith and Sadler, 2013) but the delivery of relatively larger bioactives is scant (Martins et al., 2015; Price et al., 2014; Wang et al., 2013b).

Moreover, there has been a recent review on the current application of metal-liganded bioactives for use in drug delivery; however, this review did not focus on additional formulation aspects that could further control bioactive release and also protect the metal complex during oral delivery. This chapter will therefore highlight recent examples of metal-liganded bioactive complexes where (a) the bioactive can form one or more coordinative bonds with the metal centre though available donor sites; (b) the bioactive may belong to, but is not limited to, an anti-cancer, anti-inflammatory, anti-microbial, or neuroactive drug class; (c) the complex

demonstrates stimuli-responsive bioactive release; and (d) additional formulation strategies have been employed.

The route of delivery of the intended metal-liganded bioactive has been established as an important factor that could influence the selective release of the bioactive, and in most instances further formulation is required. For example, a copper-liganded naproxen (Npx) complex, $[Cu_2(Npx)_4(dmso)_2]$, was previously prepared and loaded into chitosan beads for the oral delivery of naproxen (Martins et al., 2015). Thereafter, a portion of the complex-loaded beads were coated with a methacrylic acid co-polymer for reducing naproxen release at gastric pH (from 55 to 20%).

Further, the preparation of two zinc metal–drug complexes based on theophylline (TPL), viz. $[Zn(TPL)_2(H_2O)_2]$ and $[Zn_2(TPL)(FA)(OH)(H_2O)]$, where FA = fumaric acid (ancillary ligand), were reported by Wang et al. (Wang et al., 2013). These complexes were encapsulated in a polymer matrix comprising of hydroxypropyl methylcellulose (HPMC) and microcrystalline cellulose (MCC). Relative to the control experiment, the metal-liganded formulations demonstrated slower drug release and the rate of release was controlled by varying the amount of MCC added, with the release mechanism varying from inconsistent delivery (free drug) to controlled and steady Fickian diffusion (Wang et al., 2013b). To this end, this chapter will also examine research employing sophisticated applications that incorporate the metal coordination strategy with additional cutting-edge formulation protocols in order to maintain the controlled stimuli-responsive metal-liganded bioactive delivery mode and prevent premature release of the bioactive.

2.2. pH-TRIGGERED BIOACTIVE RELEASE

2.2.1. Bioinspired Materials

Metal biomolecule frameworks (bioMOFs) are fabricated using endogenous molecules or bioactives as structural entities (Mantion et al., 2008). This synthetic design endows the framework with minimal toxicity concerns and/or minimizes the amount of bridging or ancillary ligands required. Moreover, this methodology negates entrapment of the bioactive via impregnation methods that lead to the two-fold advantage of (a) a high drug loading capability (Shen et al., 2017) and (b) controlled release systems. The latter design is due to the fact that the interpenetrated metal-liganded bioactive bonds allow for slower release of the bioactive in physiological media (Rojas et al., 2017). An example of this behaviour was observed for a novel MOF, with formula $[Zn_2(ppa)2(1,3\text{-}bdc)(H_2O)]_2H_2O$, where ppa = pipemidic acid (bioactive), and bdc = 1,3-benzenedicarboxylate (low toxic ancillary ligand) (Duan et al., 2015) (Figure 2.1). The ambidentate nature of pipemidic acid and bidentate properties of bdc are

the structural building blocks for the generation of the MOF (Figure 2.1a–c). The corresponding *in vitro* release kinetics of Hppa from the MOF with particle size distribution of 25–40 µm was recorded in simulated gastric fluid (SGF, pH = 2), body fluid (SBF, pH = 7.4) and intestinum crassum fluid (SIC, pH = 8.3), respectively (Figure 2.1d). The results depict a pH-responsive delivery of Hppa, with controlled release (38.1%) over 48 h observed at the highest pH values tested. It was reported that the significant release rate in SGF is due to the free protons competing for donor sites on pipemidic acid, which resulted in MOF degradation and evident drug release. Nonetheless, this limitation could be rectified through possible additional formulation steps. As a nascent field, future research endeavours should consider the investigation of *in vivo* stimuli-triggered degradation efficiency, and cell culture studies should be undertaken to verify the biocompatibility of the system. Possible considerations should also include the sole use of biomolecules as ancillary or pillaring ligands for production of the MOF to ensure overall improved biocompatibility.

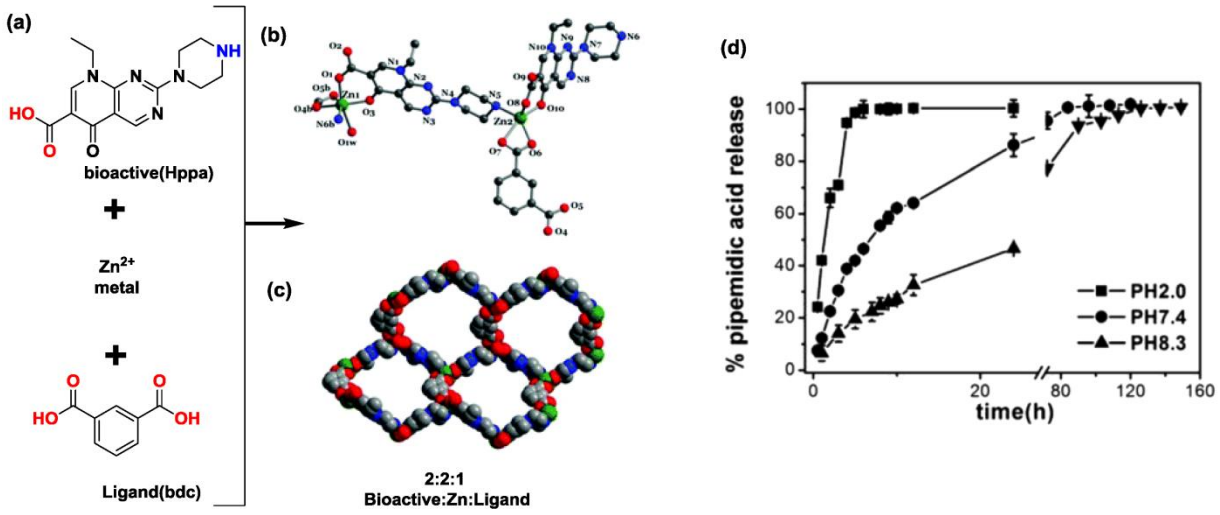


Figure 2.1. (**a**,**b**) Graphical representation based on X-ray single-crystal diffraction data of complexation between Zn ions (green), with O donor in Hppa, in bdc (red) with another Zn ion with N donor in Hppa (blue); (**c**) The structure of the MOF a 2D interpenetrated network with 6-membered rings; (**d**) Reported release profile of Hppa from MOF. Reproduced with permission from the Royal Society of Chemistry (Duan et al., 2015).

A bioMOF with remarkable biocompatibility was exemplified by the application of magnesium-liganded olsalazine bioMOF (Figure 2.2a) for the co-delivery of olsalazine and entrapped phenethylamine (Levine et al., 2016). Notably, the BioMOF achieved an unsurpassed loading of 86 wt % drug in the framework. The bioMOF was then assessed for *in vitro* release capabilities and it was reported that under physiological conditions of pH 7.4 the respective release of phenethylamine and olsalazine was 95 and 50% after 3 h (Figure 2.2b). The

mechanism of release of olsalazine was much slower due to the nature of the interpenetrated Mg-liganded olsalazine bonds further highlighting the benefit of employing this bioMOF design. As the system has already shown merited biocompatibility, forthcoming research endeavors should consider tailoring the release mechanism, followed by *in vivo* verification of the drug delivery performance.

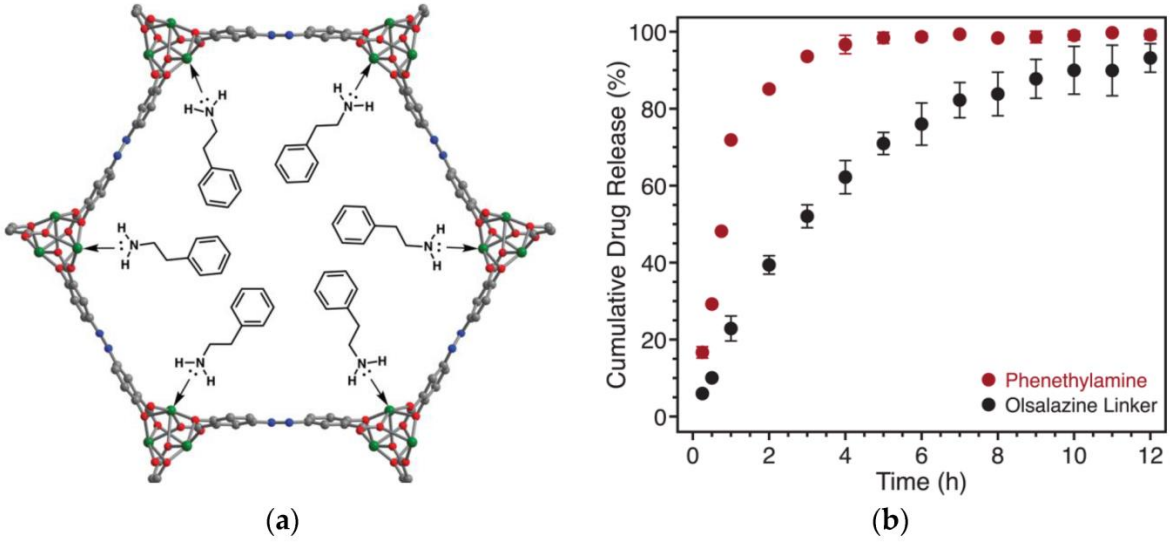


Figure 2.2. (**a**) Coordination between phenethylamine and available sites of Mg^{2+}. The illustrated model is proposed from X-ray powder diffraction data, where green, red, blue, and gray spheres represent Mg, O, N, and C atoms, respectively. The hydrogen atoms have been removed for clarity; (**b**) the observed release of both phenethylamine and olsalazine from the MOF in phosphate buffer medium of pH 7.4, at 37 °C. Reproduced from with permission from the American Chemical Society (Levine et al., 2016).

Another example of a bioinspired drug delivery system involved the preparation of Fe-liganded doxorubicin (DOX) formulated into transferrin-inspired nanoparticles (NPs) (He et al., 2017). The pH-triggered release of DOX was suitable for intracellular release at the acidic tumour site. This was evident in the release of 73.6% and 59.3% of DOX observed at pH 4.5 and 5.5, respectively, which simulated the conditions of the tumour microenvironment. The *in vitro* release at pH 6.5 (extracellular tumour, milieu) and 7.4 was 33.5% and 25.6%, respectively (He et al., 2017). The pH-responsive Fe-liganded DOX bond cleave was also verified through *in vivo* studies using a mouse model through intravenous administration of the prepared NPs.

Furthermore, the introduction of the ferric ion was beneficial to the rational design of the biomimetic drug delivery system (BDDS) in the following conditions: (a) higher loading of DOX was obtained for Fe formulations as compared to the control NPs; (b) the ferric ion also served as a crosslinking agent to increase the stability of Tf-inspired NPs; and (c) the ferric ion coordination sphere was large enough to also promote self-assembly for the formation of the

Tf-inspired NPs through coordinative bonds (He et al., 2017). The use of metal coordination in this study demonstrates the versatility of metal ions and such smart delivery systems could also be extended to targeted delivery applications by employing the metal as a linker for antibody drug-based conjugates.

2.2.2. Self-Assembled Metal-Liganded Bioactives

The complexation of Minocycline Hydrochloride (MH) with Ca(II) and Mg(II) ions in the presence of dextran sulphate (DS) was undertaken. This rational design involved the metal cations in the metal-liganded MH complex, enabling ionic interactions with the negative donors on the DS polysaccharide backbone to fabricate a DS-metal ion-MH complex (Zhang et al., 2015). The metal-liganded MH chelates were stable at pH 7.5; however, at pH 6.0 the drug release was more significant. Sustained release under pathology-induced tissue acidosis was observed over 71 days as the metal-liganded MH complexes have strong coordinative bonds that can result in controlled bioactive release. This system could easily be applied to other bioactives; however, these bioactives must have a high affinity to bind to the metal centres and also must have more than one donor available for coordination in order to promote chelate formation, which will facilitate controlled drug release.

Bai and co-workers established a coordination interaction occurring at a neutral pH between metal ions (e.g., Cu^{2+}) and the common anticancer drug, DOX, with dissociation in acidic environments, thus potentially enabling precise drug release in cancer cells (Bai et al., 2015). Another group of pH-responsive assemblies thus includes polymeric micelles formulated with poly(ethyleneglycol)-b-poly(2-hydroxyethylmethacrylate-Boc-histidine)-b-poly(styrene) (PEG-PBHE-PS) with metal-liganded bioactive complexation (Figure 2.3a) (Bai et al., 2015). In this system, copper was coordinated to both the biocompatible ancillary ligand, histidine, and to the bioactive DOX, and loadings up to 47.4%of DOX were obtained as compared to 12% for control micelles (with no metal coordination present). The metal complexation strategy therefore promoted the drug loading ability of this fabrication methodology. The release of DOX at a lower pH of 5 was more pronounced than at a higher pH of 7.4 (Figure 2.3b), and it was concluded that coordinative bond cleavage between metal and bioactive was the rate-determining step for drug release as opposed to simple diffusion kinetics (McNamara et al., 2006; Zayat et al., 2013). The improved drug loading and smart intracellular delivery warrant further analysis of this system via *in vivo* experiments to verify the therapeutic efficacy.

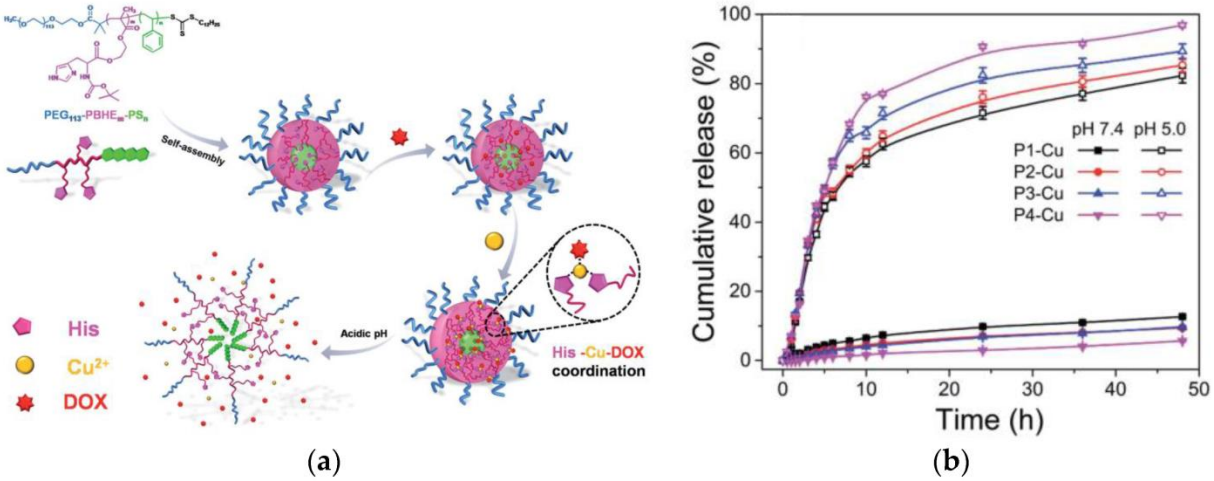


Figure 2.3. (**a**) Scheme depicting drug loading into PEG113-PBHEm-PSn micelles promoted by the metal coordination of copper to both doxorubicin and histidine followed by (**b**) pH-responsive release of the bioactive. Reproduced with permission from the Royal Chemical Society (Bai et al., 2015).

2.3. LIGHT-TRIGGERED BIOACTIVE RELEASE

2.3.1. Ruthenium Cage Complexes

Ruthenium (Ru) metal centres have been reported for the preparation of octahedral Ru(II) polypyridyl complexes, which release neuro-actives upon light irradiation (Zayat et al., 2013). The coordination chemistry of octahedral Ru(II) polypyridyl complexes offers the possibility of caging an extended range of molecules, including amino acids, nucleotides, neurotransmitters, and fluorescent probes (Zayat et al., 2013). In addition, these Ru-based caged compounds are responsive to visible light, unlike other photo triggers, and can be photolyzed employing green light. These characteristics enable the use of simple and inexpensive equipment (Zayat et al., 2013). Ru(II) polypyridyl complexes are also active in the two-photon regime, a property that widens their scope to systems that use infrared light to achieve high precision and penetrability (Zayat et al., 2013). These complexes were reported to release 4-aminopyridine (4AP) (Zayat et al., 2003) and -aminobutyric acid (GABA) (Rial Verde et al., 2008). The design of these complexes incorporates the inherent photo-physical properties of the Ru(II) polypyridyl cation, and the photo-responsive cleavage of the weaker [metal-bioactive bond] to release the bioactive. The reported complex containing Ru-linked 4-AP was obtained at a good yield using a simple one-step synthetic approach and demonstrated successive controlled release of the two molecules of 4AP molecules incorporated, evidenced by Nuclear Magnetic Resonance (NMR) studies (Zayat et al., 2003). The corresponding biological activity was observed by the activation of neuronal firing in a leech ganglion (Zayat et al., 2003). Similarly, the complex RuBi-GABA (Figure 2.4) was

reported to release GABA; coupled with high tissue penetration, less phototoxicity, and faster photo-release kinetics compared to other UV light- sensitive caged compounds (Rial Verde et al., 2008). *In vitro* tests demonstrated no effect on endogenous GABAergic or glutamatergic transmission at concentrations effective for measurable release. In a related *in vivo* study (mouse cortex), photo-release of GABA from a new derivative indicated that high formulation doses were tolerable (Lopes-dos-Santos et al., 2011).

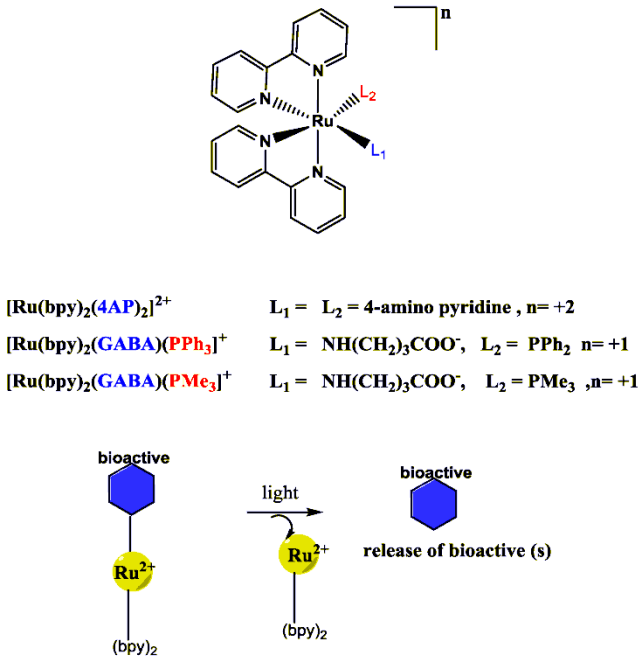


Figure 2.4. Ru(II) polypyridyl complexes that release neuroactives upon light irradiation.

Ru(II) polypyridyl complexes have shown potential for light-triggered delivery of drugs with labile bonds, with possible activation by visible and infrared light, the latter being the ideal photodynamic therapy region (Knoll et al., 2015; Sharma et al., 2015). Various Ru(II) polypyridyl complexes with luminescent capabilities have been investigated for applications as cellular probes and organelle stains (Fernández-Moreira et al., 2009). The possible combination of the previously mentioned properties of Ru(II) propyridyl complexes for the design of a luminescent and photoreactive complex for double application in light-triggered drug delivery and cell imaging was recently investigated (Karaoun and Renfrew, 2015).

Ru(II) polypyridyl complexes containing imidazole-based ligands have been demonstrated to reversibly modify the physicochemical properties of the coordinated drug. The antifungal econazole, which is currently being investigated as an anticancer agent, was used as an imidazole-based model drug due to its poor pharmacokinetics. A prodrug delivery system

could therefore increase the effective dose of econazole, thereby positively impacting the effectiveness of this drug in treating various diseases (Karaoun and Renfrew, 2015). Ru(II) complexes containing one or two econazole ligands were successfully prepared in a single step with moderate yield. The complex with two econazole ligands (Figure 2.5) was an inactive and relatively safe prodrug of econazole, which could be activated by the use of green light. This complex displayed improved water stability and solubility, photo-selective toxicity, and favourable intracellular accumulation compared to the free drug. The low to moderate toxicity of this complex was observed in the absence of light but nanomolar IC_{50} values were noted upon combination of the complex with green light. The luminescence of this complex allowed for its visualization in live cells and drug release observation in actual time by the deactivation of the luminescence response. It must be noted, however, that after prolonged light activation the complex releases one bioactive molecule, which results in the non-fluorescent product, $[Ru(o\text{-}phen)_2(EZ)(H_2O)]^{2+}$ (Figure 2.5). Further research is therefore required to fully optimize these complexes for sustained delivery and imaging abilities. A Ru(II) complex with dual properties of photo-activated drug delivery and luminescence was therefore successfully obtained (Karaoun and Renfrew, 2015). This approach could be extended for the delivery of drugs with similar chemical (imidazole-based) and pharmacokinetic properties to the model drug employed in this study, especially anticancer drug candidates that suffer from unfavourable pharmacokinetics and low tumour cell accumulation and selectivity.

From the literature, it is evident that ruthenium polypyridyl-linked neurochemical complexes provide rapid delivery and higher yields relative to other caged compounds. Moreover, a judicious choice of the ancillary ligand results in safer visible light stimulation as compared to UV light. However, *in vivo* design challenges such as adapting *in vitro* experiments and identifying the appropriate animal model to test the complexes must still be overcome to confirm the effectiveness of these compounds (Karaoun and Renfrew, 2015).

Chan and co-workers have recently investigated the use of photolabile Ru(II) complexes that can bind and release a purine model drug. It was demonstrated that the change of the ancillary ligand affected the stability and photo lability of the complex (Chan et al., 2017). The work undertaken emphasizes the versatility of the metal complex towards achieving optimized drug release behaviour with minimal synthesis steps required. Nonetheless, *in vivo* studies should be undertaken.

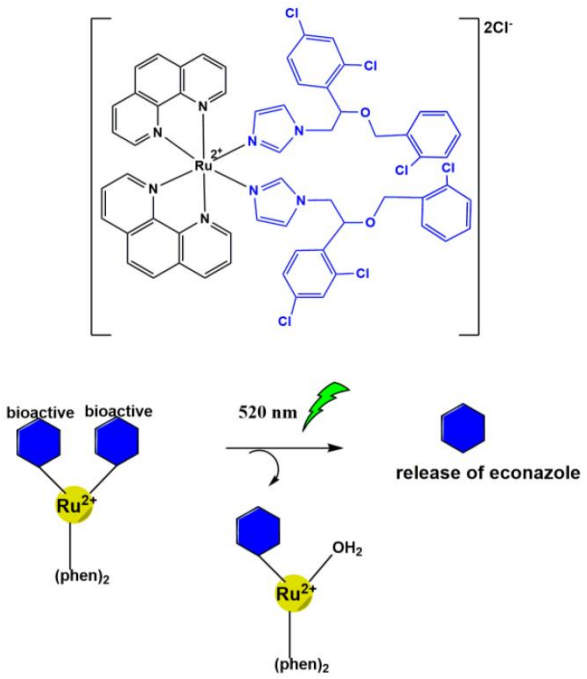


Figure 2.5. Activation of Ru(II) complex by green light with release of econazole.

2.4. REDOX-TRIGGERED BIOACTIVE RELEASE

Compared to Co^{3+} complexes, which cannot undergo ligand exchange, complexes of Co^{2+} undergo simple ligand exchange, which endows these metal complexes with drug carrier functionality. Bioactive release usually ensues after ligand exchange by other nucleophiles in the biological milieu occurs. Moreover, both +2 and +3 cobalt species have been reported to possess no significant cell toxicity (Dabrowiak, 2017; Law et al., 2017) at known doses. Pioneering work by Failes and co-workers therefore demonstrated that cobalt complexation to available "O" donor sites on metalloproteinase (MMP) inhibitors could result in two-fold design benefits (Failes et al., 2007). Firstly, MMPs such as Marimastat® have shown anti-cancer activity; however, this is limited in clinical application due to its poor oral bioavailability and proposed deactivation though interactions between the hydroxamic moieties in the presence of biomolecules (Failes et al., 2007). Hence, complexation with Co(III)-tris(2-methylpyridyl)amine metal precursor (Co(III)-TPA) can prevent the Marimastat molecule from undergoing the above-mentioned *in vivo* deactivation reactions. Secondly, the electrochemical properties of cobalt(III) could be used to selectively deliver Marimastat to hypoxic cells (Munteanu and Suntharalingam, 2015). The delivery mechanism was proposed to occur in the anaerobic environment of tumour cells (highly negative redox potential), which promotes the reduction of cobalt(III) to the reactive cobalt(II), allowing the release of the bioactive via ligand exchange (Figure 2.6) (Ware et al., 1998). An *in vitro* MMP assay was

used to establish the level of effectiveness of the cobalt(III) complex as a carrier for Marimastat and demonstrated the stability of that complex outside of a reducing environment, thereby preventing it from being deactivated prior to reaching the tumour site (Ware et al., 1998). *In vivo* studies have verified the release of Marimastat; however, further work to investigate the *in vivo* fate of the cobalt metal carrier is necessitated.

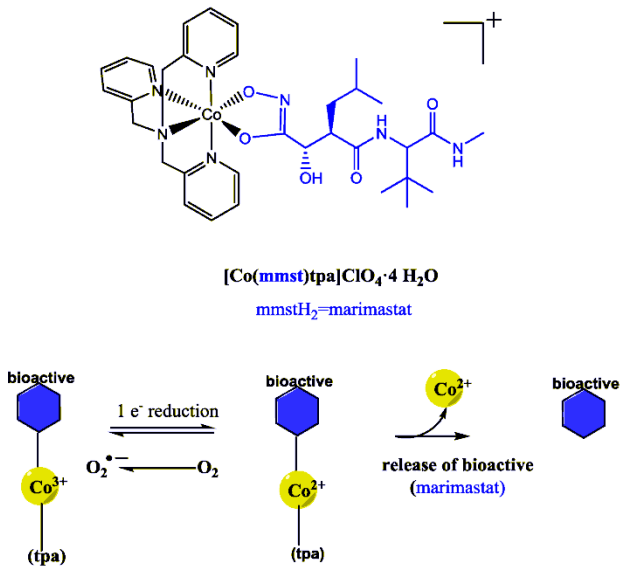


Figure 2.6. Proposed mechanism for the release of bioactive from a cobalt metal complex.

Bustamante and co-workers aimed to develop new prototypes of a bioreductive drug by investigating the coordination of lawsone (2-hydroxy-1,4-naphtoquinone, HNQ) to transition metal ions (Bustamante et al., 2013). They thus reported dimerization of lawsone upon reaction with $Co(BF_4)_2_6H_2O$ and N,N-bis(pyridin-2-ylmethyl)ethylenediamine (py_2en), producing a $bhnq^{2-}$ ligand (deprotonated form of HNQ) that ultimately coordinated to the Co(III) metal centre in a single step to form the coordination complex $[Co(bhnq)(py_2en)]BF^{4-}$. The redox reactivity of the complex was observed in the presence of the reducing agent, ascorbic acid, under various oxygen concentrations and the results revealed that the reaction time between the metal complex and ascorbic acid is indirectly proportional to the concentration of oxygen (Bustamante et al., 2013). This phenomenon could have been caused by either redox cycling, with Co(II) being oxidized back to Co(III) by oxygen prior to ligand dissociation, or competition between the Co(II) and the reducing agent for oxygen (Bustamante et al., 2013). Furthermore, cyclic voltammetry experiments revealed that the metal complex obtained in this study can be easily reduced in the biological environment, and its Co(II) reduced form may be sufficiently inert to undergo redox cycling (Bustamante et al., 2013). The dissociation of $bhnq^{2-}$ after reduction with ascorbic acid is oxygen-dependent, suggesting the involvement of redox

cycling (Bustamante et al., 2013). This study showed the ability of HNQ to act as a model for the development of a bioreductive prodrug through metal complexation. Although there have been positive outcomes from the use of cobalt as a drug carrier, other factors in biological media that may affect the rate of ligand exchange to release the drug warrant further research.

2.5. ION ACTIVATION-TRIGGERED RELEASE OF BIOACTIVE

An example of the incorporation of both a polymeric support with stimuli-driven drug release was recently demonstrated by Lago and co-workers (Lago et al., 2016). The fabricated polymer-loaded metal-liganded bioactive was prepared via a one-pot synthesis in water/ethanol solvent systems. Notably, the change in coordination geometry between the two complexes (1) and (2) depicted in Figure 2.6 resulted in an initial quick release followed by a slower dissociation release. The coordinated bioactive is released in a controlled manner by ligand exchange with phosphate anions due to competitive binding, i.e., the Zn metal centre exhibits preferential binding to the phosphate ions.

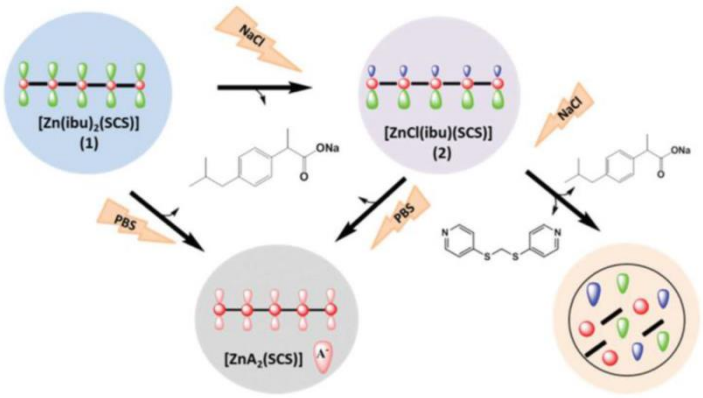


Figure 2.6. Graphical representation of the coordinating polymer based on (4-pyridylthio)methane (SCS) repeat units (black solid line), which is coordinated to the Zn-liganded Ibuprofen complex (Zn show in red and ibuprofen in green) followed by the anion exchange-triggered release of ibuprofen. Reproduced with permission from the Royal Chemical Society (Bustamante et al., 2013).

2.6. CONCLUDING REMARKS

In summary, metal-liganded bioactive stimuli-triggered release offers an innovative route for the development of controlled release vehicles. Based on the systems highlighted, several secondary routes have been pursued to create feasible and hierarchical designs that include bioMOFs, self-assemblies, and polymeric metal complexes. Preliminary proof of concept that metal–bioactive complex formation does occur and improves the performance of the bioactive

is still required. Metal drug carriers have shown great potential for overcoming the limitations of marketed drugs by achieving improved pharmacokinetics with selective and controlled drug release of the parent drug.

However, there are further challenges faced in the translation of these systems into market-ready formulations. In fact, extensive studies should focus on the stability of the metal-liganded complex after *in vivo* administration and the *in vivo* fate of the metal carrier after drug release has occurred. Toxicity must be considered when working with metal complexes in medicine; however, efficient cell targeting in combination with stimuli-responsive release drug release systems would enable the safe delivery of the bioactive and will therefore negate bioaccumulation and toxicity issues. It must be noted that current drug delivery developments have placed an emphasis on macromolecular delivery vehicles (e.g., nanoparticles, dendrimers, liposomes), which present with challenges in achieving a well-defined particle size, and possess poor solubility, and retarded degradation with organ accumulation. Thus, toxicity concerns such as blood clots, cardiovascular damage, and hypersensitivity reactions exist. Metal complexes do not notably affect the parent drug size and are small-molecule, well-defined drug delivery systems, and are thus exempt from a number of these limitations (Renfrew, 2014a). Furthermore, with the advancements in cellular imaging, a fluorescent functionalized metal-liganded carrier offers a strategy to investigate the pathways of metal trafficking. An understanding of these pathways will enable the development of optimized metal carriers that circumvent the perceived toxicity issues. Moreover, when metal-liganded bioactives are prepared they react in known stoichiometric ratios, and, coupled with full characterization, the exact metal content can be calculated. The resulting formulations are then systematically screened for cytotoxicity.

Nonetheless, the nascent technologies highlighted in this chapter could spur research into metal carriers as future novel drug delivery systems (DDSs). A summary of these DDSs is presented in Table 2.1.

Table 2.1. Summary of recent stimuli responsive metal-liganded bioactive drug delivery systems.

Metal	Bioactive	Highlights	Ref
Zn(II)	Pipedemic acid	pH-triggered release of bioactive from the bioactive interpenetrated MOF.	(Duan et al., 2015)
Mg(II)	Olsalazine Phenethylamine	Enhanced biocompatible carrier with programmed co delivery of an interpenetrated bioactive and entrapped model drug.	(Levine et al., 2016)
Fe(III)	Doxorubicin	Biomimetic delivery of an anti-cancer drug.	(He et al., 2017)
	Minocycline HCl	Sustained release triggered by pathology-induced tissue acidosis.	(Zhang et al., 2015)
	Purine model drug		(Chan et al., 2017)
Ru(II)	4-aminopyridine	Versatile light-activated carrier for neuroactives and econazole ligands with addition of imaging potential. New reports for purine anti-cancer model drugs	(Zayat et al., 2003)
	GABA		(Rial Verde et al., 2008)
Co(III)	Metalloproteinase	Controlled bioreductive release demonstrated	(Failes et al., 2007)
Zn(II)	Ibuprofen	Release is based on ligand exchange mechanisms.	(Lago et al., 2016)

Based on the review of the varying stimuli responsive metal-liganded bioactive delivery systems, the following considerations should be implemented in future developments:

(a) *In vitro* studies must include metal-liganded bioactive release in a physiologically-simulated milieu to fully account for the stability, release mechanism, and possible free metal ion interactions.

(b) Possible inclusion of additional formulation science to overcome challenges faced in the physiological milieu (e.g., enteric targeting for oral systems).

(c) Evaluating whether the drug release kinetics observed translates to *in vivo* efficiency.

(d) Inclusion of in-depth *in vitro* cytotoxicity analyses in applicable cell lines and *in vivo* studies to mitigate the perceived risks involved in using metal carriers.

CHAPTER 3
SYNTHESIS, CHARACTERIZATION AND *IN VITRO* PERMEATION, DISSOLUTION AND CYTOTOXIC EVALUATION OF RUTHENIUM(II)-LIGANDED SULPIRIDE AND AMINO ALCOHOL

3.1. INTRODUCTION

Many drug candidates that reach the clinical trial phase are unsuccessful due to several limitations, including poor pharmacokinetic properties. Such shortcomings also affect a considerable number of therapeutic agents already on the market (Gershell and Atkins, 2003; Karaoun and Renfrew, 2015; Kola and Landis, 2004). A possible solution to these problems is the design of drug delivery systems with the ability to overcome these limitations, thus pharmaceutical scientists are exploring various drug delivery strategies (Tiwari et al., 2012). Such strategies include the intentional, reversible modification of the physiochemical characteristics of a pharmaceutical in clinical use through the formation of a coordination complex with a transition metal (Renfrew, 2014; Thompson and Orvig, 2003). The rapid advances of coordination complexes, also known as metal complexes, as functional materials (catalysts, magnetic and porous materials) have motivated scientists in the pharmaceuticals and medicinal chemistry fields to focus on the research of metal complexes to investigate their potential in medical applications (Ma and Moulton, 2011; Zadrozny et al., 2012; Zhang et al., 2012). Coordination complexes using the metal as a drug carrier have subsequently shown their usefulness as both diagnostic and therapeutic agents (Lu et al., 2015; Mjos and Orvig, 2014). Metal carriers are a simple drug delivery strategy with the ability to induce pharmacokinetic changes to improve aqueous and lipid solubility, bioavailability, permeation and to achieve controlled drug release, while avoiding the time-consuming and costly drug discovery process (M'bitsi-Ibouily et al., 2017; Wang et al., 2013a). A recent study showed pharmacokinetic improvement of the standard drug for the treatment of hypothyroidism through metal coordination. In fact, a zinc-coordinated form of the drug was synthesized and formulated into coated gelatin capsules, which were orally administered to rats to achieve sustained drug release. The metal-coordinated drug exhibited slower absorption and prolonged bioavailability over time, compared to the free drug. It was demonstrated that both the slower rate of drug absorption and its sustained release were the result of a mechanism by which the drug's molecules separate from the metal complex by exchange with endogenous ligands before absorption into the bloodstream. The ligand exchange rate contribute to the slower rate of drug delivery (extended drug release) as well as the extended period of drug's absorption (Da Conceição et al., 2018).

Aqueous solubility improvement of a drug through metal complexation has been previously demonstrated by Ross and Riley who observed an increase in the aqueous solubility of lomefloxacin in the presence of calcium, magnesium, aluminium and iron ions (Ross and Riley, 1992). Shaikh and co-workers later synthesised a bismuth(III)-norfloxacin complex and investigated its pH-solubility profile. Up to pH 6.5.,the complexed drug showed higher aqueous solubility than the free drug, after which the solubility of the drug in the metal complex declined while that of the free drug remained unchanged (Shaikh et al., 2007). A further study in this area was conducted by Breda and co-workers on aluminium (III) complexes of ciprofloxacin and norfloxacin. Bioactives in both complexes exhibited higher aqueous solubility than the respective free drugs in the pH range 2-9 (Breda et al., 2009).

The manipulation of lipophilicity can be used as a drug delivery strategy to promote the enhanced diffusion of a drug through lipid membranes such as the blood-brain-barrier and the intestinal membrane (Chang et al., 2016; Parikh et al., 2010). Pinto and co-workers have previously demonstrated that ferrocene–encephalin, an example of a organometallic linker conjugated to a neuropeptide, resulted in increased BBB penetration of [Leu5]-enkephalin (Pinto et al., 2009). Metal complexation could therefore be used to enhance the lipid solubility and thus the permeation of drugs through the lipid membranes.

The presence of bonds highly responsive to their environment within transition metals allows them to exhibit controlled drug release. Stimuli-responsive complexes can therefore be designed that are inert under normal physiological conditions but become labile with a change in environment such as redox status, pH or the localised application of light. The voluntary deactivation of the bioactive through metal complexation can reduce the incidence of undesirable effects (Renfrew, 2014b). Ruthenium metal complexes have shown great potential for use as therapeutic compounds (Bergamo and Sava, 2011). Such metal complexes have many benefits, including improved water solubility, thus improved bioavailability, and increased lipophilicity for better absorption through the cell membrane (Piccariello, 2013). In addition to that, the metal complexing strategy results in relatively long half-lives, which allow for fewer administrations of the drug (Lentz et al., 2009). Furthermore, ruthenium complexes can also be used as inert structures with extended valance space available for additional auxiliary ligands and drugs (Maksimoska et al., 2008; Scrase et al., 2015).

As previously mentioned in Chapter 1, Section 1.1, SPR in a BCS class IV drug with low aqueous solubility, limited intestinal permeability, burst release and poor bioavailability.

This chapter focuses on the investigation of ruthenium (Ru) metal as a possible drug carrier with the ability to enhance the intestinal permeability and to retard the release of the drug

bonded to it. The antipsychotic drug sulpiride is a good candidate for this work due to its low intestinal permeability and burst drug release. The following five amino alcohols are used as ancillary ligands to synthesise ternary metal complexes of sulpiride: L1 = (R)-(+)-2-amino-3-phenyl-1-propanol, L2 = ethanolamine, L3 = (S)-(+)-2-amino-1-propanol, L4 = 3-amino-1-propanol, L5 = (S)-(+)-2-pyrrolidinemethanol. These molecules help stabilise the complex without directly interfering with its chemistry. Different ones are used to investigate their possible effect on the properties of the [Ru(II) – SPR] complex. The determination of the stability constant of the [Ru(II) – SPR] complex, the synthesis and characterization of five ternary ruthenium (II) complexes with general formula [Ru(*p* -cymene)(L)(SPR)]PF_6, as well as, solubility, dissolution, permeation and cytotoxicity studies of the drug incorporated in the metal complexes are reported.

3.2. MATERIALS AND METHODS

3.2.1. Materials

All chemicals used were of the analytical reagent grade and of the highest available purity. Sulpiride (SPR), (R)-(+)-2-amino-3-phenyl-1-propanol ($C_9H_{13}NO$, L1), ethanolamine (C_2H_7NO, L2), (S)-(+)-2-amino-1-propanol (C_3H_9NO, L3), 3-amino-1-propanol (C_3H_9NO, L4), (S)-(+)-2-pyrrolidinemethanol ($C_5H_{11}NO$, L5), triethylamine (TEA), ammonium hexafluorophosphate (NH_4PF_6) and dichloro(*p*-cymene)ruthenium(II) dimer were all purchased from Sigma-Aldrich and used as received. Sodium chloride, potassium chloride, disodium hydrogen phosphate and monopotassium phosphate were all purchased from Merck and used as received to prepare phosphate-buffered saline (PBS) following methods from the US Pharmacopeia. Eglonyl® 50 mg capsules were purchased from a local pharmacy. Organic solvents were purchased from Sigma-Aldrich and included dichloromethane (DCM), methanol (MeOH) and pentane. Dichloromethane and methanol were dried using a suitable drying agent under nitrogen and stored over 3Å molecular sieves prior to use. Millipore water was used where needed.

3.2.2. Instruments

Infrared spectra were recorded in the wavenumber region 4000-650 cm^{-1} on a Spectrum 100 FTIR spectrometer (Perkin-Elmer Inc. MA, USA) equipped with the attenuated total reflectance (ATR) sampling device. ^{1}H, ^{13}C and ^{31}P NMR spectra were recorded on a 300 MHz Bruker AVANCE II and 500 MHz Bruker AVANCE II spectrometer (Bruker Avance Biospin Germany) at the Department of Chemistry of the University of the Witwatersrand (Johannesburg, South Africa). All signals were confirmed by the ^{1}H-^{1}H COSY and ^{1}H-^{13}C HSQC experiments. A temperature-modulated differential scanning calorimeter (Mettler Toledo DSC1 STARe System, Switzerland) was used to investigate the thermal behaviour of the metal complexes. The thermogravimetric (TG and DTG) analyses were performed under a nitrogen atmosphere with a heating rate of 10°C.min^{-1} using the Thermogravimetric Analyzer TGA 4000 (Perkin-Elmer Inc. MA, USA). The UV-Vis measurements were recorded on a Lambda 25 UV/VIS Spectrophotometer (Perkin-Elmer Inc. MA, USA). The fluorescence spectrum was recorded on a Perkin Elmer LS-40 fluorescence spectrophotometer (Perkin-Elmer Inc. MA, USA).

3.2.3. Formation/Dissociation constant of the complex [Ru(p-cymene)Cl(SPR)]

3.2.3.1. Preparation of $1x10^{-1}$ M [Ru(p-cymene)Cl_2] and $1x10^{-1}$ M SPR

[Ru(*p*-cymene)Cl_2] (0.6124 g, 1 mmol, M. Wt. = 612.4 $g.mol^{-1}$) was dissolved in dry methanol and made up to the mark in a 100 mL volumetric flask.
SPR (0.34 g, 1 mmol, M. Wt. = 341.43 $g.mol^{-1}$) was dissolved in dry methanol and made up to the mark in a 100 mL volumetric flask.

3.2.3.2. Procedure for continuous variation method (Job's method)

The stoichiometric ratio of SPR to Ru(II) in the complex was determined by Job's method of equimolar solutions (Renny et al., 2013; Tirmizi et al., 2012). Ru(*p*-cymene)Cl_2 $1x10^{-1}$ M stock solution (0, 1, 2, …, 6 mL) was pipetted out and transferred into seven 50 mL volumetric flasks and an aliquot (6, 5,…, 0 mL) of $1x10^{-1}$ M SPR was added, respectively in such a way that the mole fraction of solution remained constant. The colour of the solution changed from brown to orange. Wavelength of maximum absorbance was noted against a blank, which appeared at 296 nm. All the measurements were made at 296 nm. The following equations were used to calculate the stability constant (K) and the dissociation constant (K_d):

$$K = \frac{[ML]}{[M]x\,[L]} = \frac{\left[\frac{A2}{A1}\right]}{\left[1 - \frac{A2}{A1}\right] * \left[C(SPR) - C(Ru) * \frac{A2}{A1}\right]} \quad (3.1)$$

Where M = amount of metal ion, L = amount of ligand, A1 = absorbance at break point, A2 = actual absorbance, C(SPR) = concentration of sulpiride and C(Ru) = concentration of ruthenium.

$$K_d = \frac{1}{K} \quad (3.2)$$

Where K = formation constant and K_d = dissociation constant.

3.2.4. Synthesis of Metal Complexes

All metal complexations were carried out under inert atmosphere of nitrogen. Dichloromethane and methanol were dried using a suitable drying agent under nitrogen and stored over 3Å molecular sieves prior to use. The synthesis procedure is summarised in Figure 3.1.

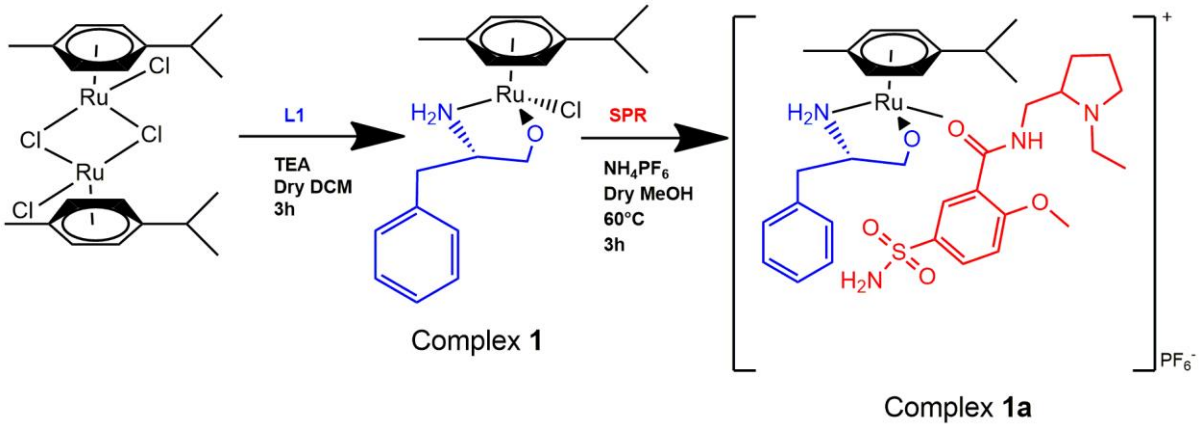


Figure 3.1. Synthesis procedure of ternary metal complexes of sulpiride. L1 is used as an example of ancillary ligand.

3.2.4.1. Representative synthesis of the precursor complexes **1-5**

The synthesis of the precursor metal complexes was adapted from literature (Heinrich et al., 2011; Tan et al., 2011). Respective dry Schlenk tubes were charged with 20 mL dry DCM, amino alcohol (1.633 mmol) and TEA (1.633 mmol; 228 µL) and left to stir for 30 minutes at room temperature. Complexes **1-5** required L1: 247 mg, L2: 100 mg, L3: 123 mg, L4: 123 mg and L5: 165 mg respectively. Dichloro(*p*-cymene)ruthenium(II) (0.816 mmol; 500 mg) was then added. The resulting orange solutions were left to stir for 3h at room temperature and thereafter solvent was removed *in vacuo* to afford the complexes **1-5**.

[Ru(*p*-cymene)Cl(L1)](**1**)

Physical state: orange powder. Yield: 657 mg (95.36%). Melting point: 160°C. Selected IR absorption bands (ATR, cm^{-1}): 871.6 (*p*-substituted aromatic ring), 730, 1585 (N-H bending), 1087 (C-H in plane bending), 871.6 (C-H out of plane bending), 1092.41. ^{1}H NMR (500 MHz,

chloroform-*d*) δ 7.70 (s, 2H, NH_2; L1), 7.22-7.11 (m, 5H, CH, CH, CH, CH, CH overlapping; L1), 5.79 (m, 4H, CH, CH, CH, CH; *p*-cymene), 3.06 (m, 2H, CH_2O; L1), 2.88 (s, 1H, CH; *p*-cymene), 2.88 (s, 1H, $CH(NH_2)$; L1), 2.62 (s, H, CH; L1), 2.50 (s, H, CH; L1), 2.09 (m, 3H, CH_3; *p*-cymene), (1.23, m, 6H, CH_3, CH_3; *p*-cymene). ^{13}C NMR (126 MHz, Chloroform-*d*) δ 137.4 (C, OH; L1), 129.3 (CH, CH; L1), 129.1 (CH, CH; L1), 128.9 (CH; L1), 126.9 (CH, CH; L1), 101.5 (C; *p*-cymene), 95.45 (C; *p*-cymene), 81.12 (CH, CH; *p*-cymene), 80.73 (CH, CH; *p*-cymene), 59.54 ($CH(NH_2)$); L1), 46.03 (CH_2; L1), 39.14 (CH_2O; L1), 30.70 (CH; *p*-cymene); 22.89 (CH_3; *p*-cymene), 21.92 (CH_3; *p*-cymene), 18.51 (CH_3; *p*-cymene). UV-VIS. λ_{max} (nm): 219, 319.

[Ru(*p*-cymene)Cl(L2)] (**2**)

Physical state: yellow residue. Yield: 445 mg (82.13%). Melting point: 148°C. Selected IR absorption bands (ATR, cm^{-1}): 875.4 (p-substituted), 730.8 (C-H bending), 1595 (C=C). ^1H NMR (500 MHz, Chloroform-*d*) δ 5.57 (d, *J* = 5.8 Hz, 2H, CH, CH; *p*-cymene), 5.42 (d, *J* = 5.7 Hz, 2H, CH, CH, *p*-cymene), 4.76 (s, 2H; NH_2), 3.75 (bs, 2H, CH_2O; L2), 3.14 (bs, 2H, $CH_2(NH_2)$, L2), 2.95 (dt, *J* = 13.5, 6.8 Hz, 1H, CH; *p*-cymene), 2.35 (s, 3H, CH_3; *p*-cymene), 1.29 (d, *J* = 6.9 Hz, 6H, CH_3, CH_3; *p*-cymene). ^{13}C NMR (126 MHz, Chloroform-*d*) δ 105.32 (C; *p*-cymene), 95.22 (C; *p*-cymene), 82.76 (CH, *p*-cymene), 80.93 (CH, *p*-cymene), 62.63 (CH_2O; L2), 52.28 ($CH_2(NH_2)$; L2), 31.03 (CH; *p*-cymene), 22.49 (CH_3; *p*-cymene), 18.48 (CH_3; *p*-cymene). UV-VIS. λ_{max} (nm): 217, 322.

[Ru(*p*-cymene)Cl(L3)] (**3**)

Physical state: brick red powder. Yield: 535 mg (94.74%). Melting point: 126°C. Selected IR absorption bands (ATR, cm^{-1}): 870.5 (p-substituted), 802.8 (C-H bending), 1087 (C-H in plane bending), 3188 (C-H stretching). ^1H NMR (500 MHz, Chloroform-*d*) δ 7.93 (s, 2H, NH_2; L3), 5.95 (d, *J* = 5.3 Hz, 1H, CH; *p*-cymene), 5.85 (s, 1H, CH; *p*-cymene), 5.82 (d, *J* = 5.4 Hz, 1H; *p*-cymene), 5.60 (m, 1H, CH; *p*-cymene), 3.24 (m, 2H, CH_2; L3), 2.90 (dt, *J* = 16.0, 8.4 Hz, 1H, CH; L3), 2.76 (s, 1H, CH; *p*-cymene), 2.12 (m, 3H, CH_3; *p*-cymene), 1.25 (dd, *J* = 6.8, 1.8 Hz, 6H, CH_3, CH_3; *p*-cymene), 1.20 (d, *J* = 6.0 Hz, 3H, CH_3; L3). ^{13}C NMR (126 MHz, Chloroform-*d*) δ 101.45 (C; *p*-cymene), 95.37 (C; *p*-cymene), 81.02 (CH; *p*-cymene), 80.74 (CH; *p*-cymene), 80.06 (CH; *p*-cymene), 78.58 (CH; *p*-cymene), 67.13 (CH_2O; L3), 39.16 ($CH(NH_2)$; L3), 30.70 (CH; *p*-cymene), 22.91 (CH_3; L3), 21.90 (CH_3, *p*-cymene), 18.47 (CH_3, *p*-cymene).UV-Vis λ_{max} (nm): 218, 319.

[Ru(*p*-cymene)Cl(L4)] (**4**)

Physical state: brick red residue. Yield: 462 mg (81.91%). Melting point: 126°C. Selected IR absorption bands (ATR, cm^{-1}): 861.3 (p-substituted), 697.7, 1579 (N-H bending), 731.2 (C-H

out of plane bending), 1465, 1579 (C-C stretching). ^{1}H NMR (500 MHz, Chloroform-*d*) δ 5.45 (d, *J* = 5.9 Hz, 2H, CH, CH; *p* -cymene), 5.37 (d, *J* = 5.9 Hz, 2H, CH, CH; *p*-cymene), 3.75 (t, *J* = 5.1 Hz, 2H, CH_2(NH); L4), 3.23 (s, 2H, CH_2O; L4), 2.97 (hept, *J* = 6.9 Hz, 1H, CH, L4), 2.24 (s, 3H, CH_3; *p*-cymene), 1.76 (m, 2H, CH_2; L4), 1.30 (d, *J* = 6.9 Hz, 6H, CH_3; *p*-cymene). ^{13}C NMR (126 MHz, Chloroform-*d*) δ 102.7 (C; *p*-cymene), 95.80 (C; *p*-cymene), 81.22 (CH; *p*-cymene), 80.41 (CH; *p*-cymene), 60.71 (CH_2O; L4), 47.61 (CH_2(NH); L4), 34.65 (CH_2; L4), 31.02 (CH; *p*-cymene), 22.40 (CH_3; *p*-cymene), 18.86 (CH_3; *p*-cymene). UV-Vis λ_{max} (nm): 217, 320.

[Ru(*p*-cymene)Cl(L5)] (**5**)

Physical state: dark orange powder. Yield: 558 mg (91.89%). Melting point: 132°C. Selected IR absorption bands (ATR, cm^{-1}): 872.9 (p-substituted), 729.2, 1469 (N-H bending), 731.2 (C-H out of plane bending), 3081 (N-H stretching), 802.7 (C-H out of plan bending). ^{1}H NMR (500 MHz, Chloroform-*d*) δ 8.45 (s, 1H, NH; L5), 6.01 (d, *J* = 32.0 Hz, 1H, CH; *p*-cymene), 5.83 (1H, CH, *p*-cymene), 5.78 (d, *J* = 46.1 Hz, 1H; *p*-cymene), 5.73 (1H, CH, *p*-cymene), 3.29 (s, 2H, CH_2O; L5), 2.97 (s, 1H, CH; *p*-cymene), 2.20 (s, 2H, CH_2(NH); L5), 2.13 (m, 3H, CH_3; *p*-cymene), 1.82 (s, 2H, CH_2; L5), 1.30 (m, 2H, CH_2; L5), 1.25 (m, 3H, CH_3; *p*-cymene). ^{13}C NMR (126 MHz, Chloroform-*d*) δ 101.66 (C; *p*-cymene), 94.20 (C; *p*-cymene), 81.42 (CH; *p*-cymene), 81.06 (CH; *p*-cymene), 80.66 (CH; *p*-cymene), 79.85 (CH; *p*-cymene), 68.61 (CH_2O; L5), 62.13 (CH(NH); L5), 49.40 (CH_2(NH); L5), 30.67 (CH; *p*-cymene); 24.87 (CH_2; L5), 21.65 (CH3; *p*-cymene), 18.28 (CH_3; *p*-cymene). UV-Vis λ_{max} (nm): 217, 318.

3.3.4.2. Representative synthesis of the final complexes **1a**-**5a**

The synthesis of the final metal complexes 1a-5a was adapted from literature (GRGURIĆ-ŠIPKA et al., 2008; Lopes et al., 2015). To respective solutions of complexes 1-5 (1.541 mmol, 1.341 mmol, 1.533 mmol, 1.336 mmol and 1.479 mmol respectively) in 20 mL methanol at 60°C, NH_4PF_6 was added (1.541 mmol, 1.341 mmol, 1.533 mmol, 1.336 mmol and 1.479 mmol respectively). The resulting orange mixtures were left to stir for 30 minutes at 60°C. SPR was then added (1.541 mmol, 1.341 mmol, 1.533 mmol, 1.336 mmol and 1.479 mmol respectively). The resulting orange solutions were left to stir for 3h at 60°C under reflux and thereafter solvent was removed *in vacuo* to afford the complexes 1a-5a. Residues were obtained which were solubilised in DCM and layered with pentane to afford the products. A cannula was used to filter the products, which were then dried *in vacuo*.

[Ru(*p*-cymene)(L1)(SPR)]PF_6 (**1a**)

Physical state: mustard yellow powder. Yield: 1.08 g (92.15%). Melting point; 237°C. Elemental anal. calcd. for $C_{34}H_{50}F_6N_4O_5PRuS$: C, 46.84; H, 5.66; N, 6.43, S, 3.68. Found: C,

46.18; H, 5.60; N, 6.28, S, 3,64. Selected IR absorption bands (ATR, cm^{-1}): 3325, 3184 (υ, NH_2), 3064 (δ, =NH), 1634 (υ, C=O), 1335 ($υ_{asym}$, SO_2), 1092 ($υ_{sym}$, SO_2). ^{1}H NMR (500 MHz, DMSO-*d6*) δ 8.38 (s, 1H, NH; SPR), 8.27 (d, *J* = 2.4 Hz, 1H, CH; SPR), 7.90 (dd, J=8.7, 2.4 Hz, 1H, CH; SPR), 7.88 (m, 2H, NH_2; SPR), 7.88 (m, 1H, CH; SPR), 7.88 (m, 5H, CH, CH, CH, CH, CH overlapping; L1), 5.81 (m, 1H, CH; *p*-cymene), 5.76 (s, 1H, CH; *p*-cymene), 5.37 (m, 2H, CH, CH; *p*-cymene), 3.97 (m, 3H, CH_3O; SPR), 3.50 (m, 2H, CH_2O; L1), 3.21 (s, 2H, CH_2(NH); SPR), 3.14 (m, 1H, CH(NH_2); L1), 2.84 (m, 2H, CH_2; SPR), 2.77 (s, 1H, CH; SPR); 2.25 (m, 2H, CH_2; L1), 2.15 (m, 1H, CH; SPR); 2.09 (m, 6H, CH3, CH3; *p*-cymene), 1.85 (m, 2H, CH_2; SPR), 1.55 (m, 2H, CH_2; SPR), 1.20 (d, J = 6.9 Hz, 1H, CH: *p*-cymene), 1.18 (m, 3H, CH_3; SPR). ^{13}C NMR (126 MHz, DMSO-*d6*) δ 163.6 (C=O; SPR), 159.2 (CO; SPR), 137 (CS; SPR), 129.9 (CH; SPR), 129.2 (CH; SPR), 128.5 (CH; L1), 126.7 (CH, L1), 122.7 (C; SPR), 112.6 (CH; SPR), 106.4 (C; *p*-cymene), 86.35 (CH; *p*-cymene), 85.50 (CH; *p*-cymene); 62.18 (CH; SPR), 60.36 (CH2O; L1), 56.58 (CH_3O; SPR); 53.82 (CH(NH_2); L1), 53.15 (CH_2; SPR), 47.67 (CH_2; L1), 45.54 (CH_2; SPR), 29.97 (CH_3; *p*-cymene), 28.12 (CH_2; SPR), 22.49 (CH_2; SPR), 21.49 (CH; *p*-cymene), 17.86 (CH_3; *p*-cymene), 13.77 (CH_3; SPR). ^{31}P-NMR (202 MHz, DMSO-d_6) δ -144.19 (d, *J* = 711.3 Hz). UV-Vis $λ_{max}$ (nm): 286, 340,377.

[Ru(*p*-cymene)(L2)(SPR)]PF_6 (**2a**)

Physical state: brown residue. Yield: 0.602 g (70.40%). Melting point: 222°C. Elemental anal. calcd. for $C_{27}H_{44}F_6N_4O_5PRuS$: C, 41.40; H, 5.62; N, 7.15, S, 4.08. Found: C, 41.21; H, 5.39; N, 7.11, S, 4.00. Selected IR absorption bands (ATR, cm^{-1}): 3324, 3189 (υ, NH_2), 3063 (δ, =NH), 1634 (υ, C=O), 1334 ($υ_{asym}$, SO_2), 1094 ($υ_{sym}$, SO_2). ^{1}H NMR (500 MHz, DMSO-d_6) δ 8.55 (s, 1H, NH; SPR), 8.25 (d, *J* = 2.2 Hz, 1H, CH; SPR), 7.90 (dd, *J* = 8.7, 2.4 Hz, 1H, CH; SPR), 7.34 (s, 1H, CH; SPR), 7.32 (s, 2H, NH_2; SPR), 5.61 (m, 2H, CH, CH; *p*-cymene), 5.44 (m, 2H, CH, CH; *p*-cymene), 3.98 (m, 3H, CH_3O; SPR), 3.58 (s, 2H, CH2(NH); SPR), 3.47 (m, 1H, CH; SPR), 3.47 (m, 1H, CH_2O; L2), 2.92 (s, 2H, CH_2(NH_2); L2), 2.85 (s, 2H, CH_2; SPR), 2.81 (d, *J* = 17.3 Hz, 1H, CH, *p*-cymene), 2.17 (s, 3H, CH_3; *p*-cymene), 2.13 (m, 2H, CH_2; SPR), 1.77 (m, 4H, CH_2, CH_2; SPR), 1.22 (d, *J* = 6.8 Hz, 6H, CH_3, CH_3; *p*-cymene), 1.17 (d, *J* = 2.7 Hz, 3H, CH_3; SPR). ^{13}C NMR (126 MHz, DMSO-d_6) δ 163.6 (C=O; SPR), 159.2 (CO; SPR), 136.4 (CS; SPR), 129.8 (CH; SPR), 128.6 (CH; SPR), 122.7 (C; SPR), 112.6 (CH; SPR), 82.50 (CH; *p*-cymene), 80.26 (CH; *p*-cymene), 61.35 (CH; SPR), 61.30 (CH_2O; L2), 56.57 (CH_3O; SPR), 53.12 (CH_2; SPR), 51.46 (CH_2(NH_2); L2); 47.63 (CH_2; SPR), 41.23 (CH_2(NH); SPR), 30.24 (CH; *p*-cymene), 28.11 (CH_2; SPR), 22.47 (CH_2; SPR), 21.94 (CH_3; *p*-cymene), 17.43 (CH_3; *p*-cymene), 13.77 (CH_3; SPR). UV-Vis $λ_{max}$ (nm): 280, 342, 378.

[Ru(*p*-cymene)(L3)(SPR)]PF_6 (**3a**)

Physical state: mustard yellow powder. Yield: 1.04 g (98.7%). Melting point; 226°C. Elemental anal. calcd. for $C_{28}H_{46}F_6N_4O_5PRuS$: C, 42.18; H, 5.77 ; N, 7.03, S, 4.02. Found: C, 41.95; H, 5.67; N, 7.00, S, 3.97. Selected IR absorption bands (ATR, cm^{-1}): 3325 3185 (υ, NH_2), 3063 (δ, =NH), 1634 (υ, C=O), 1335 ($υ_{asym}$, SO_2), 1094 ($υ_{sym}$, SO_2). ^{1}H NMR (500 MHz, DMSO-d_6) δ 8.39 (s, 1H, NH; SPR), 8.27 (d, *J* = 2.4 Hz, 1H, CH; SPR), 7.89 (dd, *J* = 8.7, 2.5 Hz, 1H, CH; SPR), 7.33 (d, *J* = 8.8 Hz, 1H, CH, SPR), 7.33 (2H, NH_2; SPR), 5.79 (d, *J* = 15.3 Hz, 4H, CH, CH, CH, CH; *p*-cymene), 3.97 (s, 3H, CH_3O; SPR), 3.51 (s, 2H, CH_2(NH); L3), 3.38 (s, 1H, CH; SPR), 3.23 (s, 2H, CH_2O; L3), 2.88 (bs, 1H, CH(NH_2); L3), 2.88 (bs, 1H, CH; *p*-cymene), 2.88 (bs, 2H, CH_2; SPR), 2.69 (s, 1H, CH; SPR), 2.24 (s, 1H, CH; SPR), 2.09 (s, 3H, CH_3; *p*-cymene), 1.69 -1.55 (m, 4H, CH_2, CH_2; SPR), 1.19 (m, 6H, CH_3, CH_3; *p*-cymene), 1.11 (m,3H, CH_3; SPR), 1.08 (m, 3H, CH_3; L3). ^{13}C NMR (126 MHz, DMSO-d_6) δ 163.6 (C=O; SPR), 159.2 (CO; SPR), 136.4 (CS; SPR), 129.8 (CH; SPR), 128.6 (CH; SPR), 122.7 (C; SPR), 112.6 (CH; SPR), 106.4 (C; *p*-cymene), 100.1 (C; *p*-cymene), 86.33 (CH; *p*-cymene), 85.49 (CH; *p*-cymene), 62.53 (CH; SPR), 62.17 (CH_2O; L3), 56.57 (CH_3O; SPR), 53.12 (CH; SPR), 48.45 (CH(NH_2); L3), 47.65 (CH; SPR), 41.54 (CH(NH); SPR), 29.95 (CH; *p*-cymene), 28.10 (CH_2; SPR), 22.46 (CH_2; SPR), 21.48 (CH_3; *p*-cymene), 17.84 (CH_3; *p*-cymene), 14.99 (CH_3; L3), 13.74 (CH_3; SPR). UV-Vis $λ_{max}$ (nm): 289, 345,377.

[Ru(*p* -cymene)(L4)(SPR)]PF_6 (**4a**)

Physical state: brown residue. Yield: 0.658 g (75.57%). Melting point: 260°C. Elemental anal. calcd. for $C_{28}H_{46}F_6N_4O_5PRuS$: C, 42.18; H, 5.77 ; N 7.03, S, 4.02. Found: C, 42.11; H, 5.74; N, 6.96, S, 4.01. Selected IR absorption bands (ATR, cm^{-1}): 3324, 3223 (υ, NH_2), 3071 (υ, =NH), 1634 (υ, C=O), 1335 ($υ_{asym}$, SO_2), 1093 ($υ_{sym}$, SO_2). ^{1}H NMR (500 MHz, DMSO-d_6) δ 8.66 (s, 1H, NH; SPR), 8.25 (m, 1H, CH; SPR), 7.91 (dd, *J* = 8.7, 2.2 Hz, 1H, CH; SPR), 7.34 (s, 2H, NH_2;SPR), 7.32 (s, 1H, CH; SPR), 5.61 (d, *J* = 5.5 Hz, 1H, CH; *p*-cymene), 5.52 (q, *J* = 5.9, 5.0 Hz, 1H,CH; *p*-cymene), 5.45 (d, *J* = 6.0 Hz, 1H,CH; *p* -cymene), 5.41 (d, *J* = 5.7 Hz, 1H,CH; *p* -cymene), 3.99 (s, 3H, CH_3O; SPR), 3.47 (m, 2H, CH_2(NH); SPR), 3.45 (m, 2H, CH_2O; L4), 3.39 (m, 1H, CH; SPR), 2.90 (m, 2H, CH_2; SPR), 2.88 (m, 2H, CH_2(NH); L4), 2.81 (dt, *J* = 13.9, 5.6 Hz, 1H, CH; *p*-cymene), 2.13 (m, 3H, CH_3; *p*-cymene), 1.84 (m, 2H, CH_2; SPR), 1.65 (m, 2H, CH_2; SPR), 1.64 (dt, *J* = 13.1, 6.6 Hz, 2H, CH_2; L4), 1.20 (d, *J* = 6.9 Hz, 6H, CH_3, CH_3; *p*-cymene), 1.18 (m, 3H, CH_3; SPR). ^{13}C NMR (126 MHz, DMSO-d_6) δ 163.7 (C=O; SPR), 159.1 (CO; SPR), 136.4 (CS; SPR), 129.8 (CH; SPR), 128.6 (CH; SPR), 122.6 (C; SPR), 112.6 (CH; SPR), 102.7 (C; *p*-cymene), 95.27 (C; *p*-cymene), 86.29 (CH; *p*-cymene), 85.44 (CH; *p*-cymene), 62.51 (CH; SPR), 58.65 (CH_2O; L4), 56.54 (CH_3O; SPR), 53.04 (CH; SPR), 47.74 (CH; SPR), 46.95 (CH(NH); L4) , 46.56 (CH; L4), 41.35 (CH_2(NH); L4), 34.99 (CH; L4), 34.83 (CH; L4), 28.01 (CH_2; SPR), 22.38 (CH_2; SPR), 21.95 (CH_3; *p*-

cymene), 21.44 (CH_3; *p*-cymene), 17.51 (CH_3; *p*-cymene), 13.58 (CH_3; SPR). UV-Vis λ_{max} (nm): 287, 345, 377.

[Ru(*p* -cymene)(L5)(SPR)]PF_6 (**5a**)

Physical state: mustard yellow powder. Yield: 1.04 g (98.6%). Melting point; 252°C. Elemental anal. calcd. for $C_{30}H_{48}F_6N_4O_5PRuS$: C, 43.76; H, 5.84 ; N 6.81, S, 3.89. Found: C, 43.61; H, 5.74; N, 6.75, S, 3,80. Selected IR absorption bands (ATR, cm^{-1}): 3383, 3328 (υ, NH_2), 3190 (υ, =NH), 1634 (υ, C=O), 1335 (υ_{asym}, SO_2), 1095 (υ_{sym}, SO_2). ^{1}H NMR (500 MHz, DMSO-d_6) δ 8.44 (s, 1H, NH; L5), 8.26 (s, 1H, CH; SPR), 7.90 (d, *J* = 8.7 Hz, 1H, CH; SPR), 7.34 (s, 1H, CH; SPR), 7.32 (s, 2H, NH_2; SPR), 5.79 (d, *J* = 15.8 Hz, 2H, CH, CH; *p*-cymene), 5.48 (dd, *J* = 118.6, 5.5 Hz, 2H, CH, CH; *p*-cymene), 3.98 (s, 3H, CH_3; SPR), 3.53 (m, 1H, CH; SPR), 3.29 (s, 2H, CH_2(NH); SPR), 3.12 (s, 2H, CH_2O; L5), 2.98 (s, 2H, CH_2(NH); L5), 2.94 (m, 2H, CH_2; SPR), 2.82 (s, 1H, CH; *p*-cymene), 2.36 (s, 2H, CH_2; SPR), 2.10 (d, *J* = 11.2 Hz, 3H, CH_3; *p*-cymene), 1.88 (m, 2H, CH_2; SPR), 1.72 (m, 2H, CH_2; L5), 1.60 (m, 2H, CH_2; SPR), 1.20 (s, 3H, CH_3; *p*-cymene), 1.11 (s, 3H, CH_3; SPR). ^{13}C NMR (126 MHz, DMSO-d_6) δ 164.10 (C=O; SPR), 159.18 (CO; SPR), 136.35 (CS; SPR), 129.92 (CH; SPR), 128.59 (CH; SPR), 122.57 (C; SPR), 106.37 (C; *p*-cymene), 101.68 (C; *p*-cymene), 86.34 (CH; *p*-cymene), 85.49 (CH; *p*-cymene); 81.83 (CH; *p*-cymene); 79.89 (CH; *p*-cymene), 60.78 (CH_2O; L5); 60.13 (CH; SPR), 56.58 (CH_3O; SPR), 53.09 (CH_2; SPR), 47.92 (CH_2; SPR), 45.59 (CH_2; L5), 44.83 (CH_2; L5); 41.10 (CH_2(NH); SPR), 29.95 (CH; *p*-cymene), 27.94 (CH_2(NH); L5), 25.76 (CH_2; SPR), 23.30 (CH_2; SPR), 22.13 (CH_3; *p*-cymene), 21.48 (CH_3; *p*-cymene), 17.85 (CH_3; *p*-cymene), 13.12 (CH_3; SPR). UV-Vis λ_{max} (nm): 274, 340,378.

Several attempts to grow single crystals of complexes **1a- 5a** for X-ray diffraction analysis were undertaken but remained unsuccessful.

The metal complexes **1a**, **3a** and **5a** were chosen for the solubility, dissolution, permeation and cytotoxicity studies described below. This is due to their favourable yields (> 90%) and physical state (powder). The products, in fact, needed to be accurately weighed for these studies; which made powder more suitable than oil residues.

3.2.5. Solubility Studies of free SPR and SPR in complexes 1a, 3a and 5a

Solubility studies were conducted in Millipore water, PBS pH 6.8, PBS pH 7.4 and methanol by adapting published methods (Madan et al., 2015; Mashhadi et al., 2016). Water was chosen as a medium to investigate the possible improvement of SPR aqueous solubility upon complexation to the metal and ancillary ligands. PBS pH 6.8 and pH 7.4 were chosen because they simulate the small intestine and the systemic environments, respectively. The

improvement of SPR solubility in these media could result in better gastrointestinal absorption of the drug, enhanced penetration of the drug through the intestinal membrane and improved bioavailability (Parikh et al., 2010). Methanol was selected because it is the organic solvent in which SPR exhibits the highest solubility *in vitro* (Murov, 2010). The aim was to investigate the effect of the metal on the solubility of the drug in methanol. A known amount of each compound was dissolved in a known quantity of each solvent (twenty replicates) and the resulting solutions were placed in an orbital shaker incubator LM-530 (Lasec, South Africa) at a speed of 25 rpm for 24 hours at 37°C. The resulting solutions were filtered. The amount of SPR dissolved in each solvent was then quantified using a UV-Vis calibration curve (Appendix D).

3.2.6. Dissolution studies of free SPR and SPR in complexes 1a, 3a and 5a

Dissolution studies of commercially available sulpiride (50 mg Eglonyl® capsules), 106 mg complex 1a, 95.4 mg complex 3a and 99.2 mg complex 5a were performed as per USP guidelines. The UV-Vis calibration curve for SPR was used to ensure that all metal complexes had an equivalent SPR amount (50 mg). All experiments were performed in triplicate. The samples were prepared by inserting them into empty capsules equivalent in size and shape to Eglonyl® capsules. DT 700 dissolution tester (Erweka, Germany) in paddle mode was used. Figure 3.2 shows a schematic of the rotating paddle method. The dissolution medium was PBS (900 mL) at different pH conditions (1.5, 6.8 and 7.4) to simulate different parts of the gastrointestinal tract. The stirring rate was 100 rpm and the temperature was kept at 37 ± 0.5°C for the duration of the experiment (24 hours). A stainless mesh ring was placed into the dissolution, below the paddle, in order to minimise sample floating. Sampling (5 mL) was done with replacement with the dissolution medium at 0.5, 1, 1.5, 2, 3, 4, 5, 6, 7, 8, 9, 10, 12 and 24 hours for all pH values investigated. Withdrawn samples were assayed for dissolved SPR using a UV-Vis calibration curve.

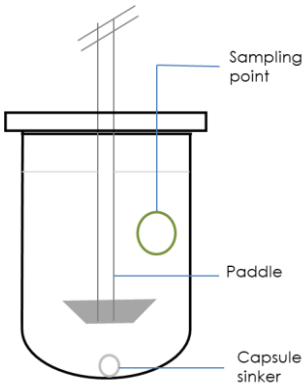


Figure 3.2. Schematic of the rotating paddle method.

3.2.7. Permeation studies of free SPR and SPR in complexes 1a, 3a and 5a

Ex vivo permeation studies were performed to evaluate the comparative intestinal absorption of free SPR against SPR in metal complexes. The close resemblance of the pig's gastrointestinal tract to that of humans motivated the choice of porcine small intestine for permeation study (Hoosain et al., 2016; Ngwuluka et al., 2017). This study was approved by the Animal Ethics Screening Committee (AESC) of the University of the Witwatersrand, Johannesburg (Ref: Reference: Gretta Mbitsi-Ibouily 14-11-14 O) and all experiments were performed in accordance with guidelines and regulations prescribed by the AESC. Intestinal tissue from euthanised pigs was obtained from at the Central Animal Service (CAS) of the University of the Witwatersrand. Porcine small intestines were surgically removed, transported to the laboratory where they were cleaned, and the exogenous tissues and subcutaneous layers carefully removed. They were then stored at -80°C for further use. On the day of the experiment, intestinal tissues were thawed at room temperature, cut in pieces prior to use and mounted on vertical Franz diffusion cells (United Scientific, South Africa). Figure 3.3 illustrates a Franz diffusion cell. Each Franz diffusion cell had a membrane area of 1.77 cm^2 exposed and a 12 mL receptor chamber capacity. The tissue membranes were mounted between the donor and receptor compartment with the apical side facing the donor compartment and the basolateral side facing the receptor medium, which was filled with PBS, pH 7.4. Each sample was done in triplicate. Samples consisted of 5 mg SPR, 10.6 mg complex 1a, 9.5 mg complex 3a and 9.9 mg complex 5a. SPR's UV-Vis calibration curve was used to ensure that all metal complexes contained equivalent amounts of SPR (5 mg). Each sample was applied to the donor compartment and 3 mL PBS, pH 6.8, was added. Temperature was kept at 37 ± 0.5°C. Samples of 0.1 mL were withdrawn at intervals 0.5, 1, 1.5, 2, 3, 4, 5, 6, 7, 8, 12 and 24 hours, and replaced with the same volume of buffer solution. Withdrawn samples were assayed for dissolved SPR using a UV-Vis calibration curve.

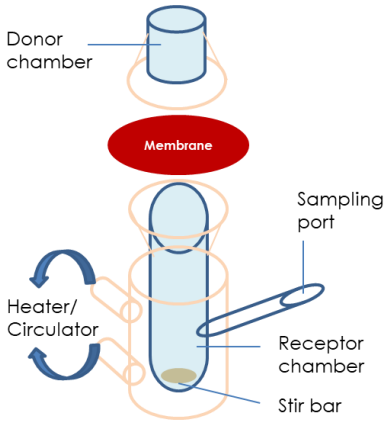


Figure 3.3. Schematic of a Franz diffusion cell.

The cumulative amount of SPR permeated across the membrane and the flux (J) values across the membrane were calculated in accordance with the formulas below:

Cumulative amount of drug permeated = $\frac{Q}{A}$ ($\mu g.cm^{-2}$) (3.3)

Where Q = amount of substance crossing the membrane (µg)
A = membrane area exposed (cm^2)

$J = \frac{Q}{At}$ ($\mu g.cm^{-2}.h^{-1}$) (3.4)

Where Q = amount of substance crossing the membrane (µg)
A = membrane area exposed (cm^2)
t = exposure time (h)

In *ex vivo* studies, confirmation of tissue integrity is essential, since any compromised tissue integrity during handling will result in inaccurate permeation results (Davies et al., 2004). Ionic conductivity as a measure of the porcine intestinal tissue integrity was determined using a SevenMulti S40 pH/electrical conductivity meter (Mettler-Toledo, Zurich, Switzerland) prior to (t_0) the experimental procedure and at t_8, t_{12} and t_{24}. The FTIR spectrum of the intestinal tissue was also collected and at t_0 t_8, t_{12} and t_{24} (Davies et al., 2004; Indermun et al., 2015).

3.2.8. In vitro toxicity testing of free SPR and SPR in complexes 1a, 3a and 5a using Caco-2 cell line

The small intestinal lumen surface area is lined with an epithelial cell monolayer, which isolates the systemic circulation from the intestinal lumen. This epithelial monolayer prevents the invasion of bacteria and toxic compounds from the gastrointestinal tract. Intestinal epithelial cells can be disturbed or damaged by either toxic chemical compounds or toxicity generated during digestion. Disturbance or damage in the intestinal epithelial tissues may result in the weakening of its protective role. Therefore, the possible cytotoxicity of free sulpiride and sulpiride in complexes 1a, 3a and 5a was investigated using Caco-2 intestinal cell line (Cellonex, South Africa), a human cell line derived from a colon adenocarcinoma. This cell line was selected due to its wide use in assays involving drug absorption following oral administration, as well as its similar characteristics to those of the absorptive intestinal epithelium (Chen et al., 2016; Igartúa et al., 2015; Meunier et al., 1995).

3.2.8.1. Caco-2 cell line culturing

Caco-2 cells (Cellonex, South Africa) were grown in culture flasks containing solution Dulbecco's Modified Eagle Medium (DMEM), supplemented with 20% fetal bovine serum with 4.0 mM l-glutamine and sodium pyruvate, with added 1 mL penicillin/streptomycin (Sigma-Aldrich; St. Louise, MO, USA). Cells were maintained in an incubator (RS Biotech Galaxy, Irvine, UK) under humidified atmosphere of 5% CO_2 at 37°C during cell growth. The cell medium was replaced every 2 to 3 days. Cells were grown until they reached 60–90% confluence before cytotoxicity tests were conducted.

3.2.8.2. Cell counting using trypan blue solution assay and a haemocytometer

When 60-90% confluence was reached, the medium was discarded from the cultured flask, followed by addition of trypsin-EDTA (3 mL) and incubation for 5 minutes to detach the cells. The cultured flask was scrapped to ensure detachment of all cells. The incubated solution was centrifuged at 1500 g for 5 minutes. The supernatant was discarded, and cells were resuspended in fresh medium 1 mL). Trypan blue solution (100 µL) was added to the suspended cells (100 µL). The disposable haemocytometer chamber was filled with a mixture of trypan blue solution added to the suspended cells. Light microscopy (Olympus CKS53 microscope, Olympus, Japan) was used to examine the chamber for cell counting. Trypan blue solution only stains dead cells. By counting unstained cell, the number of living cells in the sample was determined.

3.2.8.3. In vitro cytotoxicity evaluation using methyl thiazolyl tetrazolium (MTT) assay

Cytotoxicity of the of free SPR and SPR in complexes 1a, 3a and 5a in Caco-2 cell line was evaluated using the MTT assay. Multi well plates (96) were seeded with Caco-2 cells at a density of $2x10^4$ cells/well and incubated for 24 hours. After culturing the cells in 96 well plates for 24 hours in the incubator (RS Biotech Galaxy, Irvine, UK) under humidified atmospheric conditions of 5% CO_2 at 37°C, the culture was removed from the incubator into a laminar flow unit. Thereafter, different concentrations of prepared SPR and complexes 1a, 3a and 5a solutions (50, 100, 250, 500 and 1000 mg/L SPR) of equal volumes were added to the initial culture media. The cells were incubated for further 24 hours at 37°C. At the end of the 24-hour incubation, 10 µL of MTT solution was added to the wells, and the 96 well plate was incubated for 4 hours to allow the conversion of MTT to formazan by mitochondrial dehydrogenase. Following the 4-hour incubation period, the medium was removed from the wells. The formazan formed crystals were dissolved by adding DMSO solution (100 µL). The plates were placed in an orbital shaker overnight. Absorbance was measured at a wavelength of 570 nm. The background absorbance of the multi well plates was measured at 690 nm and

was subtracted from the 570nm measurement. The resulting measurements were presented as percentage cell viability (mean ± standard deviation). Equation (5) was used to calculate the percentage cell viability:

$$\text{Percentage cell viability} = \frac{Mean\ absorbance\ at\ each\ concentration}{Mean\ absorbance\ of\ control} \times 100 \qquad (3.5)$$

3.3. RESULTS AND DISCUSSION

3.3.1. Formation/Dissociation constant of the complex [Ru(p-cymene)Cl(SPR)]

The metal to ligand ratio and the stability constant of complex [Ru(*p*-cymene)Cl(SPR)] were determined using the continuous variation method, also known as Job's method. Experimental data of absorbance at room temperature are shown in Table 3.1 and the Job's curve in Figure 3.2 shows a maximum absorbance at a mole ratio X_{Ru} = 0.33, indicating the formation of a complex having 1:2 metal to ligand ratio. In Figure 1, the extrapolated value at the point of cross section on the Job's curve corresponds to the total absorbance of the complex, if the complex formation had been completed. Since the complex is dissociative in nature, the actual absorbance is somewhat lower than the absorbance measured at break point.

Table 3.1. Experimental data of ruthenium(II)-sulpiride complex by continuous variation method.

Sr. No.	Metal concentration (x10^{-4} M)	Ligand concentration (x10^{-4} M)	XRu (mole fraction of Ru)	Mean absorbance at 288 nm (Room T)
1	0	12	0	0,019
2	2	10	0,167	0,092
3	4	8	0,333	0,228
4	6	6	0,5	0,170
5	8	4	0,667	0,099
6	10	2	0,833	0,061
7	12	0	1	0,014

From the experimental data (Table 3.1) and the Job's curve (Figure 3.4), A1, A2, C(Ru) and C(SPR) were obtained and used in equations (1) and (2) to calculate the complex's formation and dissociation constants. The formation constant of the complex (log K = 5.45) is between 3 and 6, indicating that the Ru(II)-SPR complex is likely to dissociate in acidic environment, such as the stomach. In the physiological pH of 7.4, however, this complex is expected to be more stable (Furia, 2006).

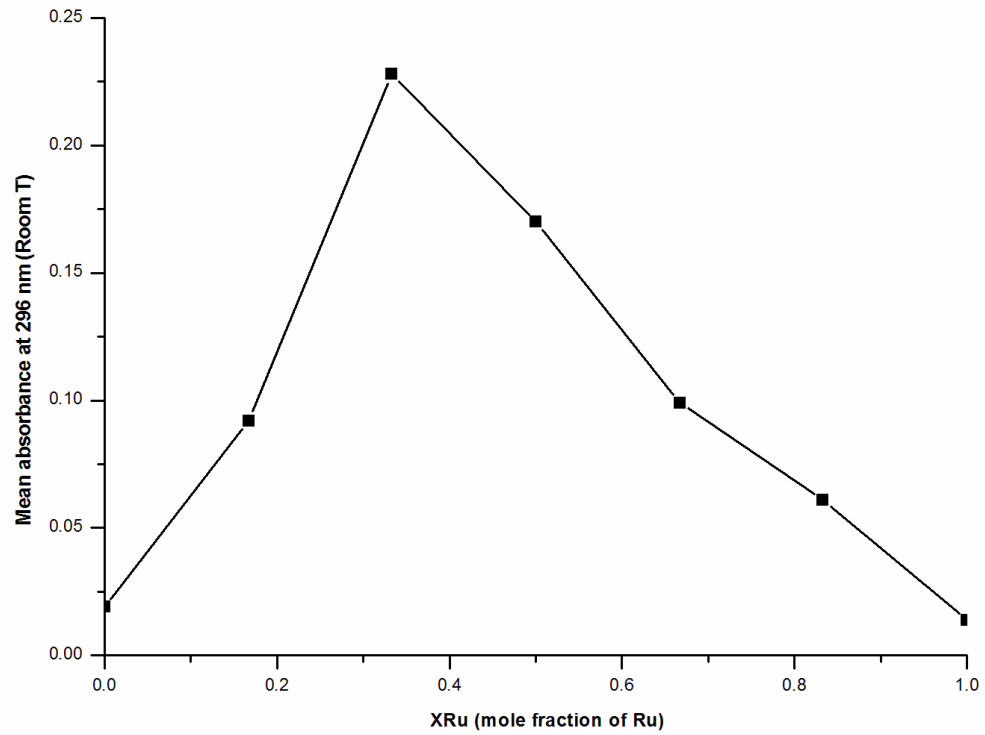


Figure 3.4. Job's curve for the formation constant of equimolar solutions of SPR and Ru (II).

3.3.2. Infrared (IR) spectra with assignments of L1-5, complexes 1-5 and complexes 1a-5a

The IR spectra of the free amino alcohols L1-5 were compared with the IR spectra of the precursor complexes **1**-**5** to identify the site of coordination involved in the chelation process**.** The IR spectra of complexes **1-5** were similar (Supplementary information, Appendix D). Figures 3.5b and 3.5c show the IR spectra of L1 and complex **1**. The observed absorption bands in the IR spectra of the amino alcohol ligands at wavenumbers in the range 3200-3600 cm^{-1} (Figure 3.5b) confirm the presence of primary OH- groups within their structure, as observed in the literature (Wang et al., 2003). The disappearance of the OH stretching band in the IR spectra of complexes **1-5** (Figure 3.5c, Appendix D) was indicative of Ru-O bond formation, as reported by Wang and co-workers (Wang et al., 2003). Upon complexation to the metal, some shifts in absorption bands of the ligands were observed. For instance, L1 has a structure with a monosubstituted aromatic ring which absorption's band shifted from 696 cm^{-1} in L1 to 872 cm^{-1} in complex **1**. There was also a shift in the NH bending bands from 1575 and 753 cm^{-1} in L1 to 1585 and 730 cm^{-1} in complex **1** (Figure 3.5b and Figure 3.5c). These shifts in the IR spectra of complexes **1-5** confirm that metal complexation occurred.

The IR spectrum of the free SPR was compared to the IR spectra of complexes **1a**-**5a** to assess coordination of SPR to the metal (Table 3.2). The IR spectra of SPR and complex **1a** are shown in Figures 3.5a and 3.5d, indicating a few differences between the two spectra.

The υ_{sym} (SO_2) and the υ_{asym} (SO_2) stretching vibrations observed at 1089 cm^{-1} and 1332 cm^{-1} respectively in the free SPR IR spectrum both shifted to higher wavenumbers in the spectrum of complex **1a** (1092 cm^{-1} for υ_{sym} (SO_2) and, 1335 cm^{-1} in for υ_{asym} (SO_2)), as displayed in Figure 3.5a, Figure 3.5d and Table 3.2. These bands are not involved in the complexation of SPR to the metal but their shift to higher wavenumbers in the metal complex may be assigned to the participation of the SO_2 group in the formation of hydrogen bond with the neighbouring atoms (Ibrahim et al., 2014; Wang et al., 2003). The υ(C=O) stretching vibration observed at 1639 cm^{-1} in the free SPR spectrum shifted to the lower wavenumber of 1634 cm^{-1} in the spectrum of complex **1a**. This confirms the involvement of the amide O in the complexation of SPR to the metal (Ibrahim et al., 2014; Wang et al., 2003). Both positive and negative shifts are also observed in the NH stretching vibrations of complex **1a** (3383 and 3164 cm^{-1} for SPR; 3325 and 3184 cm^{-1} for complex **1a**) while the NH stretching vibration at 3085 cm^{-1} in the free SPR spectrum shifted to a lower wavenumber of 3063 cm^{-1} in the spectrum of complex **1a**. The shifts in these bands may be assigned to either the keto-enol form or hydrogen bond formation (Mohamed and Soliman, 2010; Wang et al., 2003). The IR spectra of complexes **2a-5a** follow a similar trend to that observed for complex **1a**, as can be observed in Table 3.2 and Appendix D. The IR spectra demonstrate that SPR binds to Ru (II) through the amide O and behaves as a neutral monodentate ligand.

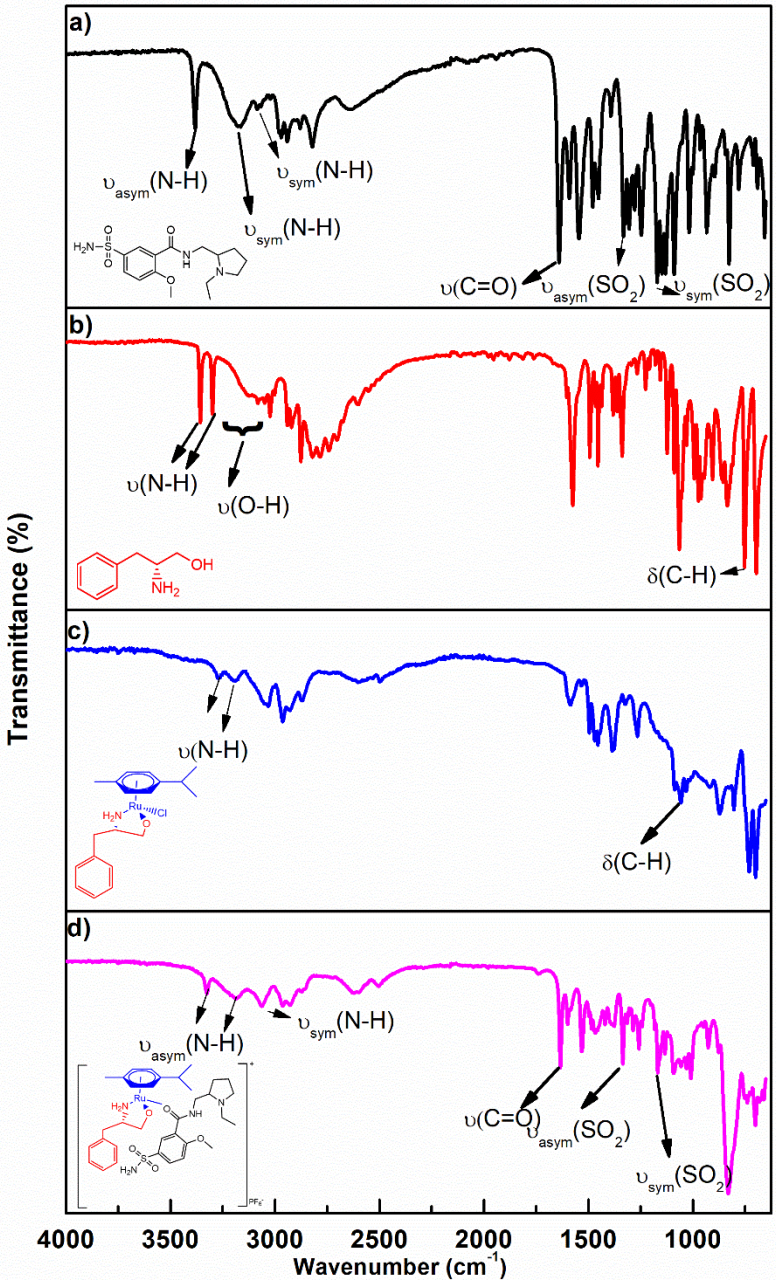


Figure 3.5. FTIR spectra of a) Sulpiride (SPR), b) (R)-(+)-2-amino-3-phenyl-1-propanol (L1), c) [Ru(p-cymene)((R)-(+)-2-amino-3-phenyl-1-propanol)] (Complex **1**) and d) [Ru(p-cymene)((R)-(+)-2-amino-3-phenyl-1-propanol)(sulpiride)]PF_6 (Complex **1a**).

Table 3.2. IR spectra (4000-650 cm^{-1}) of the SPR drug and its ternary metal complexes.

Compound	υ(C=O)	υ $_{asym}$(SO_2)	υ $_{sym}$(SO_2)	υ =(NH)	υ(NH)
Sulpiride	1639	1332	1089	3085	3383, 3164
Complex 1a	1634	1335	1092	3063	3325, 3184
Complex 2a	1634	1335	1094	3063	3324, 3189
Complex 3a	1634	1335	1094	3063	3325, 3185
Complex 4a	1634	1335	1094	3071	3324, 3223
Complex 5a	1634	1335	1095	3190	3383, 3328

3.3.3. NMR spectra with assignments of L1-5, complexes 1-5 and complexes 1a-5a

The ^{1}H and ^{13}C NMR spectra of L1-5 were compared to the spectra of complexes **1-5**. To be noted were the downfield shift in the NH_2 band in the complexes, relative to the free ligands. For example, ^{1}H NMR signal at δ 2.07 ppm was assigned to the protons attached to the nitrogen on L1 (Figure 3.6b) and this peak appeared relative downfield (δ 7.70 ppm) on the spectrum of complex **1** (Figure 3.7c). Additionally, two signals were assigned to the protons in $C^{A}H_2(OH)$ in L1 (δ 3.68 and 3.45 ppm; Figure 3.6b), which were replaced by a single signal, relative upfield in complex **1** for $C^{A}H_2O$ (δ 3.06 ppm; Figure 3.7c). A similar upfield shift was also observed for the proton attached to C^{B} in complex **1** (δ 2.88 ppm; Figure 3.7c), relative to L1 (δ 3.16 ppm; Figure 3.6b). These ^{1}H NMR signals shifts are indicative of metal coordination to the ligand, especially since both N and O participate in bond formation between the metal and the ligand. Similar shifts (either upfield or downfield) were observed in the ^{1}H NMR spectra of complexes **2-5**, as compared to L2-5 (Appendix D). The ^{13}C NMR spectrum of complex **1** (Figure 3.9c), likewise, displayed shielded C^{A} (δ 39.14 ppm) and deshielded C^{B} (δ 59.54 ppm), compared to the ^{13}C NMR spectrum of L1 (Figure 3.9b) where these peaks appeared at δ 40.96 and 54.31 ppm respectively. A similar trend was observed in the ^{13}C NMR spectra of complexes **2-5**, when compared to the ^{13}C NMR spectra of L2-5 (Appendix D). The appearance of new peaks in the ^{1}H and ^{13}C NMR spectra of complexes **1-5**, corresponding to the *p*-cymene molecule, was further proof that metal coordination took place (Figure 3.6, Figure 3.7, Figure 3.8, Figure 3.9 and Appendix D).

The comparative ^{1}H NMR spectra of SPR and complex **1a** are shown in Figure 3.6a and Figure 3.7d respectively. The presence of SPR in complex **1a** was confirmed by the appearance of new bands in its ^{1}H NMR spectrum, corresponding to SPR. Several chemical shifts were observed upon complexation of SPR to the metal centre. For example, the signal at δ 8.35 ppm was attributed to the nitrogen proton in the free SPR (Figure 3.6a) and this band appeared relatively downfield at δ 8.38 ppm in complex **1a** (Figure 3.7d), as well as complexes **2a-5a** (Appendix D). The comparative ^{13}C NMR spectra of SPR and complex **1a** are shown in Figure 3.9a and Figure 3.9d respectively. Compared to the ^{13}C NMR spectrum of complex **1** (Figure

3.9c), there are new signals in the ^{13}C NMR spectrum of complex **1a** (Figure 3.9d) that correspond to the signals of free SPR (Figure 3.9a). The NMR signal at $C^{15}=O$ was of particular importance since the amide O has been previously shown to participate in the coordination of SPR to metal (Mohamed and Soliman, 2010). This peak, appearing at δ 163.5 ppm in free SPR (Figure 3.9a, Table 3.3), was deshielded to δ 163.6 ppm for complexes **1a-3a** and to δ 163.7 ppm for complex **4a** (Figure 3.9d, Table 3.3), confirming the binding of SPR to Ru (II) through the amide O as a neutral monodentate ligand. The proposed structures of complex **1** and complex **1a** are shown along with the NMR spectra (Figure 3.6, Figure 3.7 and Figure 3.9). The chemical shifts were generally small, implying the minimal delocalisation of spin density from the metal into molecular orbitals of ligands (Mavuso et al., 2016).

The presence of the PF_6^- counterion for complex **1a** was confirmed by the characteristic septet in ^{31}P NMR spectrum (Figure 3.8e) centred at -144.1 ppm. This is due to all 6 equivalent fluorine coupling with phosphorous.

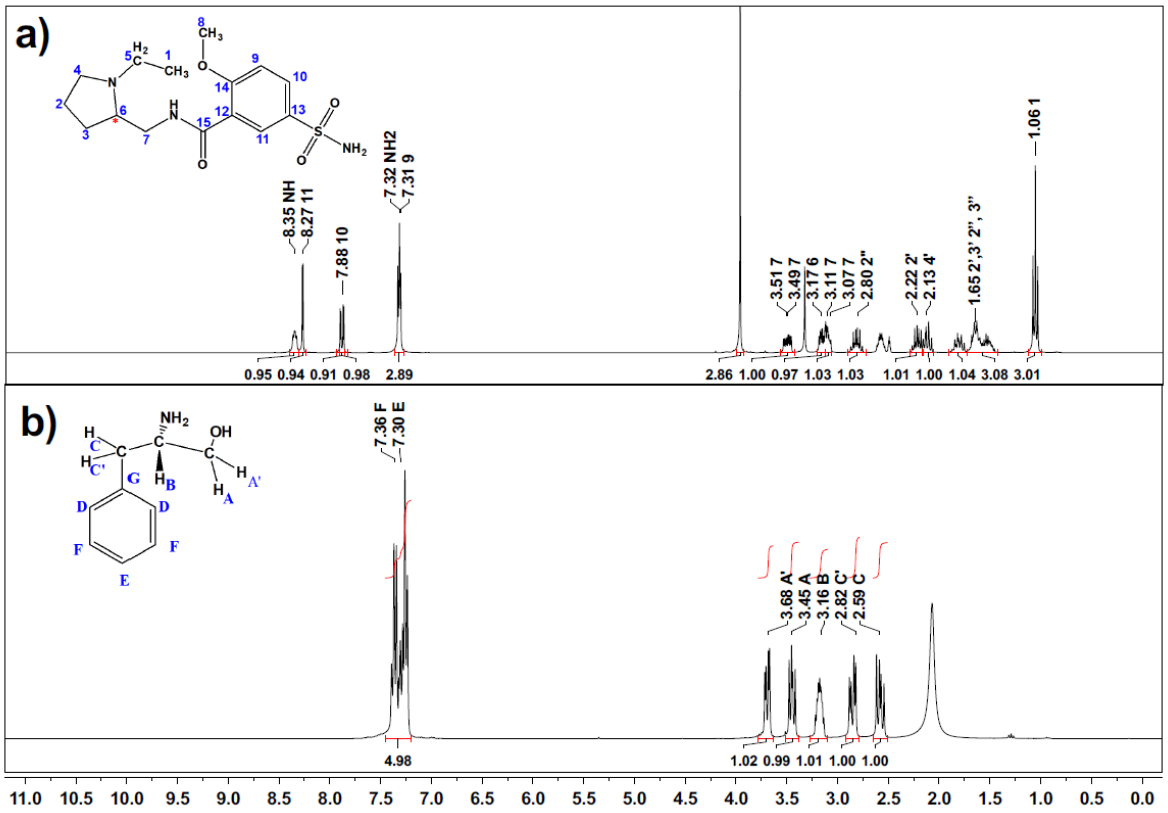


Figure 3.6. ^1H NMR spectra with assignments of a) Sulpiride (SPR) in dmso-d6 and b) (R)-(+)-2-amino-3-phenyl-1-propanol (L1) in $CDCl_3$-d.

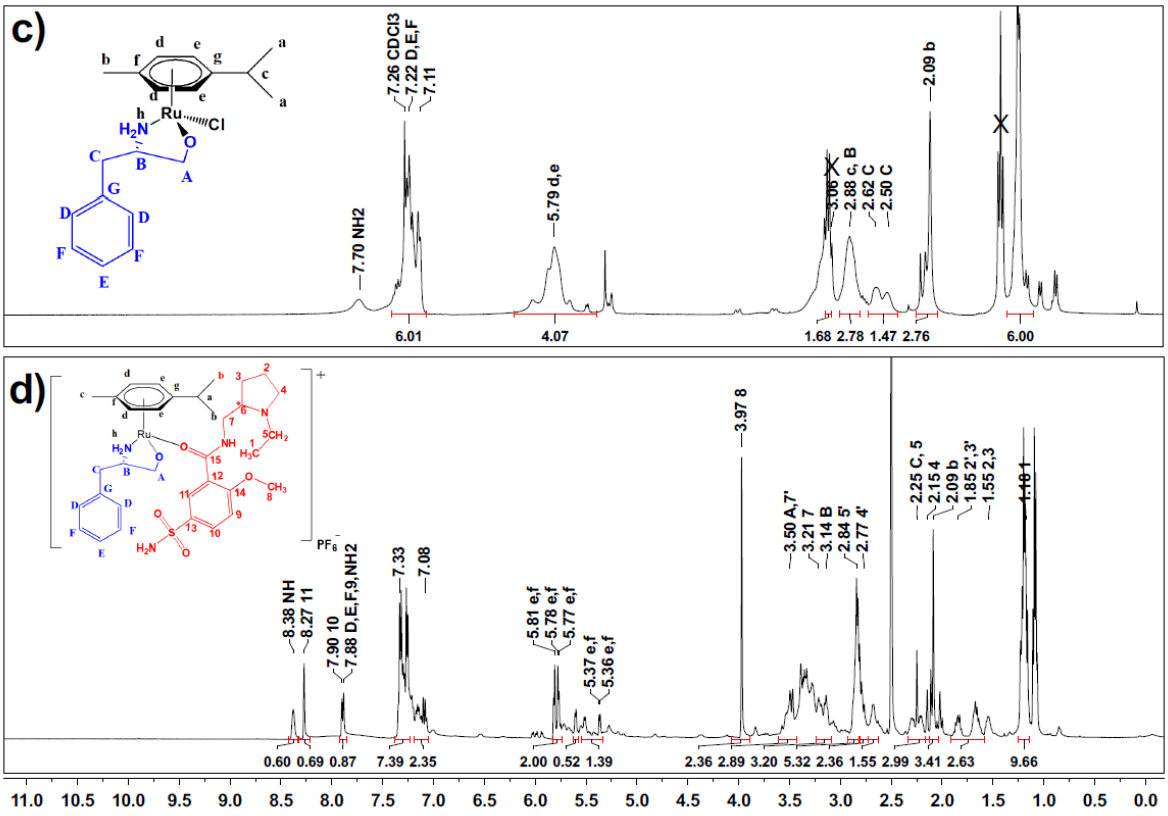


Figure 3.7. ^{1}H NMR spectra with assignments of c) [Ru(p-cymene)((R)-(+)-2-amino-3-phenyl-1-propanol)] (Complex **1**) in dmso-d6, d) [Ru(p-cymene)((R)-(+)-2-amino-3-phenyl-1-propanol)(sulpiride)]PF_6 (Complex **1a**) in dmso-d6.

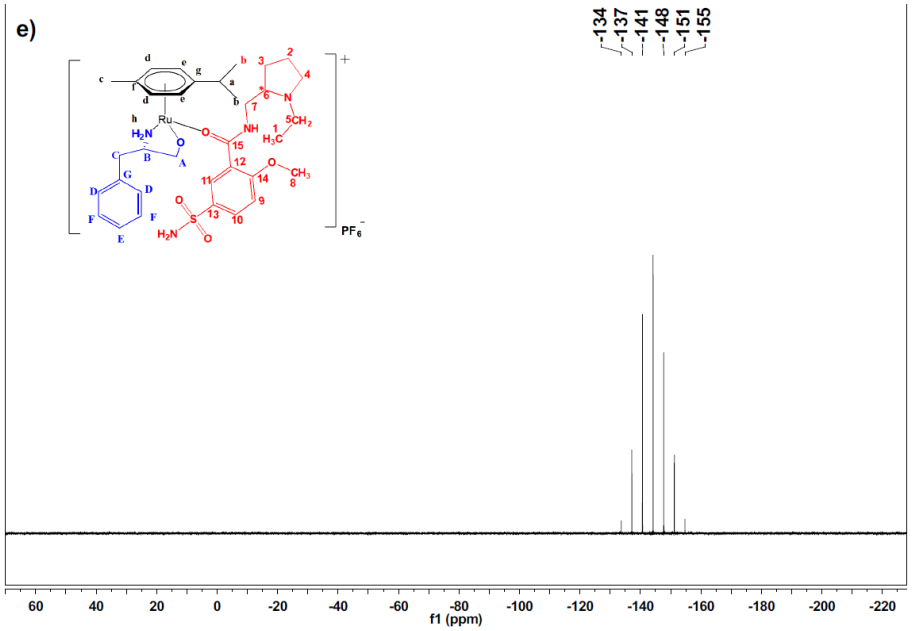
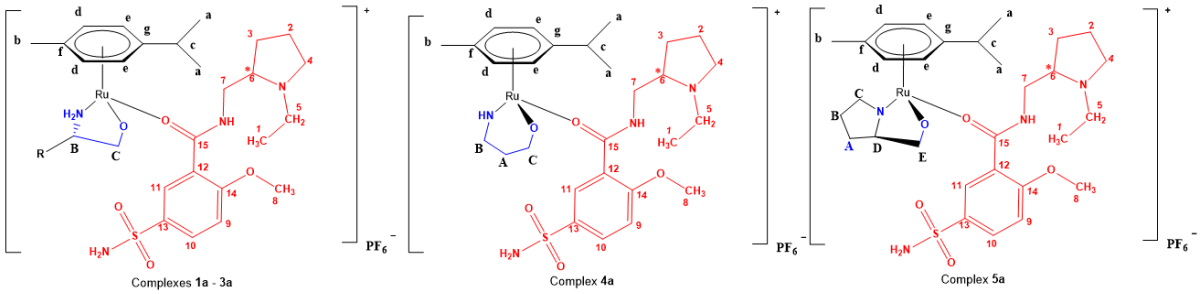


Figure 3.8. ^{31}P NMR spectrum with assignments for e) [Ru(p-cymene)((R)-(+)-2-amino-3-phenyl-1-propanol)(sulpiride)]PF_6 (Complex **1a**) in dmso-d6.

Table 3.3.Selected ^{1}H NMR (500 MHz, DMSO-d6) and ^{13}C NMR (126 MHz, DMSO-d6) chemical shifts (ppm) of sulpiride and complexes **1a-5a.**



	O-CH_3 ^{1}H NMR	^{13}C NMR	CH_2(NH) ^{1}H NMR	^{13}C NMR	C=O ^{13}C NMR
Sulpiride	3.97 (s)	56.56	3.21 (m)	41.67	163.51
Complex 1a	3.97 (s)	56.58	3.21 (s)	41.56	163.6
Complex 2a	3.98 (m)	56.57	3,58 (s)	41.23	163.6
Complex 3a	3.97 (s)	56.57	3.51 (s)	41.54	163.6
Complex 4a	3.99 (s)	56.54	3.47 (m)	41.35	163.7
Complex 5a	3.98 (m)	56.58	3.29 (m)	41.10	164.1

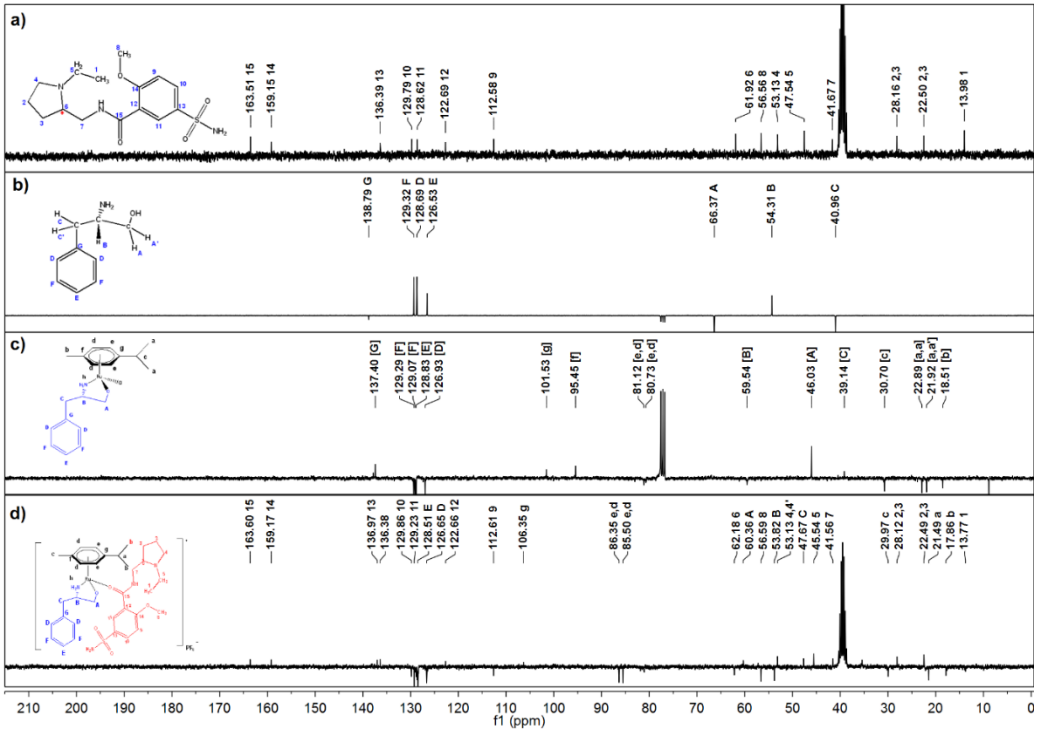


Figure 3.9.^{13}C NMR spectra with assignments of a) Sulpiride (SPR) in dmso-d6, b) (R)-(+)-2-amino-3-phenyl-1-propanol (L1) in $CDCl_3$-d, c) [Ru(p-cymene)((R)-(+)-2-amino-3-phenyl-1-propanol)] (Complex **1**) in dmso-d6 and d) [Ru(p-cymene)((R)-(+)-2-amino-3-phenyl-1-propanol)(sulpiride)]PF_6 (Complex **1a**) in dmso-d6.

3.3.4. Thermal analyses (TG, DTG and DSC) studies of L1-5, complexes 1-5 and complexes 1a-5a

The TGA/DTG and DSC analyses of free SPR, the precursor complexes **1-5** and the final metal complexes **1a-5a** were carried out with heating rates of 10°C.min^{-1} under nitrogen atmosphere and the weight loss was measured from ambient temperature to 400°C and 900°C for DSC and TGA/DTG respectively.

The thermal analyses of SPR and its ternary Ru(II) metal complexes are summarised in Table 3.4. Figure 3.10 and Figure 3.11 display the TG curves of SPR, complex **1** and complex **1a** and the DSC curves for the same compounds respectively.

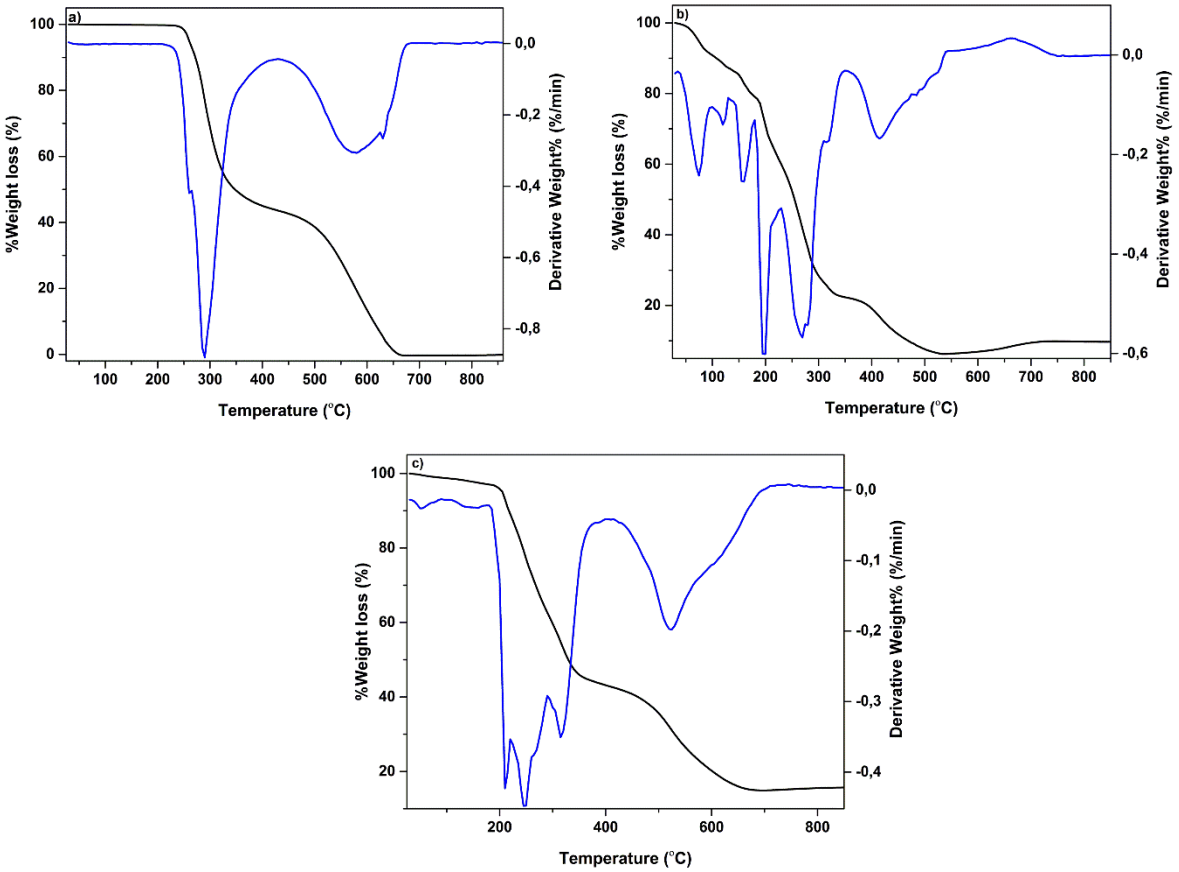


Figure 3.10. TGA thermograms of a) Sulpiride (SPR), b) [Ru(*p*-cymene)((R)-(+)-2-amino-3-phenyl-1-propanol)] (Complex **1**) and c) [Ru(*p*-cymene)((R)-(+)-2-amino-3-phenyl-1-propanol)(sulpiride)]PF_6 (Complex **1a**).

The TG curve of SPR shows a total weight loss of 99.94% (99.87%) which is observed in two successive decomposition steps (Figure 3.10a). The first weight loss of 57.01% (59.16%) in the range of 249 to 443 °C may be assigned to the decomposition of the molecule $C_7H_8NO_4S$. The second weight loss of 42.93 (40.71%), within the temperature range of 443 to 900 °C, is

attributable to the decomposition of $C_8H_{15}N_2$. The decomposition weight losses were found in agreement with the starting formula weight.

The TG curve of complex **1** (Figure 3.10b) displays two decomposition steps, corresponding to the loss of L1 in the TG range 30-250°C (approximately 60% of complex **1**), followed by the loss of the *p*-cymene molecule in the TG range 250-900°C (approximately 30% of complex **1**). The decomposition of complex **1** ended with Ru oxide (RuO) as a metallic residue.

The TG curves of the Ru (II) metal complexes of SPR are similar and show three decomposition steps in the temperature range 30 to 900°C (Table 3.4). All complexes started decomposition with the loss of SPR and end with RuO as a metallic residue (Table 3.4). The first decomposition step happened in the range of 30 to 343°C, during which 54.047% (53.16%) of complex **1a** was lost. In this step, SPR was lost from complex **1a** (Figure 3.10c, Table 3.4). The second two decomposition steps were within the temperature range 343 to 900°C, 30.18% (31.55%) of complex **1a** was lost. These steps correspond to the loss of L1, as well as the benzene ring from the Ru(*p*-cymene) molecule (Figure 3.10c, Table 3.4). As depicted in Table 3.4 and Appendix D, complexes **2a-5a** had a similar TG decomposition profile to complex **1a** in the temperature range 30 to 900°C.

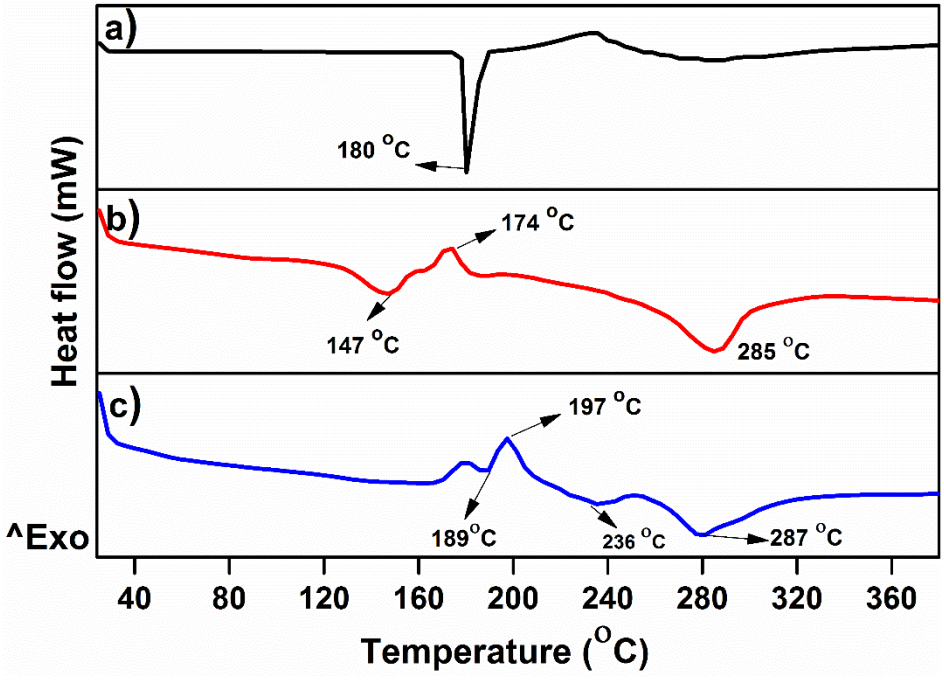


Figure 3.11. DSC curves of a) Sulpiride (SPR), b) [Ru(*p*-cymene)((R)-(+)-2-amino-3-phenyl-1-propanol)] (Complex **1**) and c) [Ru(*p*-cymene)((R)-(+)-2-amino-3-phenyl-1-propanol)(sulpiride)]PF_6 (Complex **1a**).

The DSC curve of SPR (Figure 3.11a, Table 3.4) shows a sharp endothermic peak at 180.1°C, which is its melting temperature (Ibrahim et al., 2014). A small and wide endothermic peak is

observed at 287.1°C (Figure 3.11a, Table 3.4), which can be associated with some decompositions, reductions or phase transitions (Kavitha and Anantha Lakshmi, 2017).

The DSC curve of complex **1** shows two wide endothermic peaks at 147.2 °C and 285 °C, corresponding to the dehydration and the melting of the complex, respectively (Figure 3.11b).

The DSC curve of complex **1a** shows three endothermic peaks (Figure 3.11c, Table 3.4). The first one, observed at 73.68°C, is small and wide and shows the dehydration of the molecule. The second wide endothermic peak at 236.1°C corresponds to the melting temperature of complex **1a** (Figure 3.11c, Table 3.4). Complex **1a** underwent further decomposition resulting in the final DSC peak at 281.7°C (Figure 3.11c, Table 3.4). The DSC curves of complexes **2a-5a** are shown in Appendix D.

Table 3.4. Thermal analyses (TG and DSC) of SPR and its series of ruthenium (II) metal complexes.

Compound	TG range (°C)	N*	% Found (calcd) Weight loss	Total weight loss	Assignment	Metallic residue found (calcd %)	DSC endothermic peaks(°C)
SPR	249-443 443-900	1 1	57.01 (59.16) 42.93 (40.71)	99.94 (99.87)	Loss of $C_7H_8NO_4S$ Loss of $C_8H_{15}N_2$		180.1 (-), 287.1 (-)
Complex 1a	30-343 343-900	1 2	54.047(53.16) 30.18 (31.55)	84.22 (84.71)	Loss of SPR Loss of $C_8H_{12}NO$ + C_6H_6	RuO 15.78 (13.99)	73.68 (-), 236.1 (-), 281.7 (-)
Complex 2a	30-357 357-900	1 2	55.6 (58.42) 26.03 (24.26)	81.65 (82.68)	Loss of SPR Loss ofC_2H_7NO + C_6H_6	Ru 18.85 (16.00)	108.8 (-), 220.7 (-), 313.1 (-)
Complex 3a	30-341 341-900	1 2	56.7 (57.08) 25.52 (25.85)	82.22 (82.93)	Loss of SPR Loss of C_3H_9NO + C_6H_6	RuO 17.78 (15.63)	137.3 (-), 223.2 (-), 286.1 (-)
Complex 4a	30-356 356-900	1 2	57.54 (57.08) 25.32 (25.85)	82.86 (82.93)	Loss of SPR Loss of $C_3H_9NO + C_6H_6$	Ru 17.78 (15.63)	144.7 (-) 306.2 (-), 316.9 (-)
Complex 5a	30-348 348-900	1 2	54.33 (54.88) 30.24 (28.71)	84.57 (83.59)	Loss of SPR Loss of $C_5H_{11}NO$ + C_6H_6	RuO 15.40 (15.03)	136.2 (-), 253.1 (-), 272.6 (-)

3.3.5. Ultraviolet-Visible (UV-Vis) spectra of SPR, complexes 1-5 and complexes 1a-5a

The UV-Vis spectra of SPR, complexes **1-5** and complexes **1a-5a** were recorded in the region 200-600 nm. Figure 3.12 shows the UV-Vis spectra of SPR, Ru(*p*-cymene)Cl_2, complex **1** and complex **1a**. The spectrum of the SPR (20 mg/L in methanol) exhibited absorption maxima at 213 and 288 nm; this is in accordance with UV-Vis studies of levosulpiride previously conducted by Siddiqi et al, as well as Manjunath et al (Manjunath et al., 2011; Siddiqi et al.,

2009). For complex **1a** these bands shifted to 212 nm and 286 nm corresponding to a ligand-to-metal charge-transfer (LMCT) complex. There was also a presence of additional bands in the range of 300-350, which was most likely due to the exchange of the chlorido ligands from ruthenium arene complexes by water molecules, as previously reported by Rilak and co-workers (Rilak et al., 2014). This would involve spectral changes in the range of 300-350 nm. Based on these spectral differences it was possible to distinguish between the parent drug and the ruthenium complex **1a**. The spectra of complexes **1**-**5** and that of SPR all show bands in the range 210 to 220 nm. The quantification of SPR was therefore carried out using the absorbance value 288 nm, which was specific to the SPR UV-vis spectrum.

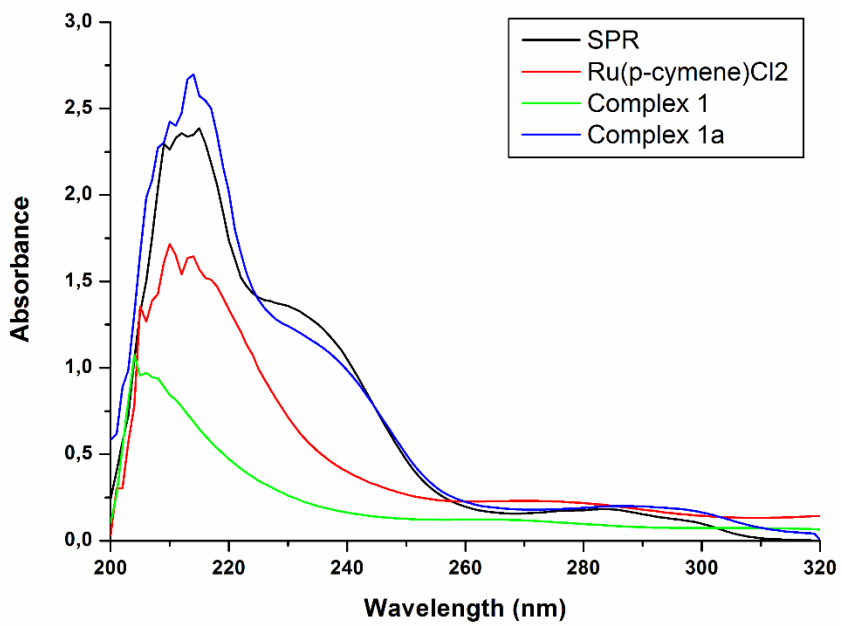


Figure 3.12. UV-Vis spectra of sulpiride (SPR), dichloro(p-cymene)ruthenium(II) dimer (Ru(p-cymene)Cl_2), [Ru(p-cymene)((R)-(+)-2-amino-3-phenyl-1-propanol)] (Complex **1**) and [Ru(p-cymene)((R)-(+)-2-amino-3-phenyl-1-propanol)(sulpiride)]PF_6 (Complex **1a**).

3.3.6. Fluorescence study

The emission characteristics of complex **1a** were examined in a methanol solution of concentration 3 x10^{-6} mol/L at room temperature. The excitations were executed at wavelengths (λex) 350 nm and 450 nm (λex/nm). The fluorescence spectrum of complex **1a** is shown in Figure 3.13, the emission (10 a.u.) was observed at 708 nm. This is a relatively low emission, as compared to reported ruthenium complexes. In fact, a recent study reported a novel ruthenium-based anticancer scaffold with remarkable fluorescence (400 a.u.), which was measured at a concentration of 4 x 10^{-7} mol/L in methanol (Subran et al., 2016). Complex **1a** is not showing significant luminescent behaviour.

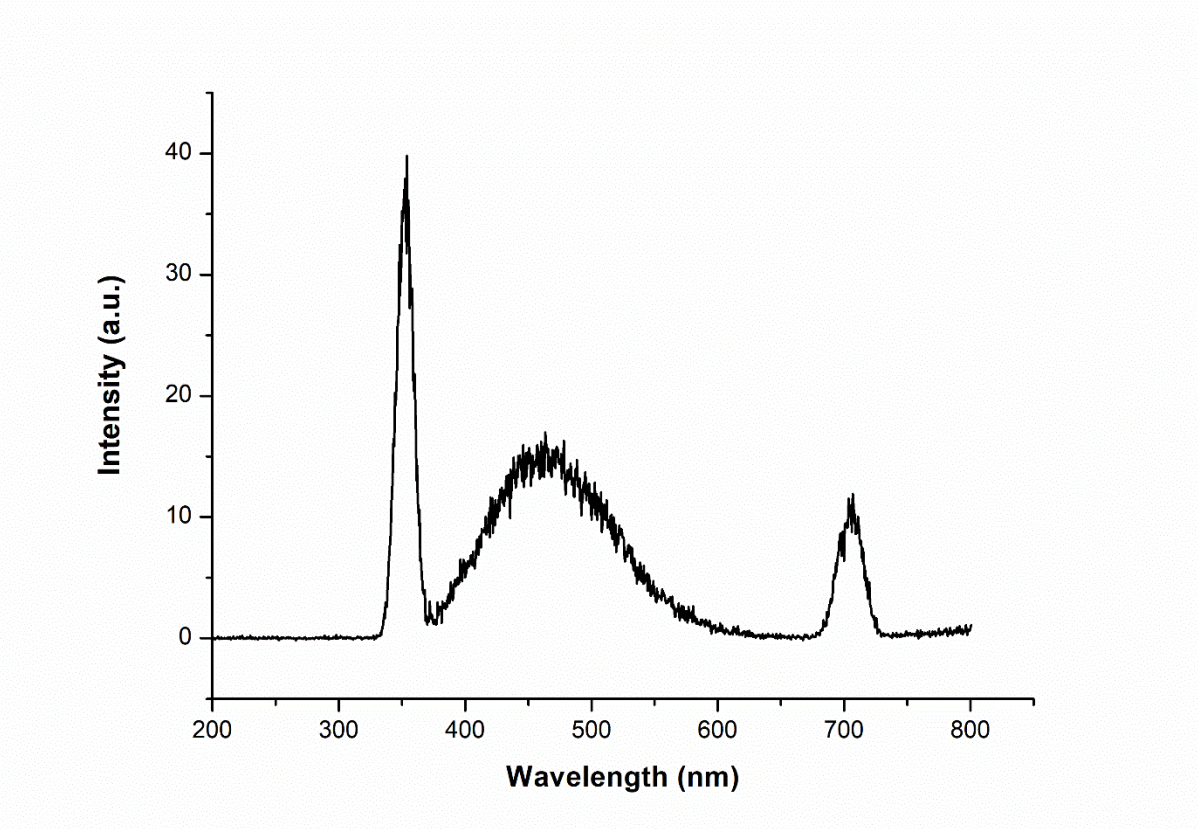


Figure 3.13. Fluorescence spectrum of complex **1a** in methanol.

Complex **1a** displayed weak MLCT due to the interaction of π* (benzene ring, electron rich group) of sulpiride and d electrons of ruthenium. Fluorescence studies revealed emissions originating from the lowest energy MLCT state, attributed to the excitation involving dπ-πligand*. Such emission properties of ruthenium (II) metal complexes were previously recorded (Małecki, 2012).

3.3.7. Solubility studies of free SPR and SPR in complexes 1a, 3a and 5a

The results of the solubility studies of free SPR and SPR in metal complexes are shown in Table 3.5. SPR in metal complexes showed improved solubility in all solvents tested compared to free SPR. The solubility of SPR in water was more than twice higher (695 mg/mL vs 1659, 1518 and 1549 mg/L for complexes **1a**, **3a** and **5a** respectively) following coordination of the drug to the metal. A similar but slightly lower trend is observed in PBS pH 6.8 and in PBS pH 7.4, while solubility improvement of SPR in methanol is also more than doubled with metal complexation.

Table 3.5. Solubility values of free SPR and SPR in Ru(II) metal complexes in different solvents (mg/L).

	Water (%RSD)	PBS pH 6.8 (%RSD)	PBS pH 7.4 (%RSD)	Methanol (%RSD)*
SPR	697 mg/L (1.18)	892 mg/L (2.99)	853 mg/L (1.83)	910 mg/L (2.80)
SPR in complex 1a	1668 mg/L (1.38)	1339 mg/L (1.64)	1287 mg/L (1.38)	1954 mg/L (3.35)
SPR in complex 3a	1529 mg/L (1.55)	1575 mg/L (2.79)	1494 mg/L (2.01)	2156 mg/L (2.29)
SPR in complex 5a	1551 mg/L (1.56)	1757 mg/L (1.18)	1621 mg/L (1.04)	2208 mg/L (2.28)

**Number of replicates for each solvent: 20*

Complexes **1a** ([Ru(p-cymene)($C_9H_{13}NO$)(SPR)]PF_6), **3a** ([Ru(p-cymene)(C_3H_9NO)(SPR)]PF_6)and **5a** ([Ru(p-cymene)($C_5H_{11}NO$)(SPR)]PF_6) each contain an ancillary ligand (L1/3/5) and the drug (SPR) attached to the metal centre. The aqueous (water, PBS buffer) solubility improvement of complexed SPR compared to free SPR may be achieved from the presence of the water soluble amino alcohols L1, L3 and L5 as ancillary ligands of SPR in complexes **1a**, **3a** and **5a** respectively. These ancillary ligands influence the environment surrounding SPR, thereby positively affecting its water solubility. Such phenomenon has been previously observed in Ru(II) metal complexes (Morais et al., 2014). The variation in complexed SPR solubility can be attributed to the differences in structure and solubility between L1, L3 and L5, which have an effect on their interactions with neighbouring molecules. Previous studies in this area have in fact shown the importance of the choice of ancillary ligand to achieve desired water solubility improvement of a drug through metal complexation (Rilak et al., 2014). Water and methanol are both polar molecules but methanol, with a polarity index value of 5.1, is somewhat less polar and therefore more lipophilic than water (polarity index 10.2) (Lough and Wainer, 1995; Murov, 2010; "Solvent Polarity Index - Chempendix," n.d.). This difference in polarity explains the higher solubility of SPR in methanol, as compared to water. The dichloro(p-cymene)ruthenium(II) dimer present in complexes **1a**, **3a** and **5a** is known to be lipophilic and has been previously shown to improve the lipophilicity of the compounds complexed to its centre (Lv et al., 2015; Pastuszko et al., 2016; Rilak et al., 2014). A similar phenomenon is observed in this study, with the highest solubility values of SPR obtained by dissolution of the metal complexes in the more lipophilic compound, methanol.

Ruthenium metal carrier therefore demonstrated the ability to improve the pharmaceutical profiles of drugs by improving both their aqueous and lipid solubility, which is advantageous for pharmaceutical formulation (Uivarosi, 2013).

3.3.8. Dissolution studies of free SPR and SPR in complexes 1a, 3a and 5a

The dissolution profiles of Eglonyl®, SPR in complex **3a** and SPR in complex **5a** are similar to each other. In PBS pH 1.5, 6.8 and 7.4, there is a burst release of the drug within 30 minutes of the dissolution test. Approximately 90, 80 and 70% of the drug is released at pH 1.5, 6.8 and 7.4 respectively for Eglonyl® and complexes **3a** and **5a**. The total amount of the drug is fully released by 2 hours for all three compounds. Complex **1a** has a slower dissolution rate compared to Eglonyl® and the other two complexes. Figure 3.14 shows the dissolution profiles of Eglonyl® and SPR in complex **1a**. A burst release of SPR is observed 30 minutes after the start of the dissolution test of complex **1a** but it is lower than that observed for Eglonyl® and SPR in complexes **3a** and **5a** in PBS; 32% and 46% SPR are released from complex **1a** in PBS pH 6.8 and 7.4 respectively within 30 minutes of the dissolution test. At all pH values, total release of the drug from complex **1a** is observed by 24 hours.

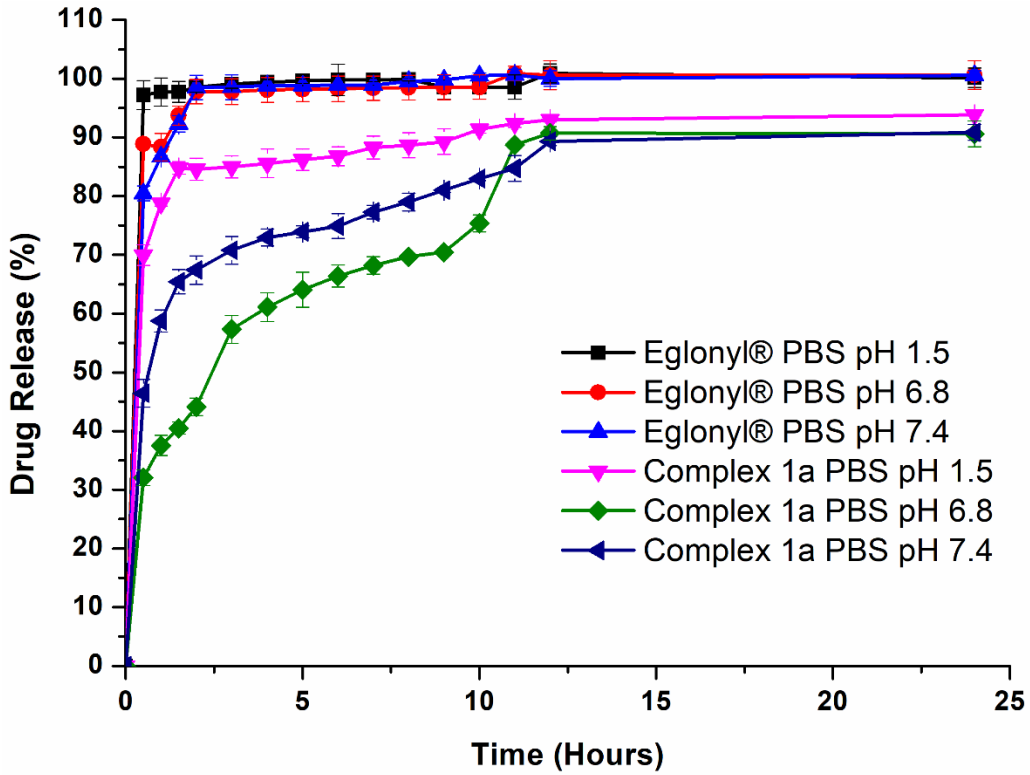


Figure 3.14. Dissolution profiles of sulpiride (SPR) and [Ru(p-cymene)((R)-(+)-2-amino-3-phenyl-1-propanol) (sulpiride)]PF_6 (Complex **1a**) in PBS buffer at different pH values.

Solubility and dissolution rate are directly proportional, increased solubility should therefore result in improved dissolution rate (Kumar et al., 2011; Kumar and Singh, 2013). However, this is not observed. Although the solubility of complexed SPR in the dissolution media is improved, the dissolution rate of SPR from the metal complexes is slower than that of free SPR. The slowest dissolution rates were observed in SPR from complex **1a**.

The formation constant of [Ru(*p*-cymene)Cl(SPR)] was determined previously in this paper and the value of 5.45 was obtained, indicating the likelihood of the Ru(II)-SPR complex to dissociate in acidic environment (Furia, 2006; Siddiqi et al., 2009). The breakage of the metal-ligand bond is therefore easier in acidic media, explaining the fast dissolution of complexed SPR in PBS pH values 1.5 and pH 6.8. In the physiological pH of 7.4, on the other hand, the [Ru(*p*-cymene)Cl(SPR)] complex is expected to be more stable, thereby limiting the release of SPR. This behaviour was, however, only observed in SPR in complex **1a**. This can be attributed to the presence of ancillary ligands with different chemical structures and properties in the complexes, which may have an influence on the stability of the [Ru(*p* -cymene)Cl(SPR)] complex (Morais et al., 2014). This would imply the ability of L1 as an ancillary ligand to SPR in complex **1a** to maintain or improve the stability of [Ru(*p*-cymene)Cl(SPR)], thus the slower dissolution of SPR from this complex, in comparison to free SPR and the other two complexes.

It has been shown that transition metal complexes are good candidates for controlled drug release because they possess bonds that are highly responsive to their environment (Renfrew, 2014). In the particular case of ruthenium complexes, their various oxidation states, different mechanisms of action and kinetics give them several advantages, including low toxicity (Griffith et al., 2008; Zhang et al., 2010). Few metal-based drugs reach their biological targets without any chemical modification, thus the importance of ligand exchange in biological activity. The mechanism of ligand exchange varies depending on both the metal and the coordinated ligand(s). The ligand exchange processes of ruthenium compounds are known to take place at slow rates in various cell lines, within the range of one to two hours, which are close to those of cellular processes (Motswainyana and Ajibade, 2015; Reedijk, 2008). This indicates that ruthenium complexes, when administered parenterally are not dissociated prior to any of their biological targets being reached. As a result, under physiological conditions (pH 7.4), metal interaction with nucleic acids, proteins and water could occur in the cells and such interactions are crucial for inducing the therapeutic effect of a drug (Motswainyana and Ajibade, 2015; Reedijk, 2008). The above-described properties of ruthenium complexes could be a further explanation for the selective release of SPR from the metal complex, leading to slower dissolution of SPR from complex **1a**. This is an advantage for SPR, as it reduces its initial burst release, which is one of the causes for its short half-life and its frequent dosing

schedule (Huang et al., 2001; Wockhardt, 2010). However, if oral delivery of SPR is to be maintained, drug formulation strategies will need to be applied to protect the metal complex containing SPR from dissociation in the acidic environment. This shows the potential of ruthenium metal complexation to the appropriate ligands to achieve sustained release of a drug.

3.3.9. Permeation studies of free SPR and SPR in complexes 1a, 3a and 5a

The values of the ionic conductivity of the porcine intestinal tissue at t_0 and t_8 were similar (18 and 17 mV respectively) and their FTIR spectra at these time points showed similar bands, both implying tissue structural integrity at t_8. At t_{12} and t_{24}, on the other hand, the ionic conductivities dropped to -8 and -22 mV but the FTIR spectra remained unchanged, implying that some of the integrity of the porcine intestinal tissue was compromised at these time points.

The cumulative permeability and cumulative relative permeability of free SPR and SPR from the Ru (II) metal complexes through the pig's small intestine were therefore determined up to 8 hours and are shown in Table 3.6.

Table 3.6. Cumulative permeability and cumulative relative permeability of free SPR, SPR released from metal complexes **1a**, **3a** and **5a**

Compound	Cumulative Permeability (μg/cm^2)	Cumulative Relative Permeability (%)
Sulpiride	88.42	14.17
Complex 1a	199.12	27.20
Complex 3a	185.64	27.09
Complex 5a	165.95	24.24

Higher amounts of SPR were permeated through the membrane from the metal complexes than the free drug. All metal complexes improved the permeation of SPR across the pig's intestinal membrane by more than 10%. Complexation to Ru (II) therefore resulted in increased permeation of the drug across the pig's intestine. This suggests that the lipophilicity of the drug is improved, thereby enhancing its diffusion through the membrane. Lipophilicity improvement through coordination to a ruthenium (II) arene molecule has been previously demonstrated and attributed to the presence of methyl groups in the ruthenium arene moiety, as is the case for dichloro(*p*-cymene)ruthenium(II) dimer (Pastuszko et al., 2016). The lipid soluble chemical groups on the metal positively affect the lipophilicity of SPR upon complexation. Coordination to the ruthenium metal could be used to enhance the lipid solubility and thus the intestinal membrane permeation of drugs.

3.3.10. Effects of free SPR and SPR in complexes 1a, 3a and 5a on Caco-2 cell viability

Figure 3.15 depicts the percentage cell viability after cell treatment with different concentrations of free SPR, SPR in complex 1a, SPR in complex 3a and SPR in complex 5a for 24 hours. No significant differences were observed in percentage cell viability of the complexed SPR, compared to the free SPR. Previously conducted intestinal absorption studies of SPR using the Caco-2 cell line to make *in vitro* model of the human intestine have also demonstrated minimal effect of SPR on Caco-2 cells (Watanabe et al., 2002b, 2002a). Ruthenium (II) metal complexes, on the other hand, have been associated with anticancer activity against a variety of human cell lines, including Caco-2. Recent studies have in fact reported moderate to high (higher than cisplatin) *in vitro* toxicity of ruthenium arene complexes against Caco-2 cell line (Gichumbi et al., 2016; Mondal et al., 2018). In these ruthenium complexes exhibiting anticancer properties, the metal in the molecule is active and therefore the tested concentrations are metal-dependent. This is not the case in the current study, where SPR is the active ligand and ruthenium is used as a drug carrier, thus the tested concentrations are SPR-dependent and contain less metal than metal-based concentrations. This lower ruthenium (II) concentration in ternary metal complexes of sulpiride could explain the lack of toxicity of the metal on the Caco-2 cells. It was noticed that the percentage cell viability slightly decreased with increased concentration of the tested compounds, which was expected, especially in the presence of ruthenium (Gouveia et al., 2018). Free and complexed SPR thus demonstrated no noticeable toxic effects on the intestinal epithelium tissue.

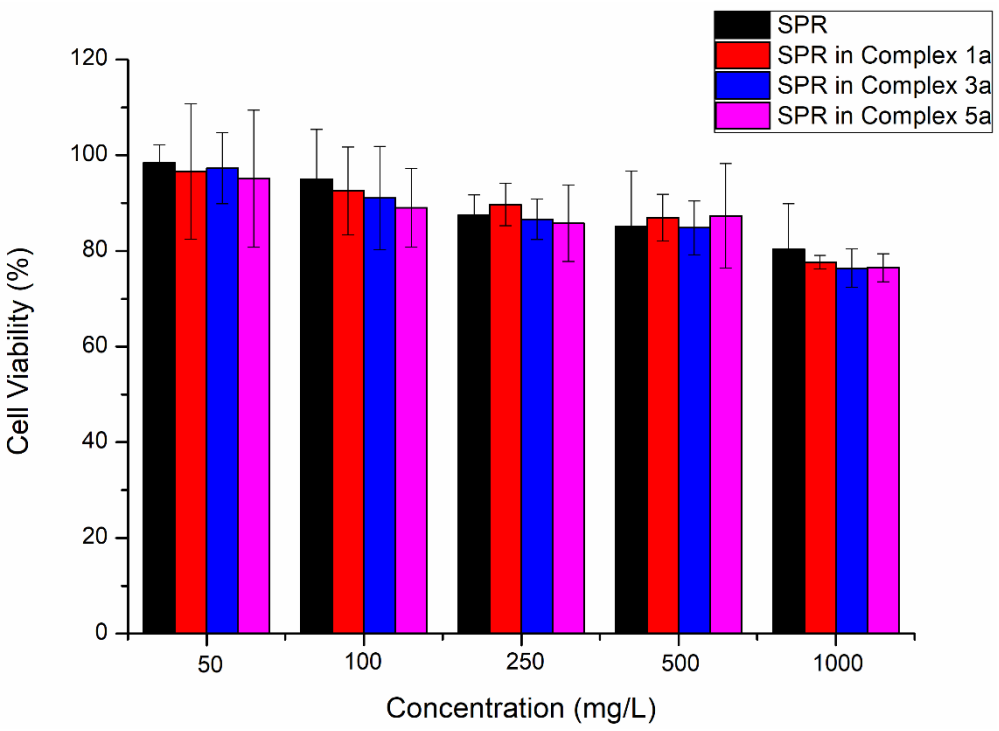


Figure 3.15. Percentage Caco-2 cell viability following treatment with SPR, complexes **1a**, **3a** and **5a.**

3.4. CONCLUDING REMARKS

It is the first time that five ruthenium(II)-liganded sulpiride and amino alcohol complexes have been successfully synthesized in a 1:1:1 ratio (metal:drug:amino alcohol) and characterized. Subsequent *in vitro* studies showed improved aqueous solubility of sulpiride when liganded to the metal, slower dissolution rate of the drug from the metal complexes, enhanced permeation of the metal-liganded drug through the pig's intestine and low cytotoxicity of the metal complexes. These results demonstrate the potential of ruthenium-based metal carrier as a non-toxic drug carrier for aqueous solubility, sustained release and permeation enhancement. Formulation studies should be undertaken to improve the drug's sustained delivery profile using ruthenium metal-based carrier and to avoid the metal-drug bond breakage in acidic environment that causes premature drug release, if oral drug delivery is to be maintained.

CHAPTER 4
DEVELOPMENT AND *IN VITRO* EVALUATION OF NOVEL METAL COMPLEX POLYMER NANOCOMPOSITE (MCPN) OF SULPIRIDE DRUG

4.1. INTRODUCTION

Metal-liganded complexes incorporated into sustained drug delivery systems via pharmaceutical strategies have been shown to be the future direction for the application of metal coordinated pharmaceuticals.

Price and co-workers reported a coordination polymer made of a polymer matrix comprising a compound containing bismuth and levodopa liganded to the bismuth. Bismuth was chosen due to its pharmaceutical acceptability as a metal, which is associated with minimal toxicity. The bismuth based polymeric oral drug delivery system enhanced gastric bioadhesion and enabled sustained dopaminergic delivery of levodopa via pharmacokinetic manipulation. The proposed delivery was reported to occur by the metal-liganded drug having good aqueous solubility that promoted motility in the intestinal lumen and improved lipid solubility. This, in turn, allowed the metal-liganded drug to penetrate into the intestinal membrane, and the release of the parent drug from the metal followed (Price et al., 2014, 2012).

Another study reported the preparation of Fe-liganded doxorubicin formulated into transferrin-inspired nanoparticles for pH-responsive drug release in the acidic tumour site. This was proven by the high release of doxorubicin in simulated conditions of the tumour microenvironment (73.6% and 59.3% at pH 4.5 and 5.5, respectively) compared to 33.5% and 25.6% doxorubicin release in the simulated extracellular tumour microenvironment at pH 6.5 and 7.4, respectively. The pH-triggered doxorubicin release was also verified *in vivo* following intravenous administration of the prepared nanoparticles to a mouse model. The presence of the ferric ion in this drug delivery system enabled higher loading of the drug into the nanoparticles, increased stability of the nanoparticles and self-assembly for the formation of the nanoparticles through coordinative bonds (He et al., 2017)

These studies highlight the versatility in the use of metal-liganded bioactives, which can be incorporated into varied drug delivery systems, such as polymer matrices and nanoparticles, to further improve the action of the metal ions on the bioactive ligand. A metal complex of sulpiride, [Ru(*p* -cymene)((R)-(+)-2-amino-3-phenyl-1-propanol)(SPR)]PF_6 was previously synthesized as described in Chapter 3, Section 3.2.4. (Figure 4.1) to investigate ruthenium metal as a possible inert drug carrier with the ability to enhance the intestinal permeability and

to retard the release of sulpiride drug. *In vitro* studies showed slower dissolution rate of the drug from the metal complex and enhanced permeation of the liganded bioactive through the pig's intestine. Although the release of sulpiride was slower when liganded to ruthenium, a high burst release was still observed in acidic pH, which revealed the necessity of formulation studies to solve this problem.

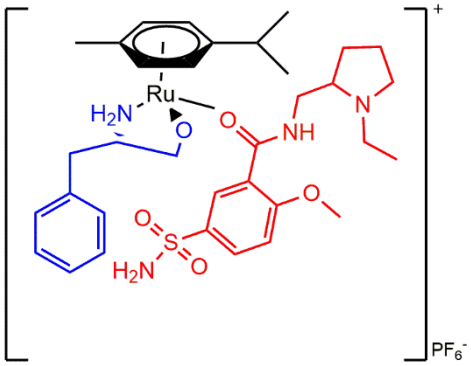


Figure 4.1. Structure of [Ru(p-cymene)((R)-(+)-2-amino-3-phenyl-1-propanol) (sulpiride)]PF_6 (Complex **1a**).

This chapter focuses on the encapsulation of the sulpiride metal complex (Complex **1a**) into polymeric (Eudragit® RS 100 and PVA) nanoparticles to obtain a novel Metal Complex Polymer Nanocomposite (MCPN) delivery system with enhanced intestinal permeability and controlled release of sulpiride.

4.2. MATERIALS AND METHODS

4.2.1. Materials

Complex **1a** (Figure 4.1.) was previously synthesised at Wits Advanced Drug Delivery Platform (WADDP) as described in Chapter 3, Section 3.2.4., the polymers Eudragit® RS 100 and polyvinyl alcohol (PVA) were obtained from Sigma-Aldrich (St Louis, MO, USA). All other materials were of analytical grade and used as received.

4.2.2. Preparation of the MCPN (emulsion solvent evaporation)

Respective formulations (F1-F9) were prepared by adapting methods published by Gaur et al. (Gaur et al., 2014). The %weight of polymers used was varied. To a stirring aqueous solution of polyvinyl alcohol (PVA) (water, PVA), a solution of Complex **1a** and Eudragit® RS 100 (methanol, Complex 1a, polymer), was added dropwise. The resulting mixture with stirred until complete removal of methanol. The resulting Metal Complex Polymer Nanocomposite

was dried at room temperature for 24 hours. The fabrication of MCPN via solvent evaporation is illustrated in Figure 4.2.

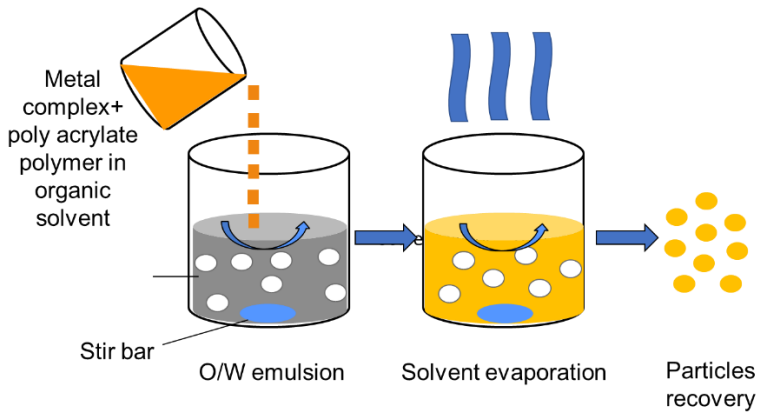


Figure 4.2. Schematic of MCPN preparation

4.2.2.1. Experimental Design

The Taguchi design method with L9 orthogonal array was used to investigate the effect of different parameters on the mean and variance of the MCPN performance and to obtain an optimal, well-functioning formulation. In this design, orthogonal arrays arrange the affecting parameters and their levels in the way most likely to affect the process. Unlike factorial design where all the possible combinations are tested, Taguchi employs a minimal number of trials by testing pairs of combinations, thereby saving both time and resources. The optimal parameters obtained from these trials are insensitive to environmental changes and other noise factors (Shravani et al., 2011). Limitations of this methods include 1) the relativity of the results obtained that do not exactly indicate what parameter has the highest effect on the performance characteristic value, 2) the difficulty in accounting for interactions between parameters and 3) the fact that the Taguchi design method is offline, thus inappropriate for a dynamically changing process such as a simulation study (Kondapalli et al., 2013). However, this experimental design is most effectively applied at early stages of development (Kondapalli et al., 2013), which made it suitable for this study.

4.1.1.1. Optimization of MCPN parameters

Three process parameters were selected for the identification of optimized formulation(s): 1) amount of complex **1a**, 2) concentration of polymer (Eudragit® RS 100) and 3) concentration of aqueous phase (PVA). Each of these parameters was of three different levels, as illustrated in Table 4.1.

Table 4.1. MCPN parameters with their respective levels

MCPN parameter	Factor assigned	Level 1	Level 2	Level 3
Amount of complex **1a** (mg)	A	100	200	300
Amount of Eudragit RS100 (mg)	B	225	300	375
Concentration of PVA (%w/v)	C	0.1	0.2	0.3

Three parameters, at three levels each, would give 27 experiments in the full factorial design (3^3). However, Taguchi experimental design gave only 9 experimental runs using the L9 orthogonal array, as shown in Table 4.2. The sequence of the experimental runs was randomized to prevent any bias. The criteria that were assessed were particle size, percentage drug entrapment efficiency, percentage drug loading, SPR intestinal permeability and SPR mean dissolution time. The statistical software (Minitab®, V14, Minitab Inc®, PA, USA) was used for each variable to determine its optimal parameters. The signal to noise (S/N) ratio for larger-the-better characteristic was chosen for all criteria. The ranks obtained for each factor will determine its effect on the drug release of the MCPN.

Table 4.2. Formulations to be prepared according to L9 orthogonal array for MCPN optimization

Formulations	Factor A (Amount of complex 1a (mg))	Factor B (Polymer (mg))	Factor C (Aqueous phase (%w/v))
F1	100	225	0.1
F2	100	300	0.2
F3	100	375	0.3
F4	200	225	0.2
F5	200	300	0.3
F6	200	375	0.1
F7	300	225	0.3
F8	300	300	0.1
F9	300	375	0.2

4.2.3. Evaluation of prepared MCPN formulations

4.2.3.1 Measurement of particle size and zeta potential

The mean particle size, polydispersity index of the size distribution and zeta potential of each formulation were determined using the Zetasizer Nano ZS (Malvern, Panalytical Ltd, UK). The MCPN formulations were subjected to a dilution of 1:1000 in distilled water.

4.2.3.2. Measurement of drug entrapment efficiency and drug loading

MCPN formulations were dissolved in methanol and the resulting solution was filtered. The filtrate was diluted and analysed for drug content using UV-Vis as previously described in Chapter 3, Section 3.2.5. The percent entrapment efficiency (%EE) and percent drug loading (%DL) were calculated using equations (1) and (2).

$$\%EE = \frac{Actual\ loading}{Theorical\ loading} \times 100 \quad (4.1)$$

$$\%DL = \frac{Weight\ of\ drug\ in\ MCPN}{Weight\ of\ MCPN} \times 100 \quad (4.2)$$

4.2.3.3. Differential Scanning Calorimetry (DSC) of complex 1a, Eudragit® RS 100 and MCPN formulations

The thermal behaviour of complex **1a**, Eudragit® RS 100 and MCPN formulations was investigated by differential scanning calorimetry using a Mettler Toledo DSC1 STARe System (Mettler Toledo, Switzerland) using a heating rate of 10°C per minute in the range 25°C - 400°C.

4.2.3.4. Fourier Transform Infrared (FTIR) Spectroscopy of complex 1a, Eudragit® RS 100 and MCPN formulations

The FTIR spectra was recorded in the wavenumber region 4000-650 cm^{-1} on a Spectrum 100 FTIR spectrometer (Perkin-Elmer Inc. MA, USA) equipped with an attenuated total reflectance (ATR) sampling device. The FTIR spectrum of each MCPN formulation was compared to that of complex **1a** and Eudragit® RS 100.

4.2.3.5. Surface morphology analysis of MCPN

The surface morphology of the MCPN was analysed using scanning electron microscopy (SEM) (Jeol JSM-120, Tokyo, Japan). A small quantity of MCPN powder was sputter coated using gold and palladium isotopes while being mounted on an aluminium spud, with an EPI coater (SPI Module TM sputter-coater and control unit, Chester, PA, USA). After coating the MCPN for 1 minute, under constant nitrogen gas conditions, the sample was analysed using a FEI Quanta 600 F (FEITM, Hillsboro, OR, USA) electron microscope at an electron acceleration voltage of 20 kV.

4.2.3.6. *Ex vivo* permeation studies of free SPR, SPR in complex **1a** and SPR in MCPN formulations

Ex vivo permeation studies were performed to evaluate the comparative intestinal absorption of MCPN formulations against free SPR and SPR in complex 1a. This study was approved by the Animal Ethics Screening Committee of the University of the Witwatersrand (Reference: Gretta Mbitsi-Ibouily 14-11-14 O*)*. Intestinal tissue from euthanised pigs was obtained from at the Central Animal Service (CAS) of the University of the Witwatersrand. Porcine small intestines were surgically removed, transported to the laboratory where they were cleaned, and the exogenous tissues and subcutaneous layers carefully removed. They were then stored at -80°C for further use. On the day of the experiment, intestinal tissues were thawed at room temperature, cut in pieces prior to use and mounted on vertical Franz diffusion cells (United Scientific, South Africa). Each Franz diffusion cell had a membrane area of 1.77 cm^2 exposed and a 12 mL receptor chamber capacity. The tissue membranes were mounted between the donor and receptor compartment with the apical side facing the donor compartment and the basolateral side facing the receptor medium, which was filled with PBS, pH 7.4. Each sample was done in triplicate. Samples consisted of SPR, complex **1a**, and MCPN formulations. SPR's UV-VIS calibration curve was used to ensure that complex **1a** and all MCPN formulations contained equivalent amounts of SPR (5 mg). Each sample was applied to the donor compartment and 3 mL PBS, pH 6.8, was added. Temperature was kept at 37 ± 0.5°C throughout the study. Samples of 0.1 mL were withdrawn at intervals 0.5, 1, 1.5, 2, 3, 4, 5, 6, 7, 8, 12 and 24 hours, and replaced with the same volume of buffer solution. Withdrawn samples were assayed for dissolved SPR using a UV-Vis calibration curve.

The cumulative amount of SPR permeated across the membrane was calculated in accordance with the formula below:

Cumulative amount of drug permeated = $\frac{Q}{A}$ ($\mu g.cm^{-2}$) (3.3)

Where Q = amount of substance crossing the membrane (µg)

A = membrane area exposed (cm^2)

In *ex vivo* studies, confirmation of tissue integrity is essential, since any compromised tissue integrity during handling will result in inaccurate permeation results (Davies et al., 2004). Ionic conductivity as a measure of the porcine intestinal tissue integrity was determined using a SevenMulti S40 pH/electrical conductivity meter (Mettler-Toledo, Zurich, Switzerland) prior to (t_0) the experimental procedure and at t_8, t_{12} and t_{24}. The FTIR spectrum of the intestinal tissue was also collected and at t_0 t_8, t_{12} and t_{24} (Davies et al., 2004; Indermun et al., 2015).

4.2.3.7. *In vitro* drug release study of free SPR, SPR in complex **1a** and SPR in MCPN formulations

Dissolution studies of commercially available sulpiride (50 mg Eglonyl® capsules), complex **1a** and MCPN formulations were performed. The equivalent amount of 50 mg of sulpiride was maintained in each sample via UV-Vis assay. The dissolution experiment for each compound was performed in triplicate. The samples were prepared by inserting them into empty capsules equivalent in size and shape to Eglonyl® capsules. DT 700 dissolution tester (Erweka, Germany) in paddle mode was used. The samples were initially inserted into 900 mL 0.1N hydrochloric acid (pH=1.2, simulated gastric fluid) for 2 hours. After 2 hours, the pH of the medium was adjusted to 6.8 (simulated intestinal fluid) by addition of 25.92 g disodium hydrogen phosphate and 10.305 g dihydrogen potassium phosphate and the dissolution study was carried out for another 4 hours. After 6 hours, the pH was increased to 7.4. (simulated blood) by adding 2.142 g of disodium hydrogen phosphate and 0.171 g of sodium chloride to the dissolution medium and the study was continued for up to 24 hours. The stirring rate was 100 rpm and the temperature was kept at 37 ± 0.5°C for the duration of the experiment (24 hours). A stainless mesh ring was placed into the dissolution vessel, below the paddle, in order to minimise sample floating. Samples (3 mL) were withdrawn at prescribed intervals of 0.5, 1, 1.5, 2, 3, 4, 5, 6, 7, 8, 9, 10, 12 and 24 hours for all pH values investigated and all sampling points sink conditions were maintained via replacement with dissolution medium. The corresponding samples were assayed for dissolved SPR using a UV-VIS calibration curve.

4.2.4. *In vitro* toxicity testing of SPR in complex 1a and optimized MCPN using Caco-2 cell line

The small intestinal lumen surface area is lined with an epithelial cell monolayer, which isolates the systemic circulation from the intestinal lumen. This epithelial monolayer prevents the invasion of bacteria and toxic compounds from the gastrointestinal tract. Intestinal epithelial cells can be disturbed or damaged by either toxic chemical compounds or toxicity generated during digestion. Disturbance or damage in the intestinal epithelial tissues may result in the weakening of its protective role. Therefore, the possible cytotoxicity sulpiride in complex **1a** and optimized MCPN was investigated using Caco-2 intestinal cell line (Cellonex, South Africa), a human cell line derived from a colon adenocarcinoma. This cell line was selected due to its wide use in assays involving drug absorption following oral administration, as well as its similar characteristics to those of the absorptive intestinal epithelium (Chen et al., 2016; Igartúa et al., 2015; Meunier et al., 1995).

4.2.4.1. Caco-2 cell line culturing

Caco-2 cells (Cellonex, South Africa) were grown in culture flasks containing solution Dulbecco's Modified Eagle Medium (DMEM), supplemented with 20% fetal bovine serum with 4.0 mM l-glutamine and sodium pyruvate, with added 1 mL penicillin/streptomycin (Sigma-Aldrich; St. Louise, MO, USA). Cells were maintained in an incubator (RS Biotech Galaxy, Irvine, UK) under humidified atmosphere of 5% CO_2 at 37°C during cell growth. The cell medium was replaced every 2 to 3 days. Cells were grown until they reached 60–90% confluence before cytotoxicity tests were conducted.

4.2.4.2. Cell counting using trypan blue solution assay and a haemocytometer

When 60-90% confluence was reached, the medium was discarded from the cultured flask, followed by addition of trypsin-EDTA (3 mL) and incubation for 5 minutes to detach the cells. The cultured flask was scrapped to ensure detachment of all cells. The incubated solution was centrifuged at 1500 g for 5 minutes. The supernatant was discarded, and cells were resuspended in fresh medium (1 mL). Trypan blue solution (100 µL) was added to the suspended cells. The disposable haemocytometer chamber was filled with a mixture of trypan blue solution added to the suspended cells. Light microscopy (Olympus CKS53 microscope, Olympus, Japan) was used to examine the chamber for cell counting. Trypan blue solution only stains dead cells. The number of living cells in the sample was determined by counting the number of unstained cells.

4.2.4.3. *In vitro* cytotoxicity evaluation using 3-4,5-Dimethylthiazol-2-yl)-2,5-Diphenyltetrazolium bromide (MTT) assay

Cytotoxicity of SPR in complex **1a** and optimized MCPN in Caco-2 cell line was evaluated using the MTT assay. Multi well plates (96) were seeded with Caco-2 cells at a density of $2x10^4$ cells/well and incubated for 24 hours. After culturing the cells in 96 well plates for 24 hours in the incubator (RS Biotech Galaxy, Irvine, UK) under humidified atmospheric conditions of 5% CO_2 at 37°C, the culture was removed from the incubator into a laminar flow unit. Thereafter, different concentrations of prepared SPR and complex **1a** and optimised MCPN solutions (50, 100, 250, 500 and 1000 mg/L SPR) of equal volumes were added to the initial culture media. The cells were incubated for further 24 hours at 37°C. At the end of the 24-hour incubation, 10 µL of MTT solution was added to the wells, and the 96 well plate was incubated for 4 hours to allow the conversion of MTT to formazan by mitochondrial dehydrogenase. Following the 4-hour incubation period, the medium was removed from the wells. The formazan formed crystals were dissolved by adding DMSO solution (100 µL). The plates were placed in an orbital shaker overnight. Absorbance was measured at a wavelength of 570 nm. The background absorbance of the multi well plates was measured at 690 nm and

was subtracted from the 570 nm measurement. The resulting measurements were presented as percentage cell viability (mean ± standard deviation). Equation (3.5) was used to calculate the percentage cell viability:

$$\text{Percentage cell viability} = \frac{Mean\ absorbance\ at\ each\ concentration}{Mean\ absorbance\ of\ control} \times 100 \quad (3.5)$$

4.3. RESULTS AND DISCUSSION

4.3.4. Particle size and zeta potential

The mean particle size, polydispersity index (PDI), zeta potential, %EE and %DL for all prepared MCPN formulations are shown in Table 4.1. The particle size of the prepared MCPN formulations ranged from 92.77±3.96 nm (F2) to 363.1±14.5 (F3). The PDI is an indication of the degree of non-uniformity of a size distribution of particles (Danaei et al., 2018). The acceptable value for PDI is 0.05-0.7; values greater than 0.7 indicate very broad size distribution and probably no suitability for dynamic light scattering technique (Yurtdaş Kırımlıoğlu and Yazan, 2016). Polydispersity indices of less than 0.3 have been reported to indicate narrow size distribution while those of less than 0.1 are considered monodispersed (NanoComposix, 2012). Table 4.3 shows that all formulations were relatively monodisperse. Zeta potential values mostly indicate moderate electrostatic stability of the MCPN formulations suspensions (-30 to -40 mV) with F7 demonstrating good stability (-58.4 mV)(Adibkia et al., 2011).

Table 4.3. Mean particle size, polydispersity index, zeta potential, percent entrapment efficiency and percent drug loading measurements for all MCPN formulations

Formulation	Particle size (nm)	Polydispersity index	Zeta potential (mV)	%EE	%DL
F1	275.8±1.13	0.176±0.037	-32.03±1.28	90.41	28.70
F2	92.77±3.96	0.166±0.045	-32.23±3.07	87.82	27.45
F3	363.1±14.5	0.294±0.019	-35.69±0.66	83.75	20.99
F4	274.6±17.6	0.225±0.034	-33.94±0.55	64.59	36.70
F5	180.0±2,52	0.236±0.055	-35.81±2.10	80.80	38.20
F6	298.7±27.5	0.234±0.076	-34.40±1.86	71.82	32.42
F7	239.3±3.82	0.258±0.057	-58.4±2.41	58.85	35.17
F8	228.1±5.80	0.303±0.052	-30.67±1.49	63.50	33.07
F9	337.8±29.7	0.269±0.024	-32.48±2.10	62.60	32.72

4.3.4.1. Taguchi analysis response for MCPN particle size

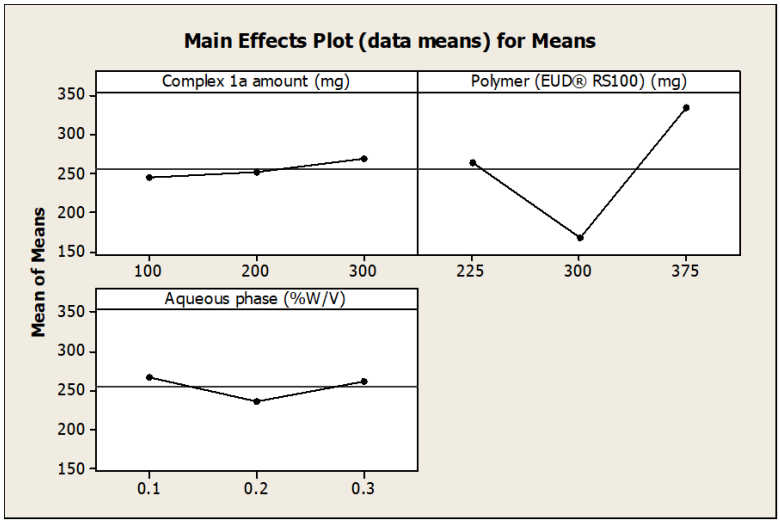


Figure 4.3. Graphs showing signal to noise ratio for MCPN particle size.

Table 4.4. Response table for means for MCPN particle size

	A	B	C
Level			
1	243.9	263.2	267.5
2	251.1	167.0	235.1
3	268.4	333.2	260.8
Delta	24.5	166.2	32.5
Rank	**3**	**1**	**2**

Figure 4.3. shows the S/N ratio and Table 4.4 shows the response table for means for MCPN formulations particle size. Taguchi analysis showed that B had the highest effect on the mean particle size of the MCPN, as indicated by the 1st rank of polymer amount for the particle size

analysis of the formulation (Table 4.4). A proportional relationship between polymer amount and mean particle size was demonstrated; in fact, the lower the amount of Eudragit® RS100, the smaller the mean particle size of the MCPN formulation (Table 4.2 and Table 4.3). Such relationship between mean particle size and polymer amount has previously been reported and explained by the possible increase in relative viscosities with increasing polymer concentration, which results in the need for more energy to disperse the system. (Gaur et al., 2014; Sharma et al., 2016).

4.3.5. Drug entrapment efficiency and drug loading

The highest %EE (F1: 90.41%, F2: 87.82%, F3: 83.75%) were observed in formulations with the lower amount of complex 1a (Table 4.2 and Table 4.3). On the other hand, % DL increased in parallel with the amount of complex 1a (Table 4.2 and Table 4.3).

4.3.5.1. Taguchi analysis response for MCPN drug entrapment efficiency and drug loading

a) b)

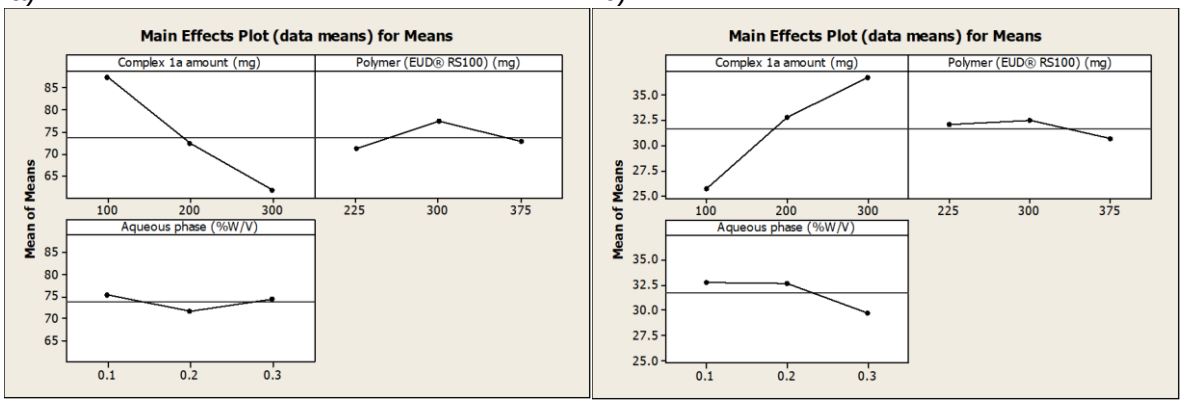


Figure 4.4. Graphs showing signal to nose ratio for a) MCPN drug entrapment efficiency and b) MCPN drug loading.

Table 4.5. Response table for means for MCPN drug entrapment efficiency and drug loading

	Drug entrapment efficiency (%)			**Drug loading (%)**		
	A	**B**	**C**	**A**	**B**	**C**
Level						
1	87.33	71.28	75.24	25.71	32.10	32.71
2	72.40	77.37	71.67	32.74	32.41	32.69
3	61.65	72.72	74.47	36.69	30.64	29.74
Delta	25.68	6.090	3.570	10.98	1.77	2.96
Rank	**1**	**2**	**3**	**1**	**3**	**2**

Figure 4.4 shows the S/N ratio and Table 4.5 shows the response table for means for MCPN drug entrapment efficiency and drug loading. Taguchi analysis showed that A had the highest

effect on the mean %EE of the MCPN formulations, as indicated by the 1st rank of amount of complex **1a** for the %EE analysis of the formulation (Table 4.5). An inversely proportional relationship between the amount of complex 1a and the %EE was demonstrated as the lowest amount of complex **1a** resulted in the highest %EE. For the mean %DL of the MCPN formulation, Taguchi analysis indicated that A had the highest effect (rank 1, Table 4.5). A parallel relationship was established between the amount of complex **1a** and the %DL of the MCPN formulation.

4.3.6. Differential scanning calorimetry (DSC) analysis of complex 1a, Eudragit RS 100 and F2

The thermograms of complex **1a**, Eudragit® RS100 and F3 are shown in Figure 4.5, highlighting the similar peaks between complex **1a** and F3 as well as between Eudragit® RS100 and F2. The DSC curve of complex **1a** showed three endothermic peaks. The first one, observed at 189°C, is small and sharp and shows the presence of sulpiride, which has been reported to show a sharp melting endotherm at 180°C (Ibrahim et al., 2014). A similar peak can be observed with a slight shift at 186°C in the thermogram of F2. The second endothermic peak at 236 °C is wide and corresponds to the melting temperature of complex 1a; this peak shifted in the thermogram of F2 and could be observed at 284°C. The increase in the melting temperature of the MCPN formulations can be attributed to the restriction of polymer chain mobility caused by the interaction between the metal complex and the polymer chain (Ramesan and Sampreeth, 2017). Complex **1a** then underwent further decomposition resulting in the final DSC peak at 287°C, which shifted to 314°C in the thermogram of F2. The thermogram of F2 showed integrity of complex **1a** after MCPN preparation with the added presence of Eudragit® RS100 marked by a sharp endotherm at 391°C and 392°C in the DSC curves of Eudragit® RS100 and F3 respectively.

Figure 4.6 shows the thermograms of all MCPN formulations, F1-F9. A similar thermal behaviour was observed for all prepared MCPN formulations.

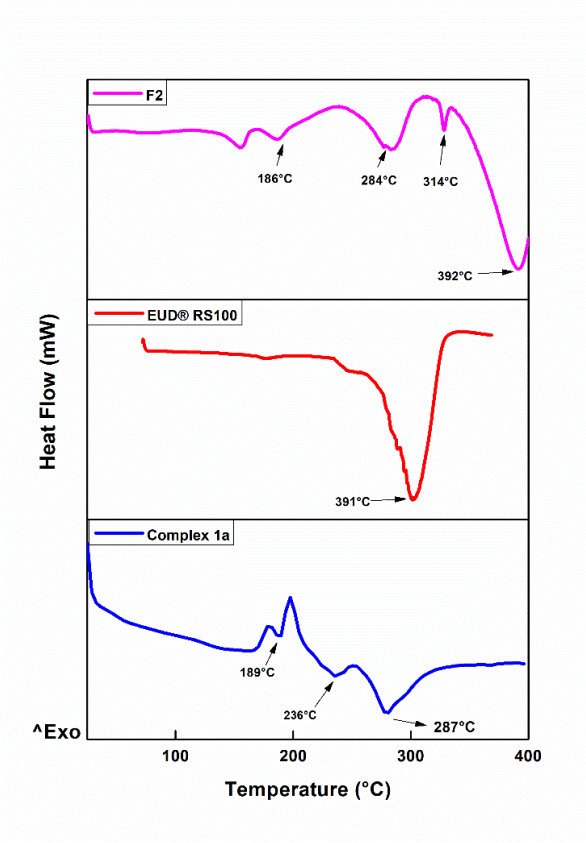


Figure 4.5. Differential scanning calorimetry thermograms for complex **1a**, Eudragit® RS100 and F2.

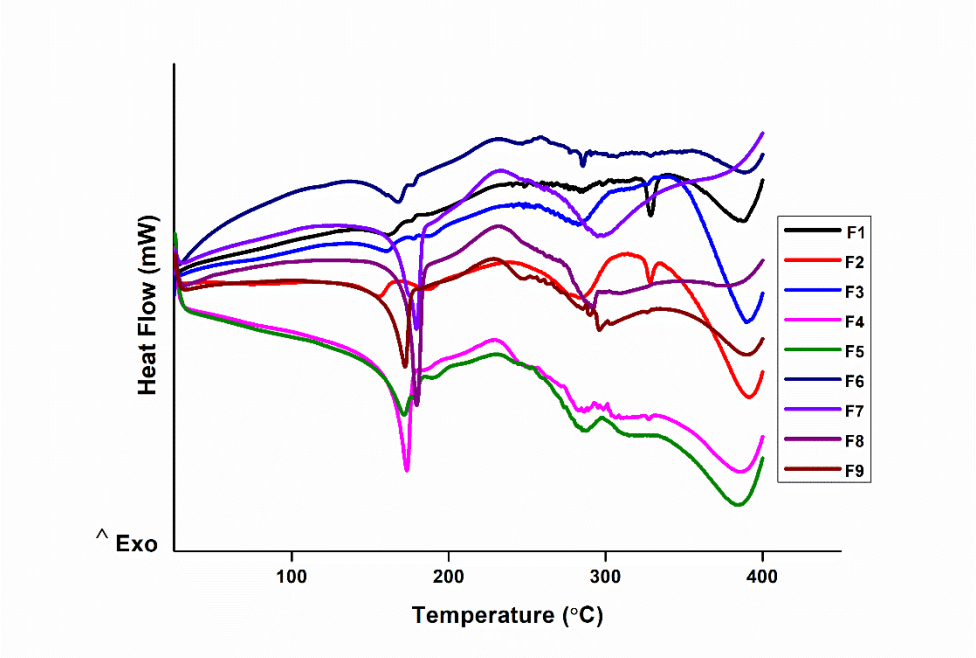


Figure 4.6. Differential scanning calorimetry thermograms for MCPN formulations F1-F9

4.3.7. Infrared (IR) spectral analysis of complex 1a, Eudragit® RS 100 and MCPN formulations

The FTIR spectra of SPR, complex **1a**, Eudragit® RS 100 and MCPN formulations F1-F9 are shown in Figure 4.7. The similarities between the spectra of SPR, complex **1a** and the spectra of F1-F9 are highlighted in green. The υ(C=O) stretching vibration observed at 1639 cm^{-1} and 1634 cm^{-1} in the spectra of SPR and complex **1a** respectively was also seen in the spectra of F1-F9 (Figure 4.7). The NH stretching vibrations (3383 cm^{-1} and 3164 cm^{-1}; 3325 cm^{-1} and 3184 cm^{-1}) and the NH stretching vibration at 3085 cm^{-1} and 3063 cm^{-1} in the spectra of SPR and complex **1a** respectively were also observed in the spectra of the MCPN formulations F1-F9 (Figure 4.7). In the spectrum of pristine Eudragit® RS100 an ester C=O stretching band at 1722 cm^{-1} is observed, which is also present in the spectra of F1-F9, proving the presence of Eudragit® RS 100 (Jain and Singh, 2010) in the MCPN formulations (Figure 4.7, highlighted in yellow). The FTIR spectra of F1-F9 revealed no distinctive changes compared to the spectrum of complex **1a**, indicating that Eudragit® RS100 was not involved in intermolecular interaction with complex **1a** in physical mixtures (Adibkia et al., 2011).

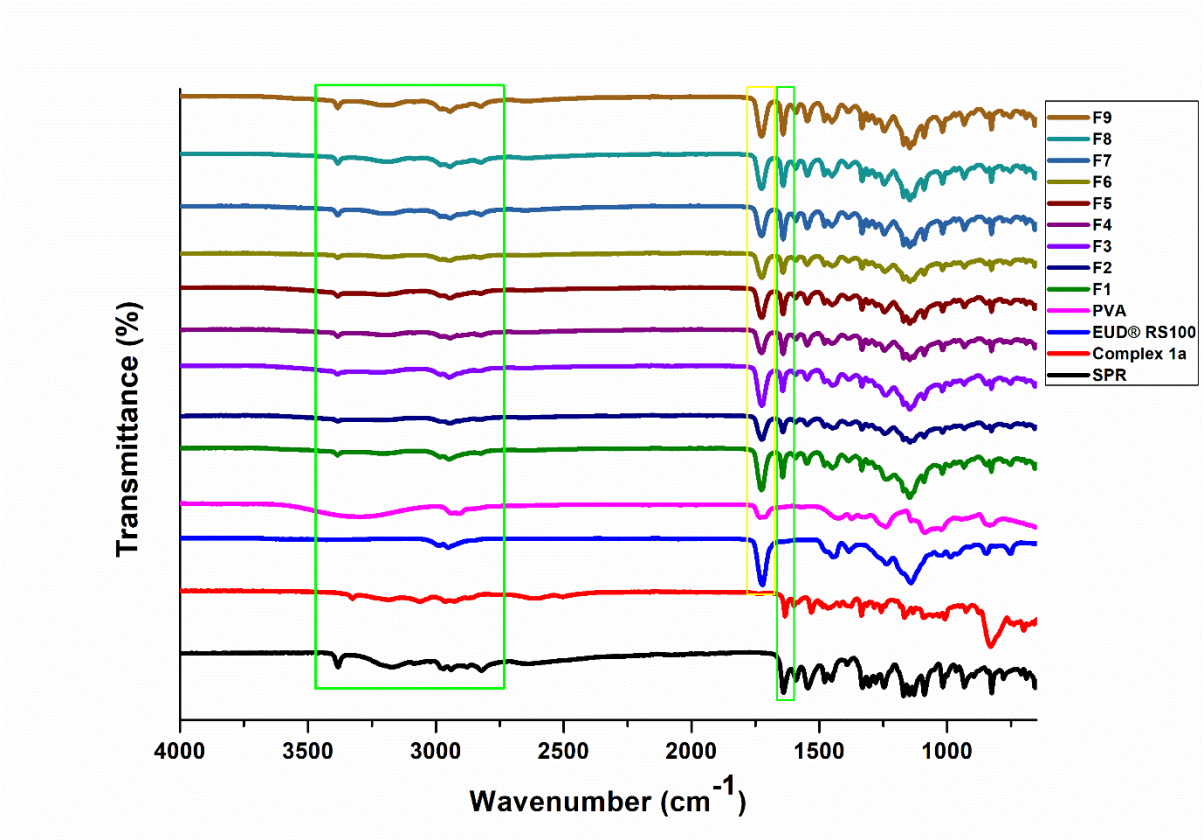


Figure 4.7. Fourier transform infrared spectra for SPR, complex **1a**, Eudragit® RS100 and F1-F9.

4.3.8. MCPN surface morphology

The scanning electron microscopic images from the F2 formulation at different magnifications are shown in Figure 4.8. SEM experiments revealed a spherical shape with a relative smooth surface for the MCPN formulations. Bottom-up techniques of nanoparticle synthesis have traditionally yielded spherical products (Zhao et al., 2017); thus this shape was expected. Nanospheres have been previously shown to improve the intestinal permeability of drugs (Zakeri-Milani et al., 2014; Zare et al., 2018), which is beneficial for this study.

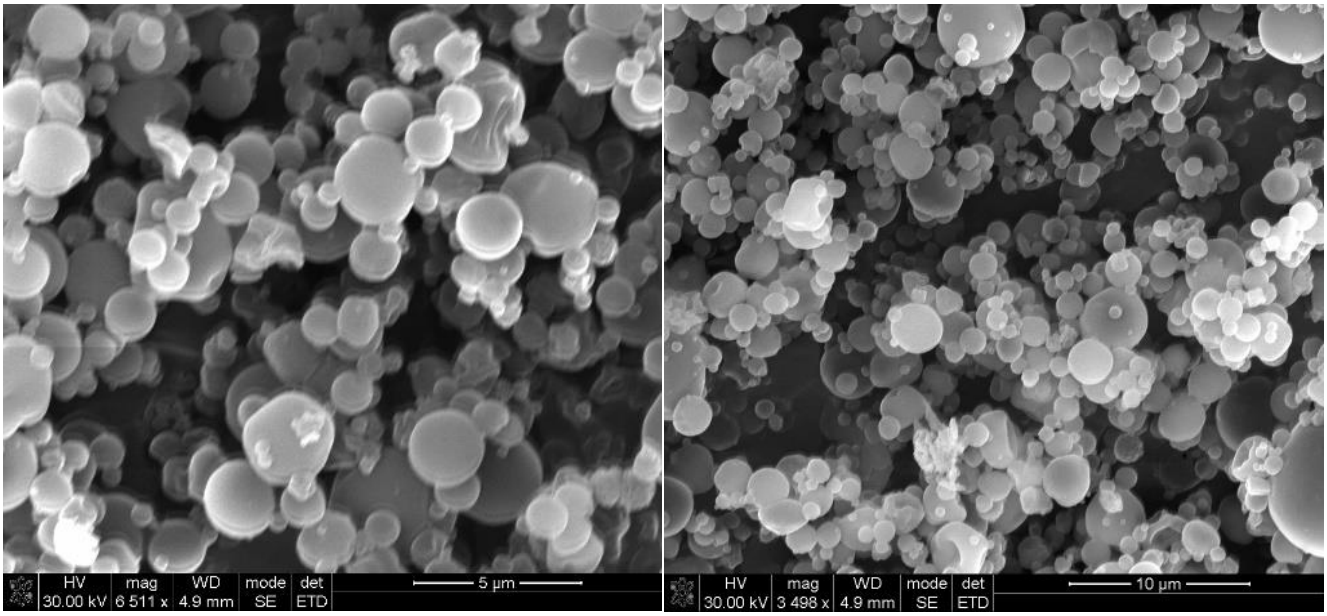


Figure 4.8. Scanning electron micrographs for F2 MCPN formulation at 6,511 and 3,498 magnification powers.

4.3.9. Permeation studies of complex 1a and MCPN formulations F1-F9

The values of the ionic conductivity of the porcine intestinal tissue at t_0 and t_8 were similar (18 and 17 mV respectively) and their FTIR spectra at these time points showed similar bands, both implying tissue structural integrity at t_8. At t_{12} and t_{24}, on the other hand, the ionic conductivities dropped to -8 and -22 mV but the FTIR spectra remained unchanged, implying that some of the integrity of the porcine intestinal tissue was compromised at these time points.

The permeation profiles of complex **1a** and MCPN formulations F1-F9 through the pig's small intestine were therefore determined up to 8 hours and are shown in Table 4.6. Higher amounts of SPR were permeated through the membrane from the MCPN formulations F1-F9 than complex **1a**. The increased intestinal permeability suggests that the lipophilicity of the drug is improved, thereby enhancing its diffusion through the membrane. This lipophilicity improvement can be attributed to the smaller size of the particles compared to that of complex

1a (Williams et al., 2016). The highest cumulative relative permeability (75.65%) was in fact observed in the MCPN formulation F2, which had the smallest particle size of 92.77±3.96 nm (Table 4.6 and Table 4.3).

Table 4.6. Cumulative permeability and cumulative relative permeability of free SPR, SPR released from complex **1a** and SPR released from MCPN formulation F1-F9

Compound	SPR Cumulative Permeability (µg/cm^2)	SPR Cumulative Relative Permeability (%)
Sulpiride	88.42	14.17
Complex **1a**	199.1	27.20
F1	218.1	30.66
F2	544.4	75.65
F3	316.2	44.02
F4	281.0	38.67
F5	223.5	31.37
F6	205,0	28.74
F7	214,2	30.18
F8	426,3	59.45
F9	322,8	45.65

4.3.9.1. Taguchi analysis response for MCPN mean dissolution time

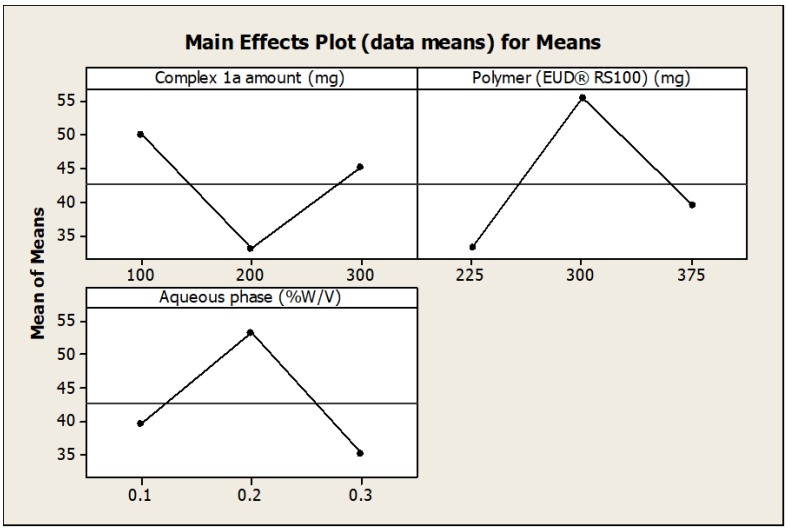


Figure 4.9. Graphs showing signal to noise ratio for SPR cumulative relative permeability

Table 4.7. Response table for means for SPR cumulative relative permeability.

	A	B	C
Level			
1	50.11	33.17	39.62
2	32.93	55.49	53.33
3	45.09	39.47	35.19
Delta	17.18	22.32	18.14
Rank	**3**	**1**	**2**

Figure 4.9 shows the S/N ratio and Table 4.7 shows the response table for means for SPR cumulative relative permeability. Taguchi analysis showed that B had the highest effect on SPR cumulative relative permeability, as indicated by the 1st rank of polymer amount for the mean SPR cumulative relative permeability (Table 4.7). Taguchi analysis of mean particle size of MCPN formulations demonstrated that the lower the amount of Eudragit® RS 100, the smaller the mean particle size of the MCPN formulation (Table 4.4). Taguchi analysis for SPR cumulative relative permeability therefore confirms the inversely proportional relationship between particle size and SPR cumulative permeability; the lower the polymer amount, the smaller the particle size and thus, the higher SPR cumulative permeability.

4.3.10. *In vitro* drug release study

In Figure 4.10 the dissolution profiles of Eglonyl®, SPR in complex **1a** and SPR in MCPN formulation F1-F9 are presented. A burst release of SPR is observed 30 minutes after the start of the dissolution test of complex **1a** (91.39%) but it is slightly lower than that observed for Eglonyl® (98.18%). Total release of sulpiride is observed 2 hours after the start of the dissolution test for both Eglonyl® and SPR in complex **1a** (Figure 4.10). The initial stage burst release is a common phenomenon in many drug release systems (Leo et al., 2000). However, in the case of sulpiride, this burst release is very high, as can be seen in Figure 4.10. The burst release of sulpiride from the MCPN formulations F1-F9 was significantly reduced, with the lowest burst release observed for F1 (14.23%) and the highest for F4 (41.70%). Nanoparticles prepared by emulsion solvent evaporation have previously been reported to exhibit an initial burst release; this is attributed to the surface adsorbed drug (Kim and Martin, 2006). Eudragit® RS 100 makes the formulations more stable in acidic pH, reducing the SPR burst release previously observed (Yelnimez, 2017). All MCPN formulations F1-F9 revealed slower drug release rates in comparison with both the commercial drug and complex **1a** (Figure 4.9); this can be attributed to the swelling property of PVA in the formulation, which has been previously showed to participate in sustained drug release (Gaur et al., 2014). The

drug release rate was not affected by increasing the Eudragit® RS 100 relative amount in the MCPN formulation.

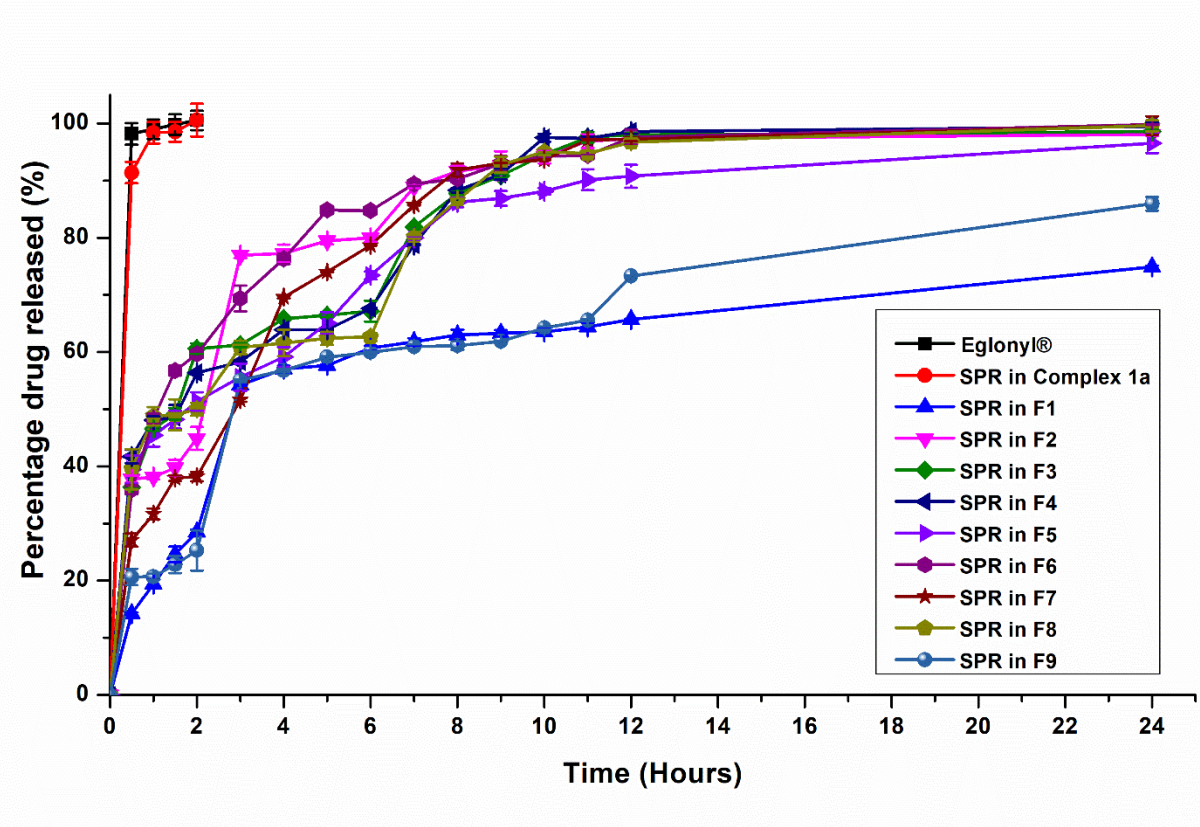


Figure 4.10. Dissolution profiles of Eglonyl®, SPR in complex **1a** and SPR in MCPN formulations F1-F9 in gastric/intestinal pH simulated solutions (pH 1.2 for first 2 hours; pH 6.8 for following 4 hours; pH 7.4 up to 24 hours).

4.3.10.1. Taguchi analysis response for SPR mean dissolution time

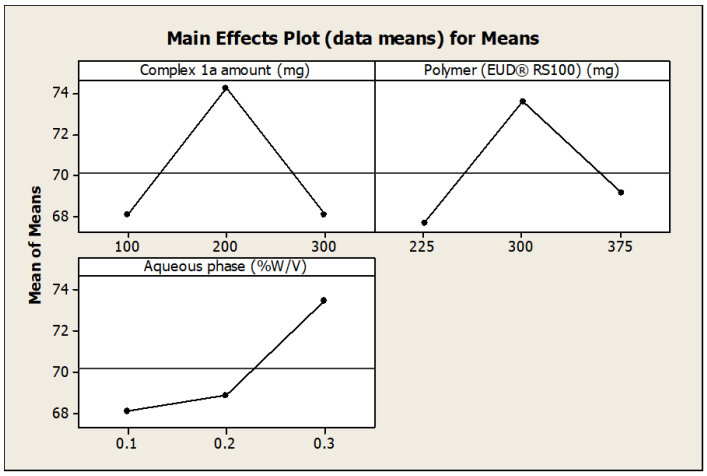


Figure 4.11. Graphs showing signal to noise ratio for SPR mean dissolution time.

Table 4.8. Response table for means for SPR mean dissolution time

Level	A	B	C
1	68.12	67.67	68.11
2	74.76	73.61	68.88
3	68.09	69.18	73.47
Delta	6.17	5.95	5.36
Rank	**1**	**2**	**3**

Figure 4.11 shows the S/N ratio and Table 4.8 shows the response table for means for MCPN mean dissolution time. Taguchi analysis showed that A had the highest effect on the mean dissolution time of the MCPN, as indicated by the 1st rank of amount of complex 1a for the mean dissolution time analysis of the formulation (Table 4.8). This confirms that the relative amount of Eudragit® RS100 in the MCPN had no effect on the drug release rate of the MCPN formulations.

4.3.11. Optimized MCPN formulation

Following Taguchi analysis of the chosen parameters and keeping in mind the aim of this study which was to synthesise a novel MCPN delivery system with enhanced intestinal permeability and controlled release of sulpiride, F2 was selected as the optimized MCPN. Figure 4.12 and Figure 4.13 show the mean particle size and average zeta potential distribution profiles for the optimized MCPN, respectively. F2 combined small particle size (Table 4.3, Figure 4.11), moderate stability (zeta potential; Table 4.3, Figure 4.12), good %EE and %DL (Table 4.3), high intestinal permeability (Table 4.6) and controlled drug release (Figure 4.10). The optimized MCPN formulation was thereafter evaluated for cytotoxic activity.

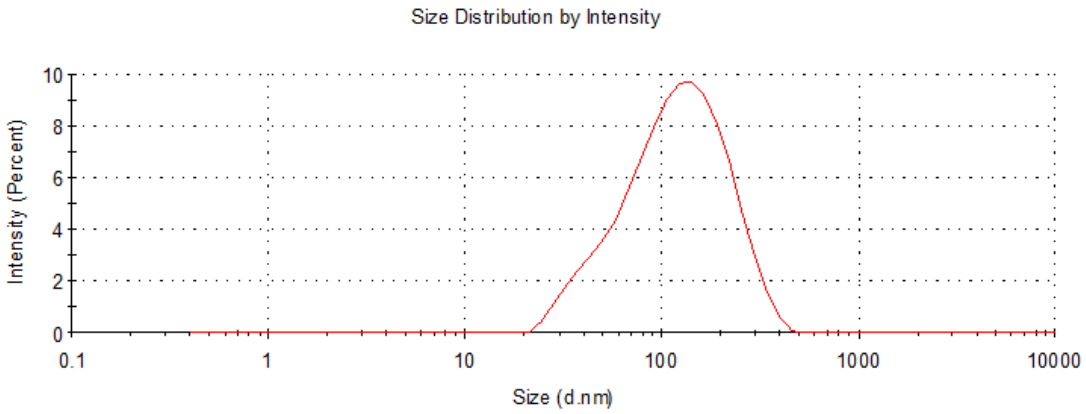


Figure 4.12. Mean particle size distribution profile for optimized MCPN.

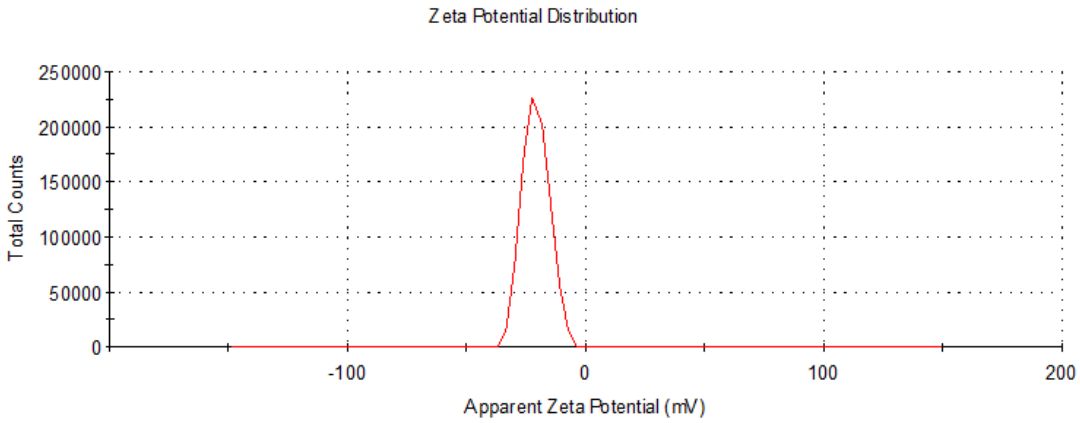


Figure 4.13. Average zeta potential distribution profile for optimized MCPN.

4.3.12. Effects of SPR in complex 1a and SPR in optimized MCPN on Caco-2 cell viability

Figure 4.14 depicts the percentage cell viability after cell treatment with different concentrations of SPR in complex **1a** and SPR in optimised MCPN formulation for 24 hours. No significant differences were observed in percentage cell viability of the optimized formulation, compared to complexed SPR. Previously conducted intestinal absorption studies of SPR using the Caco-2 cell line to make an in *vitro* model of the human intestine have also demonstrated minimal effect of SPR on Caco-2 cells (Watanabe et al., 2002b, 2002a). Ruthenium (II) metal complexes, on the other hand, have been associated with anticancer activity against a variety of human cell lines, including Caco-2. Recent studies have in fact reported moderate to high (higher than cisplatin) *in vitro* toxicity of ruthenium arene complexes against Caco-2 cell line (Gichumbi et al., 2016; Mondal et al., 2018). In these ruthenium complexes exhibiting anticancer properties, the metal in the molecule is active and therefore the tested concentrations are metal-dependent. This is not the case in the current study, where SPR is the active ligand and ruthenium is used as a drug carrier, thus the tested concentrations are SPR-dependent and contain less metal than metal-based concentrations. This lower ruthenium (II) concentration in ternary metal complexes of sulpiride relative to other ruthenium metallo drugs could explain the lack of toxicity of the metal on the Caco-2 cells. It was noticed that the percentage cell viability slightly decreased with increased concentration of the tested compounds, which was expected, especially in the presence of ruthenium (Gouveia et al., 2018). Ternary metal complex of SPR and optimized MCPN formulation thus demonstrated no noticeable toxic effects on the intestinal epithelium tissue.

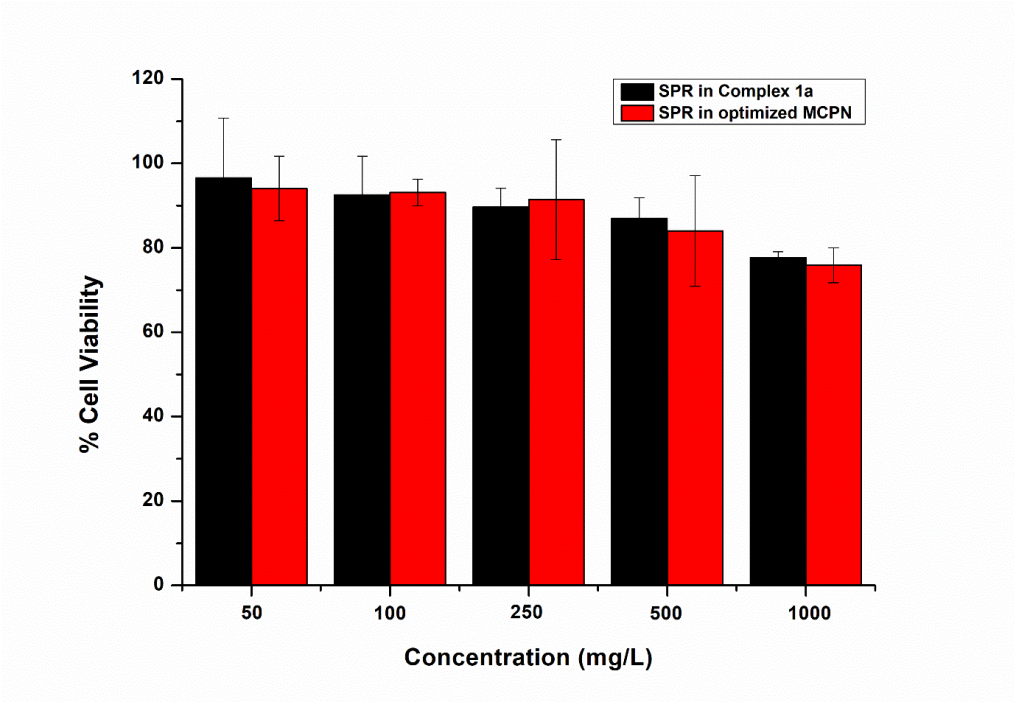


Figure 4.14. Percentage Caco 2 cell viability following treatment with complex **1a** and optimized MCPN.

4.4. CONCLUDING REMARKS

Metal Complex Polymer Nanocomposite (MCPN) were successfully formulated through encapsulation of metal-liganded SPR into polymeric nanoparticles and evaluated for sulpiride intestinal permeability *ex vivo* and *in vitro* drug release in simulated physiological conditions. The chosen polymer blend resulted in the formulation of MCPN with reasonable particle size (92.77±3.96-363.1±14.5), which resulted in relative increased intestinal permeability capacity of the drug (30.18-75.65%). The use of metal complexation enabled acceptable %EE (58.85-90.41) and %DL (20.99-38.20) of SPR into the MCPN. Intestinal permeability assessment showed enhanced permeation of sulpiride from the MCPN as compared to the original ternary metal complex, through a 2-fold mechanism: 1) the enhancement of lipid solubility of SPR through metal complexation and 2) the improvement of transmembrane permeability through the nano-sized formulation. Dissolution studies showed significantly reduced burst release of sulpiride from the MCPN, through the pH-responsiveness of Eudragit® RS 100, and a sustained drug delivery profile up to 24 hours, through the action of Eudragit® RS 100 and PVA polymers. MCPN delivery system may therefore be considered as a potential candidate for intestinal permeability improvement and controlled release of sulpiride drug with minimal toxicity. However, animal studies are recommended to investigate and correlate the bioavailability of sulpiride from the MCPN *in vivo*.

CHAPTER 5
IN VIVO ANALYSIS OF THE METAL COMPLEX POLYMER NANOCOMPOSITE IN RELATION TO MARKETED FORUMULATION IN THE LARGE WHITE PIG

5.1. INTRODUCTION

In vivo animal studies are a critical step in the development and evaluation of any new drug delivery system to ensure desired drug delivery outcomes within a living organism. Although *in vitro* drug release studies aim to simulate *in vivo* environments, they do not exactly replicate the operation and impact of an *in vivo* environment on drug delivery systems, thus the need to assess the delivery system within a living organism. The data generated can be used to assess the safety and efficacy of a delivery system and to help predict the pharmacokinetics and pharmacodynamics of the system in humans (Ngwuluka et al., 2017). The selection of an appropriate animal model depends on factors such as dosage form and frequency of dosing, as well as the ability to closely mimic the conditions and effects in humans (Gutierrez et al., 2015).

The Large White Pig model (*Sus scrofa domesticus*) was selected to evaluate the release rate of the optimized MCPN in comparison to the currently marketed SPR conventional formulation (Eglonyl®). The pig model was chosen because of the many similarities the pig shares with humans such as size, physiology, anatomy, metabolic profile and longer lifespan (Gutierrez et al., 2015). The close resemblance of its gastrointestinal tract to that of humans is of particular interest for the purpose of this study, making this animal model best suited for *in vivo* studies of oral drug delivery (Hoosain et al., 2016; Ngwuluka et al., 2017). Pigs have a relatively minimal cost of maintenance and their large size is an added advantage as it allows for multiple blood sampling for achievable drug release studies (Kobayashi et al., 2012).

This chapter involves the oral *in vivo* administration of the conventional Eglonyl® capsules and the optimized MCPN formulated into capsules equivalent in size and shape to the Eglonyl® capsules, for assessment of the performance, safety and tolerability of the optimized MCPN in the Large White Pig model. This chapter critically evaluates the pharmacokinetic behaviour of the optimized MCPN, in comparison to the current commercially available SPR formulation.

5.1. MATERIALS AND METHODS

5.1.1. Materials

UPLC grade solvents used for UPLC method development and measurements included acetonitrile (ACN) 200 (ROMIL- SpS™ Super Purity Solvent (CH_3CN), Assay >99.9%), acetone purchased from Merck (Darmstadt, Germany), dichloromethane, triethylamine and naproxen sodium, used as an internal standard were all purchased from Sigma Aldrich (Sigma Aldrich (Pty) Ltd., St. Louis, MO, USA). All other solvents and chemicals were of analytical grade and utilized without any further purification. The Acquity UPLC® BEH Shield C18 RP 1.7 µm column (2.1x100mm) was used to separate analytes. The sample vials used were 2 mL ANSI48 vials which were LCMC certified and clear, pre-slit silicone screw-top vials. Eglonyl® 50 mg capsules were a gift from a local pharmacy.

5.1.2. Methods

5.1.2.1. Habituation of pigs prior to the start of the study

A total of 6 healthy female Large White Pigs of an average weight of 35 kgs were employed in the study. Pigs were housed in a farm unit maintained under a 12-hour light and dark cycle and fed a commercial diet. The animals were initially housed in group and were later housed individually. Figure 5.1 is a digital photograph showing the farm unit, housing of the pigs and the daily habituation process. Habituation was necessary prior to formulation administration in order to reduce the challenges associated with handling the animals for administration of formulations and blood sampling. The habituation process involved visiting the animals twice daily, feeding them, brushing them and giving them treats such as raisins.



Figure 5.1. Digital images of (a) farm unit, (b) group housing, (c) individual housing and (d) daily habituation.

5.1.2.2. Surgical attachment of a catheter into the jugular vein for blood sampling

5.1.2.2.1. Surgical preparation of Large White Pigs

All Large White Pigs were anaesthetized using Midazolam 0.3mg/kg, topical procaine and ketamine HCL 11mg/kg (Figure 5.2). The anaesthesia in pigs was maintained by medical oxygen (100%) and isoflurane gas (2%) for approximately 30-60 minutes (Figure 5.2) to allow enough time for the surgical implantation of the catheter into the jugular vein.

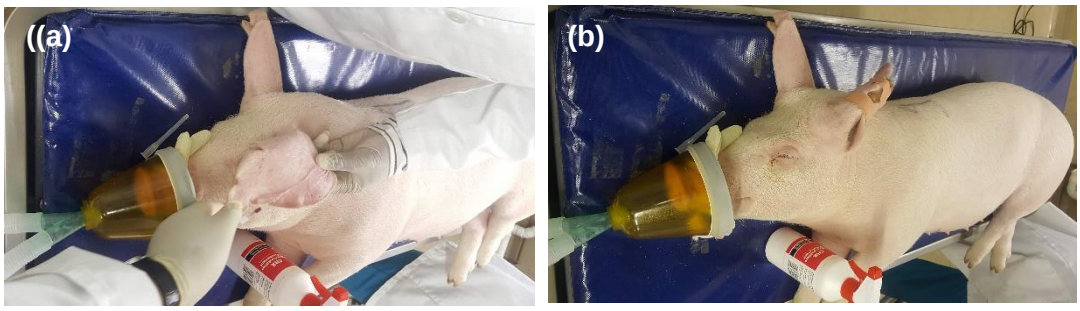


Figure 5.2. Digital images of (a) anaesthetics administration and (b) anaesthesia maintenance.

5.2.3.1.2. Surgical implantation of the catheter into the jugular vein

The surgical implantation of catheters into the pigs' jugular vein was undertaken after two weeks of habituation. The surgical insertion of the 7-gauge double lumen 40cm catheter (CS-28702, Arrow Deutchland GmbH, and Erding, Germany) into the jugular vein was carried. The jugular vein was exposed by an incision made to the lateral part of the neck (Figure 5.3). The jugular vein was isolated by blunt segmentation and a two-lumen 10 cm central venous catheter was inserted into the lumen of the vein (Figure 5.3). A technique called purse suture was used to fasten the inserted catheter into the wall of the vein. The catheter remaining after insertion was tunnelled subcutaneously to an exit point towards the cranial position, at the dorsal aspect of the scapula, which was stitched to avoid detachment (Figure 5.3). The external injection ports of the catheter were sutured to the skin to prevent excess bending. Blood samples were taken with heparinised saline (5000IU heparin in 1L of 0.9% saline). Buprenorphine 0.05mg/kg and Carpofen 4mg/kg intramuscularly were administered to manage the pain and inflammation. After surgery, all pigs were observed critically to ensure full recovery from anaesthesia. Prior to any oral dosing, all pigs were allowed complete recovery for a period of at least 10 days, during which the catheters were flushed twice a day using heparinised saline to avoid any blockage.

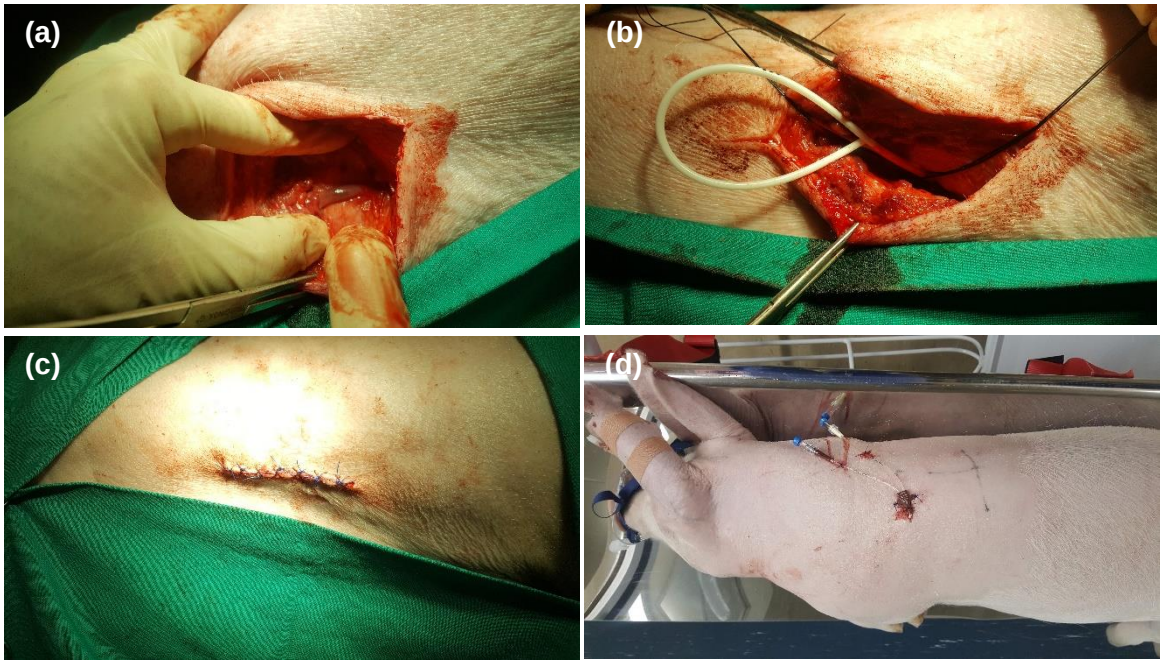


Figure 5.3. Digital pictures of (a) exposed jugular vein, (b) intra-jugular catheter insertion, (c) post-surgical suture and (d) external injection ports of the intra-jugular catheter.

5.2.3.3. *In vivo* analysis using the Large White pig model

In vivo analysis was conducted on six female Large White pigs (approx. 35kg), on which the intra-jugular catheter was implanted, as described in section 5.2.3.2 (Figure 5.4). The same animals were used in two different groups after an appropriate wash-out period. Within each group, five pigs served as the experimental component with the remaining pig serving as control. Group 1 was administered the conventional capsule Eglonyl® (conventional group) while group 2 was administered the MCPN capsule (experimental group). Each analysis was conducted for a period of 24 hours. After completion of the study, each pig was euthanized with euthapent sodium injection (20 mL) administered via the intra-jugular catheter.

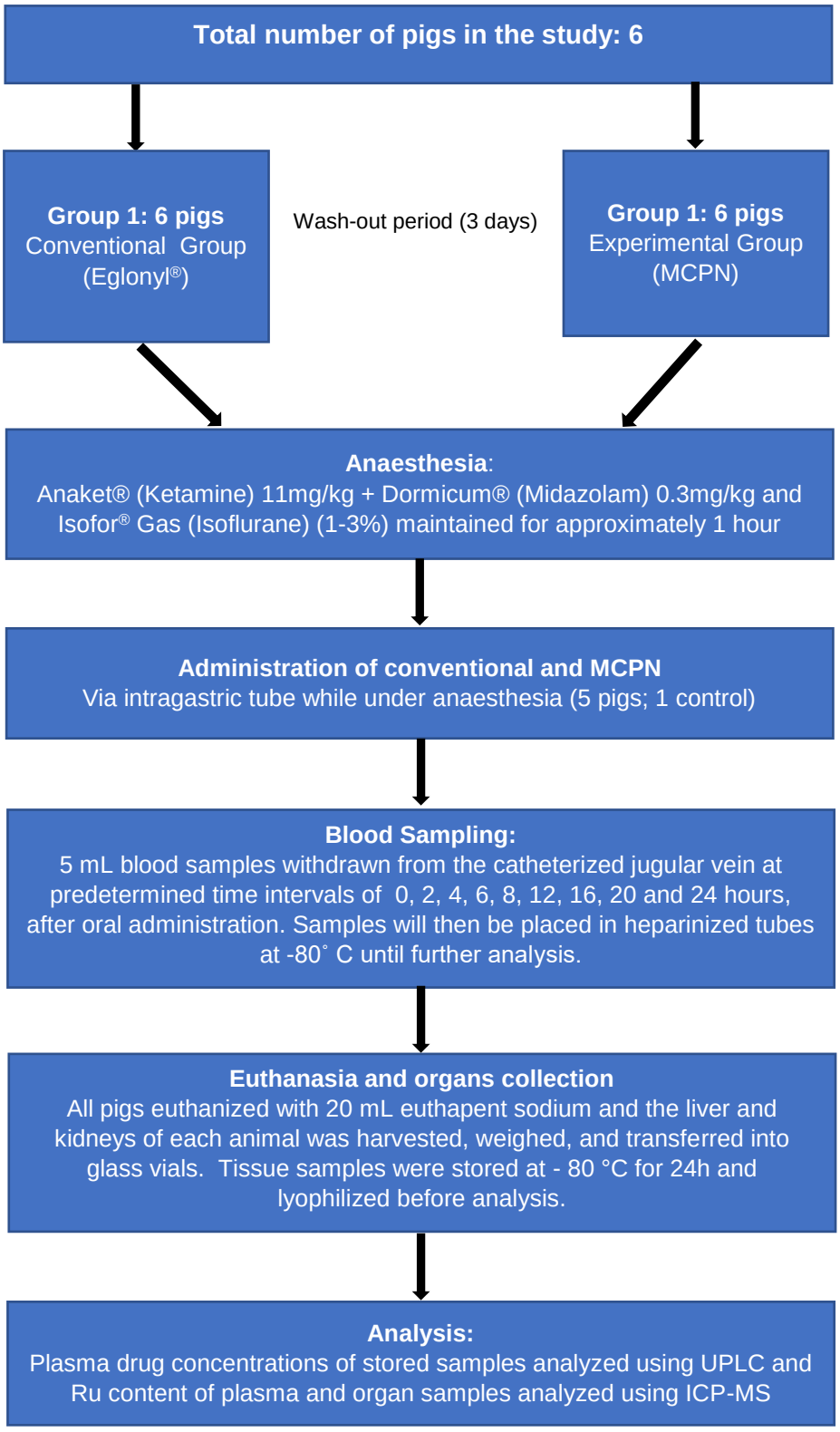


Figure 5.4. Flow diagram illustrating the allocation of pigs into the conventional and experimental groups for *in vivo* studies.

5.2.3.4. Eglonyl® and MCPN capsule administration to the large white pigs

Pigs were fasted overnight and the following day prior to dosing. Five pigs were sequentially anaesthetized by injecting Ketamine HCL (40 mg/Kg) through the implanted catheter. The anaesthesia was maintained using topical procaine and oxygen (Figure 5.5). Once the pig was stable on anaesthesia, an intragastric tube was inserted all the way into the stomach while the pig was lifted in an upright manner (Figure 5.5). One capsule was administered through the intragastric tube, followed by a small amount of water. The respective administration of Eglonyl® and MCPN capsules was separated by a 3-day wash-out period. After administration, each pig was taken back to its pen, and was observed until the animal gained full recovery and consciousness.



Figure 5.5. Digital pictures of (a) anaesthesia maintenance, (b) and (c) intragastric tube insertion for capsule administration

5.2.3.5. Intravenous (IV) sulpiride administration to the large white pig

The required dose of sulpiride (50 mg) was dissolved in 10 mL water for injection for each pig. These solutions were then aseptically inserted and sealed into vials. The IV formulation was administered to each pig using sterilized syringes through the inserted catheter over 2 minutes. No anaesthesia or any form of restraint was necessary. The results obtained from this group were used to populate bioavailability (F) values for calculation using equation (5.1):

$$F = \frac{F(oral)}{F(IV)} = \frac{AUC0-t\ (oral)}{AUC0-t(IV)} \quad (5.1)$$

Where

F(oral) = bioavailability of sulpiride oral formulation (Eglonyl® or MCPN)

F(IV) = bioavailability of IV sulpiride and

$AUC_{0\text{-}t}$ (oral) = area under the plasma profile curve (AUC) of the sulpiride oral formulation (Eglonyl® or MCPN)

$AUC_{0\text{-}t}$ (IV) = area under the plasma profile curve (AUC) of IV sulpiride

5.2.3.6. Collection and handling of animals' blood samples

Blood sampling from the catheters was straightforward, no anaesthesia nor any form of restraint was necessary. In Figure 5.6. the blood sampling process is illustrated. Blood was sampled in order to determine the concentration of sulpiride that reached the systemic circulation of the pig at different time intervals. Sterilized syringes were used for the collection of blood samples from the inserted catheters. The collected blood was placed in lithium heparin tubes (BD Vacutainers, Franklin Lakes, NJ, USA). Blood was collected before any drug administration (t_0) and after administration of the drug at 2, 4, 6, 8, 12, 16, 20 and 24-hour time points. The sampled blood was centrifuged at 3000 rpm for 15 minutes to obtain plasma, which was stored at -80°C until analysis.

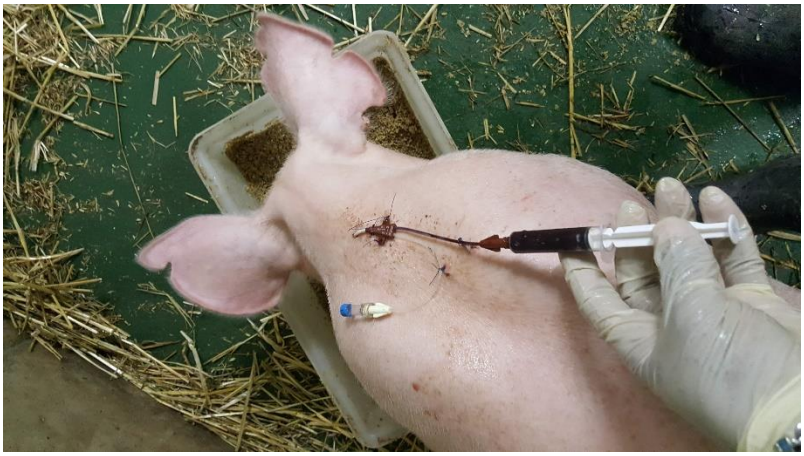


Figure 5.6. Blood sampling process though the external ports of the intra-jugular catheter.

5.2.3.7. Quantification of *in vivo* Release of the formulations administered using Ultra-Performance Liquid Chromatography Analysis

An Ultra-Performance Liquid Chromatography (UPLC) method was employed using a Waters® ACQUITY™ LC system (Waters®, Milford, MA, USA) coupled with a photodiode array detector (PDA), and Empower® Pro Software (Waters®, Milford, MA, USA). The UPLC apparatus was fitted with an Acquity UPLC® BEH Shield C18 RP column (2.1 x 100 mm), with a particle size of 1.7 µm. For analysis of sulpiride from the formulations an isocratic method with a run time of 2 minutes was used employing triethylamine (0.5%): acetonitrile: methanol [10:5:85 v/v/v] (solvent A) and acetonitrile 100% (solvent B) as the mobile phase in a 50:50 ratio. The flow rate was 0.3 mL/minute with an injection volume of 10µL. The PDA detector was set at 300nm. Naproxen sodium was used as the internal standard (IS). The table below details the mobile phases/solvents used during UPLC analysis.

Table 5.1. Mobile phases and prime solvents used for determination of sulpiride in pigs' plasma samples

Solvent/Mobile Phase	**Solvent Concentrations**
Strong wash	Acetonitrile (ACN) (90%): Double de-ionized water (10%).
Weak wash	Acetonitrile (ACN) (10%): Double de-ionized water (90%).
Solvent A line	Triethylamine (0.5%): ACN: Methanol [10:5:85]
Solvent B1 line	Acetonitrile (ACN) (100%)
Solvent B2 line	Methanol (100%)

5.2.3.7.1. Preparation of calibration standards

Standard stock solutions of sulpiride as well as the IS naproxen sodium were prepared with the UPLC mobile phase. A working standard solution of sulpiride (200 µg/mL) was used to prepare the calibration standards with concentrations ranging between 0.2-200 µg/mL via dilution of appropriate quantities of the stock solution with the mobile phase prior to injection into the UPLC.

5.2.3.7.2. Calibration sample preparation of plasma employing liquid-liquid extraction

In vivo frozen blank plasma samples were allowed to thaw at room temperature (±25°C). Aliquots of plasma (500 µL) were transferred to polypropylene tubes. A 500 µL aliquot of drug stock solution; 1N sodium hydroxide (500 µL) and ethyl acetate: methanol (5:1 %v/v) (2000 µL) was then added to the tube and vortexed for 2 minutes. The mixture was then centrifuged at 5000 rpm for 10 minutes. The supernatant was collected and placed in a polytop bottle, to which 200 µL of mobile phase was added; subsequently the mixture was dried under the

influence of nitrogen. To the dried residue 1000 µL of mobile phase was added for dilution of the drug residue. The IS standard solution (200 µg/mL, 500 µl) was added and the sample was vortexed for 1 minute prior to injection. Solutions after completion of extraction were transferred to Waters® certified UPLC vials (ANSI48) for analysis. UPLC measurements were done in triplicate.

5.2.3.7.3. Validation of liquid-liquid extraction methodologies

The precision and accuracy of the extraction procedures was determined via repetition of the extractions mentioned above on five consecutive days in order to establish the inter-day precision and accuracy, and intra-day variability. This involved numerous UPLC analysis runs of samples within a 24-hour period. A measure of accuracy was achieved by using the mean percentage error, which is centred on the variances between actual and predicted concentrations. The percentage yield of extraction was calculated by comparing the area under the curve (AUC) when extracted from plasma (AUC_{plasma}) and when extracted from standard solutions ($AUC_{standard}$ solution) at an equal concentration using equation (5.2):

$$\%Etraction\ yield = \frac{AUCplasma}{Aucstandard}\ x\ 100 \qquad (5.2)$$

5.2.3.7.4. Construction of calibration curves for the quantification of sulpiride release

Blank plasma samples were thawed at room temperature (±25°C). Aliquots (100 µL) of blank plasma were transferred to polypropylene tubes and was then spiked with standard solutions of sulpiride and metoclopramide (IS) at varying concentrations. The mixture was then vortexed for 2 minutes and the extraction procedure was performed as previously described. The drug/IS AUC ratios were plotted against the corresponding drug concentration (µg/mL) and the statistical R^2 value was derived for the obtained curve.

5.2.3.8. Pharmacokinetic modelling using non-compartmental analysis

Based on the *in vitro* and *in vivo* release dynamics of sulpiride from the MCPN, non-compartmental analysis was performed utilizing pharmacokinetic data analysis and the use of PKSolver, a menu-driven add-in program for Microsoft Excel.

Non-compartmental analysis was applied to quantitatively evaluate and predict *in vivo* outcome of sulpiride from the MCPN via modelling of the concentration-time data by means of an appropriate pharmacokinetic non-compartmental model.

5.2.3.9. Establishment of *in vitro-in vivo* correlation

The establishment of an appropriate *in vitro* to *in vivo* correlation is crucial for the development of a novel drug delivery system. The *in vitro-in vivo* correlation can be useful for the improvement or adjustments of a developed system without the need to conduct thorough *in vivo* studies at each developmental stage (Emami, 2006). R software (V3.5.2) RIVIVC package (Copyright 2018, the R foundation for statistical computing), was employed for establishment of a Level A IVIVC. A Level A IVIVC is a correlation between the *in vitro* drug dissolution profile and *in vivo* drug absorption profile. Input data for this correlation therefore included *in vitro* MCPN, as well as the relevant pharmacokinetic data. For the evaluation of an IVIVC model, development and validation is required. The development of level A IVIVC model therefore follows a two-stage process:

1. Deconvolution: the observed fraction of the drug absorbed is estimated based on the Wagner-Nelson method. The IVIVC model is thereafter developed using the observed fraction of the drug absorbed and that of the drug dissolved. Based on the IVIVC model used, the predicted fraction of the drug absorbed is thereafter calculated from the observed fraction of the drug dissolved.

2. Convolution: the predicted fraction of the drug absorbed is then convolved to the predicted concentrations instituting the convolution method. The predictability of a level A correlation thereafter focuses on estimating the percent prediction error (%PE) between the observed and predicted concentration profiles (Emami, 2006).

5.2.3.10. Inductively coupled plasma-mass spectrometry (ICP-MS) for Ru element quantification in plasma and organs

Blood was collected using heparin containing tubes at 2, 8, 12 and 24 timepoints after the first dosing. The blood samples were centrifuged at 2800 rpm for 15 min, and the supernatant plasma was transferred into microcentrifuge tubes and maintained at −80 °C until analysis.

The pigs were terminated at the end of the study (24 h after MCPN administration) using 20 mL euthapent sodium and the liver and kidneys of each animal was harvested, weighed, and transferred into glass vials. The tissue samples were initially stored at - 80 °C and then lyophilized before analysis.

Prior analysis, appropriate mass of each sample was weighed in pre-cleaned microwave vessels. Suprapure nitric acid (10 mL) was added to each sample, which was then heated up to 180°C for 10 minutes and held at 180°C for another 10 minutes in a Mars 6^{TM} digestion system (CEM corporation, USA). Analysis was performed on a PerkinElmer 300X ICP-MS

(Perkin-Elmer Inc. MA, USA). The instrument was calibrated with calibration standards ranging from 0 to 10 µg/L Ru using Rh as an internal standard. The final samples were diluted and Rh added to each before analysis. The wavelength of emission was set at 101 for Ru and 103 for Rh. The limit of quantification (LOQ) was 0.05 µg/kg.

5.2. RESULTS AND DISCUSSION

5.2.1. Behavioural evaluation of pigs post-surgery

Post-surgical implantation of the catheter into the jugular vein, the pigs were slightly lethargic due to the effects of the anesthesia. Once the anesthesia wore off the animals displayed their usual levels of activity and appetite. Blood sampling proved to be straightforward and time efficient, thus proving the feasibility of using jugular catheters for this purpose. Administration of the MCPN to the animals showed no adverse effects and there was a 100% survival rate of the pigs.

5.2.2. Validation of the liquid-liquid extraction procedure

For sulpiride extraction, the mean variations of the intra-day and inter-day precision validation studies were determined to be 0.16% and 0.20%. The mean extraction yield of sulpiride from plasma was determined to be 95.2% (SD ± 2.15). The liquid-liquid extraction procedure used proved its efficacy to achieve a high degree of recovery of sulpiride.

5.2.3. *In vivo* release of sulpiride from the MCPN

The UPLC chromatogram of sulpiride and its IS are shown in Figure 5.7. The UPLC chromatogram displays a retention time of 8.13 for sulpiride. In Figure 5.8, the UPLC calibration curve for plasma sulpiride at 300 nm is shown ($y = 0.094x + 0.012$, $r^2 = 0.99$).

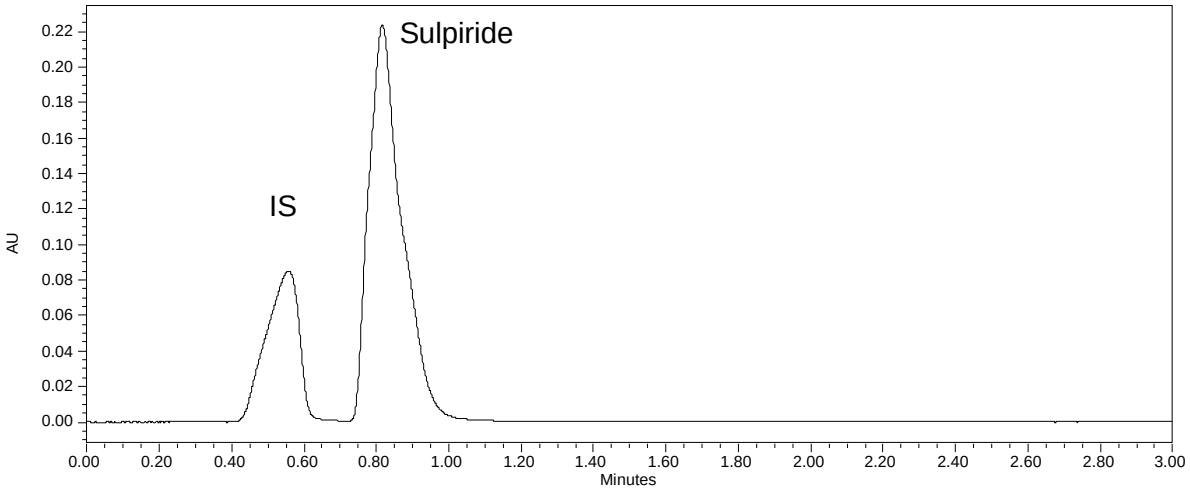


Figure 5.7. Chromatogram of sulpiride in plasma with its internal standard

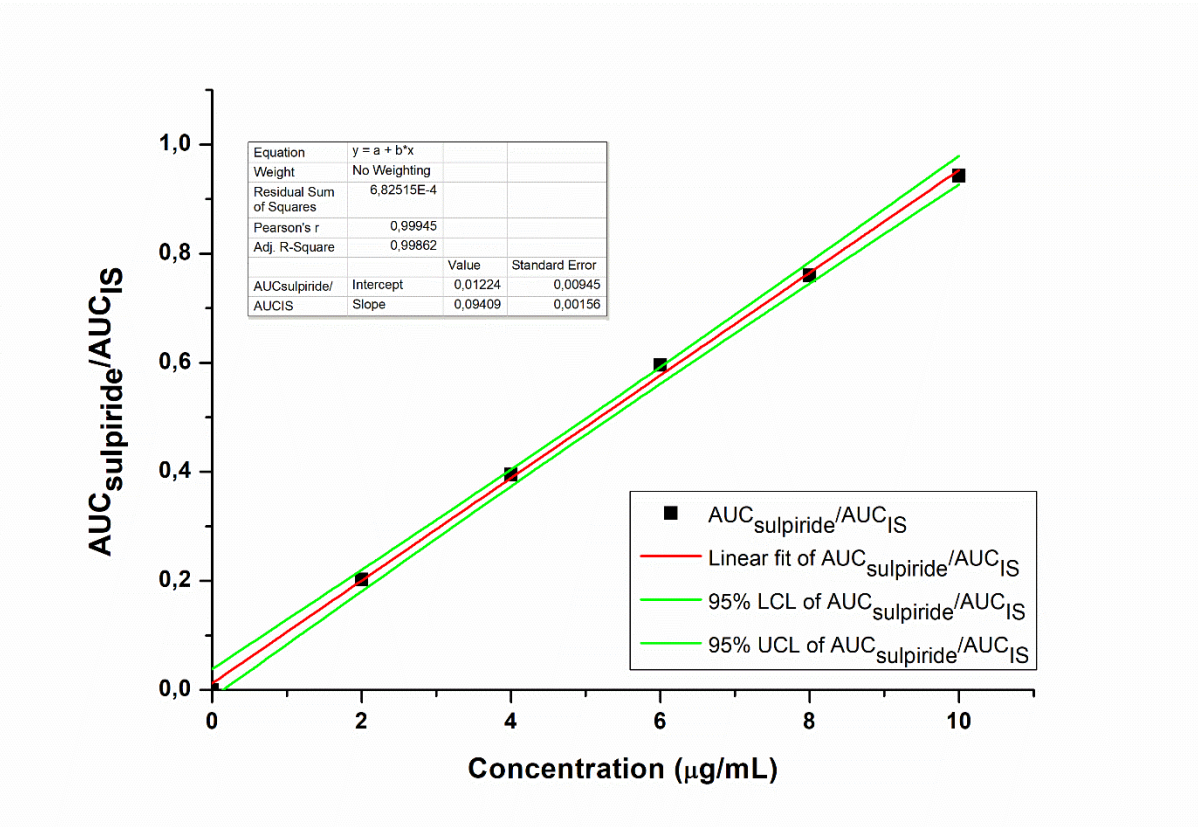


Figure 5.8. Calibration curve of sulpiride at 300 nm

The plasma concentration profiles of sulpiride from Eglonyl® (conventional) and MCPN capsules are depicted in Figure 5.9. The plasma concentration profile of sulpiride displays noticeable differences when administered as the MCPN capsule as compared to the conventional capsule. Conventional capsules achieved a lower maximum plasma

concentration (C_{max} = 0.8719 µg/mL) of sulpiride at an earlier time (t_{max} = 6 hours) as compared to the MCPN, where a C_{max} of 0.9894 µg/mL was achieved at a t_{max} of 12 hours. The MCPN achieved more steady state plasma concentrations throughout the duration of the study, as displayed in Figure 5.9. This may result in the decrease of adverse effects experienced due to unstable drug concentrations, ultimately positively affecting patient compliance. Conventional capsules may achieve consistent plasma concentrations through multiple daily administrations. The MCPN shows potential efficacy in a single dose, thus making the treatment regimen simpler.

The conventional capsule (Eglonyl®) exhibited a rapid rise in SPR plasma concentration, reaching a peak at 6 hours, which was followed by a drastic reduction in the drug's plasma concentration for the subsequent 8 hours (Figure 5.9). This may be the result of the sensitivity of sulpiride to gastric pH and the lack of drug-release control mechanisms within the conventional formulation.

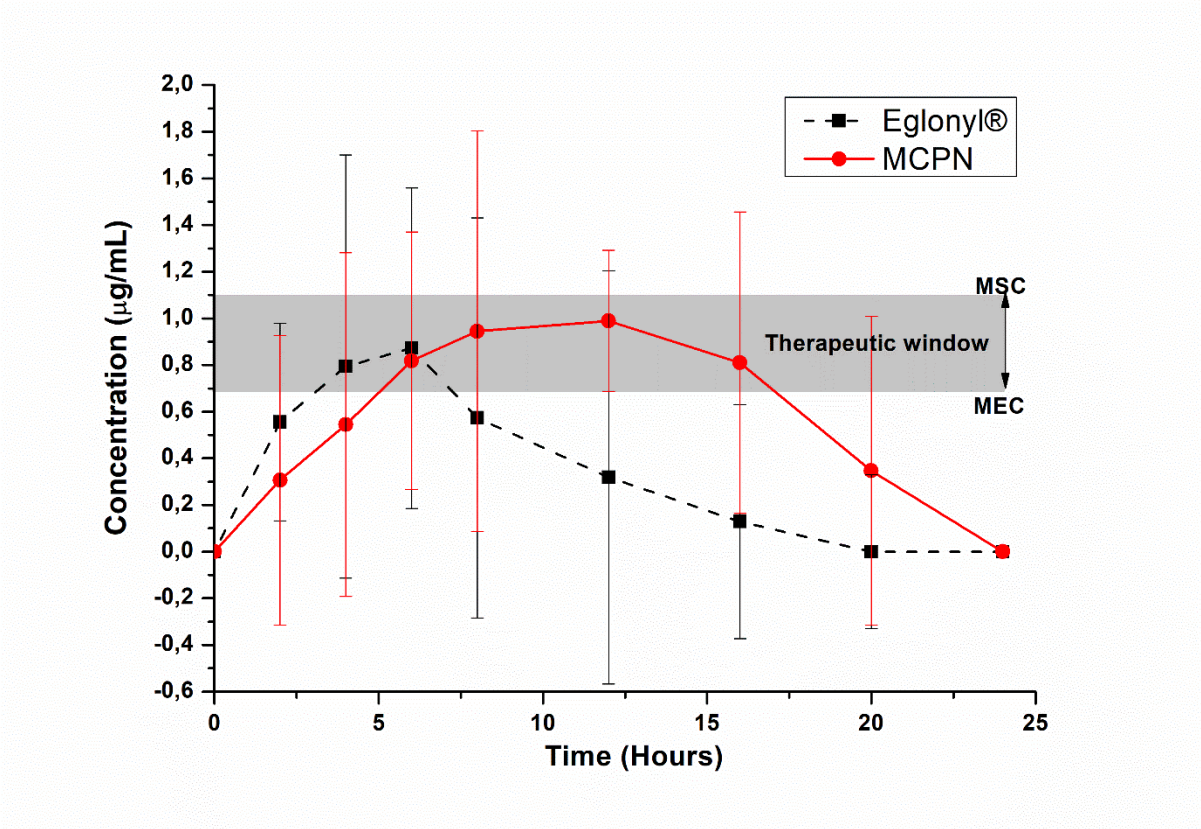


Figure 5.9. Plasma concentration profiles of sulpiride from Eglonyl® (conventional) and MCPN capsules (MEC=Minimum Effective Concentration; MSC=Maximum Safe Concentration).

The MCPN formulation exhibited a lower drug release (0.3067 µg/mL) compared to the conventional capsule (0.5556 µg/mL) 2 hours post-dosing (Figure 5.9). This may be due to the gastric pH protection provided by the MCPN. By 6 hours post-dosing, the MCPN and the conventional capsule showed comparable plasma concentrations of the drug (0.8180 µg/mL

and 0.8719 µg/mL respectively). This may be attributed to the increase in pH in the intestine that favorizes drug release from the MCPN. In fact, by the end of the time spent in the intestine (2-6 hours), the MCPN had released more than double (0.8180 µg/mL) the amount of drug released at the exit of the gastric environment (0.3067 µg/mL).

From 6 hours post-dosing, the conventional and MCPN formulations entered the systemic circulation. While a decrease in plasma concentration of the drug was observed for the conventional formulation, the MCPN exhibited a consistent ascension in SPR plasma concentration up to 12 hours post-dosing, followed by a consistent decrease in the subsequent 12 hours (Figure 5.9). The increase in SPR plasma concentration after the MCPN entered the systemic circulation may be due to the increased intestinal permeability of the formulation, as discussed in Chapter 4 section 4.3.6. This allows for more SPR going from the intestine into the blood, thus the increased plasma concentrations. On the other hand, the conventional capsules have low intestinal membrane permeability, thus the lower SPR plasma concentrations 6 hours post-dosing.

5.2.4. Interpretation of the extravascular non-compartmental pharmacokinetic model analysis

The extravascular pharmacokinetic analysis results of the non-compartmental analysis of sulpiride from Eglonyl® and the MCPN are displayed in Table 5.2. Pharmacokinetic parameters of sulpiride from the MCPN show prolonged $t_{1/2}$ and MRT, increased t_{max} and higher C_{max} compared to the conventional capsule. Improved therapeutic levels of sulpiride in the Large White Pig were reached and maintained up to 24 hours by the MCPN.

For bioavailability calculations, the AUC0-t. values (7,69 µg/ml*h, 14,06 µg/ml*h and 25,43 µg/ml*h for Eglonyl®, MCPN and IV sulpiride respectively) were obtained from the extravascular pharmacokinetic analysis results of the non-compartmental analysis of sulpiride (Table 5.2). The bioavailability of Eglonyl® was 30.26%, which is in accordance with the literature that reports SPR bioavailability of approximately 30% (Chitneni et al., 2011; Huang et al., 2001). The bioavailability of MCPN was 55.30%. The improved systemic exposure of sulpiride, resulting in the higher bioavailability of the MCPN compared to the conventional capsule was caused by three factors: 1) the pH-responsive drug release from the MCPN which allows protection of sulpiride in the gastric pH; 2) the presence of the metal carrier in the MCPN and 3) the reduced average particle size of the MCPN which both allow increased sulpiride permeation through the intestinal membrane to the systemic circulation. The MCPN allows minimal amounts of the drug to be lost in the gastric acidic environment, thus an increased amount of drug is available at the intestinal membrane. At the intestinal membrane, the

presence of the metal carrier provides improved lipid solubility to the drug and the nano size of the MCPN further allows enhanced drug permeation through the membrane; therefore, a higher amount of sulpiride permeates through the intestinal membrane to the systemic circulation. An increased amount of sulpiride is consequently available in the systemic circulation. This sequence of events results in enhancement of sulpiride bioavailability by MCPN.

Table 5.2. Extravascular pharmacokinetic analysis results of the non-compartmental analysis of sulpiride from Eglonyl® and the MCPN

Parameter	Unit	Value
	Eglonyl® extravascular non-compartmental model	
Lambda_z	1/h	0,186242143
$t_{1/2}$	h	3,721752601
T_{max}	h	6
C_{max}	µg/ml	0,871954463
T_{lag}	h	0
C_{last}_obs/Cmax		0,147501229
AUC $_{0-t}$	µg/ml*h	7,694521301
AUC $_{0-inf}$_obs	µg/ml*h	8,385097307
AUC $_{0-t/0-inf}$_obs		0,917642458
AUMC $_{0-inf}$_obs	µg/ml*h^2	66,96556539
MRT $_{0-inf}$_obs	h	7,986259781
Vz/F_obs	(mg)/(µg/ml)	32,01724335
Cl/F_obs	(mg)/(µg/ml)/h	5,962960019
	MCPN extravascular non-compartmental model	
Lambda_z	1/h	0,130932095
$t_{1/2}$	h	5,293944015
T_{max}	h	12
C_{max}	µg/ml	0,989458686
T_{lag}	h	0
C_{last}_obs/Cmax		0,350828858
AUC $_{0-t}$	µg/ml*h	14,06351908
AUC $_{0-inf}$_obs	µg/ml*h	16,71474574
AUC $_{0-t/0-inf}$_obs		0,841383967
AUMC $_{0-inf}$_obs	µg/ml*h^2	224,5509361
MRT $_{0-inf}$_obs	h	13,43430164
Vz/F_obs	(mg)/(µg/ml)	22,84673335
Cl/F_obs	(mg)/(µg/ml)/h	2,991370661
	IV SPR extravascular non-compartmental model	
Lambda_z	1/h	0,061903898
$t_{1/2}$	h	11,19714914
T_{max}	h	1
C_{max}	µg/ml	1,925914339
C_0	µg/ml	2,012967638
C_{last}_obs/Cmax		0,259763979
AUC $_{0-t}$	µg/ml*h	25,42972748
AUC $_{0-inf}$_obs	µg/ml*h	33,51133763
AUC $_{0-t/0-inf}$_obs		0,758839523
AUMC $_{0-inf}$_obs	µg/ml*h^2	499,9340313
MRT $_{0-inf}$_obs	h	14,918355
Vz_obs	(mg)/(µg/ml)	24,10239738
Cl_obs	(mg)/(µg/ml)/h	1,492032355

Lambda z: 1st order rate constant of the terminal (log-linear) portion of the curve terminal elimination rate constant.

$t_{1/2}$: Terminal phase half-life. The time it takes for the concentration levels to fall to 50% of their value.

T_{max}: Time at which the maximum concentration (Cmax) is reached.

C_{max}: Maximum reached concentration occurring at Tmax.

C_{last}: The last quantifiable concentration following dosing.

AUC_{0-t}: Area Under the Curve (AUC) from the dosing time to the last measurable concentration.

AUC_{0-inf} obs: AUC from dosing time extrapolated to infinity based on the last observed concentration.

$AUMC_{0-inf}$ obs: AUMC extrapolated to infinity based on the last observed concentration.

MRT_{0-inf} obs: Mean residence time (average amount of time the drug remains in a compartment or system) extrapolated to infinity.

5.2.5. *In vitro-in vivo* correlation establishment

A Level A IVIVC was established for the evaluation of sulpiride release. This approach uses the data provided by both the *in vitro* dissolution and *in vivo* absorption curves of the drug and relies directly on each of the time points analysed (Amann et al., 2010; Emami, 2006). The amount of sulpiride absorbed following administration of MCPN was therefore calculated by the Wagner Nelson method using the linear trapezoidal rule. For the construction of a Level A IVIVC, the percentage of drug absorbed up to time *t* was plotted versus the amount of drug released *in vitro* (Figure 5.10).

The pharmacokinetic data obtained from this analysis complies with the requirements of deconvolution via convolution, as sulpiride release from the MCPN was determined via a non-compartmental pharmacokinetic model.

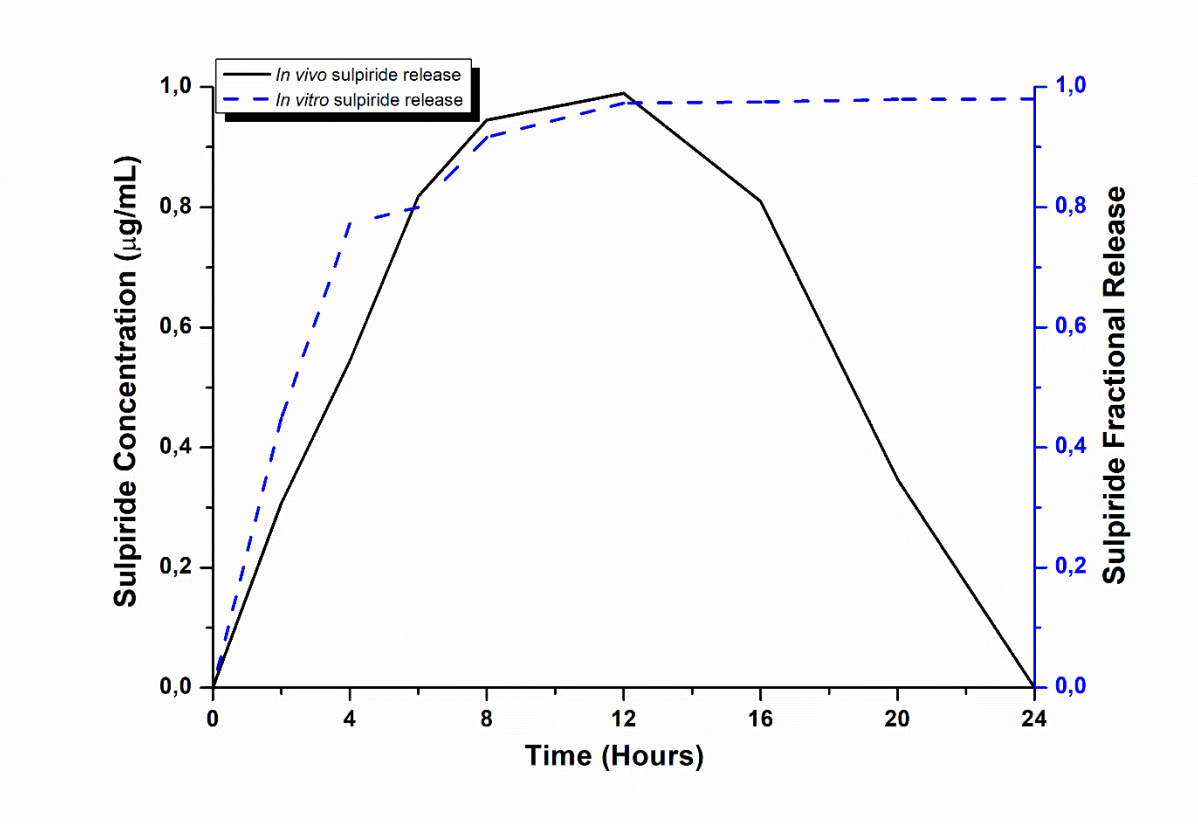


Figure 5.10. *In vitro* and *in vivo* drug release profiles of sulpiride from the MCPN obtained by deconvolution analysis.

The level A IVIVC analysis for sulpiride yielded a levy plot with an R^2 values of 0.7908 (Figure 5.11). *In vitro* data was therefore was predictive of *in vivo* data with 79% accuracy for sulpiride. Although the plots determined were not precisely superimposable, based on qualitative parameters of the fit, a Level A correlation was established. The observed results showed a slower *in vivo* absorption compared to the *in vitro* dissolution up to 6 hours; this may be attributed to the gastrointestinal transit time between simulated gastric and intestinal conditions employed during *in vitro* studies which did not directly translate to release *in vivo.* From 6 hours after MCPN administration, the *in vivo* absorption of sulpiride becomes quicker compared to the *in vitro* dissolution, this may be attributed to the improved intestinal permeability of the MCPN as discussed in Chapter 4, Section 4.3.6.

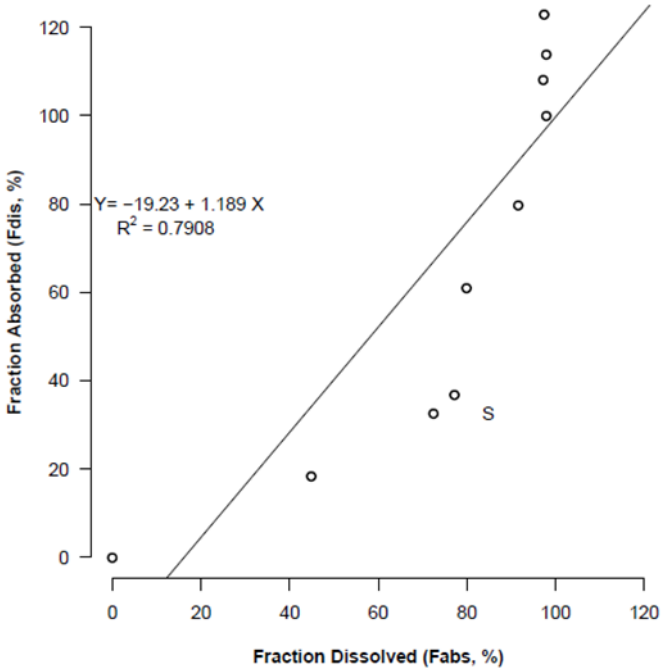


Figure 5.11. Levy plot depicting the relationship between the percentage of sulpiride released *in vitro* and the percentage of sulpiride released *in vivo*.

The prediction errors (PE) for C_{max} and $AUC_{0\text{-}inf}$ for this Level A IVIVC analysis were calculated to be 5.36% and 13.97% respectively. The second value is higher than the specified 10% PE for a good Level A correlation, but still within the 15% requirement for an individual formulation.

5.2.6. Ru element quantification in plasma, liver and kidneys of each pig

The amount of Ru was quantified in the plasma, liver and kidney of each pig to determine the fate of the metal after MCPN administration and any toxicity that may be associated with it. The pigs' plasma levels of ruthenium at different timepoints are shown in Table 5.3. Pig 1 was the control animal to which no MCPN was administered, which explains the absence of Ru in its plasma. Ru plasma concentrations of pigs 2-5 were comparable. Ru was mostly present in detectable concentrations (1.6 – 13.1 µg/kg) from 8 hours after MCPN administration and declined overtime. This is in accordance with previous studies in mice that have demonstrated a rapid decay of Ru plasma levels (Bytzek et al., 2011; Cocchietto and Sava, 2000). These results show that a low amount of Ru can be found in plasma after MCPN administration, however, the metal does not accumulate in the blood. There is therefore a low risk of any hematological toxicity of Ru to the host associated to MCPN formulation.

Table 5.3. Total Ru concentrations in pigs plasma (µg/kg) at different time points post MCPN dosing

	2 hours	4 hours	8 hours	12 hours	24 hours
Pig 1	0.0	0.0	0.0	0.0	0.0
Pig 2	0.0	0.0	1.9	2.9	0.0
Pig 3	0.0	0.0	13.1	2.8	2.0
Pig 4	0.0	0.0	0.0	2.4	0.0
Pig 5	0.0	1.8	1.8	2.8	0.0
Pig 6	0.0	0.0	1.8	1.8	1.6

The amount of ruthenium found in the kidneys and livers of the pigs 24 hours post MCPN oral administration are shown in Table 5.4. Pig 1 was the control animal to which the MCPN formulation was not administered, thus no Ru was detected in liver nor kidneys. Ru was detected only in the liver of pig 3 (9.1 µg/kg) and in the kidneys of 4 of the 5 MCPN-treated pigs (7.1 -16.8 µg/kg). The Ru tissue concentrations obtained are relatively low compared to the ones reported in mice after a 1-day IV treatment with NAMI-A, $1.5x10^4$ µg/kg for liver and $2.5x10^4$µg/kg for kidneys respectively. Although the Ru dose in NAMI-A is higher than in MCPN and the dosage form is different, this comparison is made to highlight the fact that the Ru concentrations observed after the 1-day treatment of mice with NAMI-A were reported to be non-toxic to the host (Cocchietto and Sava, 2000; Vadori et al., 2013). The Ru levels reported here are even lower and thus also non-toxic. Therefore, MCPN formulation did not exhibit any Ru associated renal nor liver toxicity to the pigs.

Table 5.4. Total Ru concentrations in pigs' livers and kidneys (µg/kg) 24 hours post MCPN dosing

	Liver	Kidneys
Pig 1	0.0	0.0
Pig 2	0.0	0.0
Pig 3	9.1	16.8
Pig 4	0.0	11.7
Pig 5	0.0	7.4
Pig 6	0.0	7.1

5.3. CONCLUDING REMARKS

The effectiveness of the MCPN was evaluated via the *in vivo* analysis in a Large White pig model. The MCPN demonstrated its superiority compared to the marketed formulation by an improved sulpiride release profile *in vivo*, achieving a higher C_{max} (0,9895 µg/mL) at an increased t_{max} (12 h), thus an enhanced bioavailability (55.30%). No adverse effects were observed in the animals after administration of the MCPN, which indicates the safety and tolerability of the developed formulation. The MCPN showed the ability to achieve controlled release of sulpiride *in vivo* and to improve its pharmacokinetic parameters. Ultimately, the MCPN could allow a reduction in the frequency of sulpiride oral administration, thereby improving patient compliance.

CHAPTER 6
CONCLUSIONS AND RECOMMENDATIONS

6.1. CONCLUSIONS

The design, development and evaluation of a novel drug delivery system by combining multiple scientific techniques has been revealed through this study with the aim of improving clinical outcomes and patient compliance in the treatment of schizophrenia. Poor patient compliance in the treatment of schizophrenia can be mostly attributed to the sub-therapeutic performance of the drugs administered and the complex pharmacotherapy offered to the patient.

The Metal Complex Polymer Nanocomposite formulated in this study was designed, developed and thoroughly evaluated with the aim of overcoming the issues of complex treatment regimens and poor pharmacokinetics while maintaining oral drug delivery in the treatment of schizophrenia. The MCPN comprised a ternary metal complex of SPR, [Ru(*p* -cymene)((R)-(+)-2-amino-3-phenyl-1-propanol)(SPR)]PF6, incorporated into polymeric (Eudragit® RS 100 and PVA) nanoparticles. The designed metal complex carrier was used to enhance the intestinal permeability and the aqueous solubility of SPR, however it still displayed a burst release in the gastric environment. Eudragit® RS 100 and PVA were then added into the formulation to provide pH-controlled SPR release and to achieve sustained SPR release. The MCPN was formulated into nano size to further improve the intestinal permeability of SPR and to target drug absorption in the small intestine region.

The MCPN oral formulation was successfully synthesized and characterized and showed its effectiveness via subsequent *ex vivo, in vitro*, and *in vivo* analyses. *Ex vivo* studies performed to determine the intestinal permeability of SPR through porcine intestine revealed improved intestinal permeability from the MCPN compared to the conventional formulation. *In vitro* release studies performed demonstrated pH-controlled, sustained drug release of SPR from the MCPN. Furthermore, *in vitro* toxicity of the optimized MCPN formulation were carried out and no noticeable toxic effects on the intestinal epithelium tissue were observed. Finally, *in vivo* studies were undertaken on the optimized MCPN formulation. The optimized MCPN capsule was orally administered to pigs and drug release profiles were obtained according to the concentration of SPR in plasma overtime. *In vivo* results showed a concrete difference in SPR plasma profiles between conventional capsule and the optimized MCPN capsule. The optimized MCPN provided sustained release of sulpiride *in vivo*. Pharmacokinetic modelling of *in vivo* results determined that sulpiride was best described by a non-compartmental model with IVIVC displaying a good relationship. A definite improvement in SPR pharmacokinetic

parameters was noticed in the optimized MCPN. The metal was shown to cause no noticeable toxicity to the host after drug release.

The aim of this study was the development through to preclinical analyses of a Metal Complex Polymer Nanocomposite for the oral administration of sulpiride. This research study enabled the development, characterization and evaluation of a novel MCPN oral delivery system, with the prospect of this system clinically enhancing therapeutic outcomes associated with the pharmacotherapy of schizophrenia.

6.2. RECOMMENDATIONS

Although the initial proof of principle process requires judicious design, rigorous synthesis and robust nanoparticle formulation, the overall integration of metal complexation and nanotechnology offers great potential towards the development of metal based bioactives, diagnostic and even theragnostic delivery systems. Despite the performance of the MCPN up to *in vivo* studies, several aspects will need to be considered for any possible large-scale production advancement. Firstly, the choice of the drug(s) to be liganded to the metal centre is of the outmost importance as it must be able to act as a ligand to the metal otherwise metal coordination will not take place. Secondly, an inert atmosphere of nitrogen is required for the metal complex synthesis and storage in order to maintain the stability of the product. Thirdly, the emulsion solvent evaporation method for nanoparticles productions is time consuming, it would be beneficial to explore faster methods of nanoparticle production that are compatible with the sample. Fourthly, to formulate a capsule containing 50 mg SPR, more MCPN is needed, which results in the use of more than one capsule equivalent in size and shape to the Eglonyl® capsule; thus, a bigger capsule should be used when formulating the MCPN. Finally, a cost-benefit analysis of the MCPN should be carried out to evaluate any additional cost of treatment to the patients.

The results up to the preclinical studies show the potential of MCPN as a candidate for scaling up. Sulpiride was used as a model drug due to its pharmacokinetic properties and the limitations associated to it but other bioactives can be incorporated into the MCPN on condition that they can act as a ligand to the metal centre, they display similar pharmacokinetics to the model drug and improved bioavailability and sustained release are required. Although the MCPN delivery system was developed for use in the treatment of schizophrenia, it is not exclusive to this disorder and can be applicable to any hydrophobic and poorly permeable drug that needs to be administered orally. Such an application of the MCPN drug delivery system is multiple drug delivery (delivery of more than one bioactive), since the metal centre has the ability to accommodate multiple ligands. This application can be useful in disease

state that require multiple drug therapy as the medications could be combined into one formulation.

The integration of classical chemistry to drug delivery is a challenging but possible and effective approach that helps to the advancement in chemically modified drug delivery systems. The research generated within this thesis will provide critical concepts and processes that can be adjusted to fit diverse pharmaceutical research undertakings.

REFERENCES

Adibkia, K., Javadzadeh, Y., Dastmalchi, S., Mohammadi, G., Niri, F.K., Alaei-Beirami, M., 2011. Naproxen-Eudragit RS100 nanoparticles: preparation and physicochemical characterization. Colloids Surf. B Biointerfaces 83, 155–159.

Agotegaray, M., Gumilar, F., Boeris, M., nica, Toso, R., Minetti, A., 2014. Enhanced Analgesic Properties and Reduced Ulcerogenic Effect of a Mononuclear Copper(II) Complex with Fenoprofen in Comparison to the Parent Drug: Promising Insights in the Treatment of Chronic Inflammatory Diseases. BioMed Res. Int. 2014, e505987.

Al-Hilal, T.A., Alam, F., Byun, Y., 2013. Oral drug delivery systems using chemical conjugates or physical complexes. Adv. Drug Deliv. Rev., Nanoparticle- and biomaterials-mediated oral delivery for drug, gene and immunotherapy 65, 845–864.

Amann, L.C., Gandal, M.J., Lin, R., Liang, Y., Siegel, S.J., 2010. In vitro-in vivo correlations of scalable PLGA-risperidone implants for the treatment of schizophrenia. Pharm. Res. 27, 1730–1737.

Bai, L., Song, F., Wang, Xiao-hui, Cao, J., Han, X., Wang, Xiu-li, Wang, Y., 2015. Ligand–metal-drug coordination based micelles for efficient intracellular doxorubicin delivery. RSC Adv. 5, 47629–47639.

Baluom, M., Friedman, M., Rubinstein, A., 2001. Improved intestinal absorption of sulpiride in rats with synchronized oral delivery systems. J. Controlled Release 70, 139–147.

Bamrungsap, S., Zhao, Z., Chen, T., Wang, L., Li, C., Fu, T., Tan, W., 2012. Nanotechnology in therapeutics: a focus on nanoparticles as a drug delivery system. Nanomed. 7, 1253–1271.

Barry, N.P.E., Sadler, P.J., 2013. Exploration of the medical periodic table: towards new targets. Chem. Commun. 49, 5106–5131.

Bergamo, A., Sava, G., 2011. Ruthenium anticancer compounds: myths and realities of the emerging metal-based drugs. Dalton Trans. Camb. Engl. 2003 40, 7817–7823.

Breda, S.A., Jimenez-Kairuz, A.F., Manzo, R.H., Olivera, M.E., 2009. Solubility behavior and biopharmaceutical classification of novel high-solubility ciprofloxacin and norfloxacin pharmaceutical derivatives. Int. J. Pharm. 371, 106–113.

Bustamante, F.L.S., Metello, J.M., de Castro, F.A.V., Pinheiro, C.B., Pereira, M.D., Lanznaster, M., 2013. Lawsone Dimerization in Cobalt(III) Complexes toward the Design of New Prototypes of Bioreductive Prodrugs. Inorg. Chem. 52, 1167–1169.

Bytzek, A.K., Boeck, K., Hermann, G., Hann, S., Keppler, B.K., Hartinger, C.G., Koellensperger, G., 2011. LC- and CZE-ICP-MS approaches for the in vivo analysis of the anticancer drug candidate sodium trans-[tetrachloridobis(1H-

indazole)ruthenate(III)] (KP1339) in mouse plasma. Met. Integr. Biometal Sci. 3, 1049–1055.

Chan, H., Ghrayche, J.B., Wei, J., Renfrew, A.K., 2017. Photolabile ruthenium(II)–purine complexes: phototoxicity, DNA binding, and light-triggered drug release. Eur. J. Inorg. Chem. 2017, 1679–1686.

Chang, S.W., Lewis, A.R., Prosser, K.E., Thompson, J.R., Gladkikh, M., Bally, M.B., Warren, J.J., Walsby, C.J., 2016. CF3 Derivatives of the anticancer ru(III) complexes KP1019, NKP-1339, and their imidazole and pyridine analogues show enhanced lipophilicity, albumin interactions, and cytotoxicity. Inorg. Chem. 55, 4850–4863.

Chen, L., Lu, X., Liang, X., Hong, D., Guan, Z., Guan, Y., Zhu, W., 2016. Mechanistic studies of the transport of peimine in the Caco-2 cell model. Acta Pharm. Sin. B 6, 125–131.

Chen, W.H., Yu, X., Cecconello, A., Sohn, Y.S., Nechushtai, R., Willner, I., 2017. Stimuli-responsive nucleic acid-functionalized metal–organic framework nanoparticles using pH- and metal-ion-dependent DNAzymes as locks. Chem. Sci. 8, 5769–5780.

Chitneni, M., Peh, K.K., Darwis, D., Abdulkarim, M., Abdullah, G.Z., Qureshi, M.J., 2011. Intestinal permeability studies of sulpiride incorporated into self-microemulsifying drug delivery system (SMEDDS). Pak. J. Pharm. Sci. 24, 113–121.

Cocchietto, M., Sava, G., 2000. Blood concentration and toxicity of the antimetastasis agent NAMI-A following repeated intravenous treatment in mice. Pharmacol. Toxicol. 87, 193–197.

Da Conceição, R.R., Fernandes, G.W., Fonseca, T.L., Bocco, B.M.L.C., Bianco, A.C., 2018. Metal coordinated poly-zinc-liothyronine provides stable circulating triiodothyronine levels in hypothyroid rats. Thyroid 28, 1425–1433.

Dabrowiak, J.C. Metals in Medicine (2nd Edition). John Wiley & Sons Ltd 2017, 321 pp.

Danaei, M., Dehghankhold, M., Ataei, S., Hasanzadeh Davarani, F., Javanmard, R., Dokhani, A., Khorasani, S., Mozafari, M.R., 2018. Impact of particle size and polydispersity index on the clinical applications of lipidic nanocarrier systems. Pharmaceutics 10, pii: E57.

Davies, D.J., Ward, R.J., Heylings, J.R., 2004. Multi-species assessment of electrical resistance as a skin integrity marker for in vitro percutaneous absorption studies. Toxicol. In Vitro 18, 351–358.

De Jong, W.H., Borm, P.J., 2008. Drug delivery and nanoparticles: Applications and hazards. Int. J. Nanomedicine 3, 133–149.

Debotton, N., Dahan, A., 2017. Applications of polymers as pharmaceutical excipients in solid oral dosage forms. Med. Res. Rev. 37, 52–97.

Dening, T.J., Rao, S., Thomas, N., Prestidge, C.A., 2016. Oral nanomedicine approaches for the treatment of psychiatric illnesses. J. Controlled Release 223, 137–156.

Dimitrijevic, I., Pantic, I., 2014. Application of nanoparticles in psychophysiology and psychiatry research. Rev. Adv. Mater. Sci. 38, 1–6.

Duan, L.N., Dang, Q.Q., Han, C.Y., Zhang, X.M., 2015. An interpenetrated bioactive nonlinear optical MOF containing a coordinated quinolone-like drug and Zn(II) for pH-responsive release. Dalton Trans. 44, 1800–1804.

Ejima, H., Richardson, J.J., Caruso, F., 2017. Metal-phenolic networks as a versatile platform to engineer nanomaterials and biointerfaces. Nano Today 12, 136–148.

Emami, J., 2006. In vitro - in vivo correlation: from theory to applications. J. Pharm. Pharm. Sci. Publ. Can. Soc. Pharm. Sci. 9, 169–189.

Failes, T.W., Cullinane, C., Diakos, C.I., Yamamoto, N., Lyons, J.G., Hambley, T.W., 2007. Studies of a cobalt(III) complex of the MMP inhibitor marimastat: A potential hypoxia-activated prodrug. Chem. – Eur. J. 13, 2974–2982.

Fernández-Moreira, V., Thorp-Greenwood, F.L., Coogan, M.P., 2009. Application of d6 transition metal complexes in fluorescence cell imaging. Chem. Commun. 46, 186–202.

Fond, G., Macgregor, A., Miot, S., 2013. Nanopsychiatry—The potential role of nanotechnologies in the future of psychiatry: A systematic review. Eur. Neuropsychopharmacol. 23, 1067–1071.

Frik, M., Fernández-Gallardo, J., Gonzalo, O., Mangas-Sanjuan, V., González-Alvarez, M., Serranodel Valle, A., Hu, C., González-Alvarez, I., Bermejo, M., Marzo, I., Contel, M., 2015. Cyclometalated iminophosphorane gold(III) and platinum(II) complexes. a highly permeable cationic platinum(II) compound with promising anticancer properties. J. Med. Chem. 58, 5825–5841.

Furia, T.E., 2006. Stability constants of various metal chelates [WWW Document]. URL http://www.coldcure.com/html/stability_constants.html (accessed 10.16.16).

Gaur, P.K., Mishra, S., Bajpai, M., 2014. Formulation and evaluation of controlled-release of telmisartan microspheres: In vitro/in vivo study. J. Food Drug Anal. 22, 542–548.

Gaynor, D., Griffith, D.M., 2012. The prevalence of metal-based drugs as therapeutic or diagnostic agents: beyond platinum. Dalton Trans. 41, 13239–13257.

Gershell, L.J., Atkins, J.H., 2003. A brief history of novel drug discovery technologies. Nat. Rev. Drug Discov. 2, 321–327.

Gichumbi, J.M., Friedrich, H.B., Omondi, B., Singh, M., Naicker, K., Chenia, H.Y., 2016. Synthesis, characterization, and cytotoxic and antimicrobial activities of ruthenium(II) arene complexes with N,N-bidentate ligands. J. Coord. Chem. 69, 3531–3544.

Gouveia, M., Figueira, J., Jardim, M.G., Castro, R., Tomás, H., Rissanen, K., Rodrigues, J., 2018. Poly(alkylidenimine) dendrimers functionalized with the organometallic moiety

[Ru(η5-C5H5)(PPh3)2]+ as Promising drugs against cisplatin-resistant cancer cells and human mesenchymal stem cells. Molecules 23, 1471.

Grgurić-Šipka, S., Alshtewi, M.A.A.M., Jeremić, D., Kaluđerović, G.N., Gómez-Ruiz, S., Žižak, Ž., Juranić, Z., Sabo, T.J., 2008. Synthesis, structural characterization and cytotoxic activity of two new organoruthenium(II) complexes. J. Serbian Chem. Soc. 73, 619–630.

Griffith, D., Cecco, S., Zangrando, E., Bergamo, A., Sava, G., Marmion, C.J., 2008. Ruthenium(III) dimethyl sulfoxide pyridinehydroxamic acid complexes as potential antimetastatic agents: synthesis, characterisation and in vitro pharmacological evaluation. J. Biol. Inorg. Chem. 13, 511–520.

Grindy, S.C., Holten-Andersen, N., 2017. Bio-inspired metal-coordinate hydrogels with programmable viscoelastic material functions controlled by longwave UV light. Soft Matter 13, 4057–4065.

Gupta, S., Kesarla, R., Omri, A., 2013. Formulation strategies to improve the bioavailability of poorly absorbed drugs with special emphasis on self-emulsifying systems. Int. Sch. Res. Not. 2013, e848043.

Gutierrez, K., Dicks, N., Glanzner, W.G., Agellon, L.B., Bordignon, V., 2015. Efficacy of the porcine species in biomedical research. Front. Genet. 6, 293.

Haas, K.L., Franz, K.J., 2009. Application of metal coordination chemistry to explore and manipulate cell biology. Chem. Rev. 109, 4921–4960.

Hambley, T.W., 2007. Developing new metal-based therapeutics: challenges and opportunities. Dalton Trans.

He, Y.J., Xing, L., Cui, P.F., Zhang, J.L., Zhu, Y., Qiao, J.B., Lyu, J.Y., Zhang, M., Luo, C.Q., Zhou, Y.X., Lu, N., Jiang, H.L., 2017. Transferrin-inspired vehicles based on pH-responsive coordination bond to combat multidrug-resistant breast cancer. Biomaterials 113, 266–278.

Heinrich, T.A., Von Poelhsitz, G., Reis, R.I., Castellano, E.E., Neves, A., Lanznaster, M., Machado, S.P., Batista, A.A., Costa-Neto, C.M., 2011. A new nitrosyl ruthenium complex: Synthesis, chemical characterization, in vitro and in vivo antitumor activities and probable mechanism of action. Eur. J. Med. Chem. 46, 3616–3622.

Hoosain, F.G., Choonara, Y.E., Kumar, P., Tomar, L.K., Tyagi, C., Toit, L.C. du, Pillay, V., 2017. In Vivo Evaluation of a PEO-Gellan Gum Semi-Interpenetrating Polymer Network for the Oral Delivery of Sulpiride. AAPS PharmSciTech 18, 654-670.

Horacek, J., Bubenikova-Valesova, V., Kopecek, M., Palenicek, T., Dockery, C., Mohr, P., Höschl, C., 2006. Mechanism of action of atypical antipsychotic drugs and the neurobiology of schizophrenia. CNS Drugs 20, 389–409.

Huang, M.C., Ho, H.O., Yeh, G.C., Ke, W.T., Lin, L.C., Bruce Hsu, T.M., Kao, C.C., Sheu, M.T., 2001. Development of a high-performance liquid chromatographic method for bioanalytical applications with sulpiride. J. Chromatogr. B. Biomed. Sci. App. 763, 157–163.

Ibrahim, W.M., AlOmrani, A.H., Yassin, A.E.B., 2014. Novel sulpiride-loaded solid lipid nanoparticles with enhanced intestinal permeability. Int. J. Nanomedicine 9, 129–144.

Igartúa, D.E., Calienni, M.N., Feas, D.A., Chiaramoni, N.S., Alonso, S.D.V., Prieto, M.J., 2015. Development of nutraceutical emulsions as risperidone delivery systems: characterization and toxicological studies. J. Pharm. Sci. 104, 4142–4152.

Indermun, S., Choonara, Y.E., Kumar, P., du Toit, L.C., Modi, G., van Vuuren, S., Luttge, R., Pillay, V., 2015. Ex vivo evaluation of a microneedle array device for transdermal application. Int. J. Pharm. 496, 351–359.

Jain, V., Singh, R., 2010. Development and characterization of Eudragit RS 100 loaded microsponges and its colonic delivery using natural polysaccharides. Acta Pol. Pharm. 67, 407–415.

Johnson, T.J., Hedge, D.D., 2002. Esomeprazole: a clinical review. Am. J. Health. Syst. Pharm. 59, 1333–1339.

Jones, P.B., Barnes, T.R.E., Davies, L., Dunn, G., Lloyd, H., Hayhurst, K.P., Murray, R.M., Markwick, A., Lewis, S.W., 2006. Randomized controlled trial of the effect on Quality of Life of second- vs first-generation antipsychotic drugs in schizophrenia: Cost Utility of the Latest Antipsychotic Drugs in Schizophrenia Study (CUtLASS 1). Arch. Gen. Psychiatry 63, 1079–1087.

Kane, J.M., Correll, C.U., 2010. Pharmacologic treatment of schizophrenia. Dialogues Clin. Neurosci. 12, 345–357.

Karaoun, N., Renfrew, A.K., 2015. A luminescent ruthenium(II) complex for light-triggered drug release and live cell imaging. Chem. Commun. 51, 14038–14041.

Kavitha, N., Anantha Lakshmi, P.V., 2017. Synthesis, characterization and thermogravimetric analysis of Co(II), Ni(II), Cu(II) and Zn(II) complexes supported by ONNO tetradentate Schiff base ligand derived from hydrazino benzoxazine. J. Saudi Chem. Soc. 21, S457–S466.

Kawabata, Y., Wada, K., Nakatani, M., Yamada, S., Onoue, S., 2011. Formulation design for poorly water-soluble drugs based on biopharmaceutics classification system: Basic approaches and practical applications. Int. J. Pharm. 420, 1–10.

Kecel-Gunduz, S., Celik, S., Ozel, A.E., Akyuz, S., 2015. Structural and vibrational spectroscopic elucidation of sulpiride in solid state. J. Biomol. Struct. Dyn. 33, 322-343

Kim, D.H., Martin, D.C., 2006. Sustained release of dexamethasone from hydrophilic matrices using PLGA nanoparticles for neural drug delivery. Biomaterials 27, 3031–3037.

Knoll, J.D., Albani, B.A., Turro, C., 2015. Excited state investigation of a new Ru(II) complex for dual reactivity with low energy light. Chem. Commun. 51, 8777–8780.

Kobayashi, E., Hishikawa, S., Teratani, T., Lefor, A.T., 2012. The pig as a model for translational research: overview of porcine animal models at Jichi Medical University. Transplant. Res. 1, 8.

Kola, I., Landis, J., 2004. Can the pharmaceutical industry reduce attrition rates? Nat. Rev. Drug Discov. 3, 711–716.

Kondapalli, S.P., Chalamalasetti, S.R., Damera, N.R., 2013. Application of Taguchi based Design of Experiments to Fusion Arc Weld Processes: A Review. Int. J. Bus. Res. Dev. 4, 1-8.

Krstic, N.S., Nikolic, R.S., Stankovic, M.N., Nikolic, N.G., Dordevic, D.M., 2015. Coordination compounds of M(II) biometal ions with acid- type anti-inflammatory drugs as ligands – A review. Trop. J. Pharm. Res. 14, 337–349.

Kumar, A., Sahoo, S.K., Padhee, K., Kochar, P.P., Satapathy, A., Pathak, N., 2011. Review on solubility enhancement techniques for hydrophobic drugs. Int. J. Compr. Pharm. 2, 1–7.

Kumar, P., Singh, C., 2013. A study on solubility enhancement methods for poorly water soluble drugs. Am. J. Pharmacol. Sci. 1, 67–73.

Kurchania, R., Sawant, S.S., Ball, R.J., 2014. Synthesis and characterization of magnetite/polyvinyl alcohol core–shell composite nanoparticles. J. Am. Ceram. Soc. 97, 3208–3215.

Lago, A.B., Pino-Cuevas, A., Carballo, R., Vázquez-López, E.M., 2016. A new metal–organic polymeric system capable of stimuli-responsive controlled release of the drug ibuprofen. Dalton Trans. 45, 1614–1621.

Lai, E.C.C., Chang, C.H., Kao Yang, Y.H., Lin, S.J., Lin, C.Y., 2013. Effectiveness of sulpiride in adult patients with schizophrenia. Schizophr. Bull. 39, 673–683.

Lai, E.C.-C., Hsieh, C.-Y., Kao Yang, Y.-H., Lin, S.-J., 2014. Detecting potential adverse reactions of sulpiride in schizophrenic patients by prescription sequence symmetry analysis. PLoS ONE 9, e89795.

Law, B.Y.K., Qu, Y.Q., Mok, S.W.F., Liu, H., Zeng, W., Han, Y., Gordillo-Martinez, F., Chan, W.-K., Wong, K.M.-C., Wong, V.K.W., Kwan Law, B.Y., Qu, Y.Q., Fai Mok, S.W., Liu, H., Zeng, W., Han, Y., Gordillo-Martinez, F., Chan, W.-K., Wong, K.M.-C., Wai Wong, V.K., 2017. New perspectives of cobalt tris(bipyridine) system: anti-cancer effect and its collateral sensitivity towards multidrug-resistant (MDR) cancers. Oncotarget 8, 55003–55021.

Lentz, F., Drescher, A., Lindauer, A., Henke, M., Hilger, R.A., Hartinger, C.G., Scheulen, M.E., Dittrich, C., Keppler, B.K., Jaehde, U., Central European Society for Anticancer Drug

Research-EWIV, 2009. Pharmacokinetics of a novel anticancer ruthenium complex (KP1019, FFC14A) in a phase I dose-escalation study. Anticancer. Drugs 20, 97–103.

Leo, E., Forni, F., Bernabei, M.T., 2000. Surface drug removal from ibuprofen-loaded PLA microspheres. Int. J. Pharm. 196, 1–9.

Leung, C.-H., Lin, S., Zhong, H.-J., Ma, D.-L., 2015. Metal complexes as potential modulators of inflammatory and autoimmune responses. Chem. Sci. 6, 871–884.

Levine, D.J., Runčevski, T., Kapelewski, M.T., Keitz, B.K., Oktawiec, J., Reed, D.A., Mason, J.A., Jiang, H.Z.H., Colwell, K.A., Legendre, C.M., FitzGerald, S.A., Long, J.R., 2016. Olsalazine-based metal–organic frameworks as biocompatible platforms for h2 adsorption and drug delivery. J. Am. Chem. Soc. 138, 10143–10150.

Liang, B., Tong, R., Wang, Z., Guo, S., Xia, H., 2014. High intensity focused ultrasound responsive metallo-supramolecular block copolymer micelles. Langmuir 30, 9524–9532.

Liang, H., Li, J., He, Y., Xu, W., Liu, S., Li, Y., Chen, Y., Li, B., 2016. Engineering Multifunctional Films Based on Metal-Phenolic Networks for Rational pH-Responsive Delivery and Cell Imaging. ACS Biomater. Sci. Engeneering 2, 317–325.

Liang, H., Zhou, B., He, Y., Pei, Y., Li, B., Li, J., 2017. Tailoring stimuli-responsive delivery system driven by metal–ligand coordination bondingring stimuli-responsive delivery system driven by metal–ligand coordination bonding. Int. J. Nanomedicine 12, 3315–3330.

Liu, W., Qin, Y., Liu, S., Xing, R., Yu, H., Chen, X., Li, K., Li, P., 2018. Synthesis of C-coordinated O-carboxymethyl chitosan metal complexes and evaluation of their antifungal activity. Sci. Rep. 8, 4845.

Loftsson, T., 2017. Drug solubilization by complexation. Int. J. Pharm. 531, 276–280.

Lopes, J.C.S., Damasceno, J.L., Oliveira, P.F., Guedes, A.P.M., Tavares, D.C., Deflon, V.M., Lopes, N.P., Pivatto, M., Batista, A.A., Maia, P.I.S., Von Poelhsitz, G., Lopes, J.C.S., Damasceno, J.L., Oliveira, P.F., Guedes, A.P.M., Tavares, D.C., Deflon, V.M., Lopes, N.P., Pivatto, M., Batista, A.A., Maia, P.I.S., Von Poelhsitz, G., 2015. Ruthenium(II) complexes containing anti-inflammatory drugs as ligands: Synthesis, characterization and in vitro cytotoxicity activities on cancer cell lines. J. Braz. Chem. Soc. 26, 1838–1847.

Lopes-dos-Santos, V., Campi, J., Filevich, O., Ribeiro, S., Etchenique, R., 2011. In vivo photorelease of GABA in the mouse cortex. Braz. J. Med. Biol. Res. 44, 688–693.

Lough, W.J., Wainer, I.W. High Performance Liquid Chromatography: Fundamental Principles and Practice. CRC Press 1995, 292 pp.

Lu, L., Liu, L.J., Chao, W., Zhong, H.J., Wang, M., Chen, X.P., Lu, J.J., Li, R., Ma, D.L., Leung, C.-H., 2015. Identification of an iridium(III) complex with anti-bacterial and anti-cancer activity. Sci. Rep. 5, 14544.

Lu, Y., Aimetti, A.A., Langer, R., Gu, Z., 2017. Bioresponsive materials. Nat. Rev. Mater. 2, 16075.

Lv, G., Guo, L., Qiu, L., Yang, H., Wang, T., Liu, H., Lin, J., 2015. Lipophilicity-dependent ruthenium N-heterocyclic carbene complexes as potential anticancer agents. Dalton Trans. 44, 7324–7331.

Ma, Z., Moulton, B., 2011. Recent advances of discrete coordination complexes and coordination polymers in drug delivery. Coord. Chem. Rev. 255, 1623–1641.

Mabrouk, M., Chejara, D.R., Mulla, J. a. S., Badhe, R.V., Choonara, Y.E., Kumar, P., du Toit, L.C., Pillay, V., 2015. Design of a novel crosslinked HEC-PAA porous hydrogel composite for dissolution rate and solubility enhancement of efavirenz. Int. J. Pharm. 490, 429–437.

Madan, J.R., Pawar, K.T., Dua, K., 2015. Solubility enhancement studies on lurasidone hydrochloride using mixed hydrotropy. Int. J. Pharm. Investig. 5, 114–120.

Maksimoska, J., Feng, L., Harms, K., Yi, C., Kissil, J., Marmorstein, R., Meggers, E., 2008. Targeting Large Kinase Active Site with Rigid, Bulky Octahedral ruthenium complexes. J. Am. Chem. Soc. 130, 15764–15765.

Małecki, J.G., 2012. Half-sandwich ruthenium(II) complexes with N- and N,(N,O)-donor ligands: molecular, electronic structures, and computational study. Struct. Chem. 23, 461–472.

Manjunath, S., Chouhan, V., Sandeep, S., 2011. Spectrophotometric estimation of Levosulpiride in bulk drug and formulations. Int. J. Pharm. Pharm. Sci. 3, 135–137.

Mantion, A., Massüger, L., Rabu, P., Palivan, C., McCusker, L.B., Taubert, A., 2008. Metal−Peptide Frameworks (MPFs): “Bioinspired” metal organic frameworks. J. Am. Chem. Soc. 130, 2517–2526.

Martins, D. de J., Hanif-Ur-Rehman, Rico, S.R.A., Costa, I. de M., Santos, A.C.P., Szszudlowski, R.G., Silva, D. de O., 2015. Interaction of chitosan beads with a copper–naproxen metallodrug. RSC Adv. 5, 90184–90192.

Mashhadi, S.M.A., Yunus, U., Bhatti, M.H., Ahmed, I., Tahir, M.N., 2016. Synthesis, characterization, solubility and stability studies of hydrate cocrystal of antitubercular Isoniazid with antioxidant and anti-bacterial Protocatechuic acid. J. Mol. Struct. 1117, 17–21.

Mavuso, S., Choonara, Y.E., Marimuthu, T., Kumar, P., du Toit, L.C., Kondiah, P.P.D., Pillay, V., 2016. A dual pH/Redox responsive copper-ligand nanoliposome bioactive complex for the treatment of chronic inflammation. Int. J. Pharm. 509, 348–359.

M’bitsi-Ibouily, G.C., Marimuthu, T., Kumar, P., du Toit, L.C., Choonara, Y.E., Kondiah, P.P.D., Pillay, V., 2017. Outlook on the application of metal-liganded bioactives for stimuli-responsive release.

McNamara, D.P., Childs, S.L., Giordano, J., Iarriccio, A., Cassidy, J., Shet, M.S., Mannion, R., O’Donnell, E., Park, A., 2006. Use of a glutaric acid cocrystal to improve oral bioavailability of a low solubility API. Pharm. Res. 23, 1888–1897.

Meunier, V., Bourrié, M., Berger, Y., Fabre, G., 1995. The human intestinal epithelial cell line Caco-2; pharmacological and pharmacokinetic applications. Cell Biol. Toxicol. 11, 187–194.

Mjos, K.D., Orvig, C., 2014. Metallodrugs in Medicinal Inorganic Chemistry. Chem. Rev. 114, 4540–4563.

Mohamed, G.G., Soliman, M.H., 2010. Synthesis, spectroscopic and thermal characterization of sulpiride complexes of iron, manganese, copper, cobalt, nickel, and zinc salts. Antibacterial and antifungal activity. Spectrochim. Acta. A. Mol. Biomol. Spectrosc. 76, 341–347.

Mondal, A., De, S., Maiti, S., Sarkar, B., Sk, A.K., Jacob, R., Moorthy, A., Paira, P., 2018. Amberlite IR-120 (H) mediated “on water” synthesis of fluorescent Ruthenium(II)-arene 8-hydroxyquinoline complexes for cancer therapy and live cell imaging. J. Photochem. Photobiol. B 178, 380–394.

Morais, T.S., Santos, F.C., Jorge, T.F., Côrte-Real, L., Madeira, P.J.A., Marques, F., Robalo, M.P., Matos, A., Santos, I., Garcia, M.H., 2014. New water-soluble ruthenium(II) cytotoxic complex: Biological activity and cellular distribution. J. Inorg. Biochem. 130, 1–14.

Motswainyana, W.M., Ajibade, P.A., 2015. Anticancer activities of mononuclear ruthenium(II) coordination complexes. Adv. Chem. 2015, 1–21.

Munteanu, C.R., Suntharalingam, K., 2015. Advances in cobalt complexes as anticancer agents. Dalton Trans. 44, 13796–13808.

Murov, S., 2010. Solvent polarity table - Miller’s Home [WWW Document]. Mill. Home. URL https://sites.google.com/site/miller00828/in/solvent-polarity-table (accessed 5.10.17).

NanoComposix, 2012. Nanocomposix’s guide to dynamic light scattering measurement and analysis - PDF [WWW Document]. URL https://docplayer.net/45227932-Nanocomposix-s-guide-to-dynamic-light-scattering-measurement-and-analysis.html (accessed 10.29.18).

Ngwuluka, N.C., Choonara, Y.E., Modi, G., du Toit, L.C., Kumar, P., Meyer, L., Snyman, T., Pillay, V., 2017. Ex vivo and in vivo characterization of interpolymeric blend/nanoenabled gastroretentive levodopa delivery systems. Park. Dis. 2017, 1-14.

Omori, I.M., Wang, J., 2009. Sulpiride versus placebo for schizophrenia. Cochrane Database Syst. Rev. CD007811.

Ostrovskii, K.P., Osipova, N.S., Vanchugova, L.V., Shipulo, E.V., Pereverzeva, É.R., Treshchalin, I.D., Maksimenko, O.O., Gel'perina, S.É., 2016. Use of proteins to increase the aqueous solubility of rifapentine. Pharm. Chem. J. 50, 407–412.

Parikh, T., Bommana, M.M., Squillante III, E., 2010. Efficacy of surface charge in targeting pegylated nanoparticles of sulpiride to the brain. Eur. J. Pharm. Biopharm. 74, 442–450.

Pastuszko, A., Majchrzak, K., Czyz, M., Kupcewicz, B., Budzisz, E., 2016. The synthesis, lipophilicity and cytotoxic effects of new ruthenium(II) arene complexes with chromone derivatives. J. Inorg. Biochem. 159, 133–141.

Piccariello, T., 2013. Metal coordinated compositions. US20130184447 A1.

Pinto, A., Hoffmanns, U., Ott, M., Fricker, G., Metzler-Nolte, N., 2009. Modification with organometallic compounds improves crossing of the blood-brain barrier of [Leu5]-enkephalin derivatives in an in vitro model system. Chembiochem Eur. J. Chem. Biol. 10, 1852–1860.

Price, J.D., Piccariello, T., Oberlender, R.A., Mulhare, M.E., Palmer, S.B., 2012. Bismuth-containing compounds, coordination polymers, methods for modulating pharmacokinetic properties of biologically active agents, and methods for treating patients. US20120115823 A1.

Price, J.D., Piccariello, T., Palmer, S., 2014. Metal-coordinated pharmaceuticals - Reducing inter-subject variability with metal-coordinated pharmaceuticals: A case study with furosemide. Drug Dev. Deliv. 14, 63–68.

Rafique, S., Idrees, M., Nasim, A., Akbar, H., Athar, A., 2010. Transition metal complexes as potential therapeutic agents. Biotechnol. Mol. Biol. Rev. 5, 38–45.

Ragheb, M.A., Eldesouki, M.A., Mohamed, M.S., 2015. DNA binding, photo-induced DNA cleavage and cytotoxicity studies of lomefloxacin and its transition metal complexes. Spectrochim. Acta. A. Mol. Biomol. Spectrosc. 138, 585–595.

Ramesan, M.T., Sampreeth, T., 2017. Synthesis, characterization, material properties and sensor application study of polyaniline/niobium doped titanium dioxide nanocomposites. J. Mater. Sci. Mater. Electron. 28, 16181–16191.

Reedijk, J., 2008. Metal-ligand exchange kinetics in platinum and ruthenium complexes. Platin. Met. Rev. 52, 2–11.

Renfrew, A.K., 2014. Transition metal complexes with bioactive ligands: mechanisms for selective ligand release and applications for drug delivery. Metallomics 6, 1324–1335.

Renny, J.S., Tomasevich, L.L., Tallmadge, E.H., Collum, D.B., 2013. Method of continuous variations: applications of job plots to the study of molecular associations in organometallic chemistry. Angew. Chem. Int. Ed Engl. 52, 11998–12013.

Rial Verde, E., Zayat, L., Etchenique, R., Yuste, R., 2008. Photorelease of GABA with visible light using an inorganic caging group. Front. Neural Circuits 2, 2.

Rilak, A., Bratsos, I., Zangrando, E., Kljun, J., Turel, I., Bugarčić, Ž.D., Alessio, E., 2014. New water-soluble ruthenium(II) terpyridine complexes for anticancer activity: synthesis, characterization, activation kinetics, and interaction with guanine derivatives. Inorg. Chem. 53, 6113–6126.

Rojas, S., Devic, T., Horcajada, P., 2017. Metal organic frameworks based on bioactive components. J. Mater. Chem. B 5, 2560–2573.

Ross, D.L., Riley, C.M., 1992. Physicochemical properties of the fluoroquinolone antimicrobials. III. Complexation of lomefloxacin with various metal ions and the effect of metal ion complexation on aqueous solubility. Int. J. Pharm. 87, 203–213.

Rössler, W., Joachim Salize, H., van Os, J., Riecher-Rössler, A., 2005. Size of burden of schizophrenia and psychotic disorders. Eur. Neuropsychopharmacol., Size & Burden of Mental Disorders in Europe 15, 399–409.

Safari, J., Zarnegar, Z., 2014. Advanced drug delivery systems: Nanotechnology of health design A review. J. Saudi Chem. Soc. 18, 85–99.

Scrase, T.G., O'Neill, M.J., Peel, A.J., Senior, P.W., Matthews, P.D., Shi, H., Boss, S.R., Barker, P.D., 2015. Selective lability of ruthenium(II) arene amino acid complexes. Inorg. Chem. 54, 3118–3124.

Shaikh, A.R., Giridhar, R., Yadav, M.R., 2007. Bismuth-norfloxacin complex: Synthesis, physicochemical and antimicrobial evaluation. Int. J. Pharm. 332, 24–30.

Sharma, N., Madan, P., Lin, S., 2016. Effect of process and formulation variables on the preparation of parenteral paclitaxel-loaded biodegradable polymeric nanoparticles: A co-surfactant study. Asian J. Pharm. Sci. 11, 404–416.

Sharma, R., Knoll, J.D., Ancona, N., Martin, P.D., Turro, C., Kodanko, J.J., 2015. Solid-Phase synthesis as a platform for the discovery of new ruthenium complexes for efficient release of photocaged ligands with visible light. Inorg. Chem. 54, 1901–1911.

Shen, S., Wu, Y., Liu, Y., Wu, D., 2017. High drug-loading nanomedicines: progress, current status, and prospects [WWW Document]. Int. J. Nanomedicine. https://doi.org/10.2147/IJN.S132780

Shravani, D., Lakshmi, P.K., Balasubramaniam, J., 2011. Preparation and optimization of various parameters of enteric coated pellets using the Taguchi L9 orthogonal array design and their characterization. Acta Pharm. Sin. B 1, 56–63.

Shweshein, K.S.A.M., Andrić, F., Radoičić, A., Zlatar, M., Gruden-Pavlović, M., Tešić, Ž., Milojković-Opsenica, D., 2014. Lipophilicity assessment of ruthenium(II)-Arene complexes by the means of reversed-phase thin-layer chromatography and DFT calculations. Sci. World J. 2014: 862796.

Siddappa, K., Mane, S.B., Manikprabhu, D., 2014. Spectral characterization and 3D molecular modeling studies of metal complexes involving the O, N-Donor environment of quinazoline-4(3H)-one schiff base and their biological studies. Sci. World J. 2014, e817365.

Siddiqi, K.S., Bano, S., Mohd, A., Khan, A.A.P., 2009. Fluorescence Enhancement of levosulpiride upon coordination with transition metal ions and spectrophotometric determination of complex formation. Anal. Lett. 42, 2192–2205.

Singh, R.V., Dwivedi, R., Joshi, S.C., 2004. Synthetic, magnetic, spectral, antimicrobial and antifertility studies of dioxomolybdenum(VI) unsymmetrical imine complexes having a N∩N donor system. Transit. Met. Chem. 29, 70–74.

Smith, N.A., Sadler, P.J., 2013. Photoactivatable metal complexes: from theory to applications in biotechnology and medicine. Philos. Trans. R. Soc. Lond. Math. Phys. Eng. Sci. 371, 20120519.

Smyth, A.M., Lawrie, S.M., 2013. The Neuroimmunology of schizophrenia. Clin. Psychopharmacol. Neurosci. Off. Sci. J. Korean Coll. Neuropsychopharmacol. 11, 107–117.

Solvent Polarity Index - Chempendix [WWW Document], n.d. . Sapling Learn. Macmillan Learn. URL https://sites.google.com/site/chempendix/hplc/solvent-polarity-index (accessed 5.10.17).

Spreckelmeyer, S., Orvig, C., Casini, A., 2014. Cellular transport mechanisms of cytotoxic metallodrugs: an overview beyond cisplatin. Mol. Basel Switz. 19, 15584–15610.

Subran, S.K., Banerjee, S., Mondal, A., Paira, P., 2016. Amberlite IR-120(H)-mediated “on water” synthesis of novel anticancer ruthenium(II)–p-cymene 2-pyridinylbenzothiazole (BTZ), 2-pyridinylbenzoxazole (BOZ) & 2-pyridinylbenzimidazole (BIZ) scaffolds. New J. Chem. 40, 10333–10343.

Tan, C., Hu, S., Liu, J., Ji, L., 2011. Synthesis, characterization, antiproliferative and anti-metastatic properties of two ruthenium-DMSO complexes containing 2,2’-biimidazole. Eur. J. Med. Chem. 46, 1555–1563.

Thompson, K.H., Orvig, C., 2003. Boon and Bane of Metal Ions in Medicine. Science 300, 936–939.

Tirmizi, S.A., Wattoo, F.H., Wattoo, M.H.S., Sarwar, S., Memon, A.N., Ghangro, A.B., 2012. Spectrophotometric study of stability constants of cimetidine–Ni(II) complex at different temperatures. Arab. J. Chem. 5, 309–314.

Tiwari, G., Tiwari, R., Sriwastawa, B., Bhati, L., Pandey, S., Pandey, P., Bannerjee, S.K., 2012. Drug delivery systems: An updated review. Int. J. Pharm. Investig. 2, 2–11.

Uivarosi, V., 2013. Metal complexes of quinolone antibiotics and their applications: an update. Mol. Basel Switz. 18, 11153–11197.

Vadori, M., Pacor, S., Vita, F., Zorzet, S., Cocchietto, M., Sava, G., 2013. Features and full reversibility of the renal toxicity of the ruthenium-based drug NAMI-A in mice. J. Inorg. Biochem., Special Issue on the Bioinorganic Chemistry of HNO 118, 21–27.

van Rijt, S.H., Sadler, P.J., 2009. Current applications and future potential for bioinorganic chemistry in the development of anticancer drugs. Drug Discov. Today 14, 1089–1097.

Wang, F., Chen, H., Parsons, S., Oswald, I.D.H., Davidson, J.E., Sadler, P.J., 2003. Kinetics of aquation and anation of ruthenium(II) arene anticancer complexes, acidity and X-ray structures of aqua adducts. Chem. – Eur. J. 9, 5810–5820.

Wang, H., Hu, T.L., Wen, R.M., Wang, Q., Bu, X.H., 2013. In vitro controlled release of theophylline from metal–drug complexes. J. Mater. Chem. B 1, 3879–3882.

Wang, J., Sampson, S. 2014. Sulpiride versus placebo for schizophrenia. Cochrane Database of Systematic Reviews 2014.

Ware, D., Palmer, H., Pruijn, F., Anderson, R., Brothers, P., Denny, W., Wilson, W., 1998. Bis(dialkyl)dithiocarbamato cobalt(III) complexes of bidentate nitrogen mustards: synthesis, reduction chemistry and biological evaluation as hypoxia-selective cytotoxins. Anticancer. Drug Des. 13, 81–103.

Watanabe, K., Sawano, T., Endo, T., Sakata, M., Sato, J., 2002a. Studies on intestinal absorption of sulpiride (2): transepithelial transport of sulpiride across the human intestinal cell line Caco-2. Biol. Pharm. Bull. 25, 1345–1350.

Watanabe, K., Sawano, T., Terada, K., Endo, T., Sakata, M., Sato, J., 2002b. Studies on intestinal absorption of sulpiride (1): Carrier-Mediated uptake of sulpiride in the human intestinal cell line Caco-2. Biol. Pharm. Bull. 25, 885–890.

Weiner, I., Gaisler, I., Schiller, D., Green, A., Zuckerman, L., Joel, D., 2000. Screening of antipsychotic drugs in animal models. Drug Dev. Res. 50, 235–249.

Williams, K.M., Gokulan, K., Cerniglia, C.E., Khare, S., 2016. Size and dose dependent effects of silver nanoparticle exposure on intestinal permeability in an in vitro model of the human gut epithelium. J. Nanobiotechnology 14, 62.

Wockhardt, 2010. Sulpiride tablets 200mg | Drugs.com [WWW Document]. URL http://www.drugs.com/uk/sulpiride-tablets-200mg-leaflet.html (accessed 3.25.14).

Yelnimez, E., 2017. Desloratadine-Eudragit® RS100 Nanoparticles: Formulation and Characterization. Turk. J. Pharm. Sci. 14, 148–156.

Yurtdaş Kırımlıoğlu, G., Yazan, Y., 2016. Formulation and in vitro characterization of polymeric nanoparticles designed for oral delivery of levofloxacin hemihydrate. Eur. Int. J. Sci. Technol. 5, 148–157.

Zadrozny, J.M., Atanasov, M., Bryan, A.M., Lin, C.-Y., Rekken, B.D., Power, P.P., Neese, F., Long, J.R., 2012. Slow magnetization dynamics in a series of two-coordinate iron(II) complexes. Chem. Sci. 4, 125–138.

Zakeri-Milani, P., Islambulchilar, Z., Majidpour, F., Jannatabadi, E., Lotfipour, F., Valizadeh, H., Zakeri-Milani, P., Islambulchilar, Z., Majidpour, F., Jannatabadi, E., Lotfipour, F., Valizadeh, H., 2014. A study on enhanced intestinal permeability of clarithromycin nanoparticles. Braz. J. Pharm. Sci. 50, 121–129.

Zare, M., Mohammadi Samani, S., Sobhani, Z., 2018. Enhanced intestinal permeation of doxorubicin using chitosan nanoparticles. Adv. Pharm. Bull. 8, 411–417.

Zayat, L., Calero, C., Alborés, P., Baraldo, L., Etchenique, R., 2003. A new strategy for neurochemical photodelivery: metal−ligand heterolytic cleavage. J. Am. Chem. Soc. 125, 882–883.

Zayat, L., Filevich, O., Baraldo, L.M., Etchenique, R., 2013. Ruthenium polypyridyl phototriggers: from beginnings to perspectives. Phil Trans R Soc A 371, 20120330.

Zhang, J.-P., Zhu, A.-X., Chen, X.-M., 2012. Single-crystal X-ray diffraction and Raman spectroscopy studies of isobaric N2 adsorption in SOD-type metal–organic zeolites. Chem. Commun. 48, 11395–11397.

Zhang, P., Chen, J., Liang, Y., 2010. DNA binding, cytotoxicity, and apoptotic-inducing activity of ruthenium(II) polypyridyl complex. Acta Biochim. Biophys. Sin. 42, 440–449.

Zhang, Z., Wang, Z., Nong, J., Nix, C.A., Ji, H.-F., Zhong, Y., 2015. Metal ion-assisted self-assembly of complexes for controlled and sustained release of minocycline for biomedical applications. Biofabrication 7, 015006.

Zhao, Y., Wang, Y., Ran, F., Cui, Y., Liu, C., Zhao, Q., Gao, Y., Wang, D., Wang, S., 2017. A comparison between sphere and rod nanoparticles regarding their in vivo biological behavior and pharmacokinetics. Sci. Rep. 7, 4131.

APPENDICES

APPENDIX A1

molecules

MDPI

Review

Outlook on the Application of Metal-Liganded Bioactives for Stimuli-Responsive Release

Gretta C. M'bitsi-Ibouily, Thashree Marimuthu, Pradeep Kumar, Lisa C. du Toit, Yahya E. Choonara, Pierre P. D. Kondiah and Viness Pillay *

Wits Advanced Drug Delivery Platform Research Unit, Department of Pharmacy and Pharmacology, School of Therapeutic Sciences, Faculty of Health Sciences, University of the Witwatersrand, Johannesburg, 7 York Road, Parktown 2193, South Africa; 362179@students.wits.ac.za (G.C.M.-I.); thashree.marimuthu@wits.ac.za (T.M.); pradeep.kumar@wits.ac.za (P.K.); lisa.dutoit@wits.ac.za (L.C.d.T.); yahya.choonara@wits.ac.za (Y.E.C.); pierre.kondiah@wits.ac.za (P.P.D.K.)

* Correspondence: viness.pillay@wits.ac.za; Tel.: +27-11-717-2274

Received: 13 October 2017; Accepted: 25 November 2017; Published: 26 November 2017

Abstract: Direct metal-liganded bioactive coordination complexes are known to be sensitive to stimuli such as pH, light, ion activation, or redox cues. This results in the controlled release of the bioactive(s). Compared to other drug delivery strategies based on metal complexation, this type of coordination negates a multi-step drug loading methodology and offers customized physiochemical properties through judicious choice of modulating ancillary ligands. Bioactive release depends on simple dissociative kinetics. Nonetheless, there are challenges encountered when translating the pure coordination chemistry into the biological and physiological landscape. The stability of the metal–bioactive complex in the biological milieu may be compromised, disrupting the stimuli-responsive release mechanism, with premature release of the bioactive. Research has therefore progressed to the incorporation of metal-liganded bioactives with established drug delivery strategies to overcome these limitations. This review will highlight and critically assess current research interventions in order to predict the direction that pharmaceutical scientists could pursue to arrive at tailored and effective metal-liganded bioactive carriers for stimuli-responsive drug release.

Keywords: metal-liganded bioactive; drug carrier; stimuli-responsive release; bioinorganic medicine

1. Introduction

Bio-inspired metal coordination has demonstrated a growth in applications in the field of drug delivery [1–3]. Recent reports have highlighted the release of the drug cargoes through the dissociation of bespoke metal–ligand bonds [4–6] or metal–biomolecule bonds [7]. An alternative approach to these methodologies is the direct coordination of the bioactive to the metal center, which results in metal-liganded bioactive complexes. These complexes are advantageous as they are capable of delivering the bioactive through selective release mechanism(s) [8]. Metal–ligand bioactives in the context of this review refer to the coordination of a market-available pharmaceutical agent to a metal center to produce a novel and more effective drug delivery system. Notably, the introduction of the metal center can control the mechanism by which the drug is delivered without changing the drug action or therapeutic activity. Furthermore, this is a relatively more facile route to enhancing both the pharmacokinetic and pharmacodynamic properties of the parent bioactive.

Approximately 60–70% of drug molecules suffer from poor aqueous solubility and/or low permeability following oral delivery [9]. The coordination of drugs to metal centers is a promising approach that has the potential to improve both the aqueous and lipid solubility of poorly absorbed bioactives [10]. The increase in lipid solubility has been primarily attributed to chelation effects, which results in a delocalization of electron density among the donors of the bioactive and/or ancillary

APPENDIX A2

www.nature.com/scientificreports

SCIENTIFIC REPORTS

OPEN

Received: 4 October 2018
Accepted: 7 February 2019
Published online: 11 March 2019

Synthesis, Characterisation and *In Vitro* Permeation, Dissolution and Cytotoxic Evaluation of Ruthenium(II)-Liganded Sulpiride and Amino Alcohol

Gretta C. M'bitsi-Ibouily[1], Thashree Marimuthu[1], Pradeep Kumar[1], Yahya E. Choonara[1], Lisa C. du Toit[1], Priyamvada Pradeep[1], Girish Modi[2] & Viness Pillay[1]

Sulpiride (SPR) is a selective antagonist of central dopamine receptors but has limited clinical use due to its poor pharmacokinetics. The aim of this study was to investigate how metal ligation to SPR may improve its solubility, intestinal permeability and prolong its half-life. The synthesis and characterisation of ternary metal complexes [Ru(*p*-cymene)(L)(SPR)]PF_6 (L1 = (R)-(+)-2-amino-3-phenyl-1-propanol, L2 = ethanolamine, L3 = (S)-(+)-2-amino-1-propanol, L4 = 3-amino-1-propanol, L5 = (S)-(+)-2-pyrrolidinemethanol) are described in this work. The stability constant of the [Ru(*p*-cymene)(SPR)] complex was determined using Job's method. The obtained value revealed higher stability of the metal complex in the physiological pH than in an acidic environment such as the stomach. The ternary metal complexes were characterised by elemental analysis, Fourier transform infrared spectroscopy (FT-IR), ^{1}H and ^{13}C nuclear magnetic resonance (NMR), differential scanning calorimetry (DSC), thermal analyses, Ultraviolet-Visible (UV-Vis). Solubility studies showed higher aqueous solubility for complexed SPR than the free drug. Dissolution profiles of SPR from the metal complexes exhibited slower dissolution rate of the drug. Permeation studies through the pig's intestine revealed enhanced membrane permeation of the complexed drug. *In vitro* methyl thiazolyl tetrazolium (MTT) assay showed no noticeable toxic effects of the ternary metal complexes on Caco-2 cell line.

Many drug candidates that reach the clinical trial phase are unsuccessful due to several limitations, including poor pharmacokinetic properties. Such shortcomings also affect a considerable number of therapeutic agents already on the market[1–3]. A possible solution to these problems is the design of drug delivery systems with the ability to overcome these limitations, thus pharmaceutical scientists are exploring various drug delivery strategies[4]. Such strategies include the intentional, reversible modification of the physiochemical characteristics of a pharmaceutical in clinical use through the formation of a coordination complex with a transition metal[5,6]. The rapid advances of coordination complexes, also known as metal complexes, as functional materials (catalysts, magnetic and porous materials) have motivated scientists in the pharmaceuticals and medicinal chemistry fields to focus on the research of metal complexes to investigate their potential in medical applications[7–9]. Coordination complexes using the metal as a drug carrier have subsequently shown their usefulness as both diagnostic and therapeutic agents[10,11]. Metal carriers are a simple drug delivery strategy with the ability to induce pharmacokinetic changes to improve aqueous and lipid solubility, bioavailability, permeation and to achieve controlled drug release, while avoiding the time-consuming and costly drug discovery process[12,13]. A recent study showed pharmacokinetic improvement of the standard drug for the treatment of hypothyroidism through metal coordination. In fact, a zinc-coordinated form of the drug was synthesized and formulated into coated gelatin capsules, which

[1]Wits Advanced Drug Delivery Platform Research Unit, Department of Pharmacy and Pharmacology, School of Therapeutic Sciences, Faculty of Health Sciences, University of the Witwatersrand, Johannesburg, 7 York Road, Parktown, 2193, South Africa. [2]Department of Neurology, Division of Neurosciences, Faculty of Health Sciences, University of the Witwatersrand, Johannesburg, 7 York Road, Parktown, 2193, South Africa. Correspondence and requests for materials should be addressed to V.P. (email: viness.pillay@wits.ac.za)

APPENDIX B1

Title: Overcoming the challenges of sulpiride pharmacokinetics through metal coordination and nanotechonology

Gretta C. M'bitsi-Ibouily[1,a], Thashree Marimuthu[2,a], Yahya E. Choonara[3,a], , Lisa C. du Toit[4,a], Pradeep Kumar[5,b], Pierre Kondiah[6,a], G. Modi[7,b], Viness Pillay*[,a]

[a] Wits Advanced Drug Delivery Platform Research Unit, Department of Pharmacy and Pharmacology, School of Therapeutic Sciences, Faculty of Health Sciences, University of the Witwatersrand, Johannesburg, 7 York Road, Parktown 2193, South Africa

[b] Department of Neurology, Division of Neurosciences, Faculty of Health Sciences, University of the Witwatersrand, Johannesburg, 7 York Road, Parktown 2193, South Africa

Introduction. Sulpiride is a selective antagonist of central dopamine receptors but has limited clinical use due to its poor pharmacokinetics. This study aimed to synthesise, characterise and investigate the mechanism by which metal ligation to sulpiride may improve its solubility and intestinal permeability and extend its half-life through sustained drug release.

Methods. New labile organometallic complexes with lipophilic and hydrophilic organic groups were prepared. To confirm coordination of sulpiride to the metal, structural elucidation was accomplished by elemental analysis, Fourier transform infrared spectroscopy (FT-IR), ^{1}H and ^{13}C nuclear magnetic resonance (NMR). Solubility studies were conducted in different solvents. *Ex vivo* permeation studies were performed employing the pig's intestinal tissue. Dissolution studies were performed in phosphate buffered saline at different pH conditions. For solubility, permeation and dissolution studies, the amount of sulpiride was quantified via UV-VIS. The metal complex with the highest potential to improve drug solubility and intestinal permeability was then formulated into polymeric nanospheres to form a metal complex-polymer nanocomposite (MCPN). The behaviour of the MCPN in gastric/intestinal pH simulated solutions was investigated to ascertain its drug releasing properties.

Results. Complexed sulpiride showed higher aqueous solubility (1668, 1529, 1551 mg/L; %RSD:1.38, 1.55, 1.56) than the free drug (697 mg/L; %RSD: 1.18). Permeation studies revealed improved permeability of the complexed drug (54.14%, 50.20%, 49.51%, %RSD: 1.75, 1.43, 1.39) than the free drug (18.91%, %RSD: 1.24). Dissolution profiles of free sulpiride and sulpiride from the metal complexes exhibited complete drug release in the first two hours in acidic pH. Permeation studies of the MCPN showed higher permeability of 96.55% (%RSD: 1.30) than the metal complex (54.14%, %RSD: 1.75). A sustained release of sulpiride from the MCPN was observed for at least 24 h.

Discussion. Metal complex-polymer nanocomposite shows potential as a sustained release drug delivery carrier for drugs with poor pharmacokinetics.

APPENDIX B2

Novel metal complex polymer nanocomposite with enhanced intestinal permeability and controlled release of sulpiride drug

Gretta C. M'bitsi-Iboully[1,a], Thashree Marimuthu[2,a], Yahya E. Choonara[3,a], Lisa C. du Toit[4,a], Pradeep Kumar[5,a], Girish Modi[6,b], Pierre P.D. Kondiah[7,a] and Viness Pillay*[,a]

[a] Wits Advanced Drug Delivery Platform Research Unit, Department of Pharmacy and Pharmacology, School of Therapeutic Sciences, Faculty of Health Sciences, University of the Witwatersrand, 7 York Road, Parktown 2193, Johannesburg, South Africa
[b] Department of Neurology, Division of Neurosciences, Faculty of Health Sciences, University of the Witwatersrand, 7 York Road, Parktown 2193, Johannesburg, South Africa

INTRODUCTION

Sulpiride (SPR) is a selective antagonist of central dopamine receptors used for the treatment of schizophrenia. However, this drug has limited clinical use due to its poor pharmacokinetics, which include short half-life and poor intestinal permeability.[1] This results in high doses of the drug being administrated and thus poor patient compliance due to side effects.

AIM

To prepare polymeric nanoparticles of a ternary metal complex of sulpiride (ruthenium(II)-liganded sulpiride and amino alcohol) to obtain a novel metal complex polymer nanocomposite (MCPN) and investigate its ability to improve the intestinal permeability of sulpiride and extend its half-life through sustained drug release.

METHODS

Preparation of MCPN

Fig.1 shows a schematic of MCPN preparation using the emulsion solvent evaporation method.

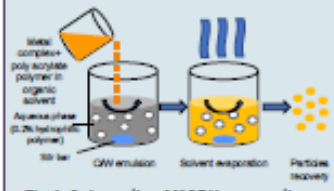


Fig.1. Schematic of MCPN preparation

Evaluation of prepared MCPN

- Mean particle size, polydispersity index (PDI) and zeta potential
- Entrapment efficiency (EE) and drug loading (DL)
- Morphological evaluation
- *Ex vivo* permeation studies (Fig.2).
- *In vitro* dug release studies (Fig.3)

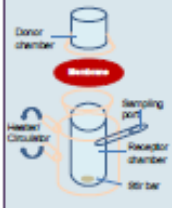


Fig.2. Schematic of Franz diffusion cell

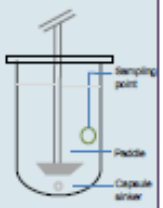


Fig.3. Schematic of rotating paddle method

RESULTS

Table 1. Mean particle size, zeta potential, percent entrapment efficiency and percent drug loading measurements for the MCPN

Particle size (nm) (±SD)	Polydispersity Index (PDI)	Zeta potential (mV) (±SD)	%EE (±SD)	%DL (±SD)
[illegible]	[illegible]	[illegible]	[illegible]	[illegible]

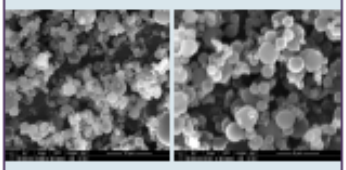


Fig. 4. Scanning electron micrographs (SEM) of MCPN

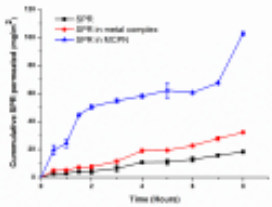


Fig.5. Permeation profiles of SPR, SPR in metal complex and SPR in MCPN when passed through the pig's intestine

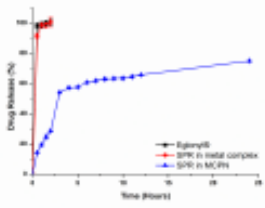


Fig.6. Dissolution profiles of Eglonyl® , SPR in metal complex and SPR in MCPN in gastric/intestinal pH simulated solutions (pH 1.2 for first 2 hours; pH 6.8 for following 4 hours; pH 7.4 up to 24 hours)

DISCUSSION

MCPN successfully prepared. Table 1 shows a monodispersed nano particle size with moderate electrostatic stability of the MCPN suspension.[2] The MCPN exhibited good EE and high DL.

Fig.4 shows SEM images of the MCPN at different magnifications, revealing a spherical shape with a relative smooth surface for the MCPN.

Fig 5. shows permeation profiles of free SPR, SPR in the metal complex and SPR in MCPN through the pig's small intestine. Higher amounts of SPR were permeated through the membrane from the MCPN. The increased intestinal permeability suggests improved lipophilicity of the drug, thus enhanced diffusion through the membrane.[3] This lipophilicity improvement can be attributed to the nano size of the MCPN.[4]

Fig.6 shows the drug release profiles of Eglonyl®, SPR in the metal complex and SPR in MCPN. The release of SPR was pH-sensitive. No SPR burst release was observed from the MCPN and a sustained drug release profile was observed up to 24 hours. The poly acrylate made the MCPN more stable in acidic pH, preventing the SPR burst release previously observed,[5] while the hydrophilic polymer enabled sustained SPR release up to 24 hours.[6]

CONCLUSION

MCPN improved SPR intestinal permeability and resulted in pH-controlled sustained release of SPR drug. MCPN shows potential for enhanced intestinal permeability and sustained release of drugs with poor pharmacokinetics

REFERENCES

1. Ibrahim *et al. Int J Nanomedicine.* 2014;9:129–44
2.Adibkia *et al. Colloids Surf B Biointerfaces.* 2011;83(1):155–9. .
3. Zakeri-Milani *et al. Colloids Surf B Biointerfaces.* 2013;103:174–81.
4. Sahoo *et al. Trop J Pharm Res.* 2005;4(1):369-375.
5. Williams *et al. J Nanobiotechnology.* 2006;14:62.
6. Yelnimez E. *Turk J Pharm Sci.* 2017;14(2):148–56.

ACKNOWLEDGEMENTS

- NRF research chair

APPENDIX C1

STRICTLY CONFIDENTIAL

ANIMAL ETHICS SCREENING COMMITTEE (AESC)

CLEARANCE CERTIFICATE NO. 2017/08/52/C

APPLICANT: Ms G Mbitsi-Iboully

SCHOOL: Pharmacy and Pharmacology
DEPARTMENT:
LOCATION:

PROJECT TITLE: In vivo assessment of innovative polymeric oral drug delivery systems in large white pigs

Number and Species

3X30(+/- 5) kg large white male pigs and 3X30(+/- 5) kg large white female pigs

Approval was given for the use of animals for the project described above at an AESC meeting held on 2017/08/29. This approval remains valid until 2019/10/08.
Unreported changes to the application may invalidate the clearance given by the AESC
An annual progress report must be provided

The use of these animals is subject to AESC guidelines for the use and care of animals, is limited to the procedures described in the application form and is subject to any additional conditions listed below:

Signed: _____ (Chairperson, AESC) Date: 11 October 2017

I am satisfied that the persons listed in this application are competent to perform the procedures therein, in terms of Section 23 (1) (c) of the Veterinary and Para-Veterinary Professions Act (19 of 1982)

Signed: _____ (Registered Veterinarian) Date: 11/10/2017

cc: Supervisor: Professor V Pillay
Director: CAS

Works 2000/lain0015/AESCCert.wps

APPENDIX C2

UNIVERSITY OF THE WITWATERSRAND, JOHANNESBURG
7 York Road, Parktown, 2193 South Africa * E-mail physiology@health.wits.ac.za * Telephone (011)717-2363 * Fax (011) 643-2765

14 November 2014

Attention: Gretta Mbitsi-Ibouily,

Re: Request for permission to collect pig tissue samples

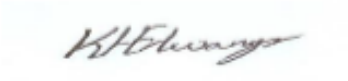
This letter serves to inform you that your request to collect tissue samples from pigs has been considered by the Exco of the AESC.

You are hereby granted permission to collect gastric and intestinal tissue from fifteen dead pigs which have been euthanased for other studies in the Central Animal Services (CAS).

Liaise with the director of the CAS to arrange the logistics.

If you would like any further information in this regard, do not hesitate to contact me.

Yours sincerely,



Kennedy Erlwanger
(Chairman: Animal Ethics Screening Committee, University of the Witwatersrand)

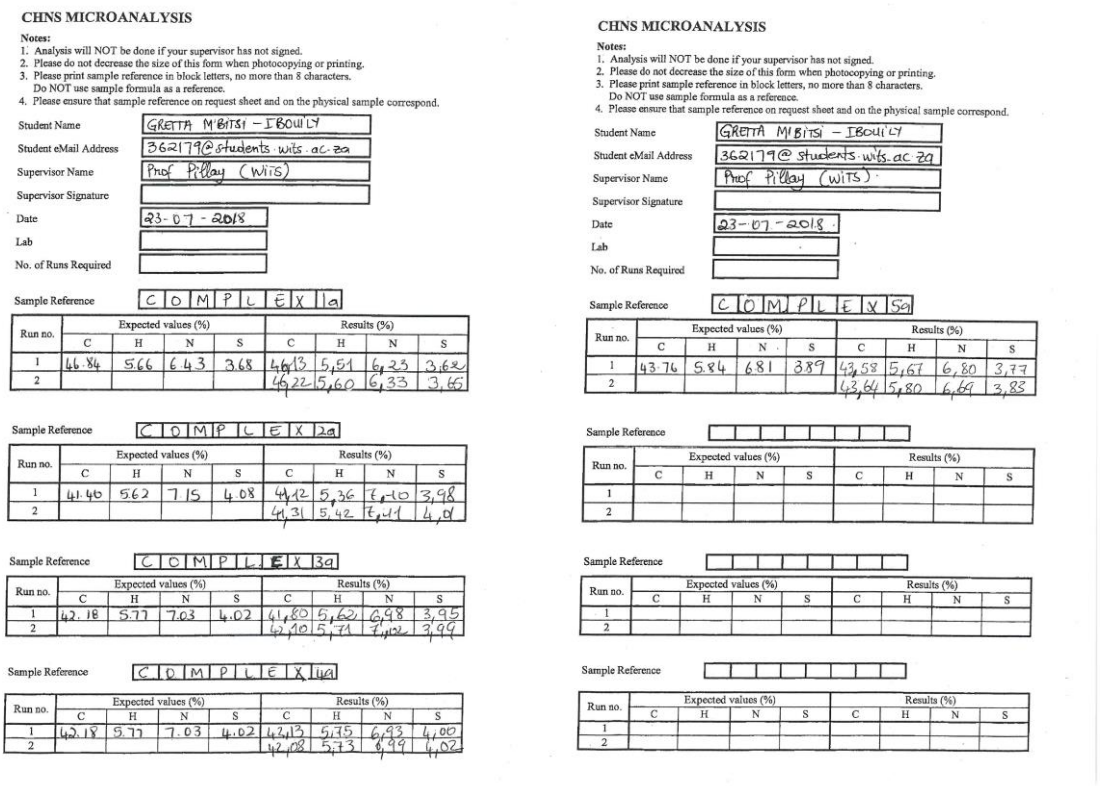
Reference: Gretta Mbitsi-Ibouily 14-11-14 O

Assoc Prof Kennedy H. Erlwanger
School of Physiology
Faculty of Health Sciences, University of the Witwatersrand
7 York Road, Parktown, 2193
SOUTH AFRICA

Private bag 3, Wits, 2050, South Africa
Tel: +27 (0)11 717 2454
Fax: + 27 (0)11 643 2765
Email: Kennedy.Erlwanger@wits.ac.za

APPENDIX D

Supplementary information is shown below.



CHNS MICROANALYSIS

Notes:
1. Analysis will NOT be done if your supervisor has not signed.
2. Please do not decrease the size of this form when photocopying or printing.
3. Please print sample reference in block letters, no more than 8 characters. Do NOT use sample formula as a reference.
4. Please ensure that sample reference on request sheet and on the physical sample correspond.

Student Name	GRETTA M'BITSI – IBOUILY
Student eMail Address	362179@students.wits.ac.za
Supervisor Name	Prof Pillay (WITS)
Supervisor Signature	
Date	23-07-2018
Lab	
No. of Runs Required	

Sample Reference: COMPLEX 1a

Run no.	Expected values (%)				Results (%)			
	C	H	N	S	C	H	N	S
1	46.84	5.66	6.43	3.68	46,13	5,51	6,23	3,62
2					46,22	5,60	6,33	3,65

Sample Reference: COMPLEX 2a

Run no.	Expected values (%)				Results (%)			
	C	H	N	S	C	H	N	S
1	41.40	5.62	7.15	4.08	4,12	5,36	[illegible]	3,98
2					4,31	5,42	[illegible]	4,01

Sample Reference: COMPLEX 3a

Run no.	Expected values (%)				Results (%)			
	C	H	N	S	C	H	N	S
1	42.18	5.77	7.03	4.02	41,80	5,62	6,98	3,95
2					42,10	5,71	[illegible]	3,99

Sample Reference: COMPLEX 4a

Run no.	Expected values (%)				Results (%)			
	C	H	N	S	C	H	N	S
1	42.18	5.77	7.03	4.02	42,13	5,75	6,93	4,00
2					42,08	5,73	6,99	4,02

CHNS MICROANALYSIS

Notes:
1. Analysis will NOT be done if your supervisor has not signed.
2. Please do not decrease the size of this form when photocopying or printing.
3. Please print sample reference in block letters, no more than 8 characters. Do NOT use sample formula as a reference.
4. Please ensure that sample reference on request sheet and on the physical sample correspond.

Student Name	GRETTA MBITSI – IBOUILY
Student eMail Address	362179@students.wits.ac.za
Supervisor Name	Prof Pillay (WITS)
Supervisor Signature	
Date	23-07-2018
Lab	
No. of Runs Required	

Sample Reference: COMPLEX 5a

Run no.	Expected values (%)				Results (%)			
	C	H	N	S	C	H	N	S
1	43.76	5.84	6.81	3.89	43,58	5,67	6,80	3,77
2					43,64	5,80	6,69	3,85

Sample Reference:

Run no.	Expected values (%)				Results (%)			
	C	H	N	S	C	H	N	S
1								
2								

Sample Reference:

Run no.	Expected values (%)				Results (%)			
	C	H	N	S	C	H	N	S
1								
2								

Sample Reference:

Run no.	Expected values (%)				Results (%)			
	C	H	N	S	C	H	N	S
1								
2								

Figure S1. Elemental analysis results of complexes 1a-5a

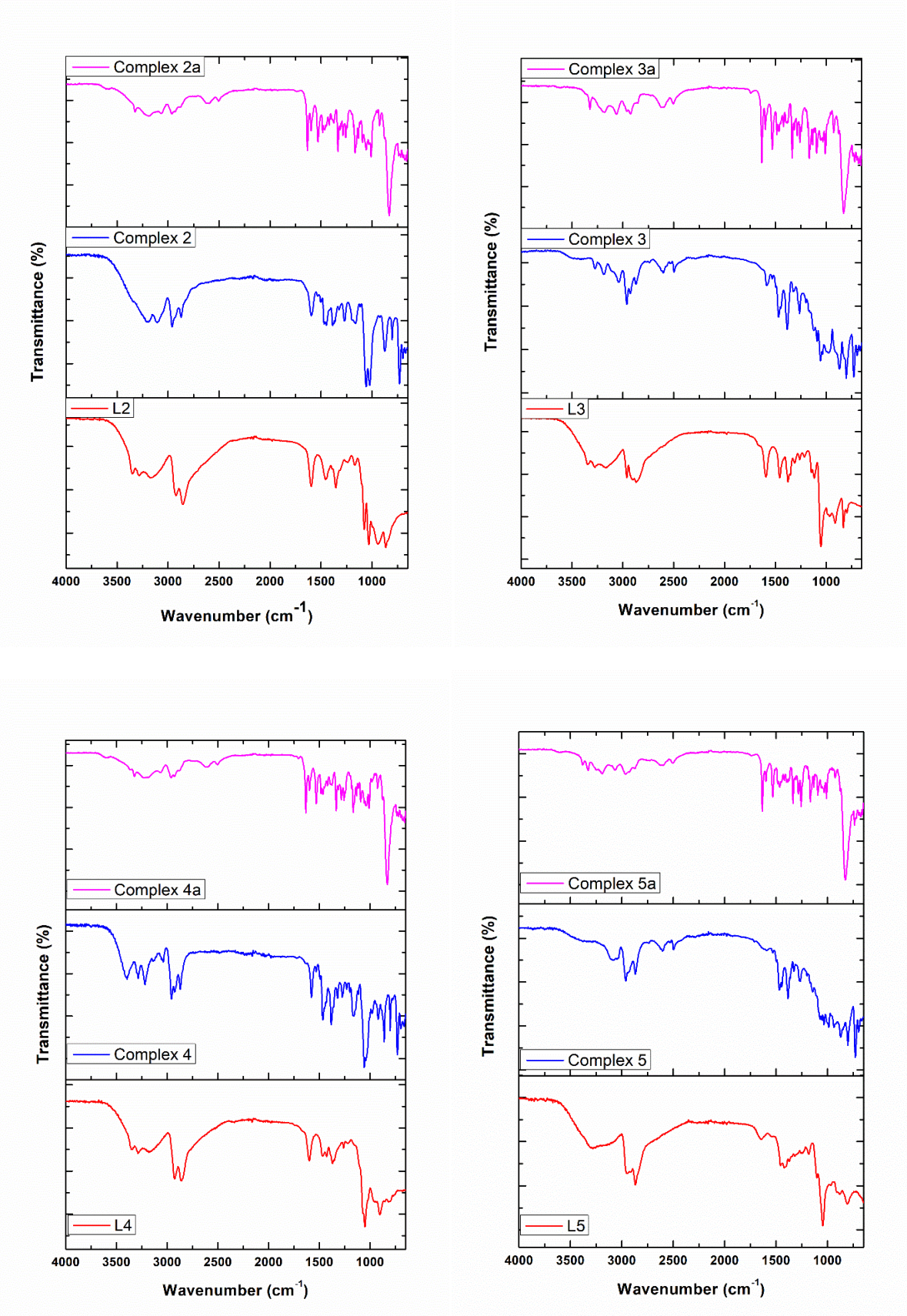
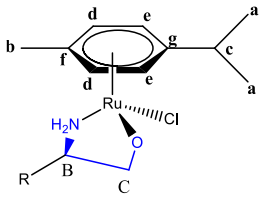


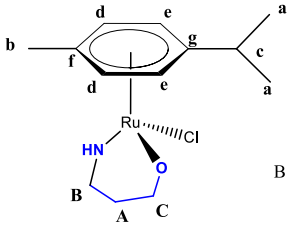
Figure S2. FTIR spectra of L2-5, Complexes **2-5** and complexes **2a-5a**

Table S1. Selected ^{1}H NMR (500 MHz, DMSO-d6) and ^{13}C NMR (126 MHz, DMSO-d6) chemical shifts (ppm) of ligands L1-L5, complexes **1-5** and complexes **1a-5a.**

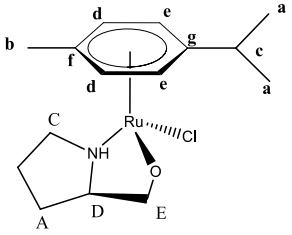


1 L1, R = CH_2-C_6H_6
2 L2, No R
3 L3, R = CH_3

Complexes 1-3



Complex 4



Complex 5

	H-C=C-H, *p*-cymene) ^{1}H NMR	^{13}C NMR	CH_2-NH_2 ^{1}H NMR	^{13}C NMR	O-CH_2 ^{1}H NMR	^{13}C NMR
L1	-	-	3.16 - 2.82(m)	54.31	3.68 (dd, J = 10.7, 3.8 Hz, 1H), 3.45 (dd, J = 10.6, 7.2 Hz, 1H)	40.96
L2	-	-	2.73 (m)	43.79	3.51 (m)	63.25
L3	-	-	2.96 (dddd, J = 10.5, 7.8, 6.5, 3.9 Hz)	48.41	3.48 (dd, J = 10.6, 4.0 Hz, 1H), 3.20 (dd, J = 10.6, 7.8 Hz, 1H)	68.17
L4	-	-	2.78-2.74 (m)	40.14	3.61-3.58 (m)	61.22
L5	-	-	2.91-2.73 (m)		3.49 (s, 1H), 3.29 (dd, J = 10.9, 7.4 Hz, 1H)	
Complex 1	5.79 (m, 4H)	81.12 (CH) 80.73 (CH)	2.88 (s)	59.54	3.06 (m)	39.14
Complex 2	5.57 (d, J = 5.8 Hz, 2H), 5.42 (d, J = 5.7 Hz, 2H)	82.76 (CH) 80.93 (CH)	3.14 (bs)	52.28	3.75 (bs),	62.63
Complex 3	5.95 (d, J = 5.3 Hz, 1H), 5.85 (s, 1H,), 5.82 (d, J = 5.4 Hz, 1H), 5.60 (m, 1H)	81.02 (CH), 80.74 (CH), 80.06 (CH), 78.58 (CH)	2.88 (bs)	39.16	3.23 (s),	67.13
Complex 4	5.45 (d, J = 5.9 Hz, 2H), 5.37 (d, J = 5.9 Hz, 2H)	81.22 (CH), 80.41 (CH)	3.75 (t, J = 5.1 Hz, 2H)	47.61	3.23 (m)	60.71
Complex 5	6.01 (d, J = 32.0 Hz, 1H), 5.83 (1H, CH), 5.78 (d, J = 46.1 Hz, 1H) 5.73 (1H, CH)	81.42 (CH), 81.06 (CH), 80.66 (CH), 79.85 (CH)	2.20 (s)	49.40	3.29 (s)	68.61
Complex 1a	5.81 (m, 1H), 5.76 (s, 1H), 5.37 (m, 2H)	86.35 (CH), 85.50 (CH)	3.14 (m)	53.82	3.50 (m)	60.36
Complex 2a	5.61 (m, 2H), 5.44 (m, 2H),	82.50 (CH), 80.26 (CH)	2.92 (s)	51.46	3.47 (m)	61.30
Complex 3a	5.79 (d, J = 15.3 Hz, 4H)	86.33 (CH), 85.49 (CH)	2.88 (bs)	48.45	3.23 (s)	62.17
Complex 4a	5.61 (d, J = 5.5 Hz, 1H), 5.52 (q, J = 5.9, 5.0 Hz), 5.45 (d, J = 6.0 Hz, 1H), 5.41 (d, J = 5.7 Hz, 1H)	86.29 (CH); 85.44 (CH)	2.88 (m)	46.95	3.45 (m)	58.65
Complex 5a	5.79 (d, J = 15.8 Hz, 2H), 5.48 (dd, J = 118.6, 5.5 Hz, 2H)	86.34 (CH), 85.49 (CH)	2.98 (s)	27.94	3.12 (s)	60.78

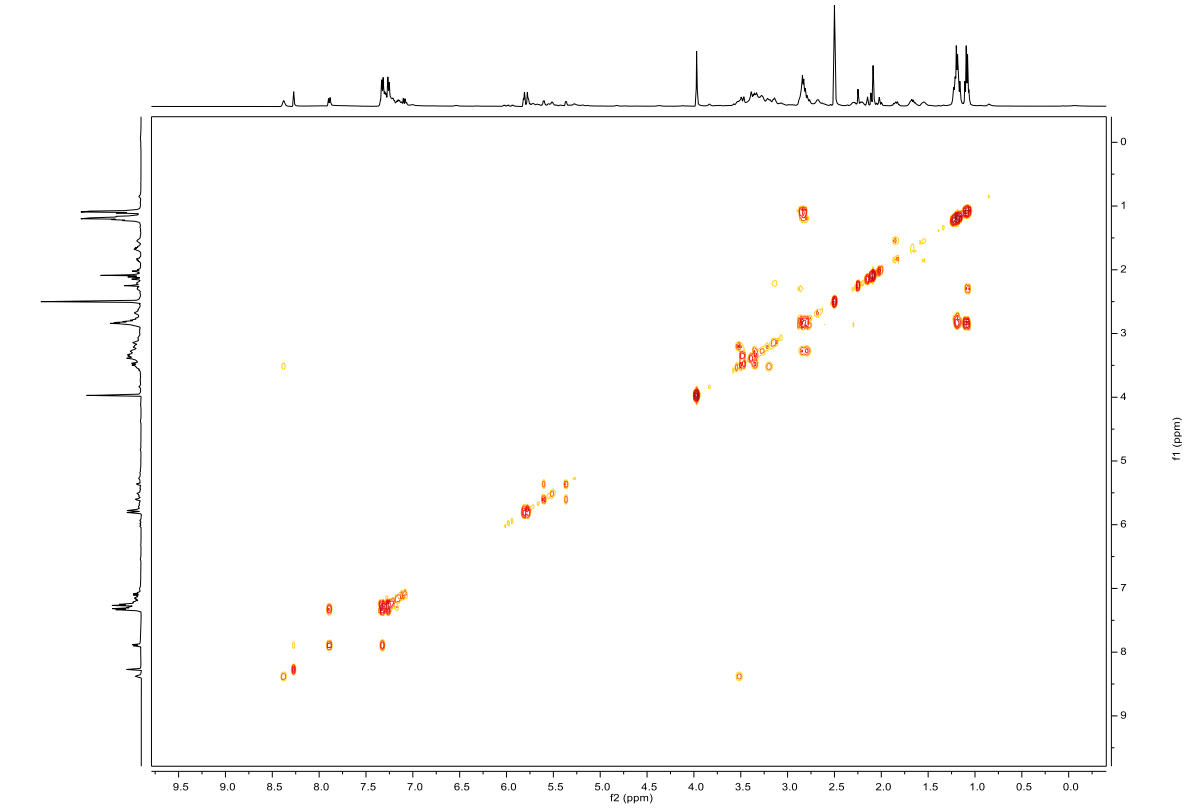


Figure S3. COSY (500 MHz, DMSO-d6) of complex **1a**

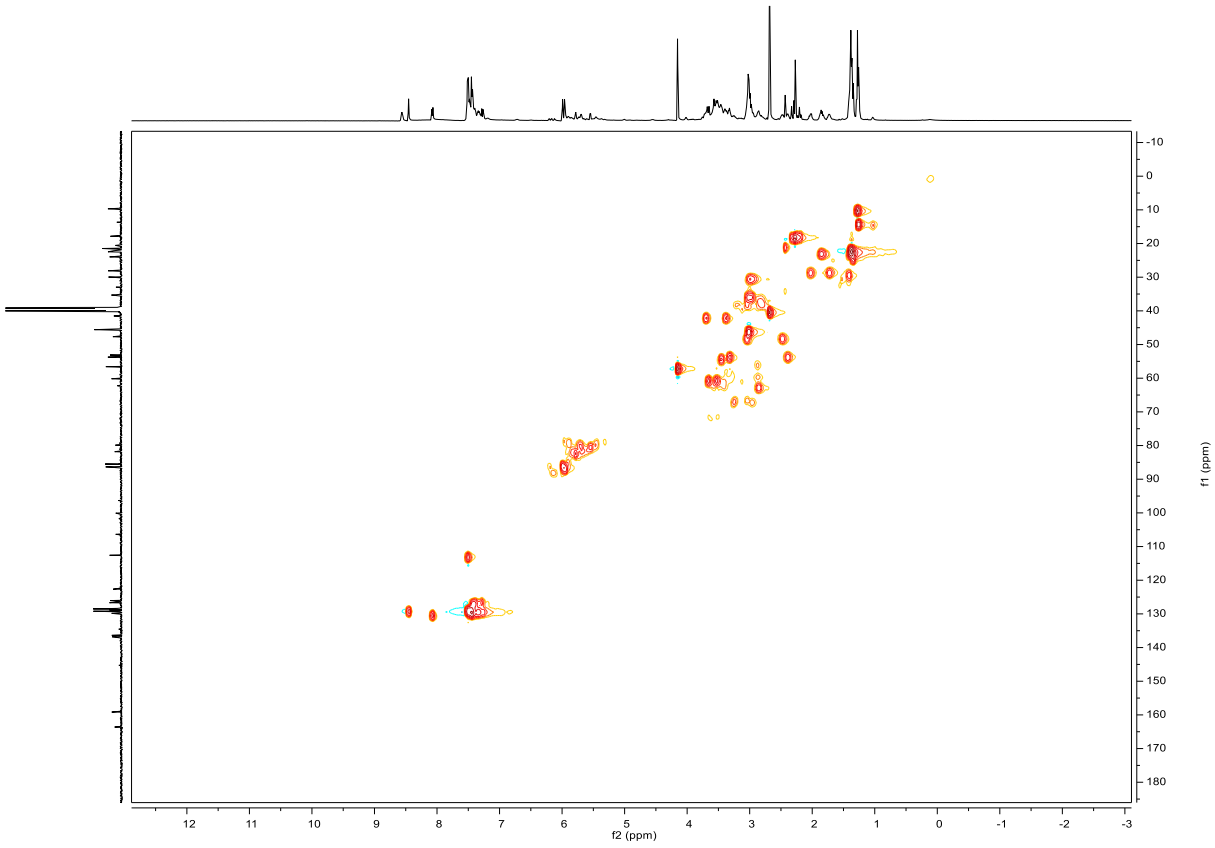


Figure S4. HMQC (500 MHz, DMSO-d6) of complex **1a**

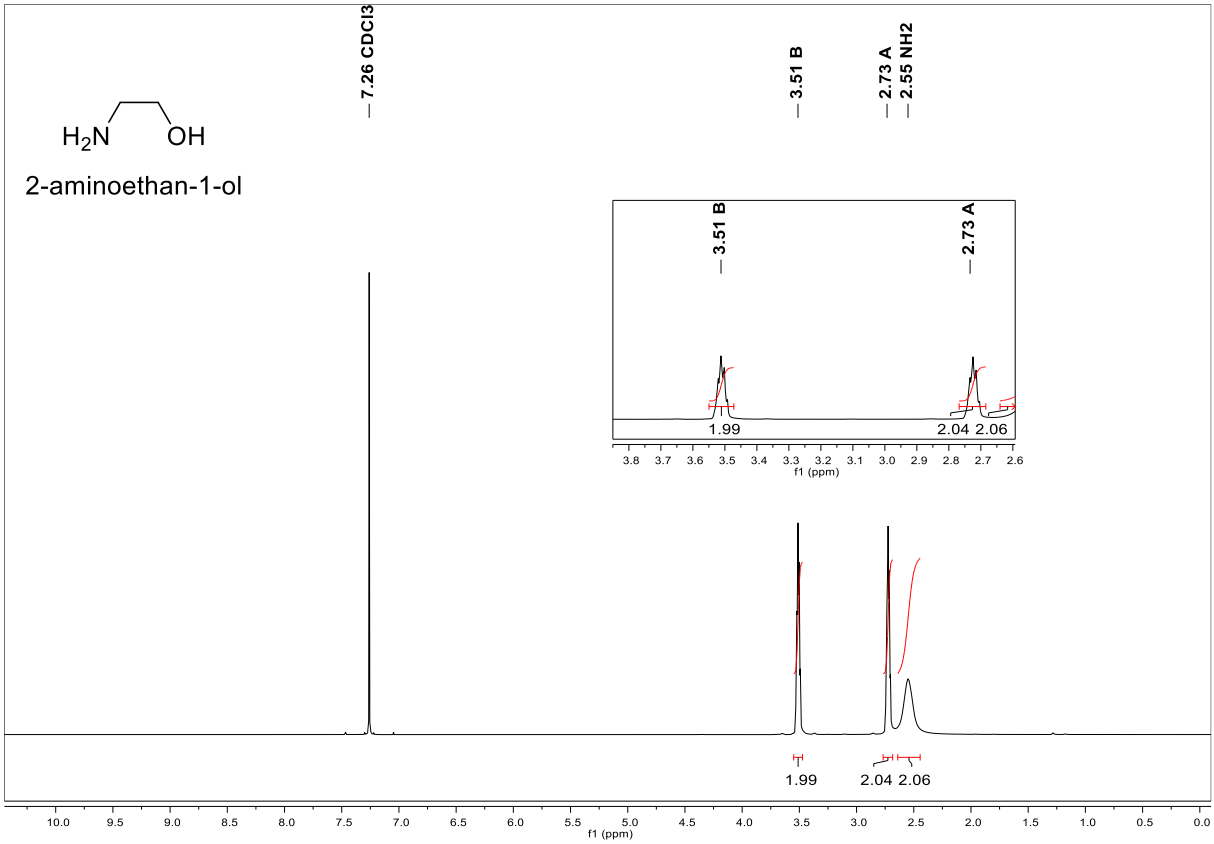


Figure S5. ^{1}H NMR (500 MHz, Chloroform-*d*) of 2-aminoethan-1-ol (L2)

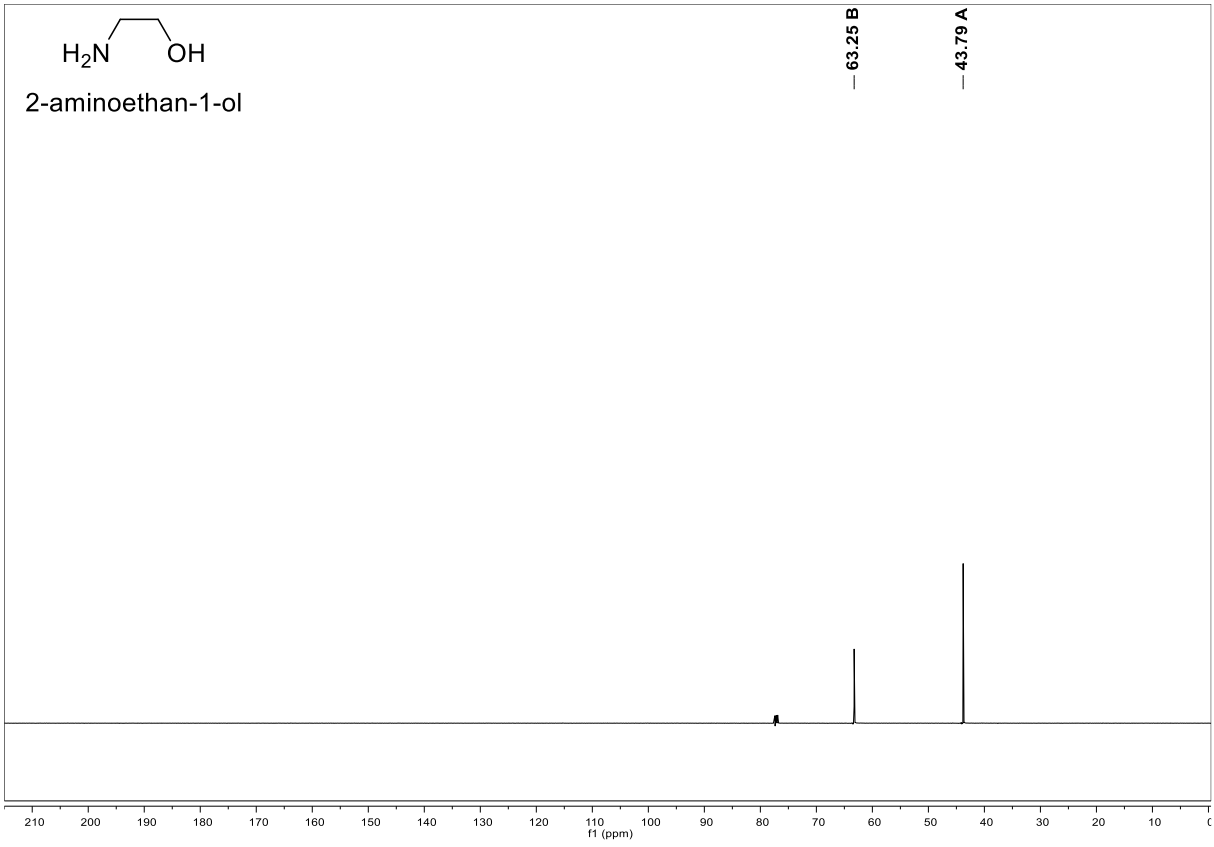


Figure S6.^{13}C NMR (126 MHz, Chloroform-*d*) of 2-aminoethan-1-ol (L2)

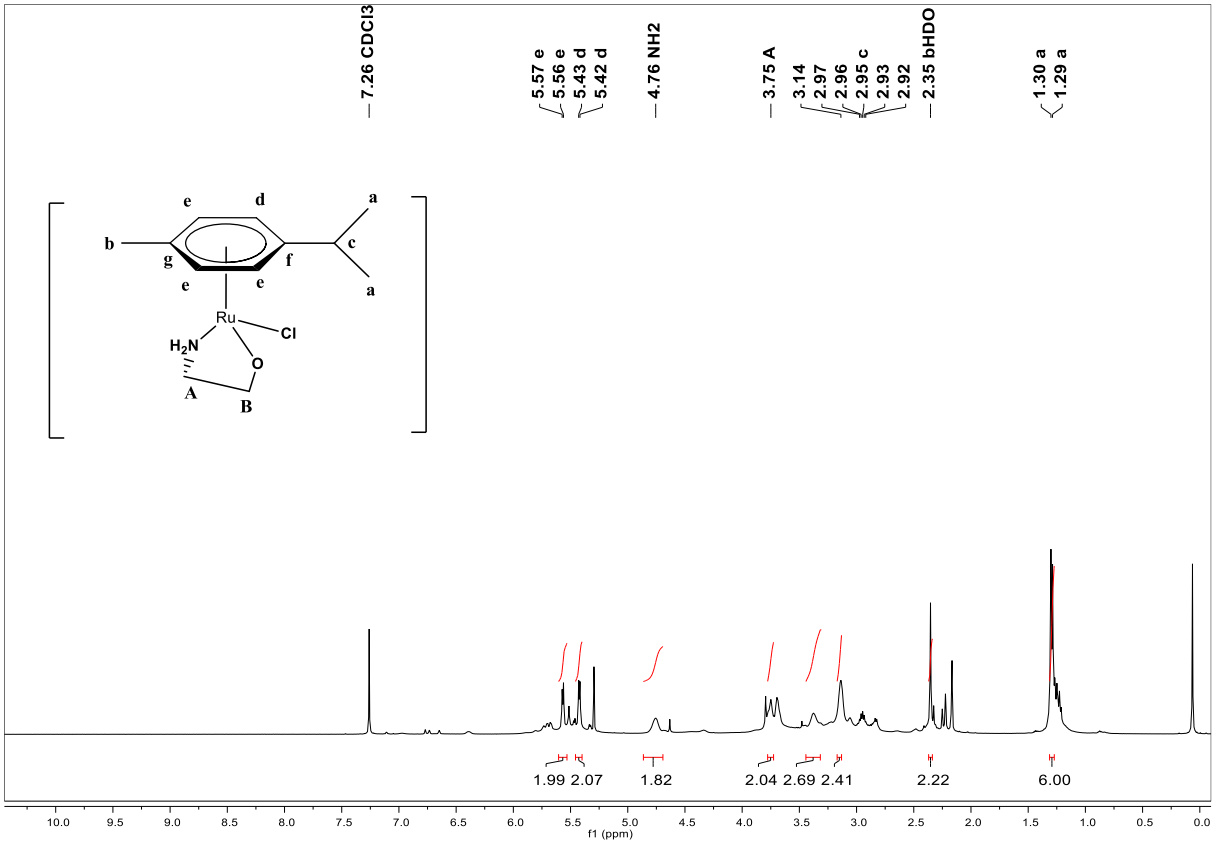


Figure S7. ^{1}H NMR (500 MHz, Chloroform-*d*) of complex **2**

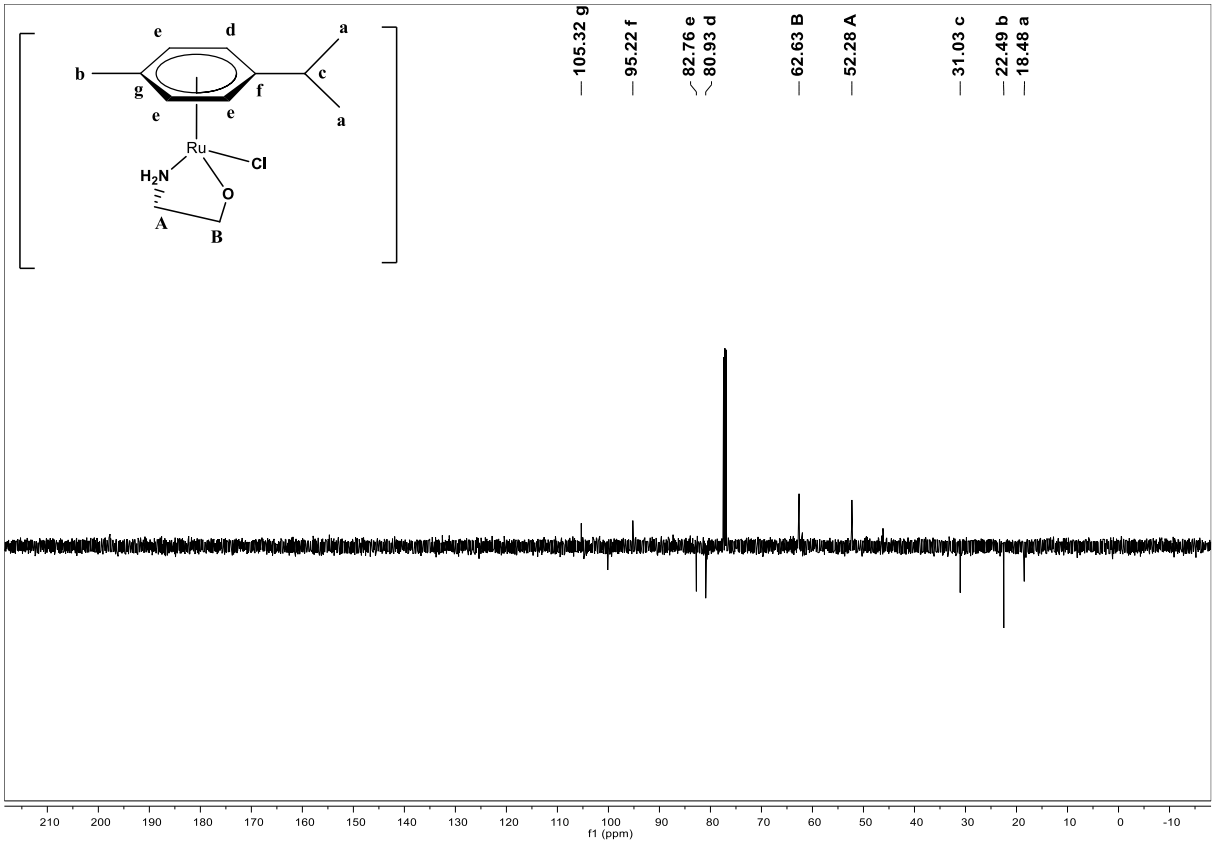


Figure S8.^{13}C NMR (126 MHz, Chloroform-*d*) of complex **2**

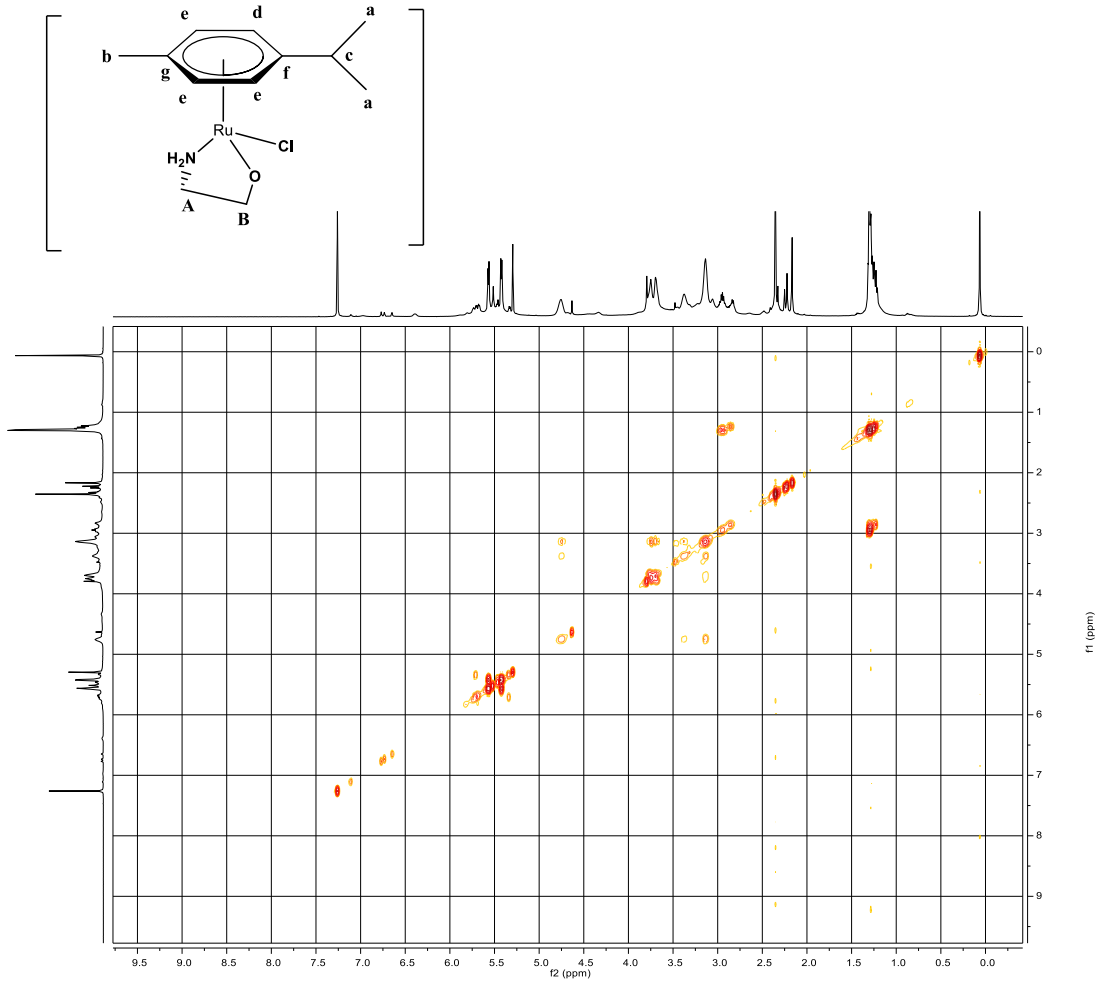


Figure S9. COSY (300 MHz, Chloroform-*d*) of complex **2**

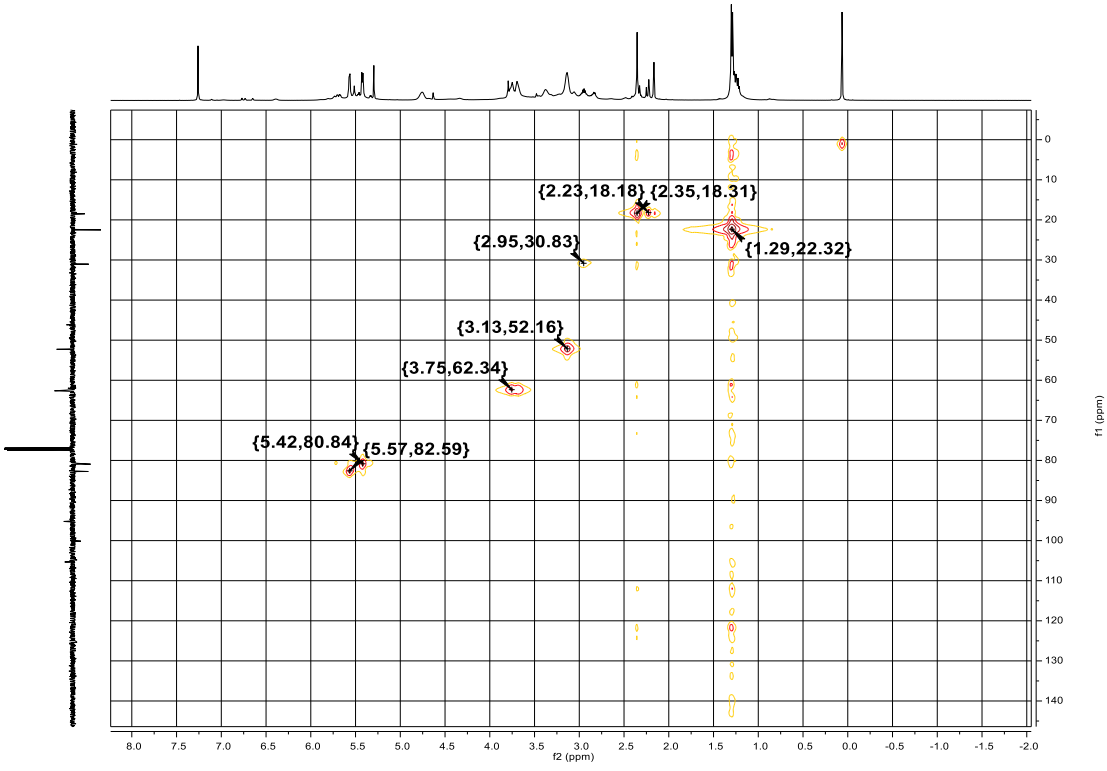


Figure S10. HMQC (126 MHz, Chloroform-*d*) of complex **2**

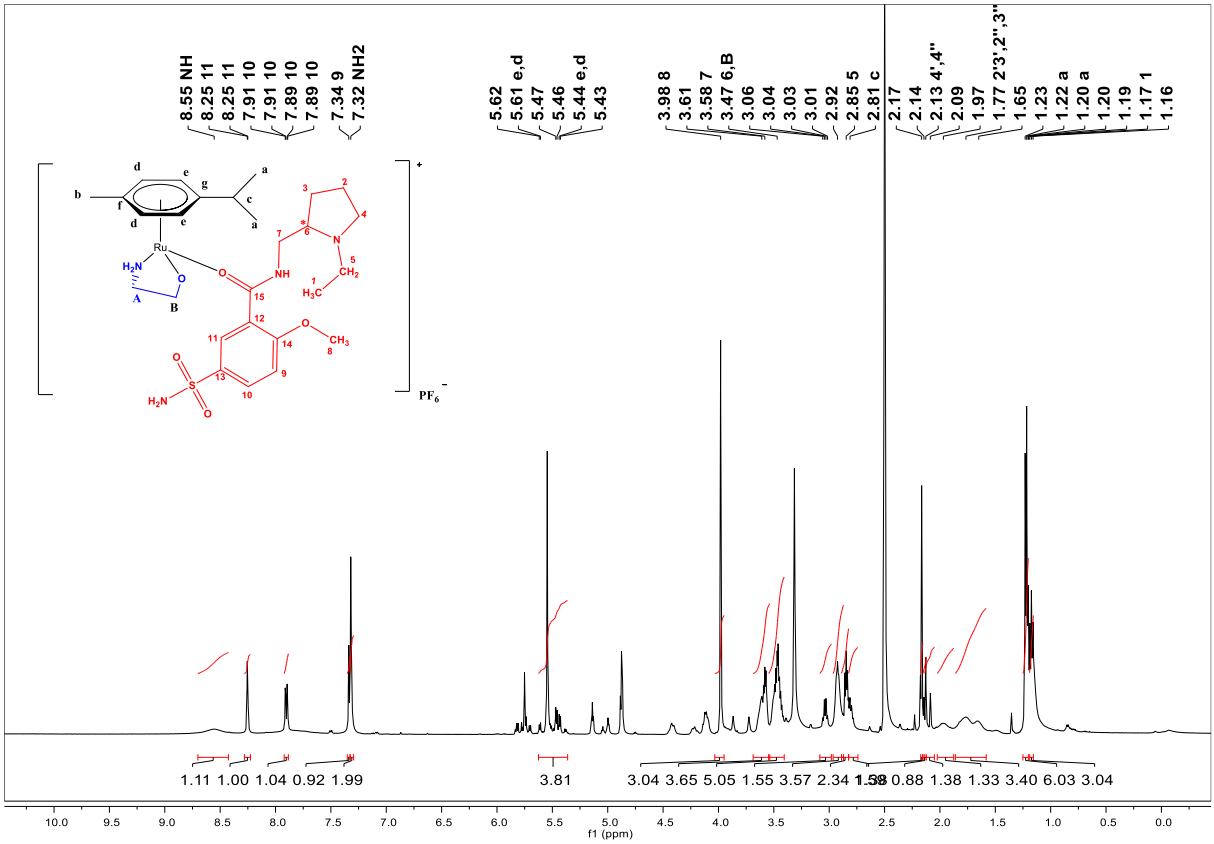


Figure S11. ^{1}H NMR (126 MHz, DMSO-d6) of complex **2a**

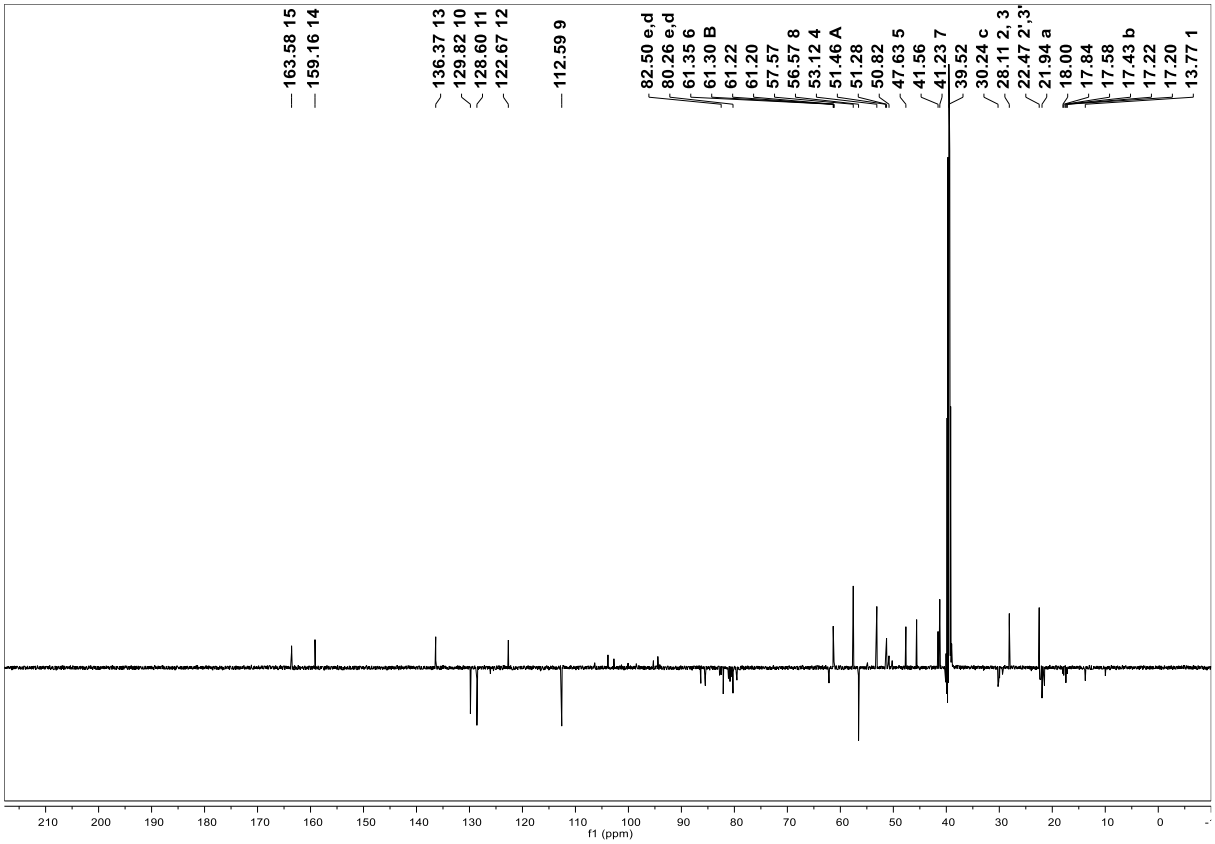


Figure S12. ^{13}C NMR (126 MHz, DMSO-d6) of complex **2a**

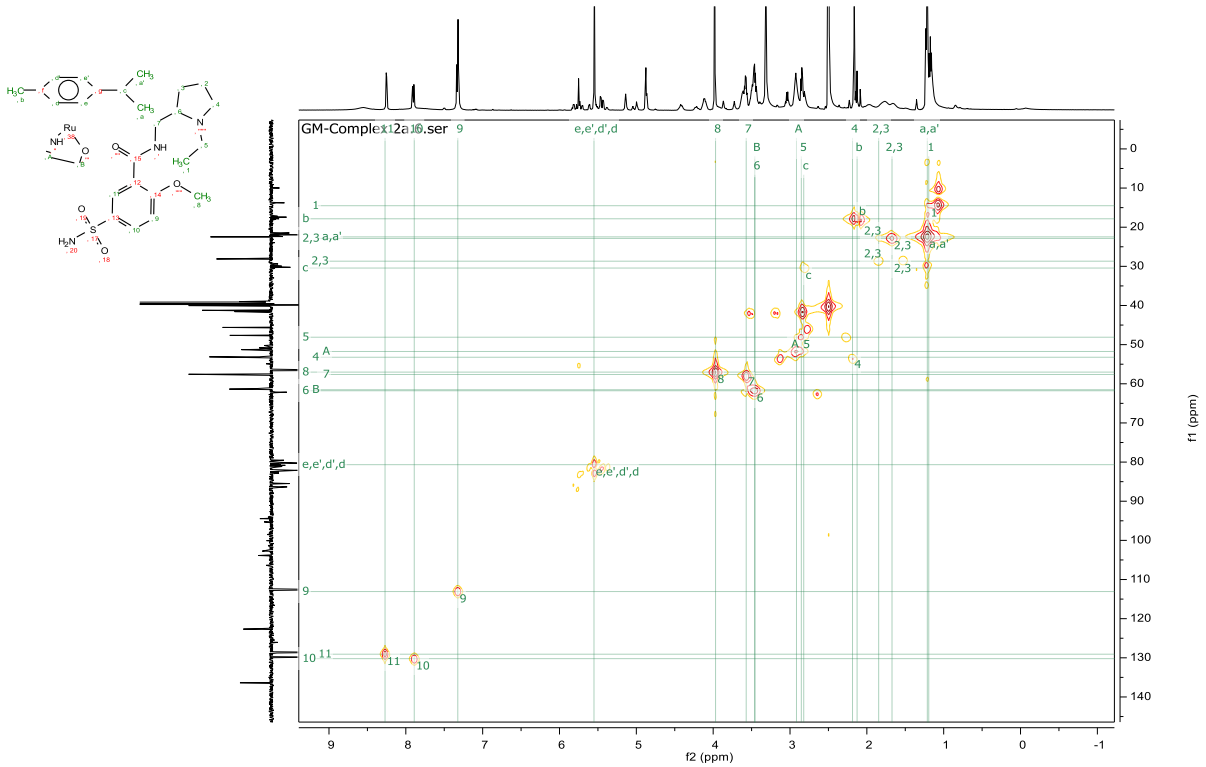


Figure S13. HMQC (126 MHz, DMSO-d6) of complex **2a**

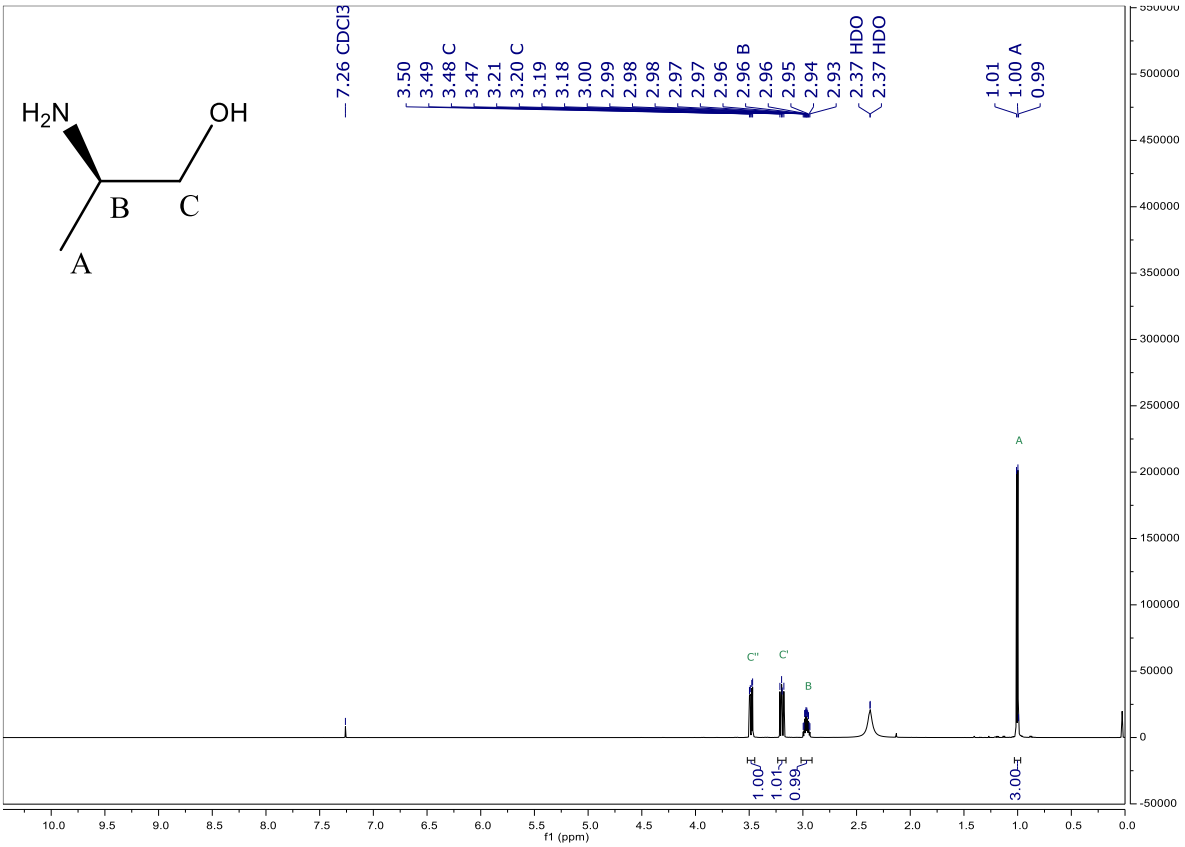


Figure S14. ^{1}H NMR (500 MHz, Chloroform-*d*) of (L3)

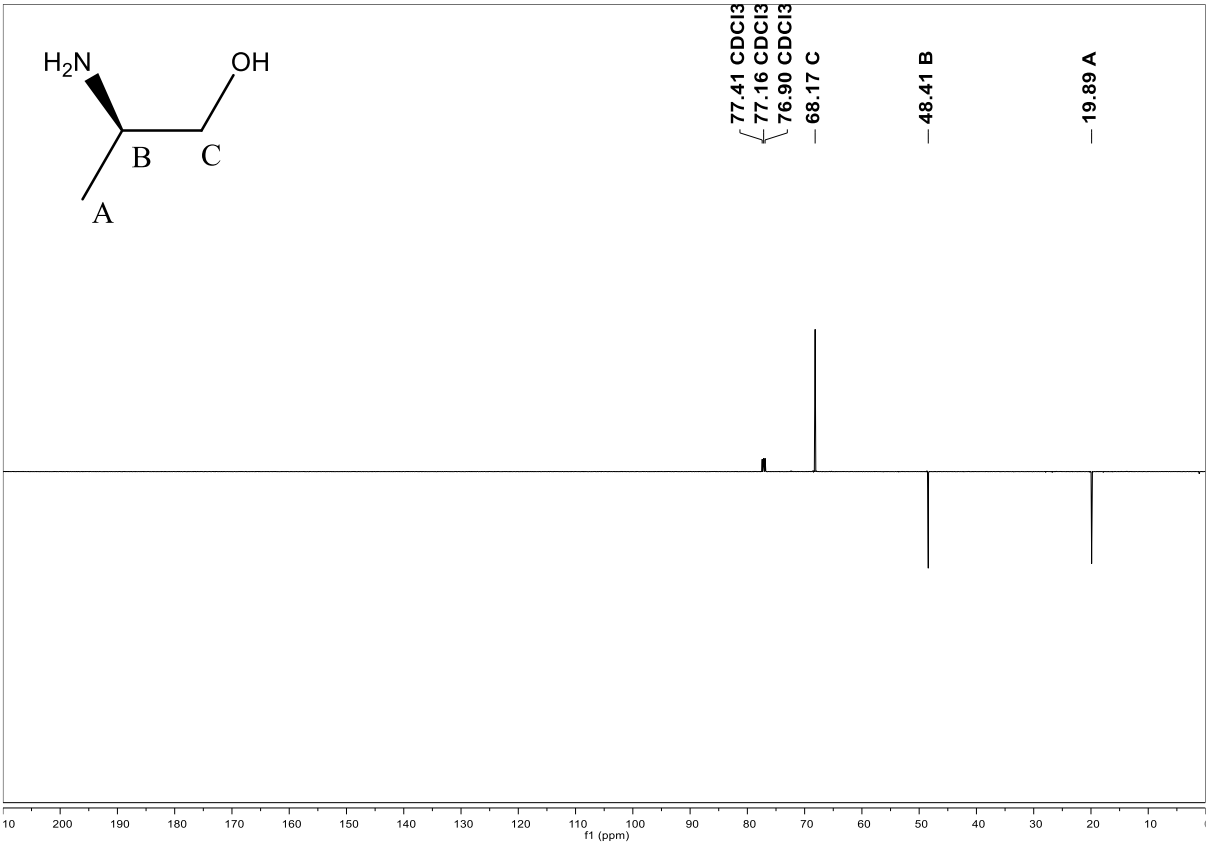


Figure S15. ^{13}C NMR (500 MHz, Chloroform-*d*) of (L3)

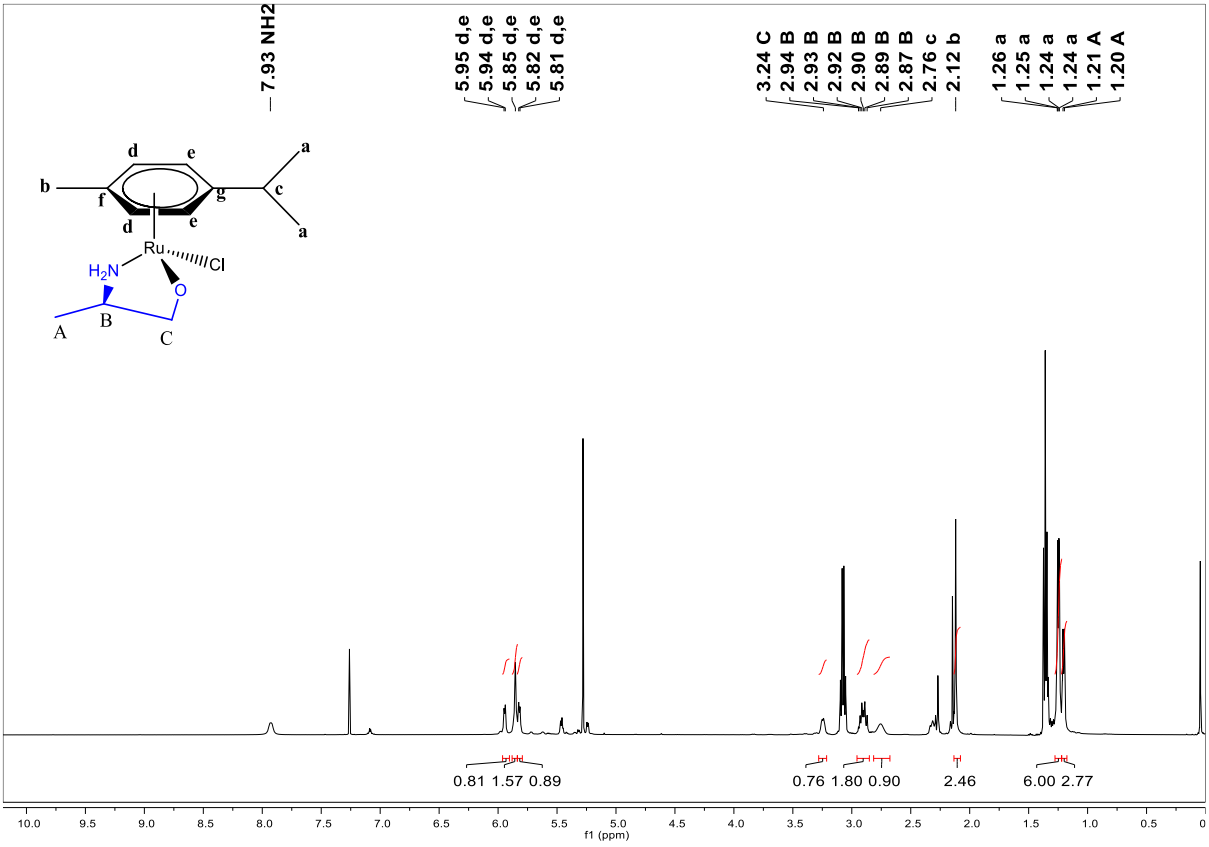


Figure S16. ^{1}H NMR (500 MHz, Chloroform-*d*) of Complex **3**

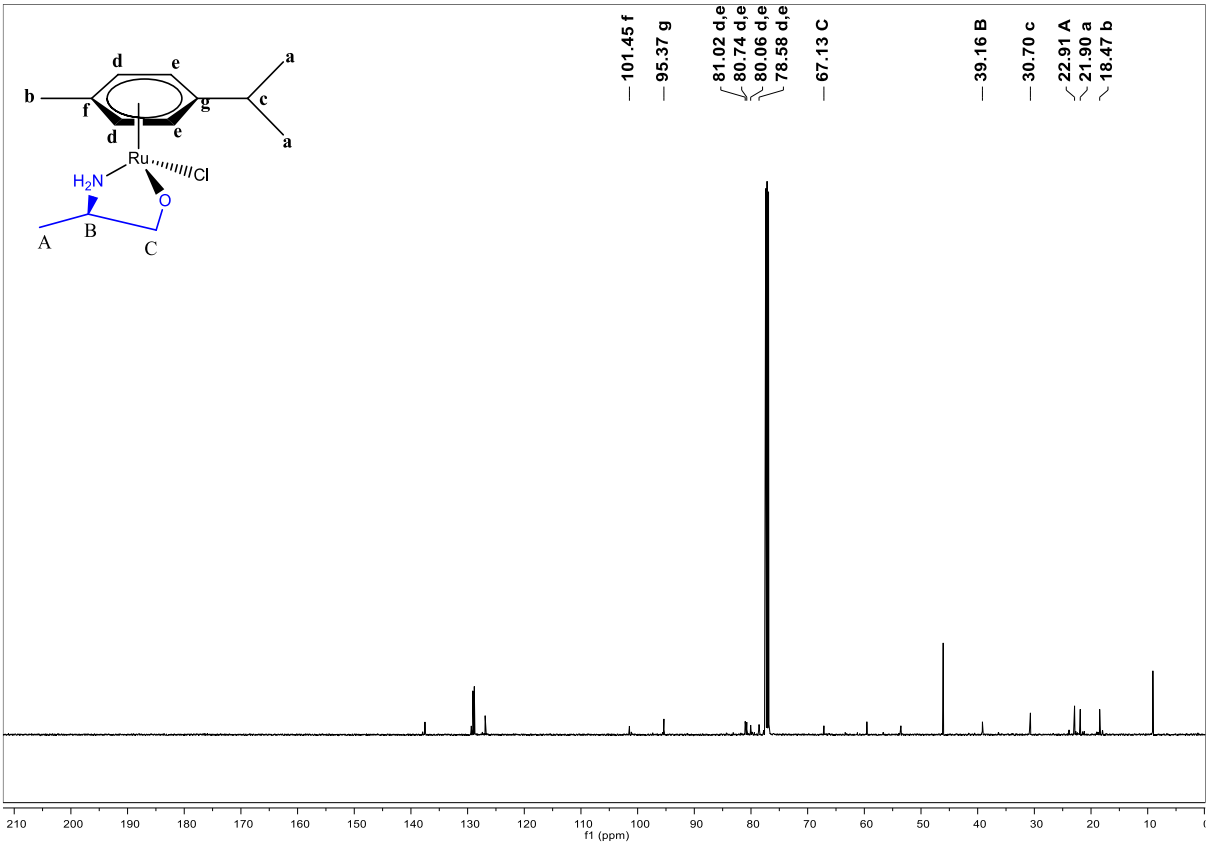


Figure S17. ^{13}C NMR (500 MHz, Chloroform-*d*) of Complex **3**

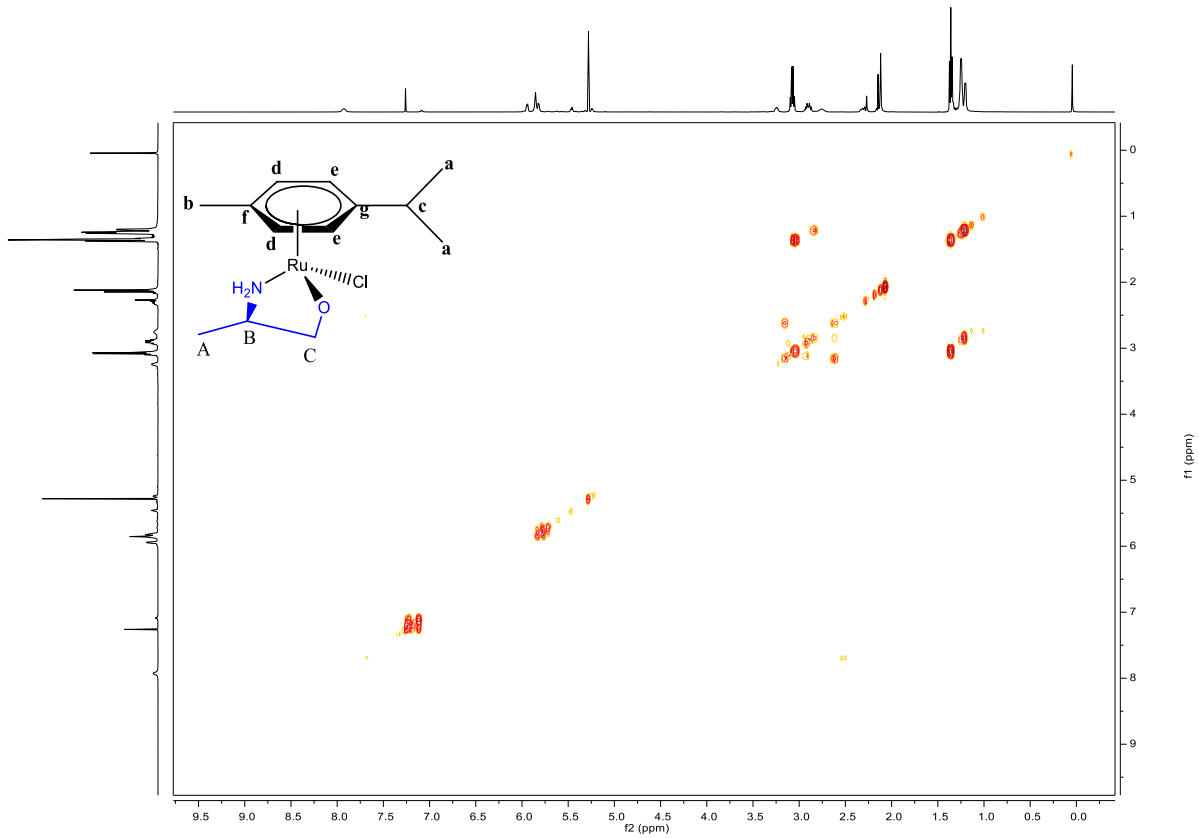


Figure S18. COSY NMR (500 MHz, Chloroform-*d*) of Complex **3**

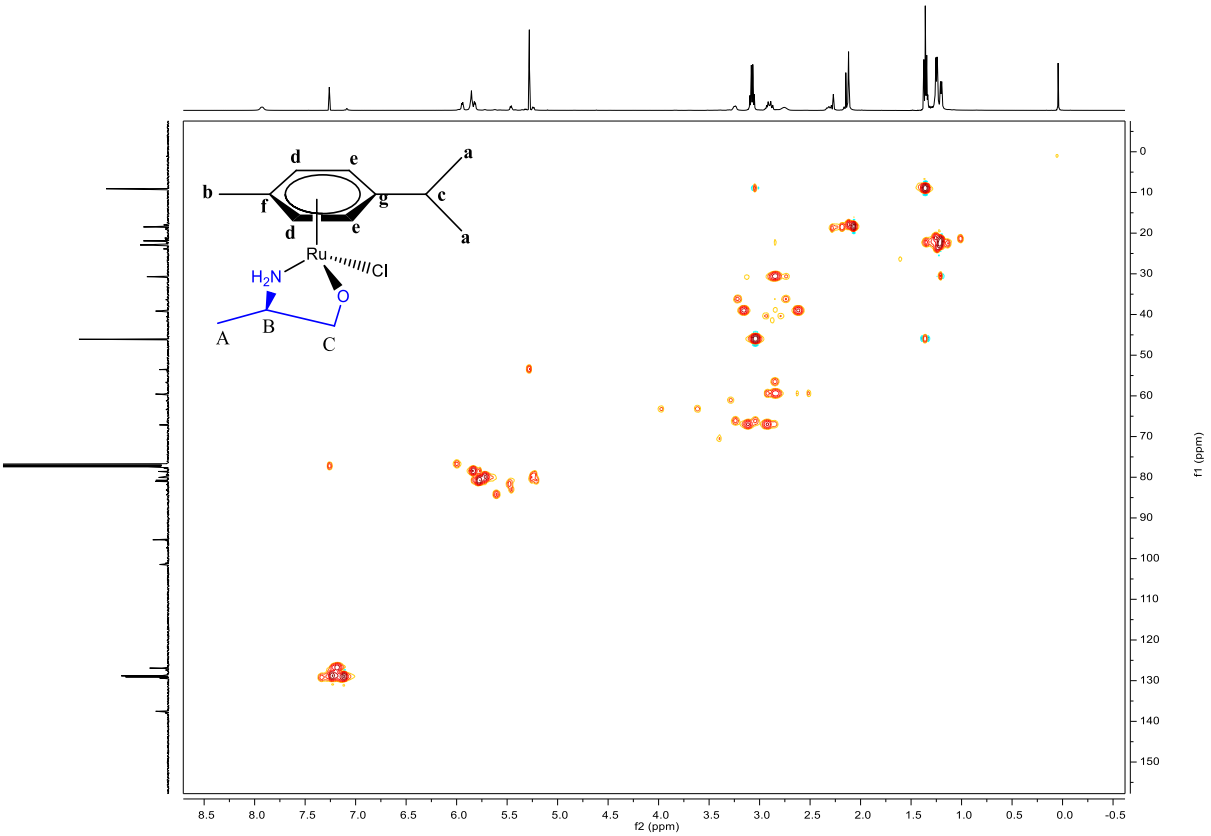


Figure S19. HSQC NMR (500 MHz, Chloroform-*d*) of Complex **3**

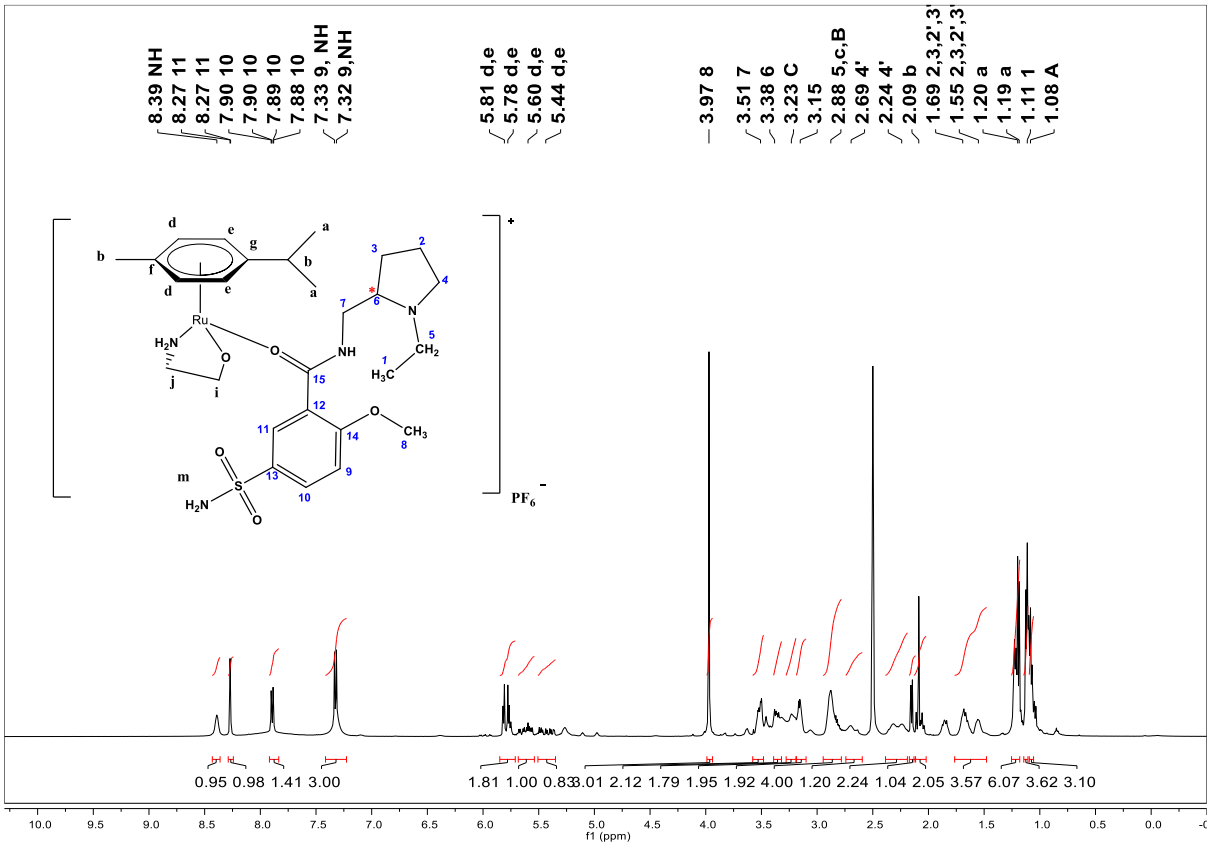


Figure S20. ^{1}H NMR (500 MHz, DMSO-*d6*) of Complex **3a**

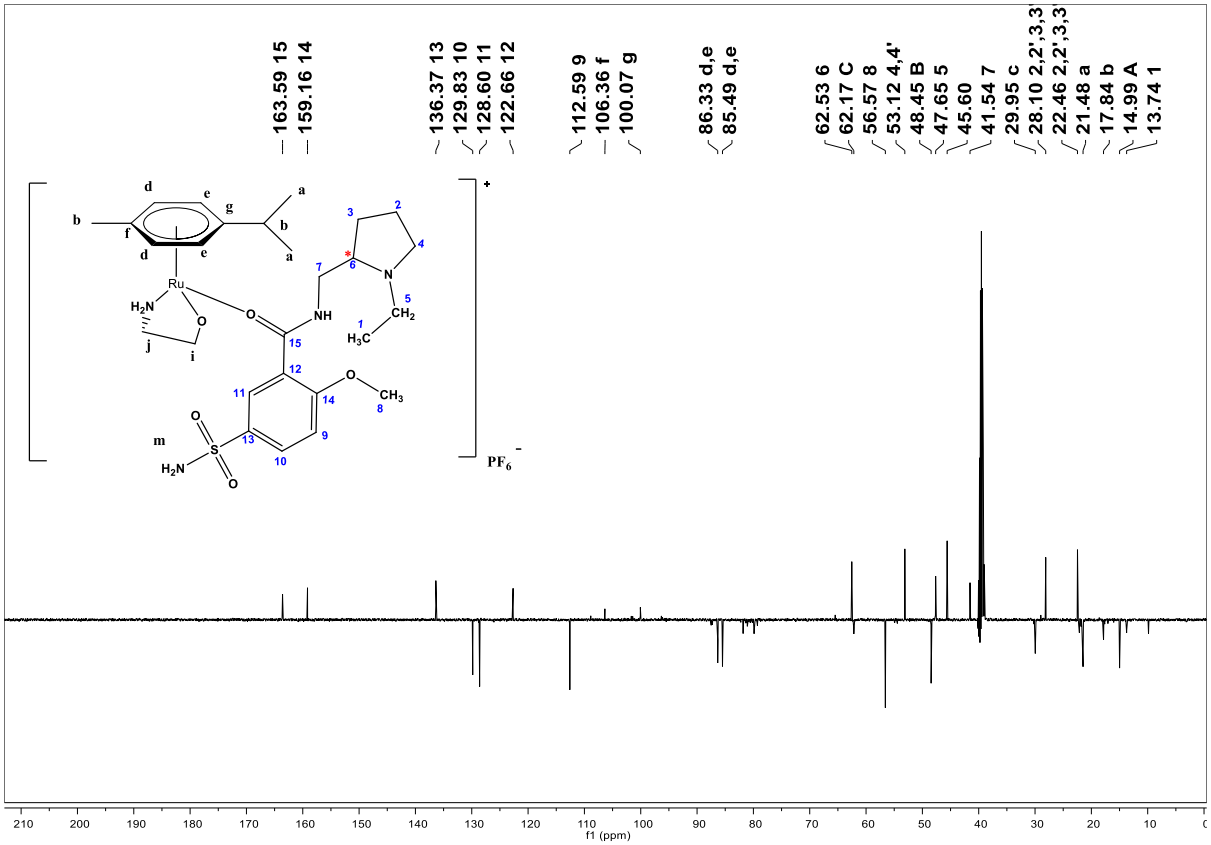


Figure S21. ^{13}C NMR (500 MHz, DMSO-*d6*) of Complex **3a**

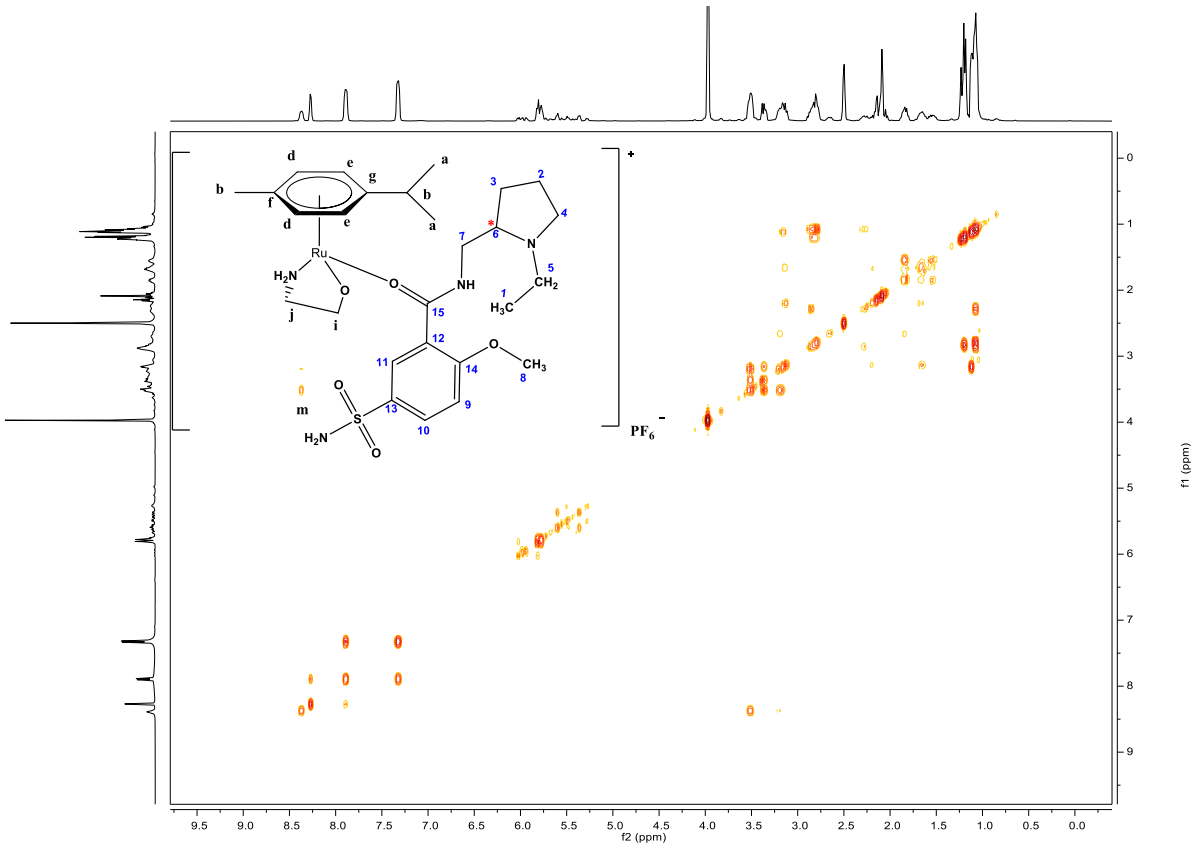


Figure S22. COSY NMR (500 MHz, , DMSO-*d6*) of Complex **3a**

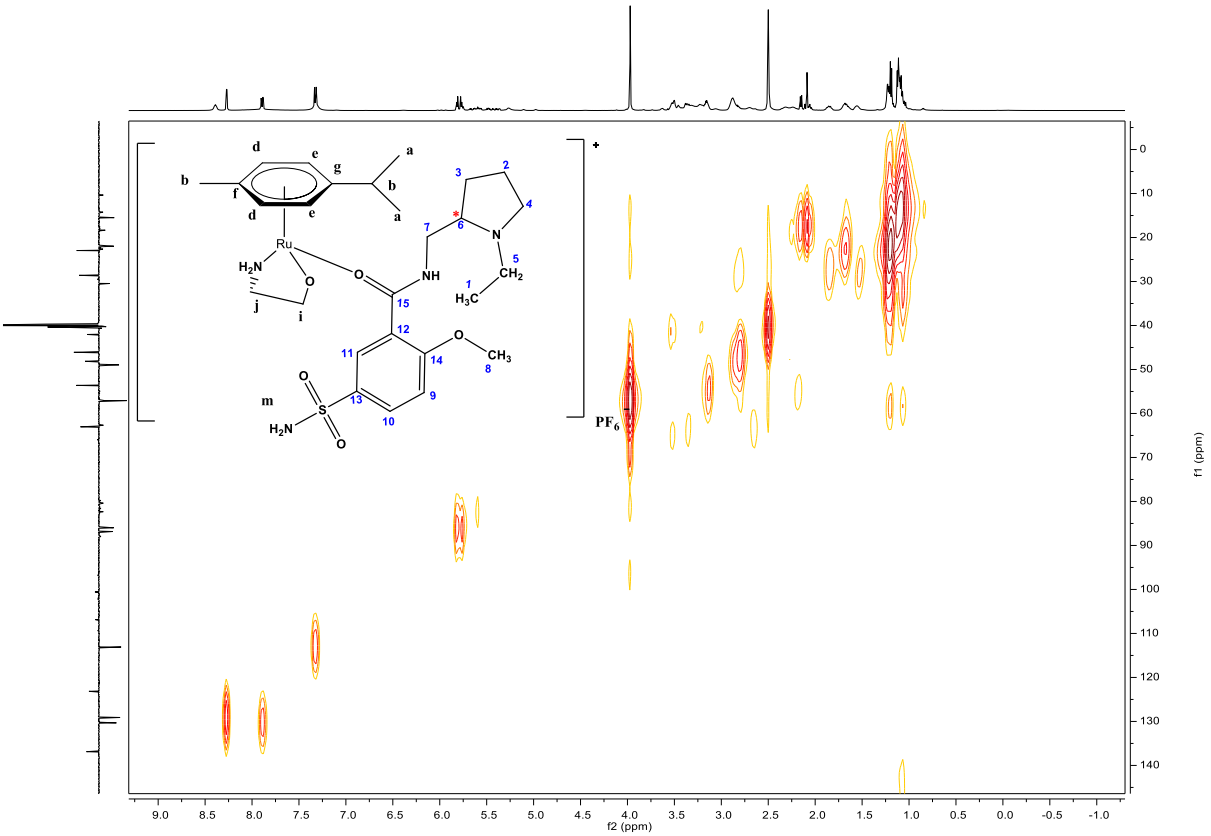


Figure S23. HSQC NMR (500 MHz, , DMSO-*d6*) of Complex **3a**

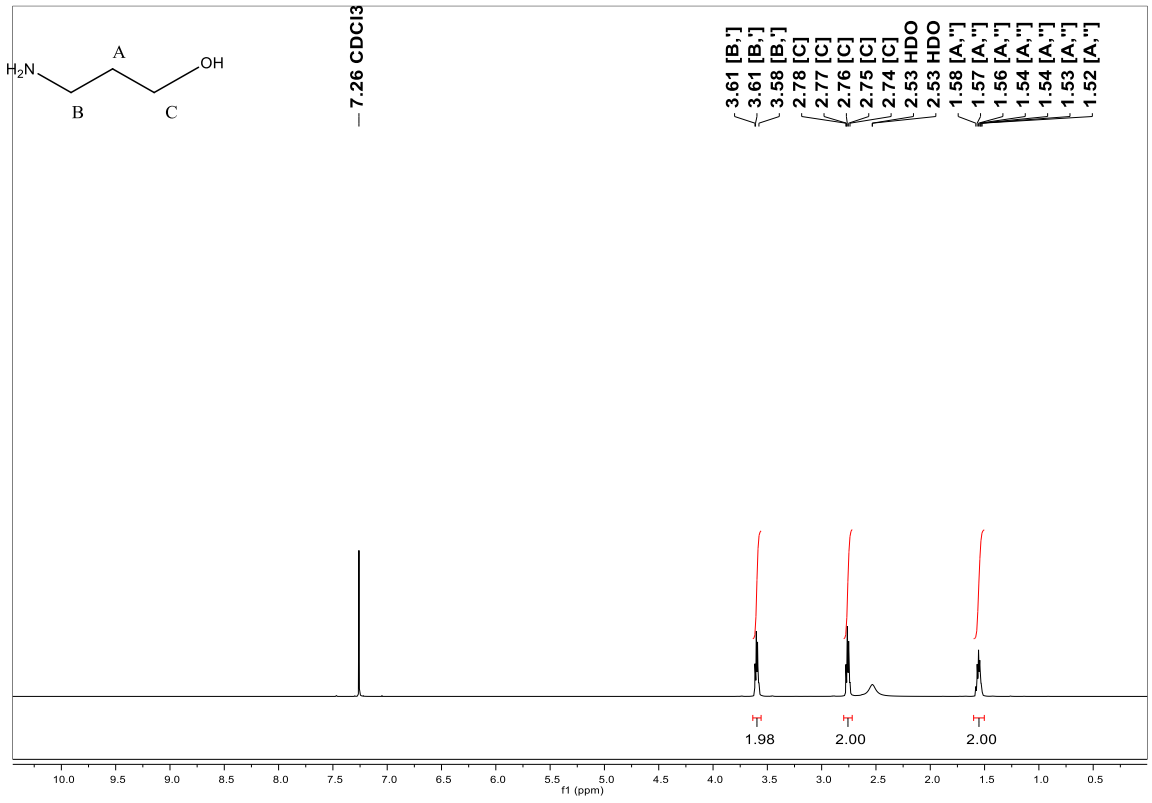


Figure S24. ^{1}H NMR (500 MHz, Chloroform-*d*) of (L4)

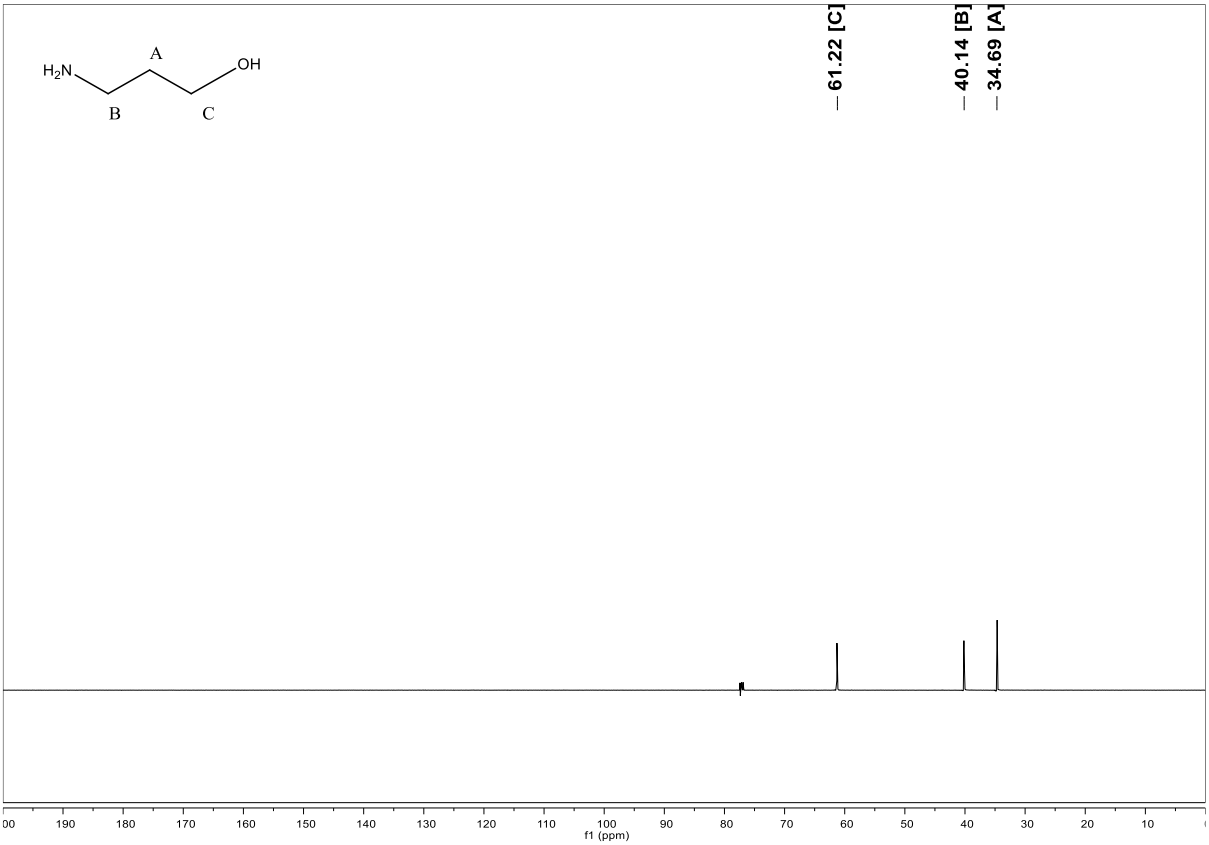


Figure S25. ^{13}C NMR (126 MHz, Chloroform-*d*) of (L4)

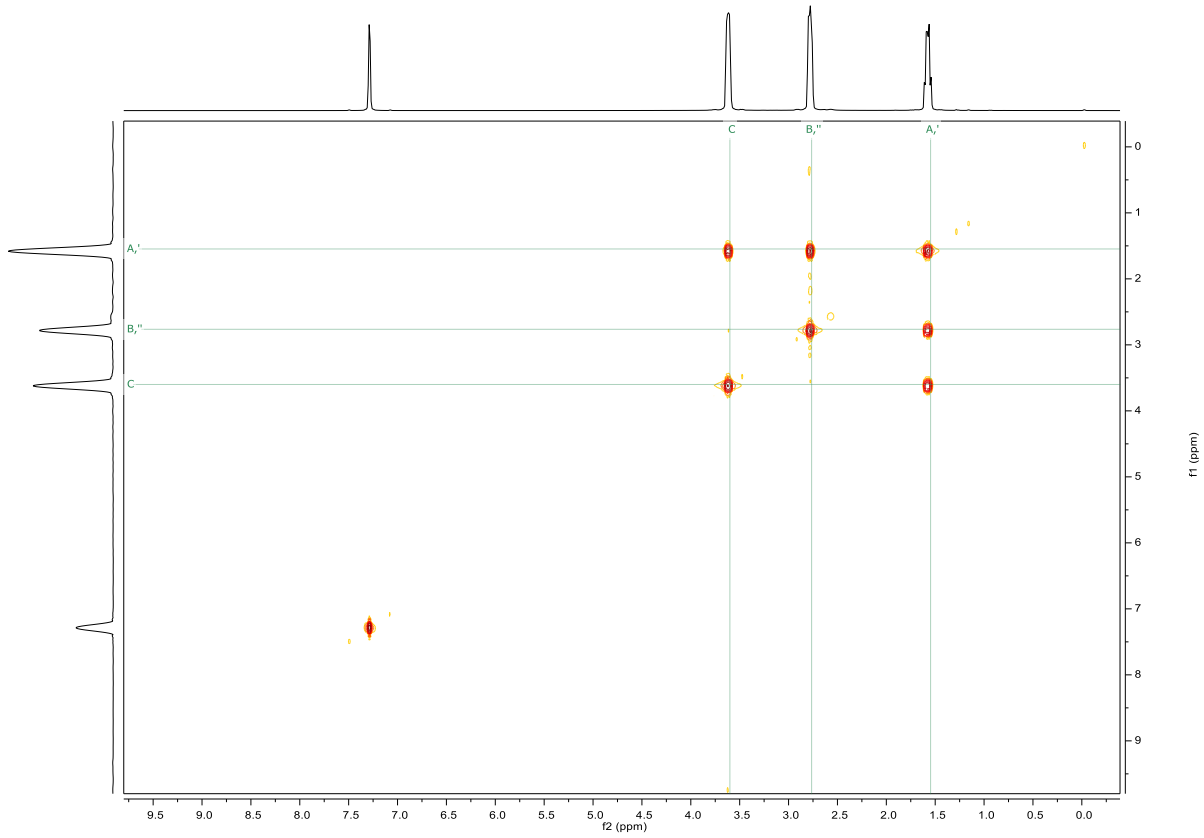


Figure S26. COSY NMR (500 MHz, Chloroform-*d*) of (L4)

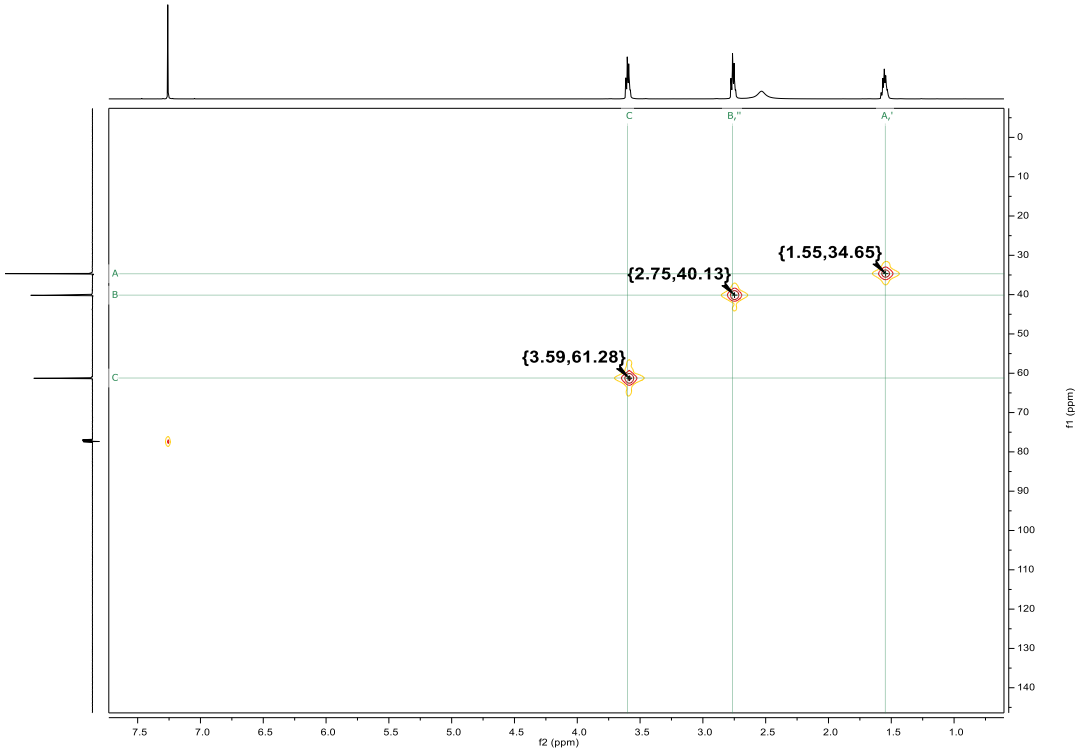


Figure S27. HMQC NMR (126 MHz, Chloroform-*d*) of (L4)

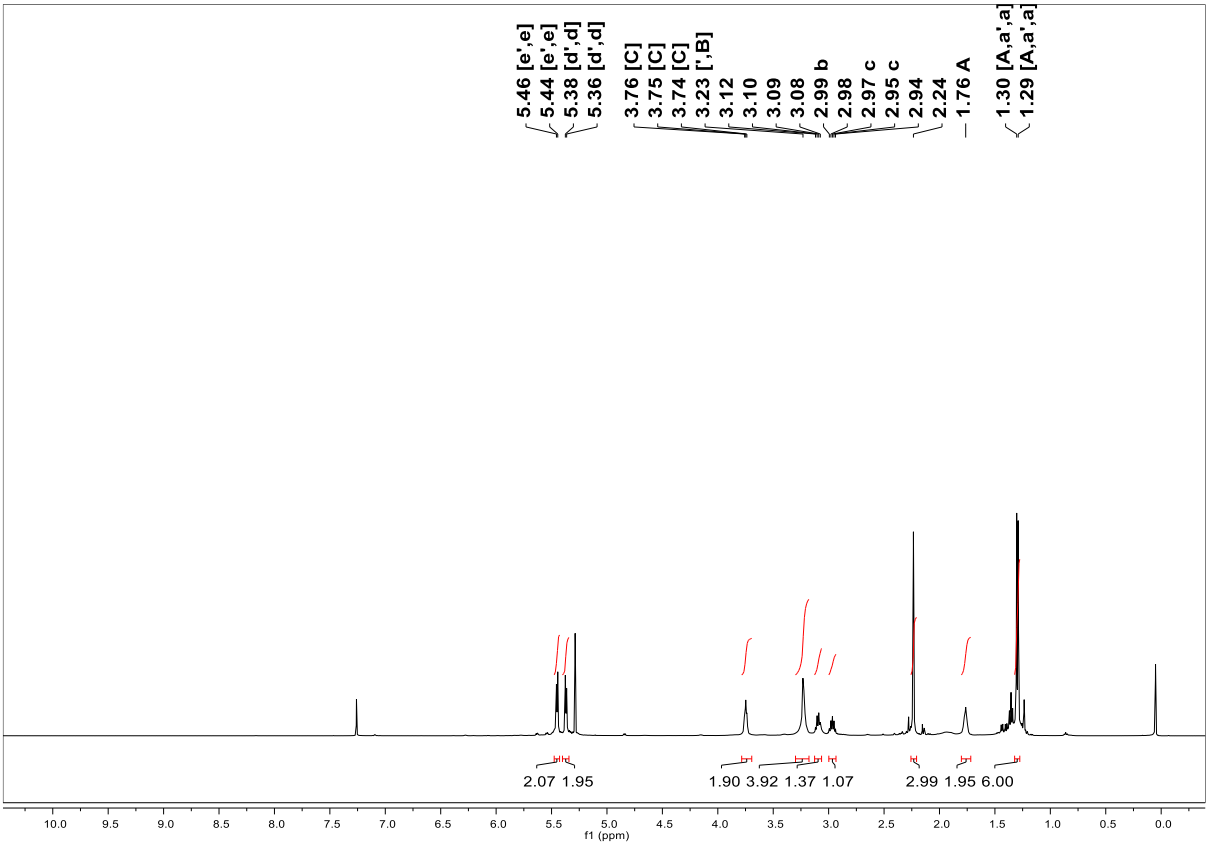


Figure S28. ^{1}H NMR (500 MHz, Chloroform-*d*) of complex **4**

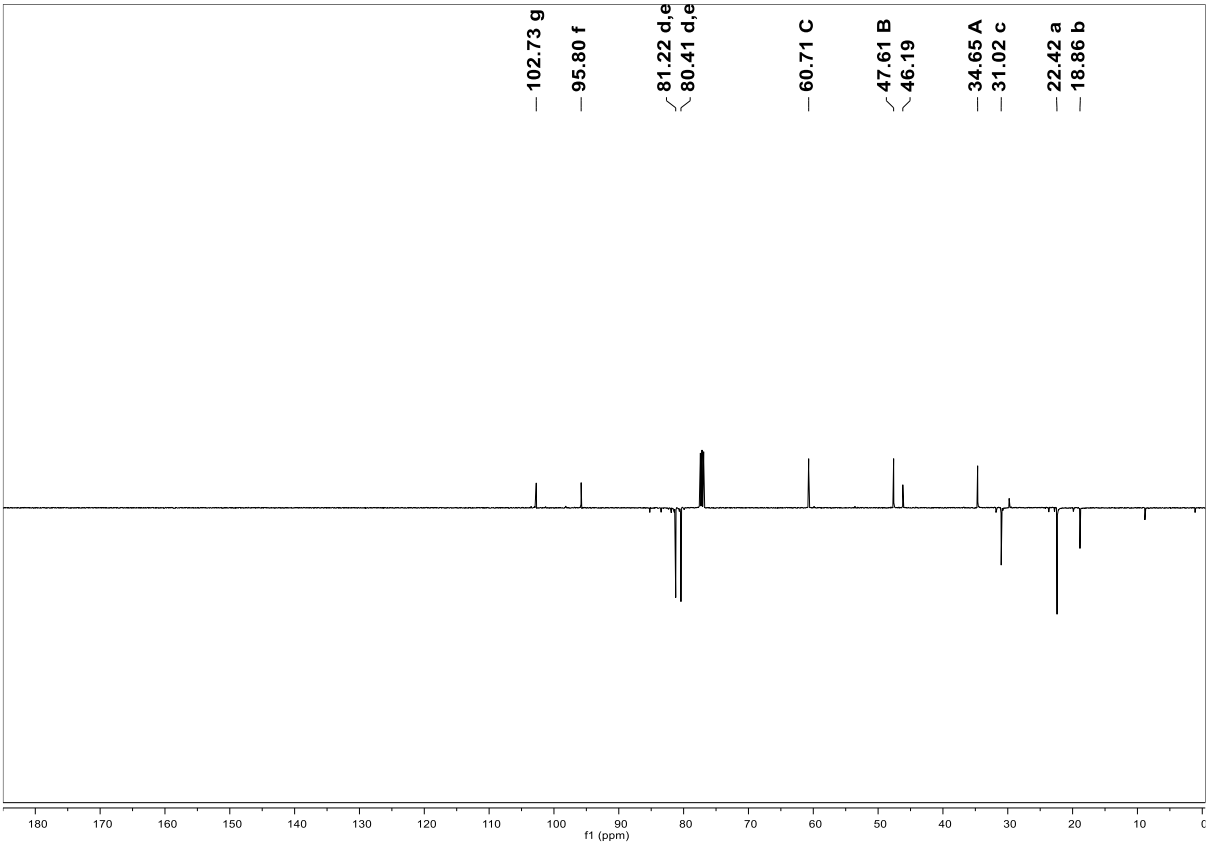


Figure S29. ^{13}C NMR (126 MHz, Chloroform-*d*) of complex **4**

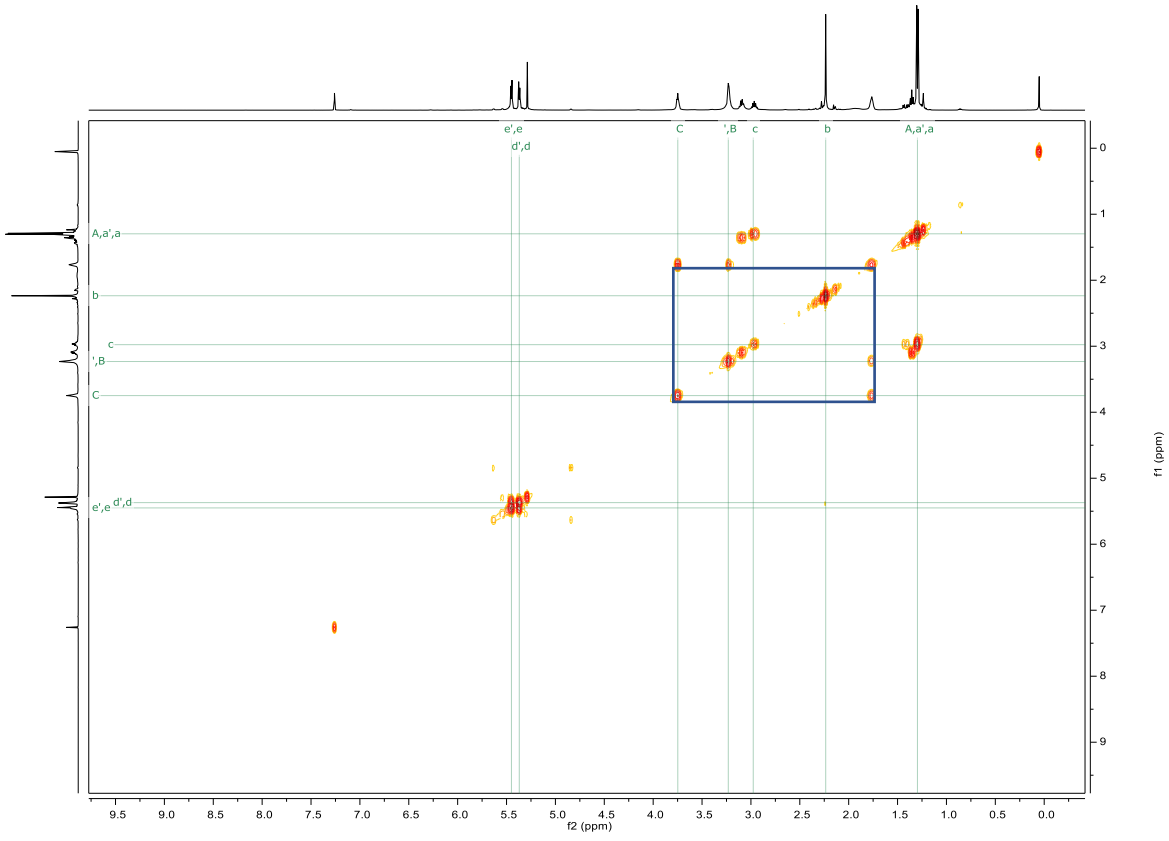


Figure S30. COSY (300 MHz, Chloroform-*d*) of complex **4**

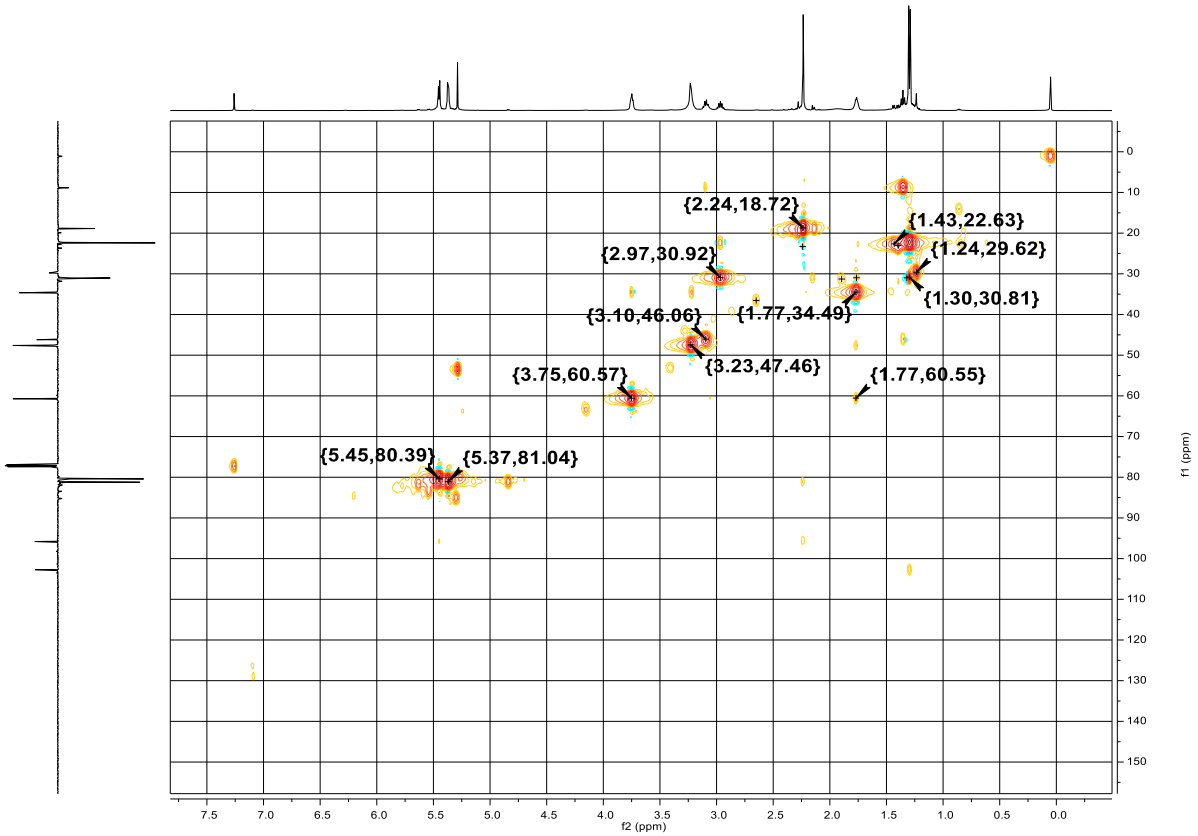


Figure S31. HMQC (126 MHz, Chloroform-*d*) of complex **4**

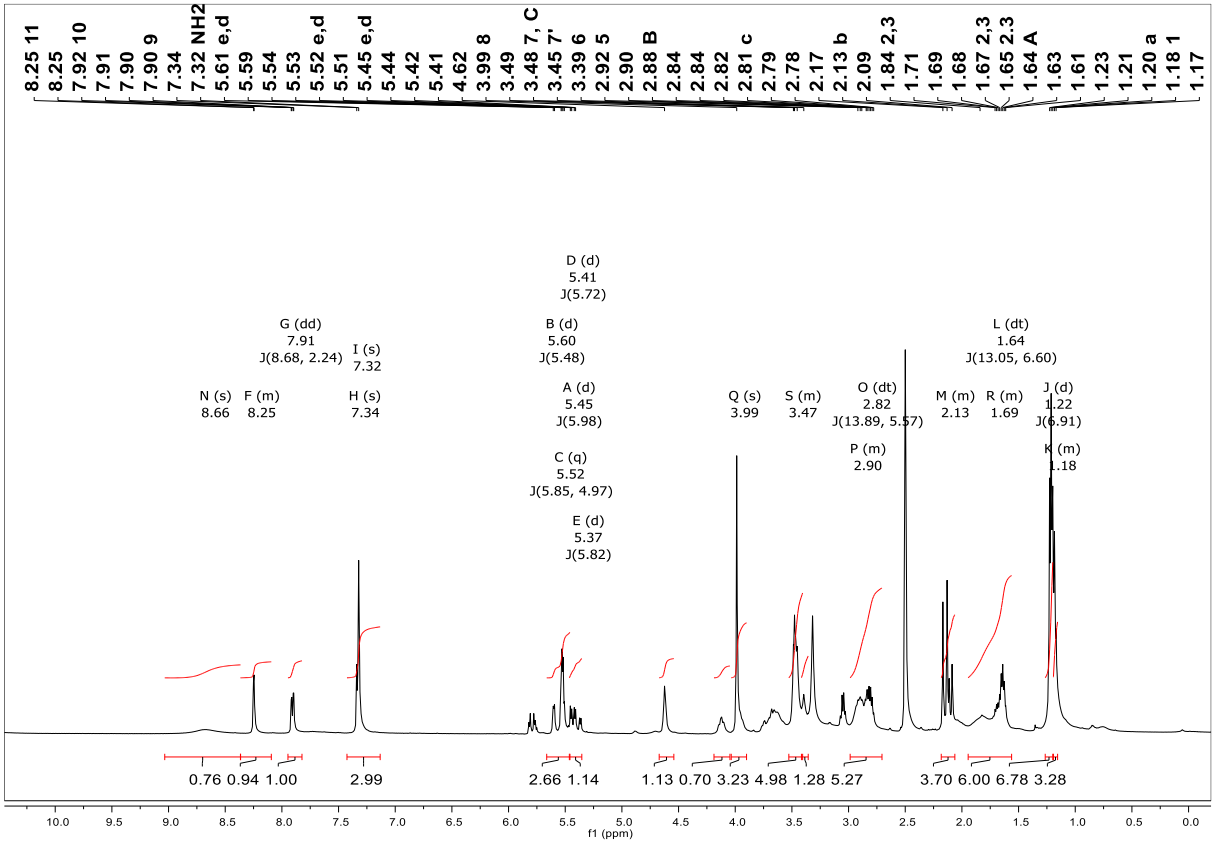


Figure S32. ^{1}H NMR (126 MHz, Chloroform-*d*) of complex **4a**

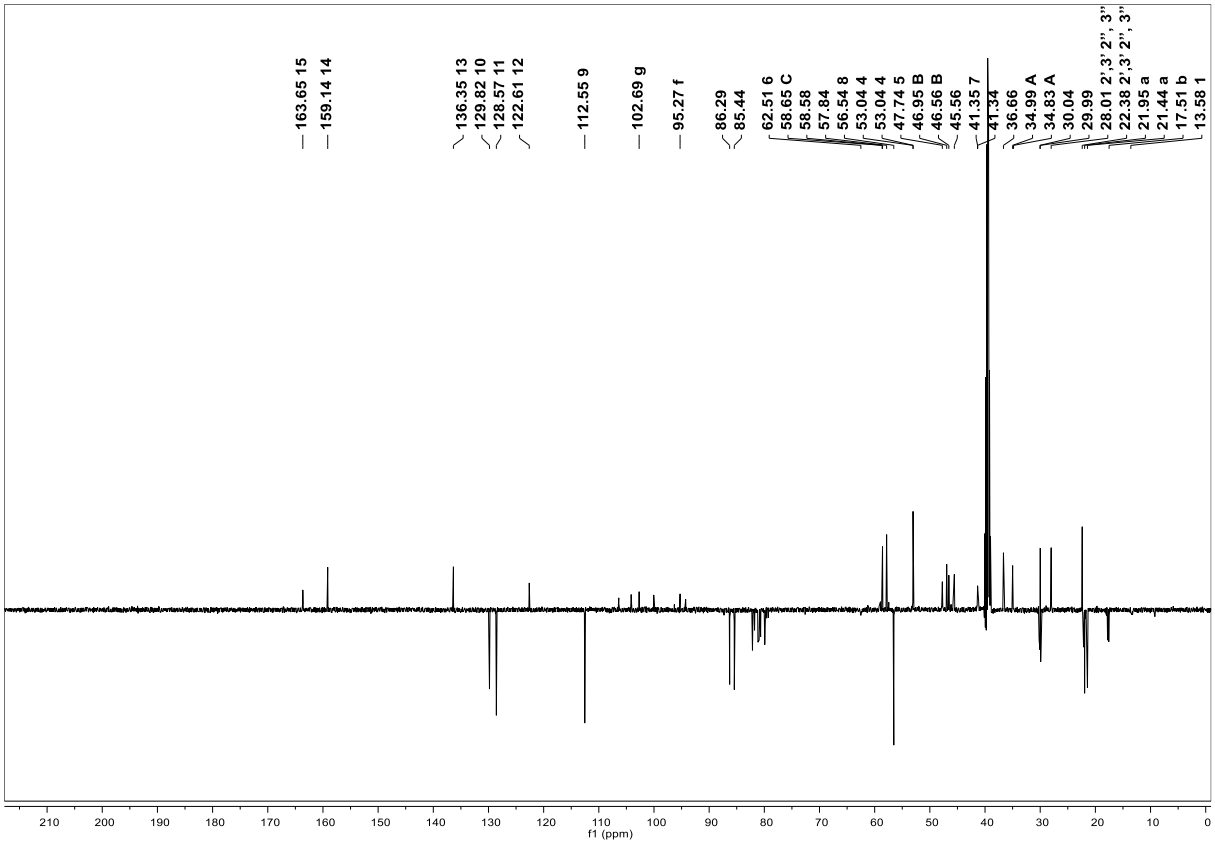


Figure S33. ^{13}C NMR (126 MHz, Chloroform-*d*) of complex **4a**

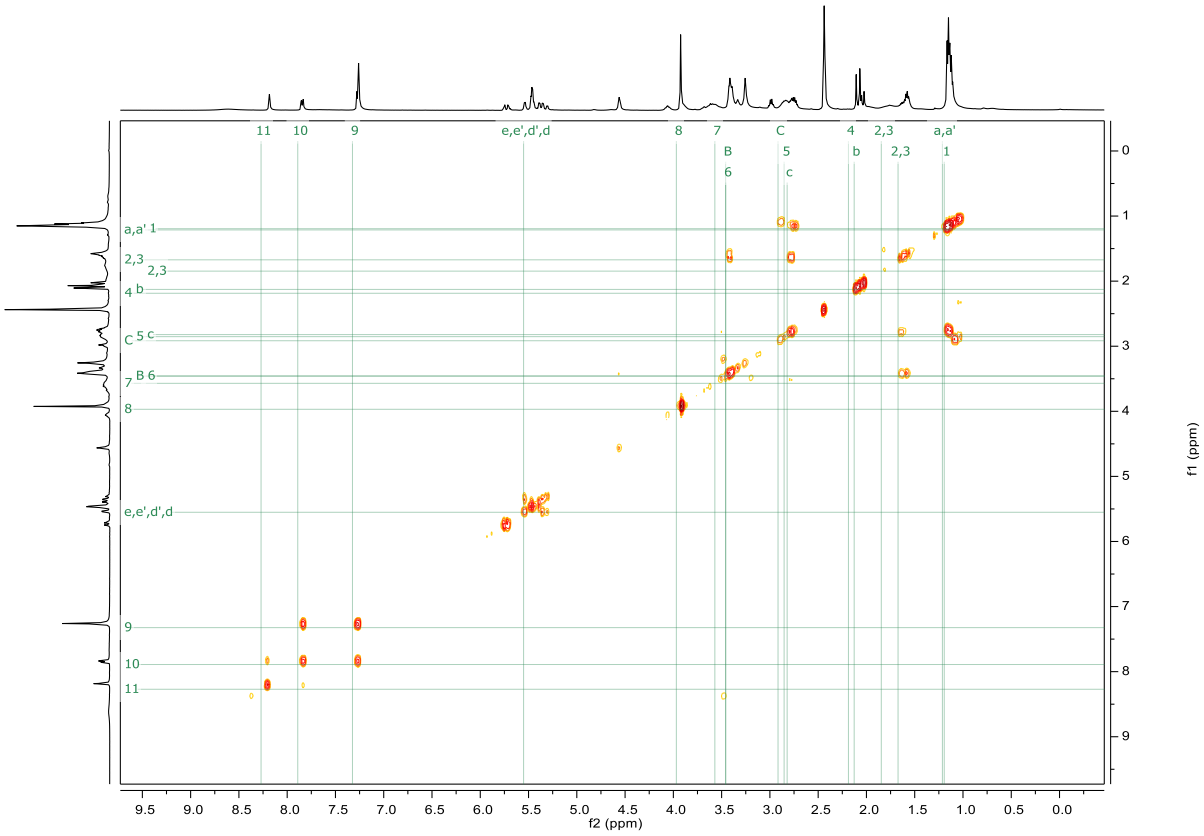


Figure S34. COSY (300 MHz, Chloroform-*d*) of complex **4a**

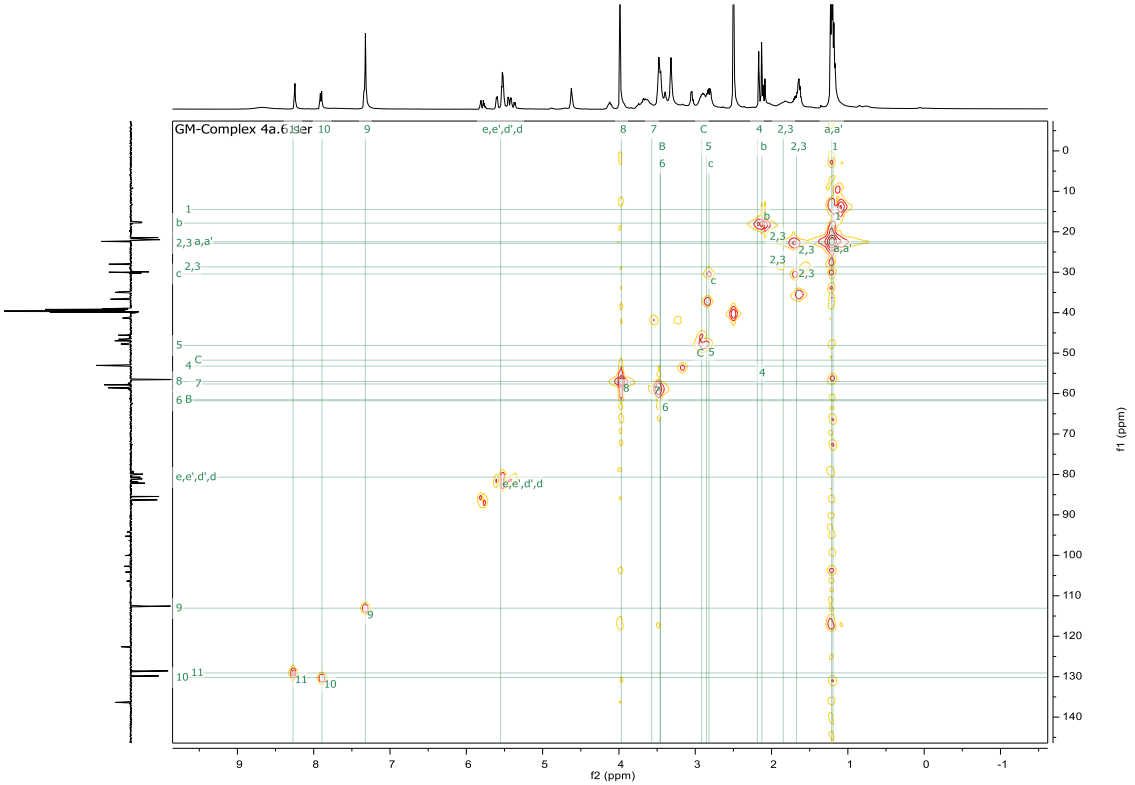


Figure S35. HMQC (126 MHz, Chloroform-*d*) of complex **4a**

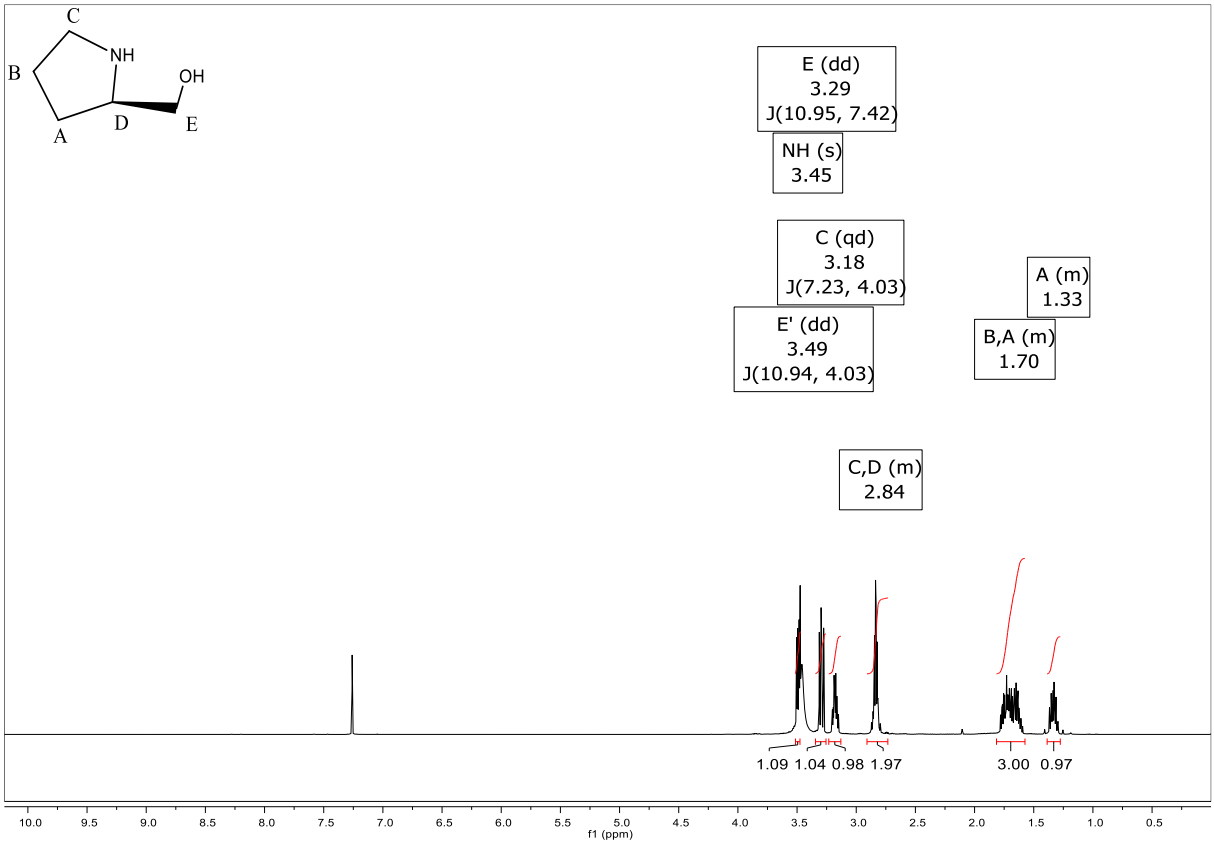


Figure S36. ^{1}H NMR (500 MHz, Chloroform-*d*) of L5

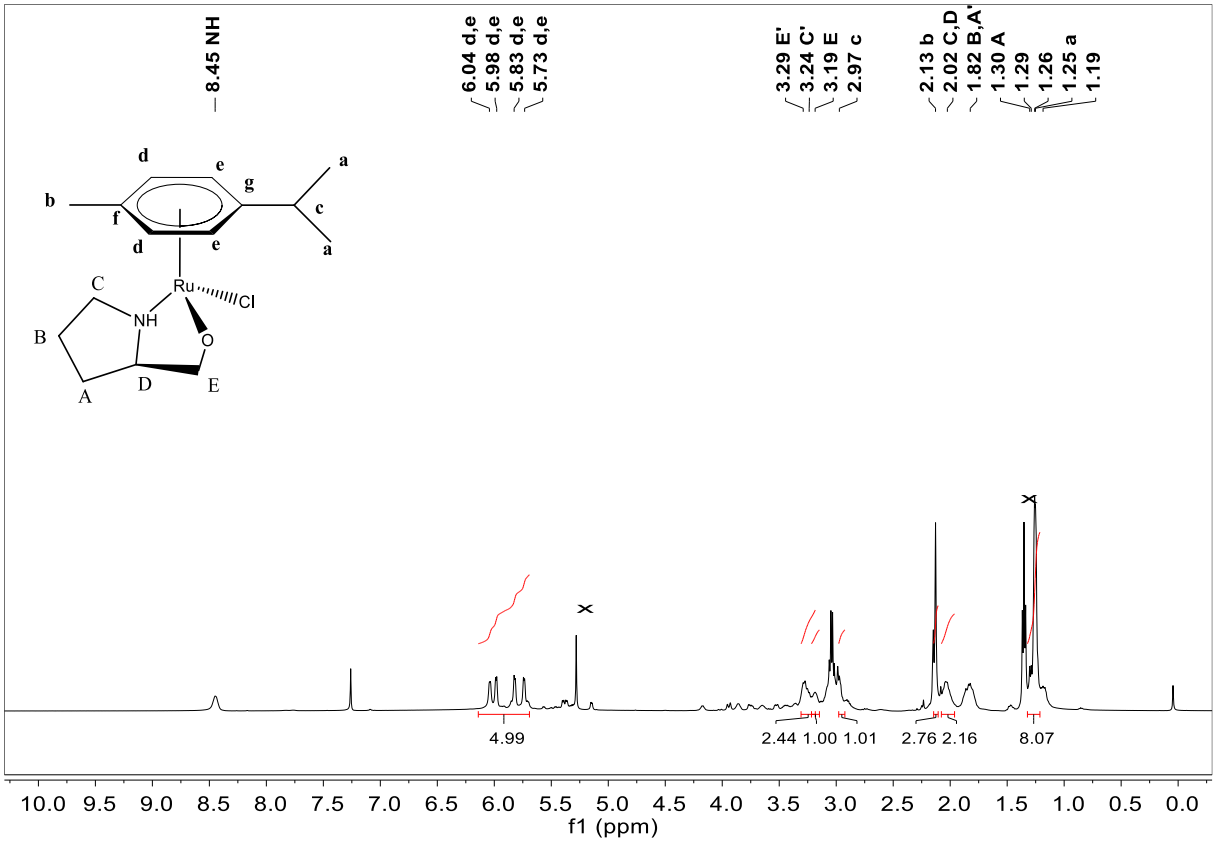


Figure S37. ^{1}H NMR (500 MHz, Chloroform-*d*) of Complex **5**

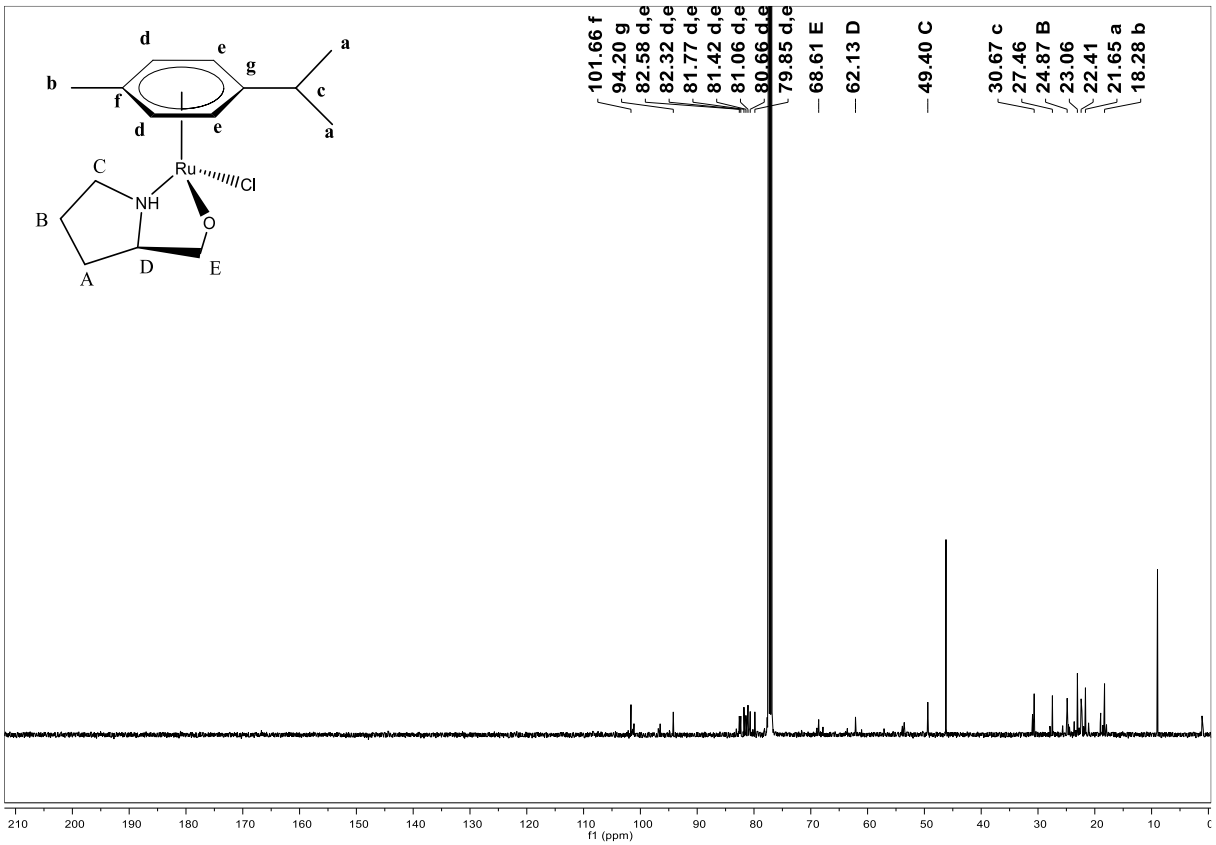


Figure S38. ^{13}C NMR (126 MHz, Chloroform-*d*) of complex **5**

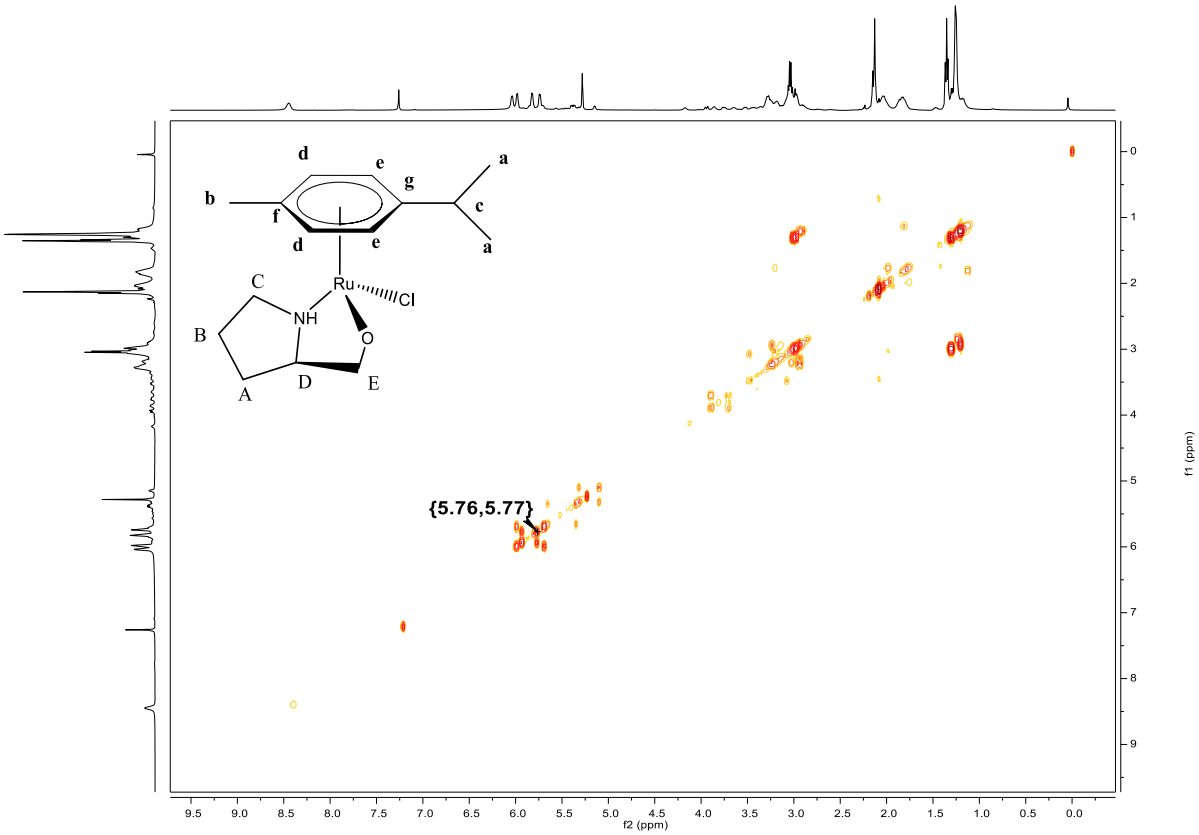


Figure S39. COSY NMR (500 MHz, Chloroform-*d*) of complex **5**

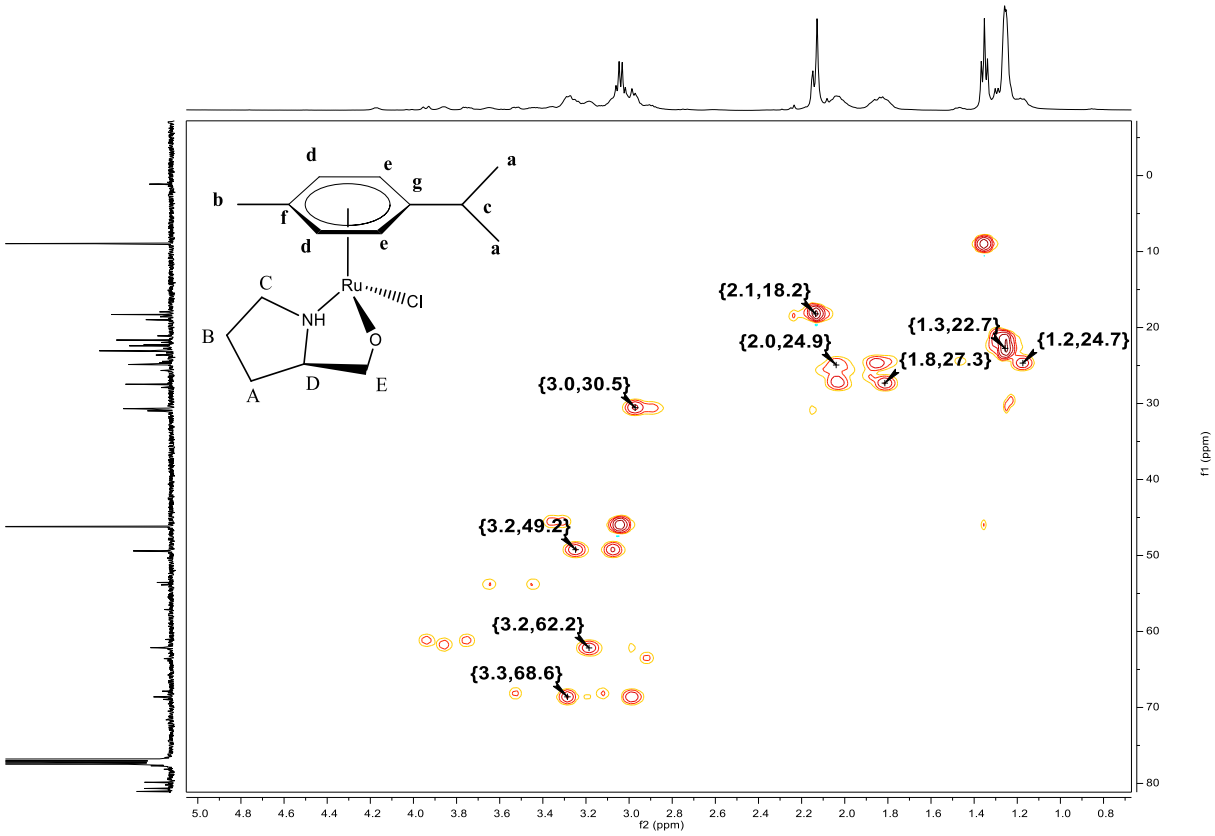


Figure S40. HMQC NMR (126 MHz, Chloroform-*d*) of complex **5**

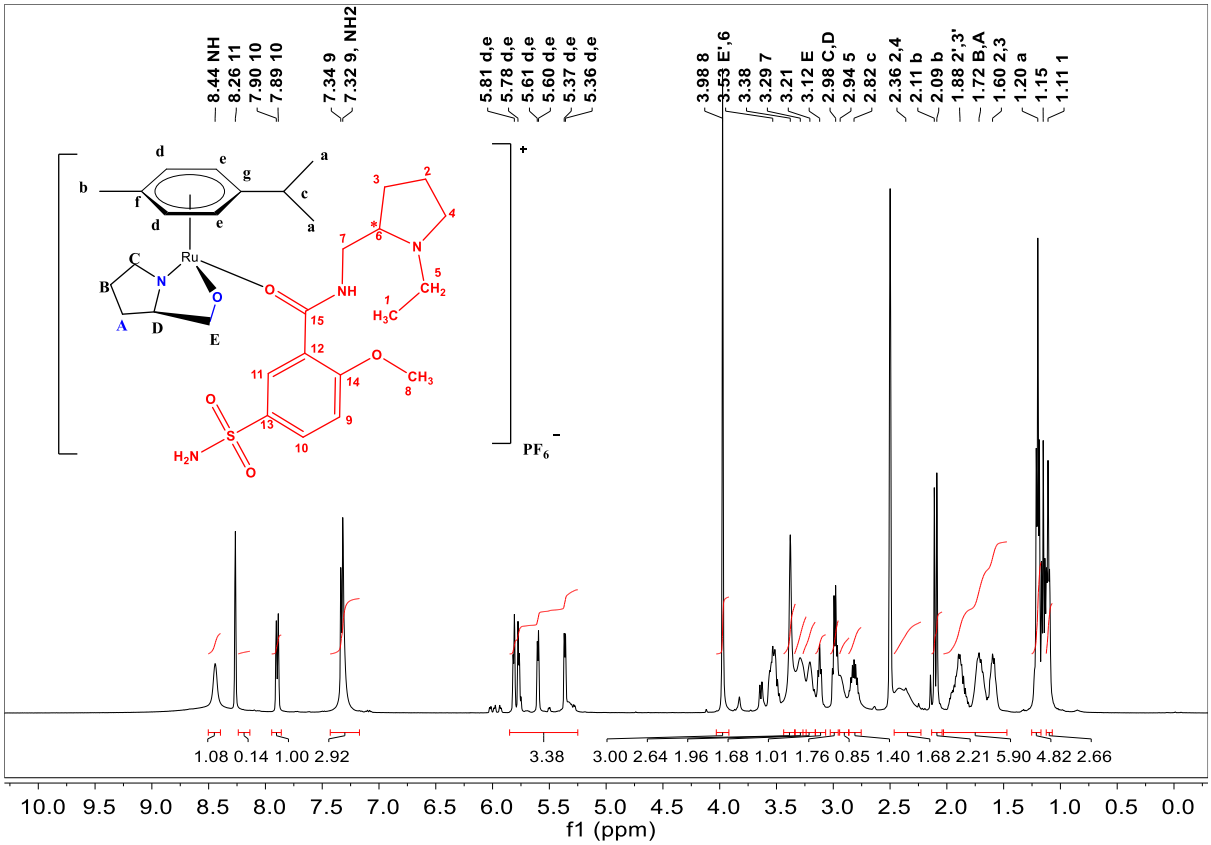


Figure S41. ^{1}H NMR (126 MHz, Chloroform-*d*) of complex **5a**

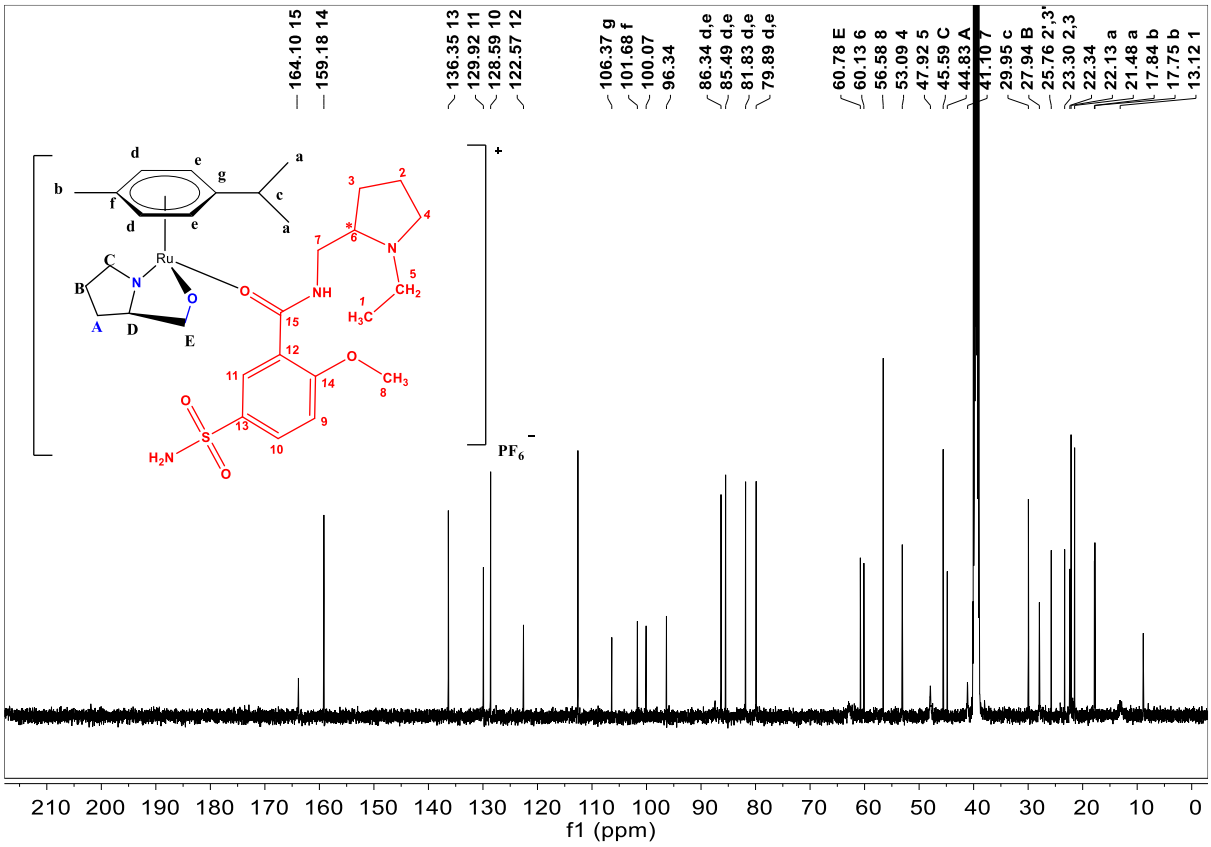


Figure S42. ^{13}C NMR (126 MHz, Chloroform-*d*) of complex **5a**

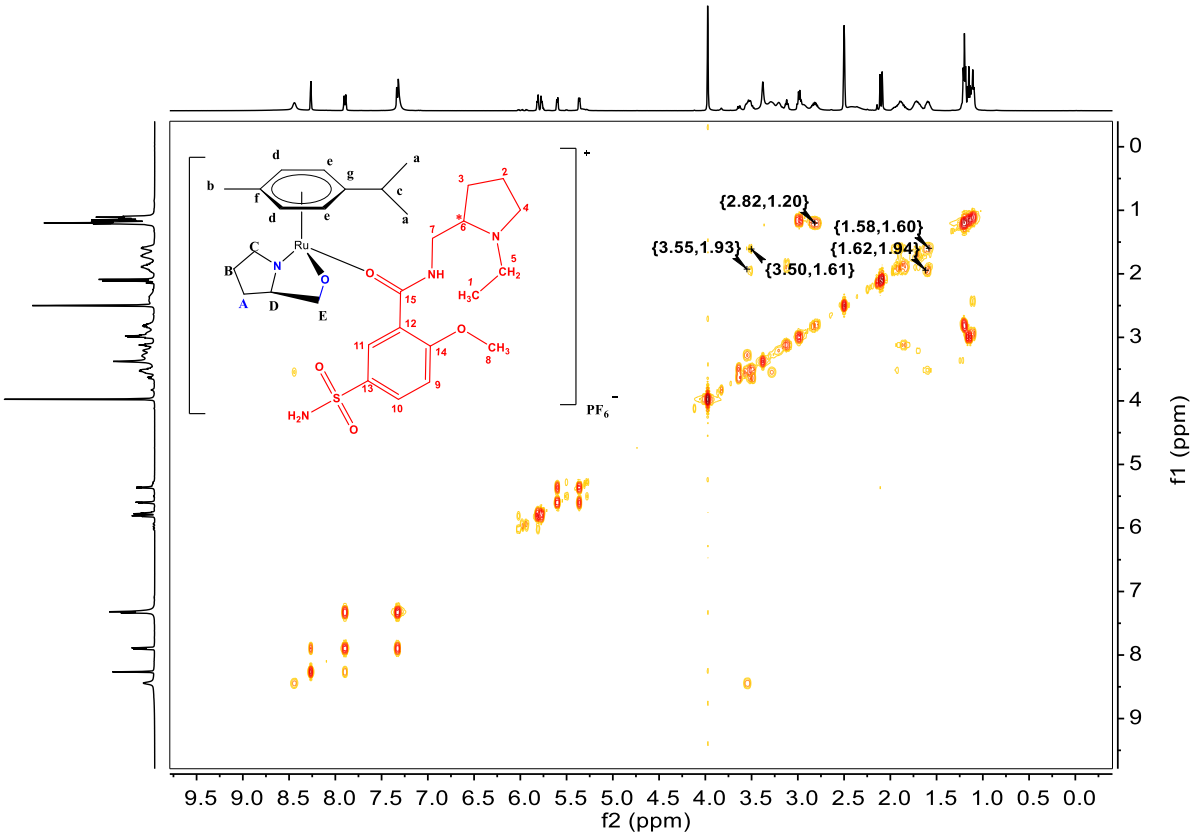


Figure S43. COSY (300 MHz, Chloroform-*d*) of complex **5a**

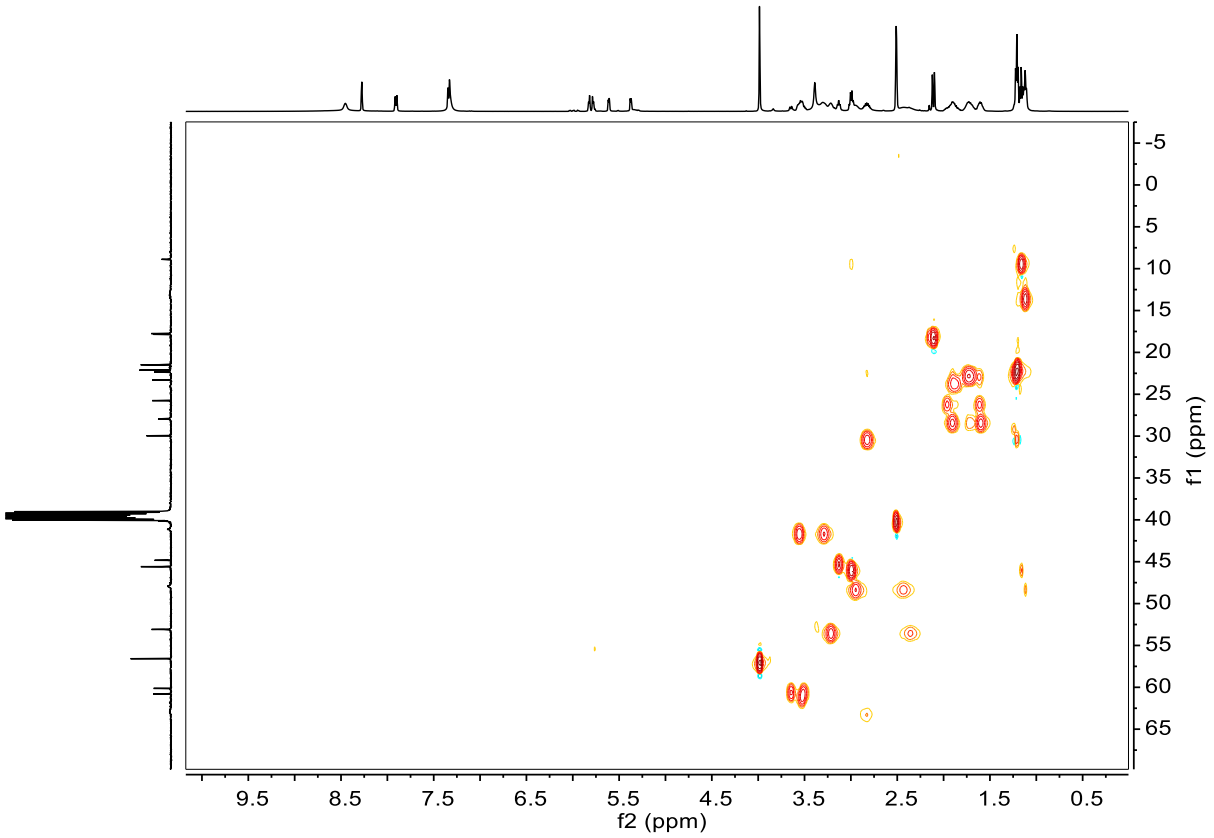


Figure S44. HMQC (126 MHz, Chloroform-*d*) of complex **5a**

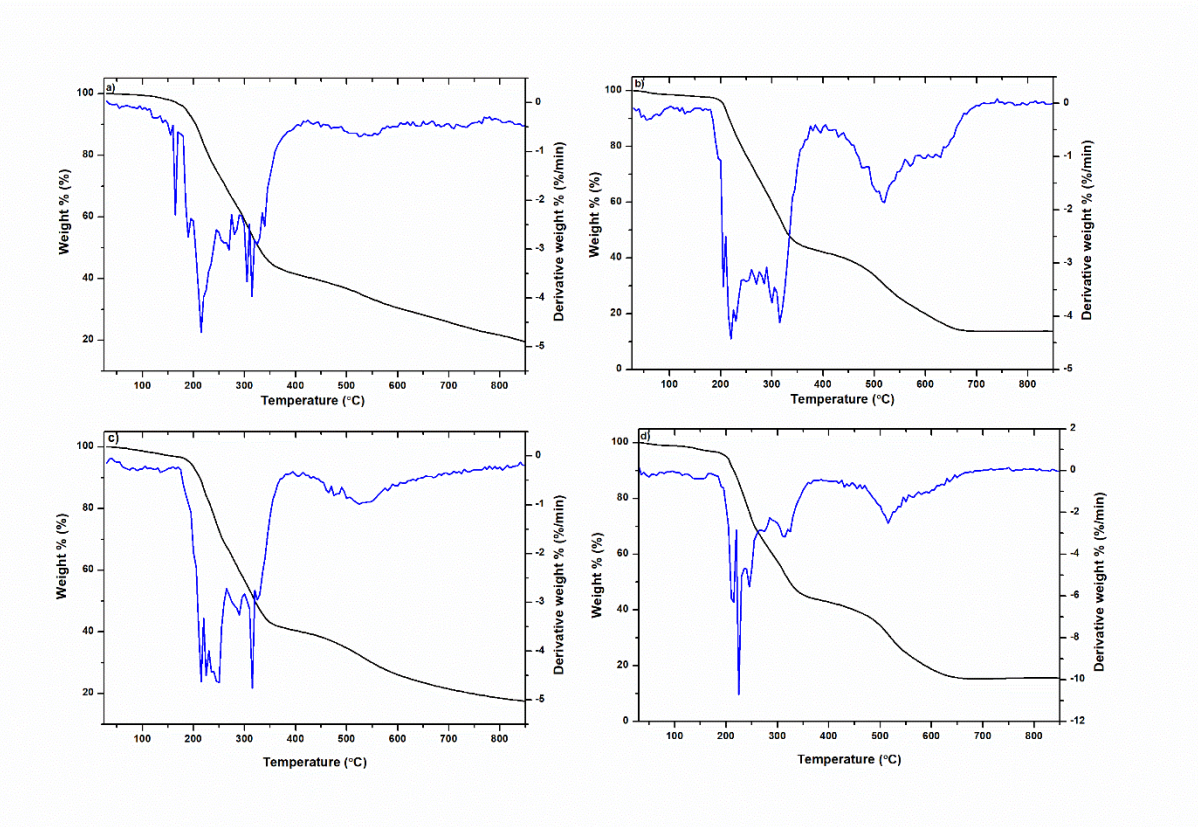


Figure S45. TGA thermograms of a) Complex **2a**, b) Complex **3a**, c) Complex **4a** and d) Complex **5a**

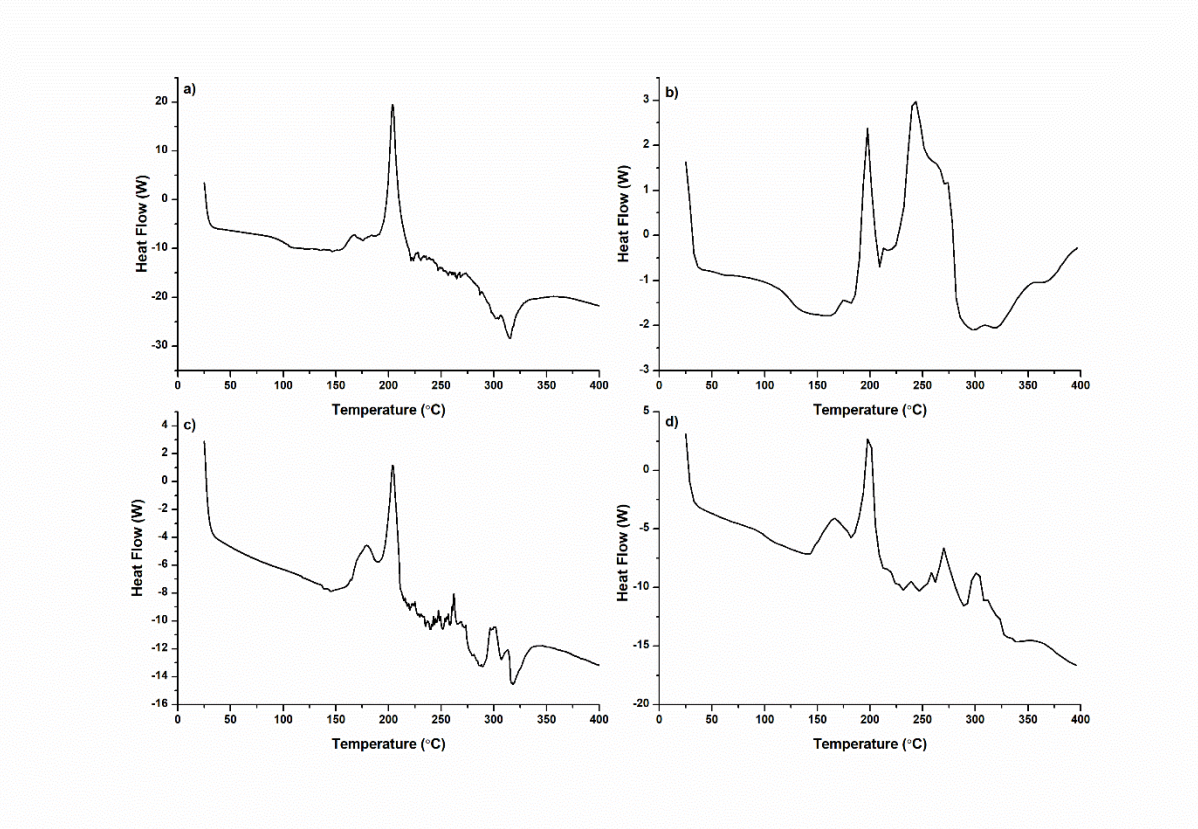


Figure S46. DSC curves of a) Complex **2a**, b) Complex **3a**, c) Complex **4a**, d) Complex **5a**

Sulpiride UV-Vis Calibration report

288 nm

Std1.Replicate1 (A)	0.1207
Std1.Replicate2 (A)	0.1209
Std1.Replicate3 (A)	0.1208
Std1.Replicate4 (A)	0.1208
Std2.Replicate1 (A)	0.2532
Std2.Replicate2 (A)	0.2531
Std2.Replicate3 (A)	0.2534
Std2.Replicate4 (A)	0.2532
Std 3.Replicate1 (A)	0.3883
Std 3.Replicate2 (A)	0.3882
Std 3.Replicate3 (A)	0.3881
Std 3.Replicate4 (A)	0.3885
Std 4.Replicate1 (A)	0.5391
Std 4.Replicate2 (A)	0.5392
Std 4.Replicate3 (A)	0.5392
Std 4.Replicate4 (A)	0.5392
Std 5.Replicate1 (A)	0.6623
Std 5.Replicate2 (A)	0.6618
Std 5.Replicate3 (A)	0.6618
Std 5.Replicate4 (A)	0.6617

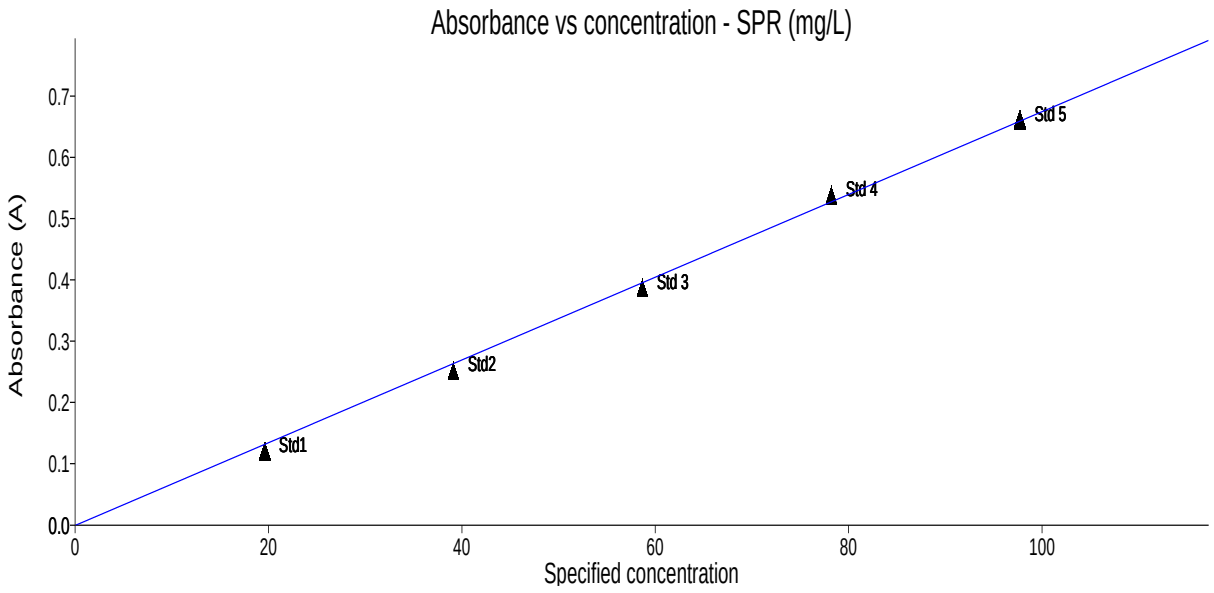


Figure S47. Sulpiride calibration curve

```
CALIBRATION REPORT


Calibration Time:       Tuesday, December 02, 2014 4:37 PM South Africa
Standard Time
User Full Name :        Analyst

Component Name:         SPR
Component Units:        mg/L

Calibration:            Calibration Curve - Linear (y=a1x+a0)
```

Baseline Correction: None

Settings (nm): Position:288.00

Force through Zero: Yes

Calibration Coefficients :
a0 = 0.000000
a1 = 0.006754

Specified Correlation Coefficient: 0.980000
Calculated Correlation Coefficient: 0.998854

Index	StandardID	Specified	Calculated	Residual
1	Std1	19.5400	17.8796	1.6604
2	Std1	19.5400	17.9035	1.6365
3	Std1	19.5400	17.8816	1.6584
4	Std1	19.5400	17.8879	1.6521
5	Std2	39.0800	37.4984	1.5816
6	Std2	39.0800	37.4815	1.5985
7	Std2	39.0800	37.5253	1.5547
8	Std2	39.0800	37.4843	1.5957
9	Std 3	58.6200	57.4918	1.1282
10	Std 3	58.6200	57.4841	1.1359
11	Std 3	58.6200	57.4591	1.1609
12	Std 3	58.6200	57.5227	1.0973
13	Std 4	78.1600	79.8186	-1.6586
14	Std 4	78.1600	79.8350	-1.6750
15	Std 4	78.1600	79.8350	-1.6750
16	Std 4	78.1600	79.8459	-1.6859
17	Std 5	97.7000	98.0626	-0.3626
18	Std 5	97.7000	97.9902	-0.2902
19	Std 5	97.7000	97.9866	-0.2866
20	Std 5	97.7000	97.9721	-0.2721